



## City Research Online

### City, University of London Institutional Repository

---

**Citation:** Wang, Z. (2021). Optimal design of wind-excited tuned mass-damper-inerter (TMDI)-equipped tall buildings. (Unpublished Doctoral thesis, City, University of London)

This is the accepted version of the paper.

This version of the publication may differ from the final published version.

---

**Permanent repository link:** <https://openaccess.city.ac.uk/id/eprint/25782/>

**Link to published version:**

**Copyright:** City Research Online aims to make research outputs of City, University of London available to a wider audience. Copyright and Moral Rights remain with the author(s) and/or copyright holders. URLs from City Research Online may be freely distributed and linked to.

**Reuse:** Copies of full items can be used for personal research or study, educational, or not-for-profit purposes without prior permission or charge. Provided that the authors, title and full bibliographic details are credited, a hyperlink and/or URL is given for the original metadata page and the content is not changed in any way.

**Optimal Design of Wind-Excited Tuned Mass-Damper-  
Inerter (TMDI)-Equipped Tall Buildings**

*Thesis by*

ZIXIAO WANG

*In partial fulfilment for the degree of  
Doctor of Philosophy*



CITY, UNIVERSITY OF LONDON

*School of Mathematics, Computer Science & Engineering*

*Department of Civil Engineering*

*Research Centre for Civil Engineering Structures*

February 2021



CITY, UNIVERSITY OF LONDON

School of Mathematics, Computer  
Science & Engineering

Research Centre for Civil  
Engineering Structures

**Optimal Design of Wind-Excited Tuned Mass-Damper-  
Inerter-Equipped Tall Buildings**

Doctoral Candidate: *Zixiao Wang*

Supervisor: *Dr Agathoklis Giaralis*

London, February 2021

# Table of contents

<b>Abstract</b> .....	v
<b>Publications</b> .....	vii
<b>Acknowledgements</b> .....	viii
<b>List of figures</b> .....	ix
<b>List of tables</b> .....	xiv
<b>List of acronyms</b> .....	xv
<b>Chapter 1 - Introduction</b> .....	1
1.1 Background and Motivation .....	1
1.1.1 Tall buildings and wind-related performance requirements .....	1
1.1.2 Human motion perception and occupant comfort criteria in wind-excited buildings .....	5
1.1.3 Wind-borne motion control of tall buildings in the cross-wind direction .....	6
1.1.4 Dynamic vibration absorbers (DVAs) for motion control of wind-excited tall buildings .....	8
1.2 Aim and objectives .....	14
1.3 Thesis organisation .....	14
<b>Chapter 2 - State of Art Review on Inerter-Based Vibration Control for Building Structures</b> .....	17
2.1 Preliminary remarks .....	17
2.2 The Inerter .....	17
2.2.1 Mechanical element and device implementations .....	19
2.2.2 Technological aspects and different inerter implementations .....	20
2.3 Inerter-based vibration control configurations .....	21
2.3.1 The tuned viscous mass damper (TVMD) .....	21
2.3.2 The tuned inerter damper (TID) .....	23
2.3.3 The tuned mass damper inerter (TMDI): a generalization of TMD and TID .....	24
2.4 Applications of TMDI to benchmark building structures .....	26
2.4.1 Earthquake engineering applications .....	26
2.4.2 Wind engineering applications .....	27
2.5 Research gaps .....	28
<b>Chapter 3 - Optimal TMDI Tuning for Wind Excited Buildings</b> .....	29
3.1 Preliminary remarks .....	29
3.2 Optimal TMDI design for occupant comfort in wind excited structures .....	30
3.2.1 Optimal design problem formulation .....	30
3.2.2 Numerical solution strategy .....	31
3.3 Modelling of case-study building structure and wind force excitation .....	32
3.3.1 Benchmark building description and finite element modelling .....	32
3.3.2 Low-order planar frame model .....	34
3.3.3 Wind force excitation model .....	36
3.4 TMDI-equipped tall building modelling and structural analysis for crosswind excitation .....	38
3.5 Optimal TMDI design for occupant comfort .....	40



3.5.1 Convexity and optimality of the TMDI design problem .....	42
3.5.2 Sensitivity of primary optimal design parameters to secondary parameters and to wind velocity .....	45
3.6 Performance-based assessment and design in optimally tuned TMDI-equipped structures.....	46
3.6.1 Peak top floor acceleration, secondary mass stroke, and inertance force .....	46
3.6.2 Trading secondary mass to inertance .....	49
3.7 Performance assessment of non-optimally designed TMDI structure.....	51
3.7.1 Robustness to detuning due to changes of benchmark structure properties .....	51
3.7.2 Performance for increased reference wind velocity, $V_{ref}$ .....	52
3.8 Closure .....	53
<b>Chapter 4 - Analytical and Numerical Investigation of TMDI Connectivity and Primary Structure Influence .....</b>	<b>56</b>
4.1 Preliminary remarks .....	56
4.2 Two-DOF modelling and analysis of TMDI-equipped continuous flexural cantilever structures .....	57
4.2.1 System description and equations of motion in time domain .....	57
4.2.2 Frequency response functions.....	60
4.2.3 Random vibration analysis for white noise excitation .....	61
4.3 OPTIMAL TMDI DESIGN USING THE TWO-DOF SIMPLIFIED MODEL.....	62
4.3.1 Optimal TMDI design for resonant harmonic loading.....	62
4.3.2 Optimal TMDI design for white noise excitation .....	65
4.4 Geometric shape variation of primary structure .....	67
4.4.1 Geometric shape definition and derivation of fundamental mode shapes.....	67
4.4.2 Verification of the simplified 2-DOF model for optimal TMDI design and performance assessment.....	71
4.5 Performance assessment of TMDI-equipped structures with different geometric shapes.....	72
4.5.1 Influence of depth ratio $R$ to free-end displacement .....	73
4.5.2 Influence of depth profile (primary structure shaping) to free-end displacement and acceleration .....	75
4.5.3 Influence of primary structure shaping to TMDI stroke and control forces.....	79
4.6 Closure .....	82
<b>Chapter 5 - Extending the Use of TMDI to High-Rise Buildings: Soft Top Floor Modification ....</b>	<b>84</b>
5.1 Preliminary remarks .....	84
5.2 Case-study coupled core-frame building and FE modelling .....	85
5.3 Low-order planar model of uncoupled case-study structure and wind force excitation.....	87
5.3.1 Stiffness matrix derivation and verification based on modal properties .....	87
5.3.2 Inherent damping modelling .....	90
5.3.3 Wind excitation model.....	91
5.4 Optimal TMDI design for serviceability performance accounting for top-storey stiffness reduction .....	92
5.4.1 Convexity and nature of achieved optimality .....	93
5.4.2 Sensitivity of optimal primary design parameters to top-storey stiffness .....	95

5.5 Performance assessment and design of optimal TMDI-equipped structure with reduced top-storey stiffness.....	96
5.5.1 Floor acceleration and secondary mass stroke .....	97
5.5.2 Inerter force and damping force.....	99
5.5.3 Trading secondary mass to inertance and/or top-storey stiffness in performance-oriented design .....	101
5.6 Influence of building properties to floor acceleration performance .....	102
5.6.1 Influence of inherent structural damping modelling.....	103
5.6.2 Influence of r/c core stiffness.....	104
5.7 Closure .....	105
<b>Chapter 6 - A Novel Sizing Optimisation Method for Minimal-Weight Skeletal Structures .....</b>	<b>107</b>
6.1 Preliminary remarks .....	107
6.2 Formulation of the structural sizing optimisation problem subject to frequency constraint ..	109
6.3 Numerical solution strategy of the optimal sizing problem .....	112
6.3.1 Iterative algorithm for resizing design variables.....	112
6.3.2 Expressing target frequency in terms of modal strain energy .....	116
6.4 Convexity of the frequency-constrained sizing optimisation problem.....	117
6.5 Illustrative application and validation of sizing optimisation method.....	118
6.6 Closure .....	120
<b>Chapter 7 - Integrated Optimal Design of DVA-Equipped Wind Excited Buildings for Weight Minimisation and Occupant Comfort.....</b>	<b>121</b>
7.1 Preliminary remarks .....	121
7.2 A novel framework for minimal-weight design of inerter-based DVA-equipped tall buildings to meet cross-wind serviceability criteria.....	122
7.3 Modelling of case-study building structure and wind force excitation model .....	124
7.3.1 Case-study building description and surrogate planar frame model .....	124
7.3.2 Crosswind force excitation model.....	125
7.3.3 Assessment for occupant comfort criteria in the crosswind direction.....	126
7.4 Re-design of uncontrolled case-study building and optimal TID tuning for occupant comfort ... ..	127
7.4.1 Re-design of uncontrolled benchmark structure for occupant comfort.....	127
7.4.2 TID-equipped tall building modelling and structural analysis for crosswind excitation... ..	128
7.4.3 Optimal TID design for minimum-weight host structure subject to occupant comfort requirement .....	129
7.5 Application of the integrated optimal design framework to the TID-equipped MRF 15-storey benchmark building.....	131
7.5.1 Performance curve of optimal TID-equipped host structure in relation to ISO6897 occupant comfort demand curve.....	131
7.5.2 Trading inertance to primary structure weight in optimally designed DVA-equipped structures for minimal weight .....	132
7.5.3 Structural weight reduction potential of optimally tuned TIDs for building structures	

deficient to occupants' comfort.....	134
7.6 Closure .....	135
<b>Chapter 8 - Concluding Remarks .....</b>	<b>137</b>
8.1 Summary of achievements and contributions.....	137
8.2 Main limitations and future directions .....	143
<b>Appendix A - Frequency domain random vibration analysis for structural response estimation to crosswind excitation forces .....</b>	<b>145</b>
<b>Appendix B - Modelling of wind loads to building structures and verification against wind tunnel force data .....</b>	<b>147</b>
B.1 Overview of wind loading to structures.....	147
B.2 Modelling of wind loads to structures in the along-wind direction .....	149
B.3 Modelling of wind loads to structures in the crosswind direction .....	151
B.4 Modelling of the spatial correlation of wind forces.....	153
B.5 Case-study structural response verification of wind models vis-à-vis experimental wind tunnel force data.....	155
<b>References .....</b>	<b>157</b>

## Abstract

In recent years, global urbanisation trends created pressing demands for residential and office space in all major cities of developed and developing countries. These demands are increasingly addressed by height-wise urban development. This is underpinned by the advent of new high strength materials and stiff lightweight structural components which enable designing and construction of tall buildings with large height-to-width aspect ratios. Indeed, slender tall buildings with rectangular floor plans achieve economical land utilisation in congested urban environments and facilitate efficient inner space organisation. However, such structures are prone to excessive wind-borne oscillations in the crosswind direction due to vortex shedding (VS) effects generated around their corner edges. These oscillations may generate floor accelerations beyond code-specific occupant comfort thresholds under moderate frequently occurring wind actions leading to serviceability failure. In this regard, the design of most slender tall buildings with rectangular plan view is commonly governed by serviceability occupant comfort criteria. At the same time, the latest sustainability requirements for new-built structures urge for minimising material usage as the portion of global carbon emissions due to building material manufacturing is rising. In this regard, this thesis addresses occupant comfort and material usage requirements in wind-excited tall buildings by equipping structures with innovative passive inerter-based dynamic vibration absorber (DVA) motion control configurations in conjunction with novel DVA-equipped tall building design approaches for weight minimisation.

To this aim, the thesis contributes an optimal tuned mass damper inerter (TMDI) design approach in which TMDI stiffness and damping properties are numerically determined via a computationally efficient scheme to minimise floor accelerations in wind-excited buildings for given inertial TMDI properties (i.e., inertance and secondary mass) and inerter element connectivity. Optimally designed TMDIs for a wide range of inertial properties and various inerter connectivities are obtained for a benchmark slender 74-storey building subjected to experimentally calibrated spatially-correlated crosswind force field accounting for VS effects. Design charts on the TMDI inertial (mass-inertance) plane are furnished demonstrating that fixed structural performance level in terms of occupant comfort can be more efficiently achieved through lightweight TMDIs if compared with classical tuned mass dampers (TMDs) as long as sufficient inertance is provided. Further, TMDI sensitivity to host structure properties and to reference wind velocity is shown to decrease by increasing inertance or by spanning more floors in connecting the secondary mass with the host structure by the inerter.

Moreover, attention is focused on examining the efficacy of the TMDI motion control potential for different dominant mode shape of buildings. This is facilitated by putting forward a novel analytical two-degree-of-freedom (2DOF) dynamical model representing TMDI-equipped slender buildings treated as continuous tapered cantilever beams with varying geometrical properties and, thus, mode shapes. It is found that reduced free-end displacement

and TMDI stroke are achieved for structures in which the ratio of flexural rigidity over mass decreases faster with height, resulting in vibration modal shapes with higher convexity. The latter is quantified through the average modal curvature shown to be well-correlated with TMDI motion control improvement. It is concluded that appropriate building shaping extends the applicability of the TMDI to structures in design situations where connecting the inerter away from the free-end is practically and economically challenging.

Inspired by the above findings, a local structural modification, top-storey softening, is proposed in conjunction with optimally tuned top-floor TMDI for improved occupant comfort performance in typical core-frame slender buildings. Comprehensive numerical data pertaining to a parametric investigation for a 34-storey steel-concrete composite core-frame structure demonstrate that the proposed top-storey softening reduces attached TMDI mass/weight requirements and inerter force for fixed floor acceleration performance and inertance. It further reduces TMDI stroke and achieves increased robustness to TMDI stiffness and damping properties as well as to the assumed inherent structural damping. It is concluded that by leveraging inertance and top-storey lateral flexibility, the proposed solution can efficiently control VS-induced floor acceleration with small additional gravitational (added weight) and horizontal (inerter and damping) forces.

Lastly, an innovative framework for the optimal design of wind-excited DVA-equipped tall buildings subject to serviceability comfort criteria is proposed, which enables minimising material usage for occupant comfort-governed building structures by exploiting the motion control capability of inerter-based DVAs. The framework relies on a novel optimal structural member sizing Lagrangian formulation for minimum-weight structural design, in conjunction with optimal DVA tuning for occupant comfort under crosswind excitation. The applicability and usefulness of the framework is exemplified by application to a routine occupant-comfort-sensitive 15-storey steel moment resisting frame (MRF) building equipped with a ground floor tuned inerter damper (TID). The inclusion of the TID together with the herein proposed design framework achieve up to 67% steel tonnage savings in meeting the ISO 6897 occupant comfort criteria. Pareto optimal solutions further demonstrate that the self-weight of lateral wind-load resisting structural systems can be traded to TID inertance, potentially leading to significant material usage reductions.

Overall, numerical data furnished in this thesis demonstrate that the herein contributed optimal design formulations and algorithms as well as the innovative inerter-based DVAs are quite promising in achieving new types of sustainable and resilient slender tall buildings to wind excitation which can address current and future demands for residential and office space in modern city centres.

## Publications

### Journal Papers:

- Wang, Z. and Giaralis, A. (2020). “Top-storey softening for enhanced mitigation of vortex shedding induced vibrations in wind-excited optimal tuned mass damper inerter (TMDI)-equipped tall buildings.” *J. Struct. Eng.*, DOI: 10.1061/(ASCE)ST.1943- 541X.0002838.
- Petrini, F., Giaralis, A., Wang, Z. (2020). “Optimal tuned mass-damper-inerter (TMDI) design in wind-excited tall buildings for occupants’ comfort serviceability performance and energy harvesting.” *Eng. Struct.*, 204: 109904.
- Wang, Z. and Giaralis, A. (2020) “Enhanced motion control performance of the tuned mass damper inerter (TMDI) through primary structure shaping.” Manuscript submitted to *Struct. Control Health Monit.* (accepted pending on minor revisions).

### Conference Papers:

- Wang, Z. and Giaralis, A. (2020). “Enhanced mitigation of floor accelerations in wind-excited tall buildings equipped with optimal mass damper inerter via localized storey softening.” XI International Conference on Structural Dynamics (EURODYN 2020), 22-24 June, Athens, Greece.
- Wang, Z. and Giaralis, A. (2020). “Parametric investigation of primary structure properties to the tuned mass-damper-inerter (TMDI) performance in motion control of white-noise excited flexural cantilevered beam.” XI International Conference on Structural Dynamics (EURODYN 2020), 22-24 June, Athens, Greece.
- Wang, Z. and Giaralis, A. (2019). “Vibration suppression and energy harvesting potential in wind excited buildings equipped with ground floor tuned inerter damper.” In: Proceedings of 9<sup>th</sup> ECCOMAS Thematic Conference on Smart Structures and Materials, 8-11 July, Paris, France.
- Petrini, F., Wang, Z., and Giaralis, A. (2018). “Simultaneous vibration suppression and energy harvesting in wind excited tall buildings equipped with the tuned mass damper inerter (TMDI).” In: Proceedings of the XV Conference of the Italian Association for Wind Engineering (IN-VENTO-2018), September 9-12, Napoli, Italy.

## Acknowledgements

Dr Agathoklis Giaralis (First supervisor)	City, University of London	For his supervision, patient support, structured guidance throughout this enlightening journey, and for his valuable advice on my academic and professional development. The many opportunities I was privileged to have had at City were largely due to his thoughtfulness and openness.
Dr Alessandro Palmeri (External Examiner)	Loughborough University	For his valuable time and effort in critiquing and annotating the thesis with insightful comments and suggestions, as well as for his constructive feedback during the viva
Dr Alfredo Camara Casado (Internal Examiner)	City, University of London	For his valuable time and effort in scrutinising and furnishing the thesis with useful amendments and suggestions
Dr Francesco Petrini	Sapienza University of Rome	For his guidance and assistance in the initial stage of this research, and for lending the wind tunnel data and the finite element model used in Chapter 3 and Appendix B of this thesis
Prof. Kuldeep Viridi	City, University of London	For the full-time employment opportunity on his research project during the third year of my PhD studies.
My parents: Mingqiu Wang and Lan Rao My partner: Qing Chao		For their understanding, encouragement, unconditional love and support during my studies in London. This thesis is dedicated to them.

## List of figures

Figure number	Figure caption	Page
1.1.	(a) Home Insurance Building in Chicago; and (b) 432 Park Avenue in New York.	1
1.2.	(a) 509m-tall Taipei 101 Tower; (b) 632m-tall Shanghai Tower; and (c) 309m-tall Sydney Centrepoint Tower.	2
1.3.	A comparison of serviceability occupant comfort criteria from different design codes for a one-year recurrence period and within the frequency range 0.1 – 1.0Hz.	6
1.4.	(a) the 600 ton, pendulum-type TMD in Taipei 101; and (b) the 1000 ton, pendulum-type TMD in Shanghai Tower.	10
1.5.	Crosswind transfer function of the top floor (a) displacement; and (b) acceleration of an uncontrolled 74-storey benchmark tall building.	12
1.6.	A n-storey lumped-mass planar frame model equipped with a (a) top-floor TMD; (b) top-floor TMDI with connectivity “p”; and (c) ground-floor TID.	13
2.1.	Analogies of mechanical and electrical elements.	18
2.2.	Schematic representation of (a) an ideal inerter element; (b) a rack-and-pinion flywheel-based inerter device with $n$ gears; and (c) viscous mass damper with a rotational inertial mass.	20
2.3.	Mechanical model of a (a) viscous damper; (b) viscous mass damper/rotational inertia viscous dampers; and (c) tuned viscous mass damper equipped undamped SDOF system.	22
2.4.	a 14-storey MRF building in Tohoku Japan that utilises viscous dampers and tuned viscous mass dampers configured in conjunction with V-shaped bracing systems for seismic control.	23
3.1.	Flowchart of the pattern search algorithm with adapted search range for optimal TMDI design.	32
3.2.	Detailed FE model of the adopted benchmark case-study tall building structure and in-plan lateral translational mode shapes.	33
3.3.	Power spectral density functions of cross-wind forces acting at different floor levels of the case-study structure.	37
3.4.	TMDI equipped lumped-mass surrogate planar frame model of the wind-excited case-study building with “p” connectivity and typical rack-and-pinion flywheel inerter device with $n$ gears.	39
3.5.	Iterative optimal TMDI design with $\mu=0.5\%$ , $\beta=20\%$ , and $p=3$ for a benchmark building with $V_{ref}=30$ m/s (a) 1 <sup>st</sup> iteration; (b) 2 <sup>nd</sup> iteration; and (c) 3 <sup>rd</sup> iteration.	42
3.6.	Objective function and design point of the optimisation problem in Eq.(21) for $\mu=0.5\%$ , $V_{ref}=30$ m/s and for different TMDI topologies and inertance ratios.	43
3.7.	Frequency response functions of top floor acceleration of the case-study structure for $V_{ref}=30$ m/s with no motion control (uncontrolled), controlled with optimal TMD ( $\mu=0.5\%$ ), and controlled with optimal TMDIs for fixed $\mu=0.5\%$ and for different TMDI topologies and inertance ratios.	44
3.8.	Optimal values of the primary design variables in $\mathbf{x}_1$ on the secondary design	45



	parameters plane.	
<b>3.9</b>	Sensitivity of the optimal values of the DVs to the variation of the wind speed. Case $\mu=0.5\%$ .	46
<b>3.10</b>	Peak top floor acceleration in $\text{mm/s}^2$ achieved with optimally designed TMDIs in different topologies and inertial properties: secondary mass ratio $\mu$ and inertance ratio $\beta$ .	47
<b>3.11</b>	Peak stroke of optimally designed TMDI in the secondary design parameters plane.	48
<b>3.12</b>	Peak inerter force of optimally designed TMDI in the secondary design parameters plane.	49
<b>3.13</b>	Performance-based design charts of TMDI for the case-study structure (a) Connectivity “-3”; (b) Various topologies for case-study structure occupants’ comfort threshold $102.9\text{mm/s}^2$ ; (c) Code-prescribed serviceability design threshold and performance of the adopted primary structure equipped with optimal TMDI with connectivity “-3”.	50
<b>3.14</b>	Robustness of optimally tuned TMDI to mass and damping properties perturbations of the case-study primary structure for $V_{\text{ref}}=30\text{m/s}$ .	52
<b>3.15</b>	Comparative performance of non-optimal TMDI under $V_{\text{ref}}=45\text{m/s}$ for retrofitting the case-study structure equipped with a TMD with $\mu=0.5\%$ optimally tuned for $V_{\text{ref}}=30\text{m/s}$ .	53
<b>4.1</b>	(a) Continuous flexural cantilevered uncontrolled (primary) structure; (b) TMDI-controlled structure; (c) Assumed deflected shape and virtually displaced deflected shape; (d) External loads acting on the primary structure; and (e) External loads acting to the TMDI mass.	57
<b>4.2</b>	Magnitude of the non-dimensional FRF, $H(\omega_1)$ , in Eq. (18) versus TMDI frequency ratio, $\nu$ , and damping ratio, $\zeta$ , for attached mass ratio $\mu=0.1\%$ , inertance ratios, $\beta=0$ (TMD) and $\beta=40\%$ , and connectivity ratios, (a) 2.5%; (b) 5.0%; and (c) 7.5%.	64
<b>4.3</b>	Magnitude of the non-dimensional FRF, $H(\omega_1)$ , in Eq. (4.18) versus TMDI frequency ratio for various secondary mass ratios, $\mu$ , inertance ratios, $\beta$ , and connectivity ratios, $CR$ .	64
<b>4.4</b>	Iterative pattern search algorithm illustration for solving the optimisation problem in Eq.(4.21) for TMDI with mass ratio $\mu=0.1\%$ , inertance ratio $\beta=40\%$ , and connectivity ratio $CR=7.5\%$ , and primary structure with $\zeta_1=2\%$ and deflected shape in Eq.(20): (a) 1 <sup>st</sup> iteration; (b) 2 <sup>nd</sup> iteration; and (c) 3 <sup>rd</sup> iteration.	66
<b>4.5</b>	Magnitude of the non-dimensional FRF, $H(\omega)$ , in Eq. (12) for optimally designed TMDIs to white noise excitation for various secondary mass ratios, $\mu$ , inertance ratios, $\beta$ , and connectivity ratios, $CR$ .	67
<b>4.6</b>	Considered geometric shapes of cantilevered beam-like primary structures.	68
<b>4.7</b>	Rigidity over mass distribution plots for all considered geometric shapes (depth profiles in Table 1) and for various depth ratios $R$ of cantilevered beam-like primary structures.	69
<b>4.8</b>	Numerically derived fundamental mode shapes and average modal curvature for primary structures with different depth profiles (shapes) and depth ratios $R$ .	70
<b>4.9</b>	Normalized mode coordinate difference between the free end and the inerter connecting location of primary structures, $\Psi(H)-\Psi(\chi)$ , with different depth profiles	71

	(shapes), depth ratios, $R$ , and inerter connectivity ratios, $CR$ .	
4.10	RMS free-end displacements of TMDI-equipped structures for attached mass $m_{TMDI}=0.1\% \times m_{Avg}^*$ and inertance $b=0.40 \times m_{Avg}^*$ for different geometric shapes and depth ratios normalized by the corresponding displacements of optimal TMD-equipped structures and plotted against $CR$ .	74
4.11	Peak free-end displacement of TMDI-equipped structures under resonant harmonic excitation for attached mass $m_{TMDI}=\mu \times m_{Avg}^*$ , inertance $b=\beta \times m_{Avg}^*$ , and various inerter connectivity ratios, $CR$ , primary structure shapes, and depth ratios $R$ . Values are normalized by the corresponding displacement of optimal TMD-equipped structures.	76
4.12	RMS free-end displacement of TMDI-equipped structures under white noise excitation for attached mass $m_{TMDI}=\mu \times m_{Avg}^*$ , inertance $b=\beta \times m_{Avg}^*$ , and various inerter connectivity ratios, $CR$ , primary structure shapes, and depth ratios $R$ . Values are normalized by the corresponding displacement of optimal TMD-equipped structures.	77
4.13	RMS free-end displacement of TMDI-equipped structures under white noise excitation as function of normalised average modal curvature (Fig.4.8(c)) for attached mass $m_{TMDI}=0.3\% \times m_{Avg}^*$ , inertance $b=0.4 \times m_{Avg}^*$ , and various inerter connectivity ratios, $CR$ , primary structure shapes, and depth ratios $R$ . Values are normalized by the corresponding displacement of optimal TMD-equipped structures.	78
4.14	RMS free-end acceleration of TMDI-equipped structures under white noise excitation for attached mass $m_{TMDI}=0.3\% \times m_{Avg}^*$ , inertance $b=0.4 \times m_{Avg}^*$ , and various inerter connectivity ratios, $CR$ , primary structure shapes, and depth ratios $R$ . Values are normalised by the corresponding acceleration of optimal TMD-equipped structures. Optimal tuning is for white noise excitation.	79
4.15	RMS TMDI attached mass stroke for TMDI-equipped structures under white noise excitation for attached mass $m_{TMDI}=0.1\% \times m_{Avg}^*$ , inertance $b=0.4 \times m_{Avg}^*$ , and various inerter connectivity ratios, $CR$ , primary structure shapes, and depth ratios $R$ . In the upper row of panels values are normalized by the corresponding stroke of TMD-equipped structures and in the bottom row of panels values are normalized by the stroke of TMDI uniform shaped structure with $CR=2.5\%$ .	80
4.16	RMS inerter resisting force (upper row of panels) and damping force (bottom row of panels) for attached mass, $m_{TMDI}=0.1\% \times m_{Avg}^*$ , inertance $b=0.4 \times m_{Avg}^*$ , and various inerter connectivity ratios, $CR$ , primary structure shapes, and depth ratios $R$ normalized by the corresponding values of optimal TMDI for the uniform primary structure with the inerter connectivity ratio, $CR=2.5\%$ .	81
4.17	RMS free-end displacement versus RMS inerter force (upper row of panels) and damping force (bottom row of panels) for attached mass, $m_{TMDI}=0.1\% \times m_{Avg}^*$ , inertance $b=0.4 \times m_{Avg}^*$ , and various inerter connectivity ratios, $CR$ , primary structure shapes, and depth ratios $R$ . All quantities are normalized by the corresponding values of optimal TMDI for the uniform primary structure ( $R=1$ ) with $CR=2.5\%$ .	82
5.1	(a) Planar graphical representation of a typical coupled core-frame building	85

	(primary structure); (b) and (c) Unmodified primary structure with different TMDI topologies; (d) Proposed structural modification with top-storey TMDI, (e) Floor acceleration transfer functions for uncontrolled and TMDI-controlled structures.	
5.2	(a) Case-study 34-storey building; (b) typical floor and core-frame lateral load-resisting system; (c) geometry of r/c core; (d) floor mass distribution.	86
5.3	Static condensation for stiffness matrix derivation of the low-order model: (a) for the central core; (b) for the perimetric frame.	88
5.4	Lowest three lateral mode shapes for the two different case-study building r/c core configurations of Table 5.2 obtained by the detailed FE and low-order model: (a) 1 <sup>st</sup> mode; (b) 2 <sup>nd</sup> mode; and (c) 3 <sup>rd</sup> mode.	89
5.5	Power spectral density functions of crosswind forces acting at different floor levels of the case-study building.	92
5.6	Iterative optimal TMDI design with $\mu=0.1\%$ and $\beta=8\%$ for the adopted case-study structure with $H_{top}=5m$ and discontinued r/c core (a) 1 <sup>st</sup> iteration; (b) 2 <sup>nd</sup> iteration; and (c) 3 <sup>rd</sup> iteration.	94
5.7	Objective function surface on the primary design variables plane (upper row of panels) and surface cross-sections along $v_{TMDI}$ at the optimal $\zeta_{TMDI}=\zeta_{opt}$ value (middle row of panels), and along $\xi_{TMDI}$ at the optimal $v_{TMDI}=v_{opt}$ value (lower row of panels) for $\mu=0.1\%$ , $\beta=6\%$ , and various top storey heights $H_{top}$ .	96
5.8	Peak acceleration percentage reduction of 32 <sup>nd</sup> floor (upper row of panels), optimal frequency ratio (middle row of panels), and secondary mass stroke (lower row of panels), in TMDI-equipped structure for various mass ratios, $\mu$ , and inertance ratios, $\beta$ , against lateral top-storey stiffness reduction.	98
5.9	Peak inerter force (upper row of panels), peak damping force (middle row of panels), and optimal damping ratios (lower row of panels) of TMDI-equipped structure for various mass ratios, $\mu$ , and inertance ratios, $\beta$ , against lateral top-storey stiffness reduction.	100
5.10	Quantification of mass-inertance-damping coefficient trade-off for (a) fixed normalized stiffness 38%; and (b) fixed performance RF=50%.	102
5.11	Normalised standard deviation of peak crosswind acceleration at 32 <sup>nd</sup> floor (upper panels) and average TMDI damping coefficient $c_{opt}$ (lower panels) as functions of inertance ratio for three inherent damping models, various mass ratios, and two top-storey heights.	103
5.12	Peak acceleration percentage reduction of 32 <sup>nd</sup> floor for optimal TMDI-equipped versus optimal TMD-equipped structures with different r/c core contributions against lateral top-storey stiffness reduction for attached mass ratio $\mu=0.1\%$ , and various inertance ratios.	104
6.1	Flowchart of sizing optimisation process for minimising material usage while satisfying the total strain energy constraint.	116
6.2	(a) The planar cantilever system consisting of two beam elements and six DOFs; (b) modal strain energy surface versus target energy plane; and (c) surface of objective function and optimal solution point.	119
6.3	variations of (a) fundamental frequency and (b) volume of structural material of the planar MRF, values normalized by corresponding values of the initial structure;	120

	and (c) Lagrange multiplier throughout the sizing optimisation process.	
<b>7.1</b>	Flowchart of novel framework for minimal-weight design of inerter-based DVA-equipped tall buildings to meet cross-wind serviceability criteria.	124
<b>7.2</b>	Benchmark building structure: (a) detailed FE model; (b) lumped floor mass distribution along building height; (c) first three mode shapes obtained by the detailed FE and by the low-order models; and (d) ground-floor TID-equipped lumped-mass planar frame model of the benchmark building structure.	125
<b>7.3</b>	Assumed wind excitation model: (a) mean wind velocity profile; (b) power spectral density functions of crosswind forces acting at different floor levels of the benchmark structure.	126
<b>7.4</b>	RMS floor accelerations of (a) initial non-optimal structure and optimally re-designed structure with target fundamental frequency 0.548 Hz and of (b) optimally re-designed structure with target fundamental frequency 0.928 Hz, together with respective ISO6897 occupant comfort thresholds; (c) variation of total weight of structure throughout the optimal re-design process.	127
<b>7.5</b>	Optimal TID design for optimised deficient structure in Figure 7.3 subject to wind excitation in Figure 7.2: (a) Objective function and optimal design point for $\beta=0.185$ ; and (b) optimal primary DV values with $\beta$ .	131
<b>7.6</b>	(a) Performance curves of uncontrolled optimised structure and of optimal TID-equipped optimised structure for inertance ratio 0.10, together with the performance demand curve by ISO6897 standard; and (b) self-weight of optimised case-study structure against fundamental frequency.	132
<b>7.7</b>	(a) Performance curves of uncontrolled optimised structure and of optimal TID-equipped optimised structure for inertance ratio 0.10, together with the performance demand curve by ISO6897 standard; and (b) self-weight of optimised case-study structure against fundamental frequency.	133
<b>7.8</b>	(a) performance surface of optimally designed TID-equipped case-study structure versus ISO6897 occupant comfort demand surface; and (b) quantification of structural self-weight-and-inertance tradeoff and pareto front in self-weight and inertance design plane.	135
<b>B.1</b>	Davenport's approach for determining the wind-induced resonant response of buildings and structures.	147
<b>B.2</b>	(a) First-order probability density function (PDF) of the turbulent along-wind force at 73 <sup>rd</sup> floor, and (b) second-order or joint PDF of turbulent along-wind forces at 37 <sup>th</sup> and 73 <sup>rd</sup> floors.	149
<b>B.3</b>	Spectrum of horizontal gustiness.	150
<b>B.4</b>	Power spectra of crosswind for side ratio (a) $1/4 \leq D/B < 3$ , and (b) $3 \leq D/B \leq 4$ .	152
<b>B.5</b>	Experimental model in the wind tunnel test.	155
<b>B.6</b>	Verification of frequency domain analysis vis-à-vis time-domain analysis using experimental wind tunnel test data in the along-wind direction.	156
<b>B.7</b>	Verification of frequency domain analysis vis-à-vis time-domain analysis using experimental wind tunnel test data in the crosswind direction.	156

## List of tables

<b>Table number</b>	<b>Table caption</b>	<b>Page</b>
<b>2.1</b>	Analogies of mechanical and electrical quantities	18 – 19
<b>3.1</b>	The first six natural frequencies and the corresponding modal participating mass ratios of the building FE model in Fig. 3.2 with all degrees-of-freedom activated.	34
<b>3.2</b>	Modal damping ratios for all 74 translational vibration modes of the planar low-order FE model representing the case-study building structure in Fig. 3.2.	35
<b>3.3</b>	Critical inertance values (%) above which the TMDI is more robust from the TMD	52
<b>4.1</b>	Analytical definition of primary structure geometric shapes in Fig.6(b) through the depth $D(x)$ and the depth ratio $R=D(0)/D(h)$ .	68
<b>4.2</b>	Absolute percentage differences of optimal TMDI tuning parameters and of RMS free-end displacements using 42-DOF detailed FE models and 2-DOF simplified models of TMDI-equipped primary structures. Optimal tuning for white noise excitation is considered.	72
<b>5.1</b>	Member sections geometry of 34-storey composite core-frame case-study building.	86
<b>5.2</b>	Comparison of modal properties of the lowest 3 translational vibration modes along principal axis y of the case-study building between the detailed FE model and the low-order model.	90
<b>6.1</b>	Non-dimensional constants relating section properties to cross-section area.	114
<b>B.1</b>	Mathematical expressions of gust spectra of the along-wind turbulence.	149 - 150
<b>B.2</b>	Mathematical expressions of force spectra of the along-wind turbulence.	151
<b>B.3</b>	Mathematical expressions of force spectra of the crosswind turbulence.	152 - 153

## List of acronyms

BC	behavioural constraint
COV	coefficient of variation
CR	connectivity ratio
DOF	degree-of-freedom
DV	design variable
DVA	dynamic vibration absorber
FE	finite element
FRF	frequency response function
LM	Lagrange multiplier
MAC	modal assurance criterion
MDOF	multi-degree-of-freedom
MRF	moment resisting frame
OC	optimality criteria
OF	objective function
OP	optimisation problem
PBD	performance-based design
PSD	power spectral density
RF	reduction factor
RIVD	rotational inertia viscous dampers
RMS	root mean square
SDOF	single-degree-of-freedom
SED	strain energy density
2-DOF	two-degree-of-freedom
TID	tuned inerter damper
TMD	tuned mass damper
TMDI	tuned mass damper inerter
TVMD	tuned viscous mass damper
VD	viscous damper
VMD	viscous mass damper
VS	vortex shedding

## Chapter 1

---

### Introduction

#### 1.1 Background and Motivation

##### 1.1.1 Tall buildings and wind-related performance requirements

Tall buildings, loosely defined as those exceeding 50m in height or 14 stories (CTBUH Height Criteria), historically emerged with the advent of lift as well as high-performance materials (e.g., wrought iron and subsequently steel) in the nineteenth century (Huang 2017) and have been primarily used for commercial and residential purposes ever since (Smith and Coull 1991). The 50m-tall Home Insurance Building (Fig. 1.1 (a)), completed in 1885 in Chicago, is generally considered as the world's first skyscraper and the first tall building supported by an iron frame (Ford 2005). In recent decades, socio-economic and political factors (e.g., population growth, intensifying urbanisation, towering landmark structures as prestige symbols, and driving further centralized economic/business development, etc.) have sparked interest and demand in designing and erecting ever more slender and taller buildings dominating the congested urban environments in developed and developing countries (Cangelli and Fais 2012). As a representative example, Fig. 1.1 (b) shows the super-slender residential tower at 432 Park Avenue in NY, USA (96 stories, 425m tall, 15:1 height to width aspect ratio), which is currently the tallest residential tower in the western hemisphere.

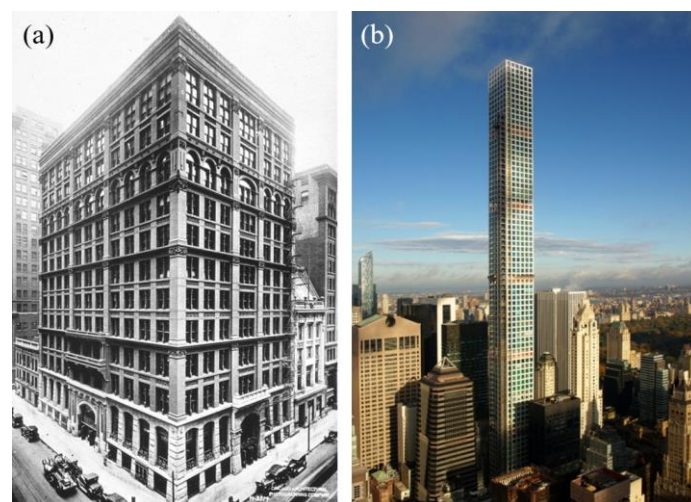


**Fig. 1.1.** (a) Home Insurance Building in Chicago ([www.americaslibrary.gov](http://www.americaslibrary.gov)); and (b) 432 Park Avenue in New York ([www.skyscrapercenter.com](http://www.skyscrapercenter.com)).

From the structural mechanics perspective, these tall, slender, and lightweight structures, are characterised by increased lateral flexibility and low inherent damping (Kareem et al. 1999). Accordingly, they can be *particularly* susceptible to large wind-borne deformations and

oscillations (Li et al. 2004, Khodaie 2020), creating two kinds of serviceability problems. The first is non-structural damage due to large inter-storey drifts in the along-wind (drag) direction. The second is occupant discomfort due to excessive floor accelerations in the crosswind (lift) direction (Simiu and Scanlan 1996). The latter issue is critical in tall building design as the human body is sensitive to motion in a broad frequency range including wind-induced building oscillations, which may cause various discomfort ranging from slight annoyance to severe dizziness, nausea, and headache (Kareem 1992, Burton et al. 2006). According to a rough criterion set by the ASCE 7-95 Standard, a building is classified as laterally flexible, thus prone to above wind-related serviceability problems, when the ratio of building height to the least horizontal dimension is larger than 4, or when the fundamental natural frequency is less than 1 Hz. Indeed, it has been noted in many tall building designs, even in earthquake-prone areas (see, e.g., Taipei 101 in Fig. 1.2(a)), that while the local strength/ductility design of the structure is governed by seismic effects, the building overall deformation and motion are dominated by wind loads (Kareem et al. 1999). And yet, many urban areas with skylines dominated by flexible cantilevered structures, including tall buildings (see Fig. 1.2 (a) and (b)) and observation/communication towers (see Fig. 1.2(c)), are located in cyclone/typhoon/hurricane-prone regions (Huang 2017).

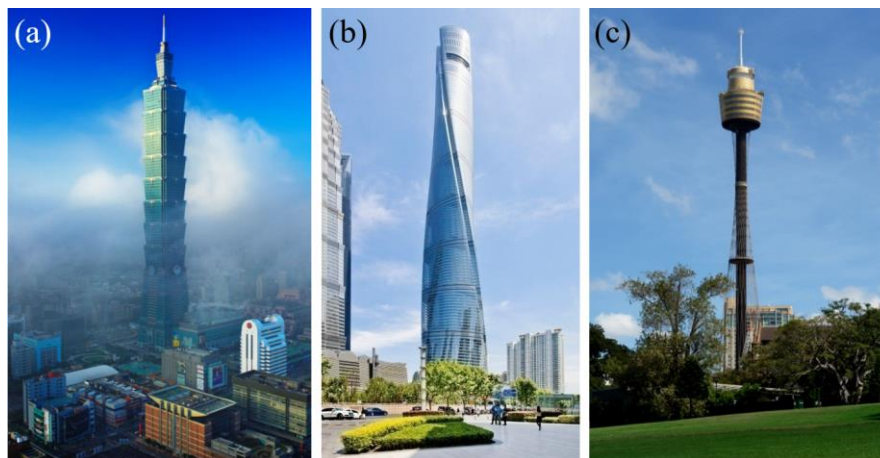


**Fig. 1.2.** (a) 509m-tall Taipei 101 Tower ([www.taipei-101.com.tw](http://www.taipei-101.com.tw)); (b) 632m-tall Shanghai Tower ([www.conniezhou.com](http://www.conniezhou.com)); and (c) 309m-tall Sydney Centrepoint Tower ([www.flickr.com/photos](http://www.flickr.com/photos)).

In this context, tall building structures in moderate and high wind-prone regions need to meet the following *requirements*:

- (i) To sustain extreme wind fronts within the expected lifespan to prevent global and local structural failures concerning strength and stability.
- (ii) To withstand major wind events statically in the along-wind direction to avoid non-structural damages to interior partitions, ceilings, door frames/windows, and external cladding/facades.



- (iii) To meet occupant comfort and habitability demands mainly in the crosswind direction under moderate/frequent wind events.
- (iv) To be sustainable and economical, minimising material consumption and environmental impacts in terms of carbon footprint.
- (v) To be efficient in terms of land usage and inner space organisation to cope with the ever-growing challenge of undersupply of urban land.

For requirement (i), with the availability of high-performance materials, innovations in structural systems, and significant advances in computer-aided simulation/engineering design, the probability of catastrophic structural failures due to wind hazards alone is fairly small (Longarini et al. 2017). Besides, the design of buildings with slenderness ratio larger than 5 is usually governed by serviceability criteria rather than structural safety (Park and Park 1998, see also Li et al. 2004). In this respect, requirements (ii) and (iii) are assessed against codified thresholds in terms of inter-storey drifts and lateral floor accelerations. To this aim, the inherently probabilistic performance-based design (PBD) framework can be applied (e.g., Ciampoli and Petrini 2012). This framework safeguards non-structural integrity and, at the same time, minimises wind-induced losses (e.g., downtime caused by loss of operability/functionality and occupant discomfort) by ensuring certain structural performance levels are met depending on the intensity of wind loads with certain annual probability of occurrence (Cui and Caracoglia 2020). Further, the requirement (iv) emphasises the demand for innovative and material-efficient structural design, achieving financial savings and cutbacks in carbon footprint as well as embodied energy consumption. Finally, the requirement (v) may lead to ever-more slender structures with regular floor plans (e.g., rectangular, square), which, in turn, are more prone to excessive wind-induced oscillations (e.g., Kwok et al. 2009, Bernardini et al. 2015).

Considering serviceability requirements (ii) and (iii) first, the total response of tall buildings under wind effects can be decomposed into three components, namely, a mean/static component, a (dynamic) background component, and a resonant component (Simiu and Scanlan 1996). The along-wind drifts caused by static and background components can be effectively contained by increasing lateral stiffness of tall buildings (Ricciardelli et al. 2003). However, the same strategy does not improve, in general, the serviceability performance associated with floor accelerations in the crosswind direction (Kareem et al. 1999, Taranath 2016), which are mostly caused by the resonant component (Huang 2017). Specifically, for tall buildings with aspect ratio (i.e., height to width) over 3, the crosswind floor accelerations are usually more severe than the along-wind ones due to the resonance of crosswind excitation frequency with one of the vibration modes of the building structure (Liang et al. 2002, Isyumov 2012). According to Solari (1985), the crosswind dynamic loads on tall buildings are induced by three mechanisms. These are along-wind turbulence, crosswind turbulence, and vortex shedding (VS) effect (also known as wake excitation), with the latter being the most dominant

of the three. In the wake excitation, vortices are created on the downside of the building and shed periodically from one side to the other when wind flows past the structure at a particular speed. This periodic shedding of vortices generates alternating low-pressure zones and giving rise to a fluctuating force in the crosswind direction (Simiu and Scanlan 1996). Consequently, occupant discomfort in the crosswind direction induced by VS effects can be critical for relatively moderate intensity *frequently occurring* wind velocities, and often governs tall building design (see, e.g., Burton et al. 2006, Kwok et al. 2009, Petrini and Ciampoli 2012, Bernardini et al. 2015, Taranath 2016).

Turning the attention to the sustainability requirement (iv), it is worth noting that current global warming is largely a result of human activities increasing greenhouse gas concentration, particularly carbon dioxide, in the atmosphere. In particular, the built environment and manufacturing of materials for building construction account for approximately 36% and 11% of global energy-related CO<sub>2</sub> emissions, respectively (International Energy Agency, 2017a, 2017b). For a building structure, its lifetime carbon emissions are composed of 1) operational emissions coming from energy consumption during service, and 2) embodied emissions associated with building materials and maintenance (BS EN 15978, 2011). Lately, major reduction in operational energy consumption achieved in newly constructed and refurbished structures has made the embodied energy to become the most dominant portion of lifetime energy consumption in buildings (European Commission 2010, Moynihan and Allwood 2014, Cabeza et al. 2013, Pacheco-Torgal et al. 2013). In this setting, one key strategy to achieving global emission reduction is to utilise materials as efficiently as possible (Allwood et al., 2011) and thereby minimise the carbon footprints of construction industry sectors through material-efficient structural design and structural optimisation. However, in the current limit-state design framework for building structures, minimum performance requirements at ultimate and serviceability limit states are established by codified rules for structural members with partial factors being introduced to ensure reliability but not embodied emissions efficiency (Orr et al. 2019). Indeed, building codes of practice neither specify upper limits on the performance criteria, nor penalise overly conservative design. This consideration might yield code-compliant but material-inefficient and eco-unfriendly structures (Orr et al. 2019). In fact, after examining 3,500 steel members from 27 buildings, an apparent reluctance to design the members above the utilisation ratio of 0.80 was observed by Dunant et al. (2018). More importantly, 63% of the members investigated therein were governed by serviceability rather than strength requirements. Further, based on the verification of 10,000 steel members in real buildings, Moynihan and Allwood (2014) showed that the average utilisation ratio was around 0.40 at the ultimate limit state, implying that more than half of the structural steel could have been saved without compromising code-specific strength criteria. To this end, building design protocols accounting for material efficiency is an important consideration to be addressed in achieving a net-zero economy.

### 1.1.2 Human motion perception and occupant comfort criteria in wind-excited buildings

Human perception and tolerance to wind-borne vibrations in tall buildings are largely subjective and depend on both psychological and physiological factors (Tamura et al. 2006). Consequently, there is currently no universally accepted serviceability comfort criterion for specifying acceptable dynamic response level in wind-excited tall buildings, and major differences exist amongst the commonly used design codes in defining tolerance thresholds (Kwok et al. 2009). Still, there is a general consensus that building occupants would more likely tolerate motions of shorter duration (i.e., time of exposure) and with a lower frequency of recurrence (Hansen et al. 1973). Thus, it is common and reasonable to assume one-hour wind duration (Simiu and Scanlan 1996) together with one-year mean recurrence interval in comfort evaluation (Tamura et al. 2004). The former corresponds to the duration beyond which winds in a typical storm may be assumed to become relatively weak (Simiu and Scanlan 1996), while the latter is considered most relevant to the daily use of buildings (Burton et al. 2015). Moreover, the frequency range for assessing building habitability to wind action is typically taken between 0.1 to 1.0 Hz (Chan and Chui 2005, Kwok et al. 2009), as the fundamental frequency of tall, slender building structures commonly falls within this range.

To better understand human response to wind-induced building motion, extensive research has been conducted over the years, including experimental testing in motion simulators (cf. Noguchi et al. 1993, Shioya and Kanda 1993, Denoon 2000, Burton et al. 2003), field experiments in real buildings (cf. Isyumov and Kilpatrick 1996, Denoon et al. 1999, Denoon 2000, and Kijewski-Correa et al. 2007), and surveys of occupants in monitored tall buildings (Kijewski-Correa et al. 2007, Lamb et al. 2013). A comprehensive literature review is provided in Kwok et al. (2009). It has been established that the floor acceleration is the quantity closely associated with human discomfort (Bernardini et al. 2015). Nevertheless, current building codes tend to use different floor acceleration metrics to define tolerance thresholds, such as the root mean square (RMS) value, peak value, and change rate of acceleration (Isyumov 1993, Boggs 1997, McNamara et al. 2002). Similarly, a literature review on the subject shows different preferences among researchers in presenting the results: some report peak accelerations, while others report RMS values. Specifically, most of the research conducted with motion simulators subjected to sinusoidal motion tend to report peak accelerations, as this is a metric that may be readily measured. On the other hand, research works that involve wind-tunnel testing and numerical simulation based on wind forcing data tend to report both peak and RMS values (Griffis 1993). To this end, it has been argued that, when the vibration persists for an extended period (e.g., 10 to 20 minutes) as is common with winds, RMS acceleration is a more representative metric for human motion perception as isolated peak accelerations may be dampened out within a few cycles (Hansen et al. 1973, Isyumov and Poole 1983, Islam et al. 1990). In every case, the relationship between peak and RMS accelerations can be described by a peak factor which varies with building frequency and wind duration (cf. Davenport 1964), though it is often taken equal to 3.5 (Griffis 1993, Kwok et al. 2009). Besides floor acceleration,

other contributing factors affecting occupant comfort include building occupancy type (cf. Fig. 1.3), motion direction, waveform (Tamura et al. 2006, Kijewski-Correa and Pirnia 2009), visual effects, and acoustic cues (Isyumov 1993).

Relying on the previous research results, standards of practice, such as ISO6897:1984, AIJ-GEH-2004, ISO10137:2007, and CNR-DT 207/2008, incorporate prescriptive provisions to regulate the occupant comfort-related performance of tall buildings subject to wind excitation. This is achieved by requiring that the wind-borne (peak or RMS) floor accelerations associated with a given recurrence interval are below a threshold which depends on the building vibration frequency (Bernardini et al. 2015). For illustration, Figure 1.3 compares serviceability comfort criteria in terms of *peak* floor acceleration from different design codes for one-year return period. Note the ISO6897 threshold curve (in terms of RMS value) has been converted to peak value, assuming a peak factor of 3.5. It is seen that, within the frequency range 0.1 – 1.0 Hz for serviceability check of tall buildings, the tolerance thresholds decrease monotonically as the vibration frequency increases, though at a slower rate. In this respect, it is important to note that the fundamental frequencies of all case-study buildings considered in this thesis are within the above frequency range, while the exposure duration is taken as 1 hour throughout the work.

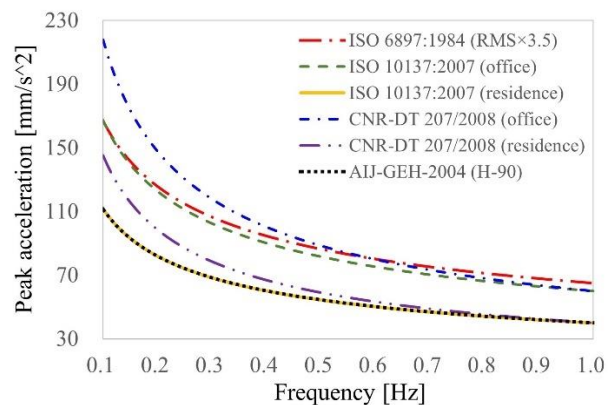


**Fig. 1.3.** A comparison of serviceability occupant comfort criteria from different design codes for a one-year recurrence period and within the frequency range 0.1 – 1.0Hz.

### 1.1.3 Wind-borne motion control of tall buildings in the cross-wind direction

For mitigation of the *resonant* response of tall buildings in the cross-wind direction, it is well-established that increasing the lateral structural stiffness is effective for suppressing lateral displacement amplitude (Kareem et al. 1999). However, the acceleration response cannot be efficiently and economically mitigated by adopting a more rigid lateral load-resisting system (Simiu and Scanlan 1996). A further downside of laterally stiffening a tall building is that the rate of change of floor acceleration, which contributes to occupant discomfort, may even increase (Kareem et al. 1999). Therefore, alternative solutions are warranted to control the VS-induced floor accelerations. In this regard, aerodynamic modifications (cf. Kwok and Bailey 1987, Kwok 1988) and use of auxiliary damping devices are both practical and effective measures to alleviate the crosswind acceleration response of tall buildings by reducing wind

action at the source and increasing energy dissipation capacity of the buildings, respectively.

According to [Amin and Ahuja \(2010\)](#), aerodynamic modifications of tall buildings comprise two groups of techniques depending on their impacts on architectural and structural concepts. These are the global/major variation of buildings' cross-section along the height (e.g., tapering, setbacks, twisting) and the local/minor tailoring of buildings' cross-sectional shape (e.g., corner chamfering or rounding, fins fitting). The former approach reduces dynamic wind effects by making vortex formation irregular and incoherent with the height ([Kim and Kanda 2013](#)). The latter approach hinders the formation of coherent wake fluctuations by altering the wind flow pattern around the structure ([Karim 1983](#), [Shimada 1995](#)). Indeed, benefits of aerodynamic shaping of buildings have been widely reported in the literature ([Dutton et al. 1990](#), [Hayashida and Iwasa 1990](#), [Amano 1995](#), [Cooper et al. 1997](#), [Kim and Kanda 2010](#), [Kim et al. 2011](#), [Tanaka et al. 2012](#), [Deng et al. 2015](#)), while the effectiveness of vertical building tapering in reducing crosswind acceleration response was confirmed by [Kim and You \(2002\)](#) and [You et al. \(2008\)](#). In practice, however, structural engineers are not always able to specify the building shape and geometry (massing), which are commonly driven by architectural considerations ([Chan and Chui 2006](#)). In this context, over the past four decades, significant effort has been devoted to developing motion control technology, with particular emphasis on the use of auxiliary damping devices ([Chu et al. 2005](#)). In this respect, motion control systems for mitigating wind-induced vibrations in tall buildings ([Yao 1972](#), [Chung et al. 2013](#), [Soto and Adeli 2013](#)) can be broadly classified into three groups, namely, active, semi-active, and passive.

In an active control system, external energy sources are required for powering the control actuators (i.e., the force delivery components), which are regulated by real-time sensors and controllers. The actuators generate the required control forces counteracting the building motion based on the system response variables measured by the sensors integrated within the structure ([Lagaros et al. 2012](#)). Examples of active control systems include active mass dampers, active tendon systems, active brace systems, and pulse generation systems. Despite adaptability to excitations and excellent control efficiency, active devices can be unreliable as they require a significant amount of external energy to generate the required control forces, which may not be available, especially during and immediately after severe natural hazards such as high winds and earthquakes ([Longarini et al. 2017](#), [Saaed et al. 2013](#)). On the other hand, semi-active control devices require relatively small power supply to make adjustments to device properties (e.g., stiffness and/or damping coefficients known as “tunable parameters” of the control system) instead of applying the control forces to the structure directly ([Saaed et al. 2013](#)). A typical semi-active control device consists of several components such as sensors for measuring input and/or output, a controller for processing measurements and generating control signals, and actuators regulating the adaptable device properties. Examples of semi-active systems are semi-active tuned mass dampers (TMDs), semi-active friction dampers, and electrorheological dampers, etc. Compared to active control systems, the main attraction of the semi-active control methods is that they are less demanding in terms of cost and external energy ([Wen and](#)

Shinozuka 1998, Lagaros et al. 2012, Tse et al. 2012). Besides, the passive components of semi-active devices can still offer some degree of protection even in a power failure (Chu et al. 2005), which is not the case for active control devices.

Finally, the most reliable and commonly applied control systems for enhanced serviceability and safety in wind-excited tall buildings are of the passive type due to their simplicity and inherent stability as they do not require any external energy to operate or structural response measurements (Christenson 2001). In principle, these systems require optimal tuning/design of the device(s) for a specific dynamic loading and rely on auxiliary damping devices to dissipate part of the input energy. According to the energy balance equation, the total input energy to an elastic system (such as wind-excited tall buildings) subjected to external excitations is equal to the sum of the kinetic energy, the elastic strain energy, the dissipated energy due to inherent structural damping, and the dissipated energy by supplementary damping devices/mechanisms, if any (Soong and Dargush 1997). This consideration intuitively suggests that the more energy is dissipated through auxiliary damping, the less severe the vibration is. Over the years, researchers and engineers have devised a variety of passive control technology, including broad-band energy dissipation devices (e.g., viscous fluid damper, viscoelastic dampers, friction damper, metallic yield dampers, etc., Kareem et al. 1999), and narrow-band reactive dynamic vibration absorbers (DVAs) which aim to suppress a single dominant response frequency. Among these control devices, the tuned mass damper (TMD), which is the most representative DVA, has become a suitable and well-established solution for vibration mitigation of wind-excited tall buildings (Elias and Matsagar 2017, 2018, Tse et al. 2012, Ierimonti et al. 2018), since its first successful application in the Centrepont Tower, Sydney (see Fig. 1.2 (c)). This is mainly owing to the fact that, although wind forces are usually broad-band, modern tall buildings with low inherent damping behave mostly as a narrow-band filter, thus inducing acceleration output within a limited frequency range around a dominant frequency close to the first natural frequency of the uncontrolled structure (Chan and Chui 2006). Consequently, the resonant response of tall buildings is, in general, dominated by the first modal response.

#### **1.1.4 Dynamic vibration absorbers (DVAs) for motion control of wind-excited tall buildings**

The concept of the DVA is one of the first strategies for passive motion control of dynamically excited mechanical and civil engineering structures (Frahm 1911). Arguably, the most widely studied and commonly used passive DVA in the literature and in practical applications is the so-called tuned mass damper (e.g., Ormondroyd and Den Hartog 1928, Brock 1946, Den Hartog 1956, Warburton and Ayorinde 1980, Randall et al. 1981, Thompson 1981, Warburton 1982, Tsai and Lin 1994, Rana and Soong 1998, Asami et al. 2002, Krenk 2005, Bakre and Jangid 2007, Ghosh and Basu 2007, Leung and Zhang 2009, Tributch and Adam 2012, Bortoluzzi et al. 2015, Salvi and Rizzi 2016). The typical TMD consists of a



secondary mass that is free to oscillate and attached to the primary structure via linear stiffeners/springs and viscous damper/dashpot elements (Elias and Matsagar, 2017). The widespread use of TMD is mainly due to its simplicity and effectiveness underpinned by the existence of simple and well-established design approaches seeking to optimally tune the TMD for minimising the response of a given dynamically excited structure for an a priori fixed attached mass (Marian and Giaralis, 2017).

Historically, the concept of the TMD was initially proposed by Ormondroyd and Den Hartog (1928), followed by the derivation of closed-formed expressions in Brock (1946) and Den Hartog (1956) for estimating optimal TMD stiffness and damping parameters that minimise the peak displacement of sinusoidal force-excited undamped single-degree-of-freedom (SDOF) primary structures. Focusing on harmonic excitations, Den Hartog (1956) demonstrated that all frequency response functions (FRFs) of a TMD-equipped undamped SDOF primary structure pass through the same two points. Following this fixed point theory, Warburton (1982) derived simple TMD design formulae minimising different response quantities of undamped SDOF primary structures under harmonic force and base excitations. More recently, Ghosh and Basu (2007) showed that the fixed point design approach can lead to near-optimal TMD vibration control performance for lightly damped single-degree-of-freedom (SDOF) primary structures with damping ratio up to 3%. Indeed, the TMD design formulae proposed in above works are valid for lightly damped multi-degree-of-freedom (MDOF) structures, provided that the vibratory motion to be suppressed is largely associated with a single/dominant structural mode (e.g. Rana and Soong 1998).

Further, to suppress vibration from higher modes, multiple distributed TMDs (MTMDs) were studied by Fujino and Abe (1992) and Kareem and Kline (1995) to overcome the limitations of single TMD systems (i.e., with a single attached mass) which can only target one vibration mode. Moreover, the use of MTMDs arranged in parallel was studied by Xu and Igusa (1992) and Yamaguchi and Harnpornchai (1993) for improving the robustness of single TMD systems to detuning effects. In MTMD configuration, each individual TMD is tuned to a different frequency such that the effective frequency band becomes wider. Nevertheless, optimal design of MTMDs is considerably more challenging than single TMD design (see, e.g., Jokic et al. 2011) due to the increased number of design variables, let alone the significantly increased weight imposed on the primary structure due to the presence of multiple secondary masses.

Focusing on civil engineering applications, much research has been carried out to investigate the effectiveness of TMDs in safeguarding the resilience of flexible cantilevered structures, such as tall buildings (Ricciardelli et al. 2003, Li et al. 2011, Lu et al. 2017), industrial chimneys (Brownjohn et al. 2009), solar towers (Carrato and Santamont 2012), and wind turbine towers (Zhao et al. 2018, Gaur et al. 2020), against dynamic environmental loads (e.g., Christopoulos and Filiatrault, 2006). Soto and Adeli (2013) conducted a comprehensive review of the application of TMDs in high-rise buildings and tall towers.

For tall building structures, typical passive TMD implementations rely on attaching a secondary mass (usually of the order of 0.25-0.75% of the total building mass or 1-2% of the modal mass, Kareem 1983) towards the top of structures via stiffeners/springs or via hangers in a pendulum-like configuration (see Fig. 1.4 (a) and (b) for the pendulum TMDs installed in Taipei 101 and Shanghai Tower, respectively). The elastic property of the spring connecting the secondary mass to the host structure is tuned/designed such that the secondary mass observes significant oscillations counterbalancing the motion of the host structure. The secondary mass is further linked to the primary structure using supplementary damping devices which are engaged from the relative motion of the attached mass with respect to the primary structure and dissipate wind-induced kinetic energy. In this regard, the optimal design of passive linear TMDs seeks to find the optimal stiffness and damping coefficients,  $k_{TMD}$  and  $c_{TMD}$ , for a given attached/secondary mass,  $m_{TMD}$  as shown in Fig. 1.4 (a). For vibration suppression of tall buildings, the TMD is generally tuned to the first natural frequency of the primary structure to control the fundamental (translational) lateral mode shape (e.g., Rana and Soong 1998, Li et al. 1999).

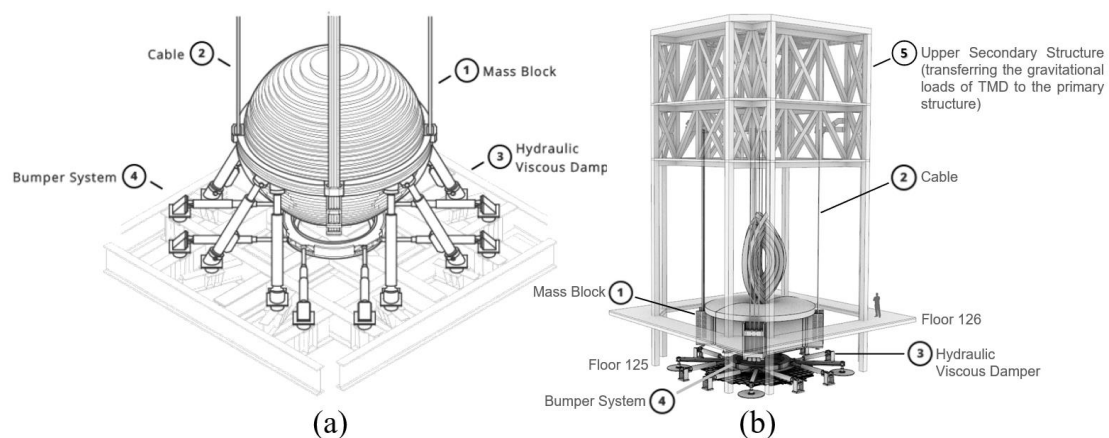


**Fig. 1.4.** (a) the 600 ton, pendulum-type TMD in Taipei 101 ([www.interestingengineering.com](http://www.interestingengineering.com)); and (b) the 1000 ton, pendulum-type TMD in Shanghai Tower (<https://www.structuremag.org/?p=12403>).

Notwithstanding successful and wide implementations of linear passive TMDs, they have two major drawbacks in suppressing wind-induced oscillations in tall buildings:

- (I) The effectiveness and applicability of TMDs depend heavily on the attached mass: the larger the attached mass the better vibration suppression and robustness to detuning is achieved (De Angelis et al. 2012). However, attached mass can rarely exceed 0.5% to 1% of the total building mass in tall buildings (Tse et al. 2012) as it becomes overly expensive to accommodate its weight and volume due to structural and architectural limitations, respectively.
- (II) TMDs may be “detuned” over time due to either unforeseen nonlinear behaviour of the TMD and/or of the host building structure, or due to changes to the dynamic properties



during the service life of the host structure. Detuning affects significantly TMD vibration suppression performance which is inherently narrow-band affecting frequencies close to the targeted dominant/fundamental natural frequency of the host structure.

In addition to the two limitations above, another *potential* shortcoming of *single* TMD systems (i.e., with one secondary mass) for wind-induced building motion control is that they can only suppress the response level associated with a particular vibration mode, as previously discussed, while for wind-induced accelerations in slender cantilevered (civil engineering) structures, non-negligible contributions may, in some cases, come from the higher modes. Indeed, through full-scale field measurements of the Canton Tower (a 604m-tall, multipurpose observation tower with tapered, elliptical cross-section located in Guangzhou, China), [Guo et al. \(2012\)](#) showed that the peak acceleration response during a particular typhoon event, measured at the highest monitored level and in the stronger (principal) direction of the tower, was dominated by the second vibration mode in that direction. Still, the power spectral density (PSD) functions of acceleration response at lower heights were found to contain non-negligible peaks from the first six modes spread over the frequency range from 0 to 2 Hz. Meanwhile, for tall rectangular buildings with side ratio (i.e., the depth-over-breadth ratio) over 3, a second spike on the PSD of crosswind force can occur at a higher frequency than the primary/dominating VS frequency (cf. Fig. B.4 (b)) due to the sub-vortex shedding effect ([Liang et al. 2002](#)). Then, non-negligible higher-mode outputs can be generated if one of the higher resonance frequencies of the structure coincides with the sub-VS frequency. As an example, [Li et al. \(2004\)](#) conducted in situ measurements of the Di Wang Tower (a 325m-tall office tower with an elongated floorplan and side ratio close to 2) during the passage of Typhoon Sally and demonstrated that while the fundamental modal response largely dominated the acceleration response in the weaker direction of the building, the second mode still accounted for 10% of the total response.

To further illustrate this point, figure 1.5 (b) and (c) examines, respectively, the absolute FRFs of the top-floor displacement and acceleration of a 74-storey benchmark structure equipped with an optimal top-floor TMD as shown in Fig. 1.5 (a) (see also [Ciampoli and Petrini 2012](#), [Spence and Gioffrè 2012](#), [Giaralis and Petrini 2017](#)). As evidenced in Fig. 1.5 (c), the uncontrolled acceleration FRF has significant resonant peaks corresponding to the higher modes at which small inputs can incur large responses, whereas, in the displacement transfer function in Fig. 1.5 (b), there are only three resonant peaks visible and the second and third peaks are much lower than the first. Moreover, it is seen in Fig. 1.5 (c) that the single TMD system, tuned to the fundamental mode of the primary structure, is unable to suppress the higher modes as the pertinent FRF (depicted by the red dashed line) overlaps with the uncontrolled, except near the fundamental frequency.

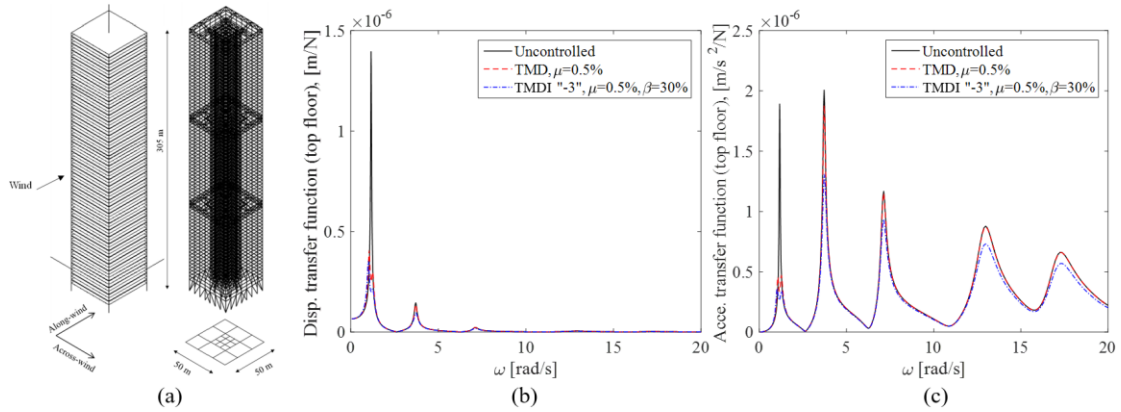


**Fig. 1.5.** Crosswind transfer function of the top floor (a) displacement; and (b) acceleration of an uncontrolled 74-storey benchmark tall building.

To overcome the above TMD shortcomings, [Giaralis and Petrini \(2017\)](#) recently explored the potential of top-floor tuned mass damper inerter (TMDI), initially proposed for seismic protection of multi-storey buildings ([Marian and Giaralis 2013, 2014](#)), in enhancing TMD vibration suppression effectiveness in wind-excited tall/slender structures subject to VS effects. The TMDI consists of a conventional linear passive TMD, in which the attached mass is linked to a different floor from the one that the TMD is attached to via an inerter element as shown in Fig. 1.5 (b). The latter is a mechanical element with negligible mass/weight, which develops a resisting force proportional to the relative acceleration of its terminals through a constant termed intertance,  $b$ , and measured in mass units (e.g., kg) ([Smith 2002](#)). [Giaralis and Petrini \(2017\)](#) showed that the TMDI reduces peak top-floor acceleration of the wind-excited 74-storey benchmark building as shown in Fig. 1.5 (a) more effectively than a same-weight TMD by considering a smaller attached mass but bigger intertance values, and/or larger TMDI topologies in which the inerter spans more stories in linking the attached mass to the host structure. The latter consideration is graphically explained in Fig. 1.5 (b), showing a top-floor TMDI in a planar  $n$ -storey frame building with the inerter spanning  $p$  floors (“ $p$ ” connectivity) and connecting the attached mass,  $m_{TMD}$ , to the  $n-p$  floor. Moreover, it is numerically shown that the inclusion of the inerter device reduces the TMD stroke significantly, and that the magnitude of the developing inerter forces can be readily accommodated by the host structure locally ([Giaralis and Petrini 2017](#)). On the other hand, it has been established that within the TMDI, the inerter endows mass amplification and higher modes damping effects to building structures ([Giaralis and Petrini 2017, Giaralis and Taflanidis 2018](#)), which can be seen by examining pertinent acceleration FRFs of TMD- and TMDI-equipped benchmark structure in Fig. 1.5 (c). These benefits render the TMDI a lightweight and more versatile solution than the TMD for controlling both broad- and narrow-band excitations.

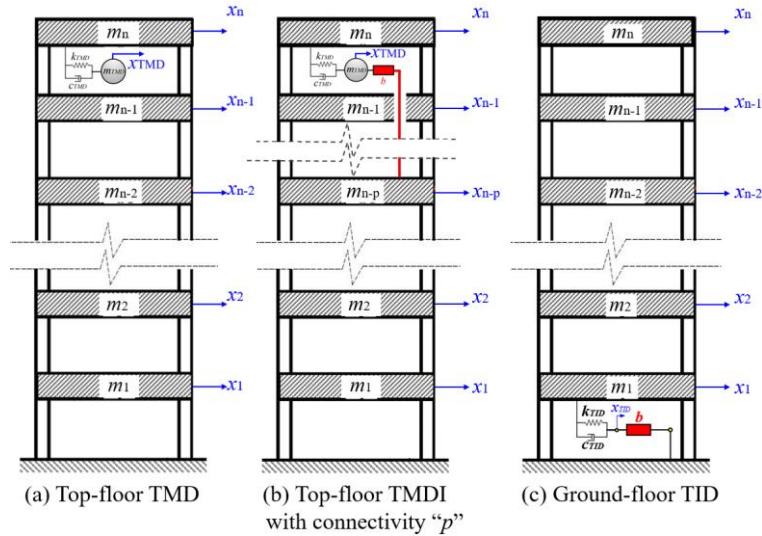


**Fig. 1.6.** A  $n$ -storey lumped-mass planar frame model equipped with (a) top-floor TMD; (b) top-floor TMDI with connectivity “ $p$ ”; and (c) ground-floor TID.

Although the TMDI suppression effectiveness has been well identified, there are still several open issues that have not been addressed in the literature hitherto and in [Giaralis and Petrini \(2017\)](#). Firstly, the latter work did not consider the optimal TMDI design for wind-excited tall buildings; only parametric analyses were undertaken to map relative trends to the response of tall buildings rather than to quantify the full potential of the TMDI for vibration control. Secondly, all previous works had only considered a given host structure with fixed mass and lateral stiffness distribution. Nevertheless, it is shown in [Pietrosanti et al. \(2020a\)](#) that the mode shape of the uncontrolled primary structure can influence the TMDI motion control performance heavily. This observation warrants further parametric and systematic investigations considering a wide range of mass and stiffness distributions of the host structure and different fundamental mode shapes. Thirdly, although improved vibration mitigation can be achieved by increasing the inerter connectivity, such a strategy may not be practical for routine slender mid- to high-rise buildings with 20-40 storeys. This is because occupying high-premium space across several upper floors of such structures for accommodating a control device is not cost-effective. Finally, thus far in the scientific literature and practical implementation of TMDIs for tall buildings, the TMDI is designed and treated as a retrofitting measure to improve the performance related to occupant comfort (i.e., in terms of floor acceleration) of inherently deficient primary structures only. Therefore, all current studies had only considered the optimal design of the control device itself for a given primary structure; no efforts had been undertaken to design the whole tall building-plus-TMDI structural system in an integrated manner. This very fact motivates the optimal design of the primary structure-plus-TMDI within a multi-objective setting, achieving simultaneous reduction in material consumption and optimal vibration control effect.

## 1.2 Aim and objectives

Building on the current state-of-the-art research on the TMDI reviewed above, the overarching aim of this PhD thesis is to develop novel performance-based tall building design approaches for occupant comfort in the cross-wind direction, underpinned by numerical solution of innovative optimisation formulations, enabling slender, lightweight, and material-efficient buildings equipped with passive TMDI devices. In this context, the following four objectives are set as stepping stones towards achieving the above aim.

- (I) Derive optimal TMDI tuning parameters, i.e. frequency ratio and damping ratio, to minimise selected structural performance (e.g., peak floor accelerations in the crosswind direction) of tall buildings related to appropriate performance criteria (e.g., occupants comfort) for given secondary mass and inertance, host structure, and wind excitation field.
- (II) Quantify the influence of the uncontrolled fundamental mode shape on TMDI vibration suppression efficacy through a thorough parametric investigation considering a wide range of primary structures modelled/simplified as continuous cantilever beams with various geometric shapes and, therefore, different mass and stiffness distribution.
- (III) Propose appropriate structural modification to tall buildings to improve the potential of TMDI for motion control, thus extend the applicability of TMDI to more routine structures.
- (IV) Develop novel integrated primary structure-plus-TMDI optimal design configurations for meeting building code-prescribed occupants' comfort criteria in tall buildings while minimising material usage for the primary structural system.

## 1.3 Thesis organisation

The thesis comprises eight chapters and two appendices followed by the list of cited references.

The current first chapter provides an introduction to the thesis by briefly discussing the needs for tall buildings and reviewing the serviceability as well as sustainability requirements related to wind action as well as current mitigation measures. It lists the objectives of the current research effort and outlines the organisation of the thesis.

Chapter 2 starts with a brief review of the development and technological aspects of the inerter device. Then, it reviews the state-of-the-art and the state-of-the-practice for the inerter-based vibration control strategies, including various inerter-based configurations, for seismically-excited and wind-excited building structures. It identifies the research gaps that have not been answered/addressed by the existing studies, thus framing research needs in the field.

The first half of Chapter 3 contributes a novel optimal TMDI design formulation, which is numerically solved by a custom-made pattern search algorithm with an adaptive search range for computational efficiency. The formulation aims to minimise the peak or RMS floor acceleration of tall buildings under specified wind excitation by seeking optimal TMDI tunable parameters for given TMDI inertial properties and inerter connectivity. Further, the second half of Chapter 3 focuses on investigating TMDI benefits numerically with different inertial properties (i.e., secondary mass/weight and inertance) configured in different inerter connectivity for -tall building structures deficient to code-prescribed occupant comfort criteria under moderate wind action. This is achieved through the application of the TMDI tuning method to a 74-storey benchmark structure equipped with a top-floor TMDI. The latter is optimally designed for a wide range of inertial properties and three different topologies through the numerical solution of the underlying optimisation problem for the benchmark building subjected to experimentally calibrated spatially-correlated crosswind force field accounting for VS effects.

Chapter 4 investigates the influence of the primary structure elastic and mass properties on the TMDI motion control performance, including the free-end displacement reduction for the primary structure, as well as the attached mass stroke, inerter and damping forces of the optimal TMDI. This is pursued through an innovative parametric study, involving a wide range of tapered beam-like cantilevered primary structures with different continuously varying flexural rigidity and mass distributions equipped with TMDIs optimally tuned to minimise the free-end peak and RMS displacement response of the primary structure subject to harmonic resonant and white noise excitation, respectively.

Chapter 5 introduces an innovative local structural modification, i.e., top-storey softening, in conjunction with an optimal top-floor TMDI, as an alternative solution to the inerter spanning more than one storey as seen in Chapter 3, for improved serviceability performance in typical mid-rise to high-rise buildings that are susceptible to wind-induced VS effects causing occupant discomfort. This is supported by adapting the optimal TMDI tuning problem, initially formulated in Chapter 3, to include the top-storey lateral stiffness as a secondary design parameter (in addition to the TMDI inertial properties), aiming to minimise acceleration of the highest occupied floor. To this end, a 34-storey composite core-frame building is taken as the primary structure for numerical investigation.

Chapter 6 presents a novel strain energy-based sizing optimisation formulation relying on optimality criteria (OC) and an associated numerical scheme for solving minimum-weight design problem of elastic frame structures with fixed layout under a single frequency constraint on any arbitrary vibration mode. The OC formulation is tailored for wind-excited tall buildings by applying the frequency constraint to the fundamental vibration mode treated as a measure of the structural lateral stiffness. The latter is generally inversely related to wind-borne acceleration response in tall buildings. In the first instance, the proposed OC approach, with

two sub-conditions for characterising the optimal structure, extend and generalise the well-known uniform-strain-energy-density criterion by introducing a rigorous, supplementary condition derived using the Lagrangian multiplier formalism. The latter condition relaxes the implicit limitation of existing energy-based OC approaches that no stress redistribution during size updating is considered even in hyperstatic structures. From a practical viewpoint, it is seen that this supplementary condition improves on the convergence of existing OC methods significantly for eigenvalue/frequency-constrained optimisation problems. A rigorous mathematical proof is provided for showing that, if a stationary point exists in the feasible solution set of the optimisation problem, the resizing algorithm is driving the initial, non-optimal structural design towards the global optimum (i.e., minimum-weight design) in the continuous design space. The method is exemplified using a planar moment resisting frame (MRF) consisting of three frame elements and is validated by a graphical optimisation method for accuracy. Pertinent numerical results from two independent/parallel sizing optimisations, performed on the same MRF but with different optimality criteria, are provided to demonstrate the influence of the second condition on the convergence of the iterative/resizing process and on the accuracy of the optimal solutions reached. The proposed resizing approach can be applied to reduce the structural self-weight of tall buildings whose lateral load resisting systems comprise mainly frame elements and their design is governed by habitability (occupants comfort) criteria.

Chapter 7 puts forth a novel structure-plus-TMDI design framework, combining the TMDI tuning method in Chapter 3 and the sizing algorithm in Chapter 6, for (structural) material use reduction of the primary structural system of VS-prone tall buildings while meeting code-prescribed occupant comfort criteria by exploiting the motion control potential of inerter-based DVAs. The proposed framework is applied to an occupant comfort sensitive 15-storey moment resisting frame building under moderate wind action equipped with a ground-floor inerter-based vibration absorber. Pareto optimal solutions for inertance and structural building weight are provided for the case study building to quantify the potential savings in material consumption and upfront cost.

Concluding remarks along with the limitations and, therefore, potential future extensions of the proposed methodologies are provided in Chapter 8. Furthermore, Appendix A reviews theoretical concepts of modelling lateral dynamic forces consistent with wind excitation in the frequency domain. Further, it outlines concepts and formulae from linear random vibration theory to obtain the peak as well as RMS response of tall buildings under wind excitations. Appendix B is informative and reviews details on wind excitation models accounting for VS effect in the crosswind direction. Further, it provides frequency- and time-domain numerical results for the 74-storey benchmark building used in Chapter 3 to verify the accuracy of the wind force modelling and the frequency domain structural analysis.



## Chapter 2

---

### State of Art Review on Inerter-Based Vibration Control for Building Structures

#### 2.1 Preliminary remarks

In recent years, inerter mechanisms have been extensively studied in the literature in conjunction with viscous dampers (VDs) and TMDs for enhanced vibration suppression of dynamically-excited civil engineering structures (Ikago et al. 2012, Lazar et al. 2014, Marian and Giaralis 2014, Zhang et al. 2017, Li et al. 2019, Taflanidis et al. 2019). The inerter element, defined by Smith (2002), is a linear massless mechanical element with two terminals resisting relative acceleration of its ends through a constant known as inertance measured in mass units (e.g., kg). As established in section 1.1.3, vibration control efficacy and robustness of conventional inertial dampers (i.e., TMD) are known to be limited by the secondary mass that can be accommodated by the host structure and their inherent narrowband nature affecting frequencies only close to the targeted vibration mode. Through incorporating an inerter device to the TMD in an appropriate configuration, these issues can be conveniently addressed by exploiting the inerter mass-amplification and higher-mode-damping attributes, thereby leading to a lightweight broadband DVA that is more efficient and robust to detuning effects and uncertainties. In the three most popular inerter-based DVA configurations, the inerter is functioning either as a motion amplifier, a mass substitute, or a mass amplifier in the forms of tuned-viscous-mass-damper (TVMD), tuned-inerter-damper (TID), and TMDI, respectively (Taflanidis et al. 2019). To this end, this chapter begins with a brief description of the inerter element and its realization/implementation through different mechanisms. Then, the three above mentioned inerter-based DVAs, as well as their advantages and limitations, are discussed in detail. Finally, the state of the art of TMDI applications is critically reviewed for seismically excited and wind-excited tall building structures.

#### 2.2 The Inerter

A standard mechanical-electrical analogy considers the correspondence of force to electrical current and of velocity to voltage. In this setting, the spring, the damper, and the mass mechanical elements correspond to the inductor, resistor, and *grounded* capacitor electrical elements, separately, (Smith 2002), as shown in Fig. 2.1. Notably, the capacitor with two terminals does not have an immediate correspondence in the mechanical domain since the mass element has only one free-to-move “terminal” (cf. Fig. 2.1). This is because the force-velocity relationship, described by Newton’s second law, relates the acceleration (i.e., the time derivative of velocity) of the mass relative to a *fixed* point in the inertial frame, implying the other mass

“terminal” is connected to the ground (Hixson 1976). Consequently, a passive electrical circuit comprising inductors, resistors, and capacitors cannot have a direct spring-dashpot-mass mechanical analogue. This lack of a direct mapping motivated Smith (2002) to define a new mechanical element, the inerter, which is perfectly analogous to the capacitor as confirmed in Table 2.1. Moreover, Smith (2002) detailed physical embodiments of the inerter concept to approximate the behaviour of the ideal inerter element through converting linear motion to rotational motion, enabling storing a large amount of kinetic energy at fast-spinning flywheels while requiring negligible mass. The latter characteristic of the inerter device corresponds to the capacitor storing electrical energy in an electrical field.

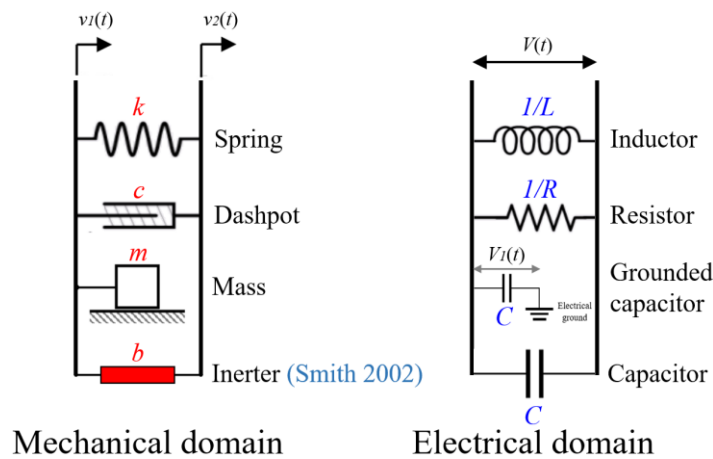


Fig. 2.1. Analogies of mechanical and electrical elements.

Table 2.1 Analogies of mechanical and electrical quantities

Mechanical domain	Electronical domain
Stiffness coefficient, $k$	Reciprocal of inductance, $1/L$
Damping coefficient, $c$	Reciprocal of resistance, $1/R$
Mass, $m$	Capacitance, $C$
Inertance, $b$	
Momentum, $p(t)=mv_1(t)$	Charge, $Q(t)=CV(t)$
Force, $f(t)$	Current, $I(t)$
Relative velocity, $v_1(t) - v_2(t)$	Voltage, $V(t)$
Force and time derivative of velocity $f = m\dot{v}_1$	Current and time derivative of voltage $Q = CV_1 \rightarrow I = C\dot{V}_1$ (grounded capacitor)
Force and time derivative of velocity $f = b(\dot{v}_1 - \dot{v}_2)$	Current and time derivative of voltage $Q = CV \rightarrow I = C\dot{V}$



Force and velocity $f = c(v_1 - v_2)$	Current and voltage $I = 1/RV$
Force and time integral of velocity $f = k \int (v_1 - v_2) dt$	Current and time integral of voltage $V = Li \rightarrow I = 1/L \int V(t) dt$

### 2.2.1 Mechanical element and device implementations

In the 2000s, the inerter was used in the suspension system of Formula 1 racing car under the name “J-damper,” which, when tuned to the resonant frequencies of the tires, reduces rapid load variation at the tire contact patch and hence increasing mechanical grip (Chen et al. 2009). Since then, several different inerter prototypes were devised and experimentally tested over the past decade, achieving inertance values orders of magnitude larger than the physical mass of the device (Smith 2020). The ideal inerter element, capable of simple realization (Smith 2002), develops a resisting force proportional to the relative acceleration of its ends as described by the following equation

$$F = b(\ddot{u}_1 - \ddot{u}_2), \quad (2.1)$$

where  $u_1$  and  $u_2$  are the displacement coordinates of the inerter terminals as shown in Fig. 2.2 (a) and, hereafter, a dot over a symbol denotes time differentiation. In the above equation, the constant of proportionality  $b$  is the so-called inertance measured in mass units (e.g., kg).

Notably, although inerter devices are nonlinear to some extent due to friction and backlash effects, a linear behaviour is observed within relatively wide frequency bands of practical interest (e.g., Papageorgiou and Smith 2005, Wang et al. 2011, Chuan et al. 2012, Takewaki et al. 2012, Swift et al. 2013). This observation justifies adopting the ideal inerter element assumption to model physical inerter devices, which paves the way for developing simplified optimal TMDI tuning and performance assessment approaches for host structures equipped with inerter-based controllers in this work.

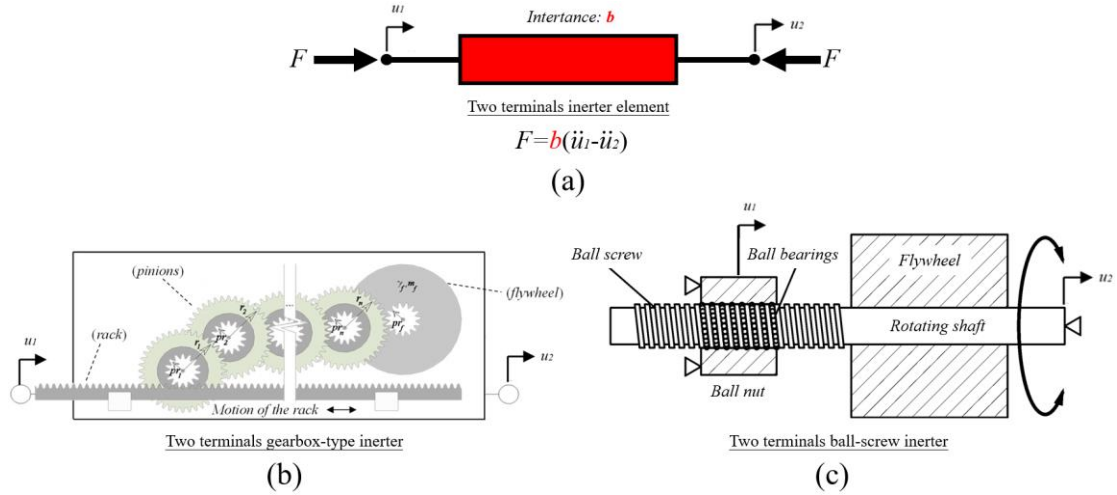


**Fig. 2.2.** Schematic representation of (a) an ideal inerter element; (b) a rack-and-pinion flywheel-based inerter device with  $n$  gears (adapted from [Petrini et al. 2020](#)); and (c) viscous mass damper with a rotational inertial mass (adapted from [Takewaki et al. 2012](#)).

## 2.2.2 Technological aspects and different inerter implementations

In the 1970s, [Kawamata et al. \(1973\)](#) introduced a novel vibration control device that makes full use of the inertial resistance of flowing liquid, which is generally viewed as the earliest realization of the inerter principle ([Ikago et al. 2012](#)). Nowadays, the most widely-known inerter implementations incorporate either rack-and-pinion (see e.g., [Smith 2002](#), [Papageorgiou and Smith 2005](#)) or ball-screw mechanisms (see, e.g., [Arakaki et al. 1999](#), [Ikago et al. 2012](#)) to transform the translational kinetic energy associated with the relative motion of the device terminals into rotational kinetic energy at a lightweight fast-spinning disk/flywheel. In the former configuration, the inertance depends primarily on the number of gears and the gearing ratio used to drive the disk, rather than on the disk's physical mass. To elaborate further on this point, consider a typical mechanical realization comprising a disk linked to a rack-and-pinion via  $n$  gears. Figure 2.2 (b) depicts such a device with  $n$  gears. The inertance of this device is given by

$$b = \left( \prod_{k=1}^n \frac{r_k^2}{pr_k^2} \right) \frac{\gamma_f^2}{pr_f^2} m_f, \quad (2.2)$$

where  $m_f$  and  $\gamma_f$  are the mass and radius of the gyration of the flywheel, respectively,  $pr_f$  is the radius of the flywheel pinion,  $r_k/(pr_k)$  is the gearing ratio of the  $k$ -th stage/gear of the gearbox with  $n$  stages. It is clearly seen in Eq. (2.2) the mass amplification effect of this inerter through the term  $\prod_{k=1}^n r_k^2 / pr_k^2$ .

In the latter case of ball-screw based inerters, the axial relative motion between the device terminals is translated to rotational motion, with amplification, by a threaded shaft with helical grooves for ball bearings acting as a ball screw as shown in Fig. 2.2 (c). The inertance of this

inerter embodiment is calculated by

$$b = \frac{1}{2} \left( \frac{2\pi}{L_d} \right)^2 (r_o^2 + r_i^2) m_f, \quad (2.3)$$

in which  $L_d$ ,  $r_o$ , and  $r_i$  denote the lead of the ball screw (i.e., the linear distance traveled by the ball nut during one full rotation), outer and inner radii of the flywheel, respectively, while  $m_f$  is the actual mass of the flywheel. It is found by [Ikago et al. \(2012\)](#) that, for this type of configuration, the mass amplification factor, i.e.,  $(2\pi/L_d)^2 (r_o^2 + r_i^2)$ , can reach several thousands.

## 2.3 Inerter-based vibration control configurations

### 2.3.1 The tuned viscous mass damper (TVMD)

One strategy to mitigate building vibrations is to increase the energy dissipation capacity of the structure through deploying supplemental damping devices (e.g., viscous, viscoelastic, friction, and hysteretic dampers) distributed in various forms (e.g., integrating dampers in diagonal, chevron, and toggle bracing systems) between adjacent floors. In theory, these devices only change the equivalent damping of the host structure but not the equivalent building mass or stiffness in practical terms. On the other hand, [Hwang et al. \(2007\)](#) proposed a new type of vibration control device termed rotational inertia viscous dampers (RIVD), as shown schematically in Fig. 2.3 (b), which is capable of increasing the equivalent mass *and* damping of a seismically excited SDOF system simultaneously through the ball-screw amplifying mechanism. Notably, the RIVD is dynamically equivalent to a viscous mass damper (VMD). To better engage the device even in structures with small drifts, the RIVDs were incorporated into a toggle bracing system to magnify the axial deformation and energy dissipation of the damper. Numerical results show that the RIVD control performance depends heavily on the lead of the ball-screw: as the lead decreases, the equivalent mass and damping of the controlled structure, and consequently, the RIVD suppression performance increases substantially. Indeed, it is evident in Eq. (2.3) that as the lead  $L_d$  reduces, the inertance coefficient  $b$  is magnified by a factor of  $1/L_d$  squared.

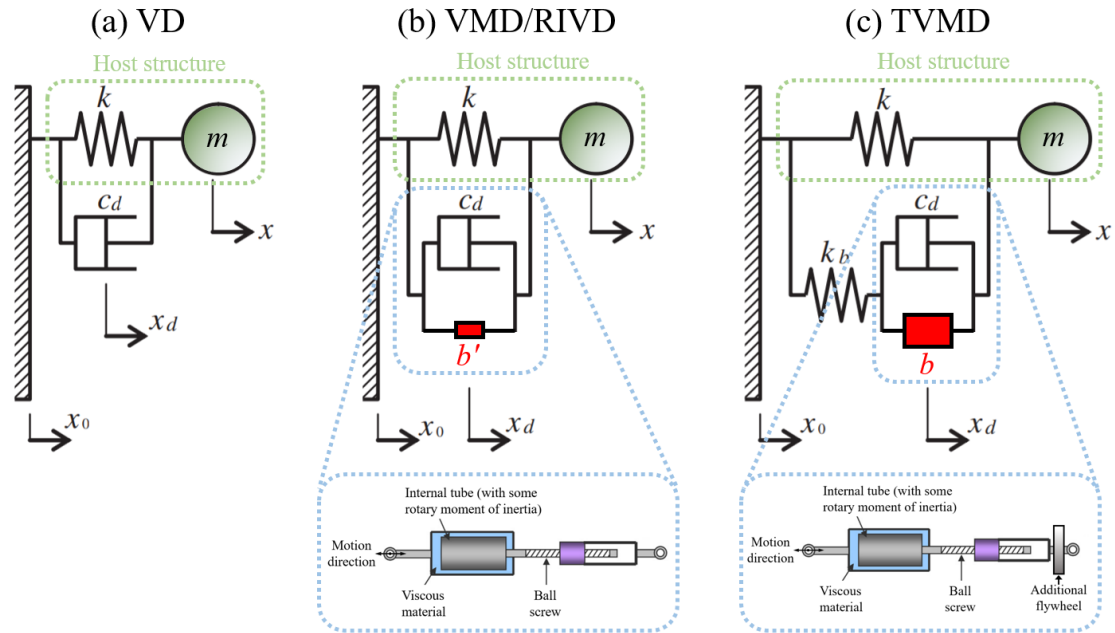


**Fig. 2.3.** Mechanical model of a (a) viscous damper; (b) viscous mass damper/rotational inertia viscous dampers; and (c) tuned viscous mass damper equipped undamped SDOF system (adapted from [Ikago et al. 2012](#)).

Building on the concept of RIVD/VMD, [Ikago et al. \(2012\)](#) developed the tuned viscous mass damper (TVMD), which is a VMD/RIVD in series with a supplementary spring and with an additional flywheel, as shown in Fig. 2.3 (c). Notably, the spring and rotational mass arrangement in the TVMD configuration behaves as a supplementary tuned oscillator that further amplifies the deformation of the damper, thereby improving the RIVD performance and avoiding the use of toggle bracing system. Further, the amplified apparent mass effect of the internal rotational tube in the VMD (cf. Fig. 2.3(b)) has not been used intentionally ([Ikago et al. 2012](#)), whereas in the case of TVMD, this amplifying effect is explicitly achieved by adding a flywheel to the device (see Fig. 2.3 (b)) such that the TVMD allows simultaneous mass and damping enhancement for the first time ([Zhang et al. 2018](#)). The TVMD system is tuned to the fundamental mode of the host structure. Closed-form solutions for optimal frequency and damping ratios of the TVMD system were derived through the fixed-points theory ([Den Hartog 1956](#)) for an undamped SDOF structure subjected to harmonic excitation and were used, as approximations, for slightly damped SDOF systems. The TVMD performance for seismic control was investigated numerically and experimentally through shaking table tests using a SDOF system equipped with a small-scale TVMD. The simulation and test results suggest that the TVMD is more effective in suppressing the displacement response of the SDOF system for ground motions having a wide range of frequency components than the conventional VD and VMD with the same damping coefficient  $c_d$  as shown in Fig. 2.3 (a) and (b).

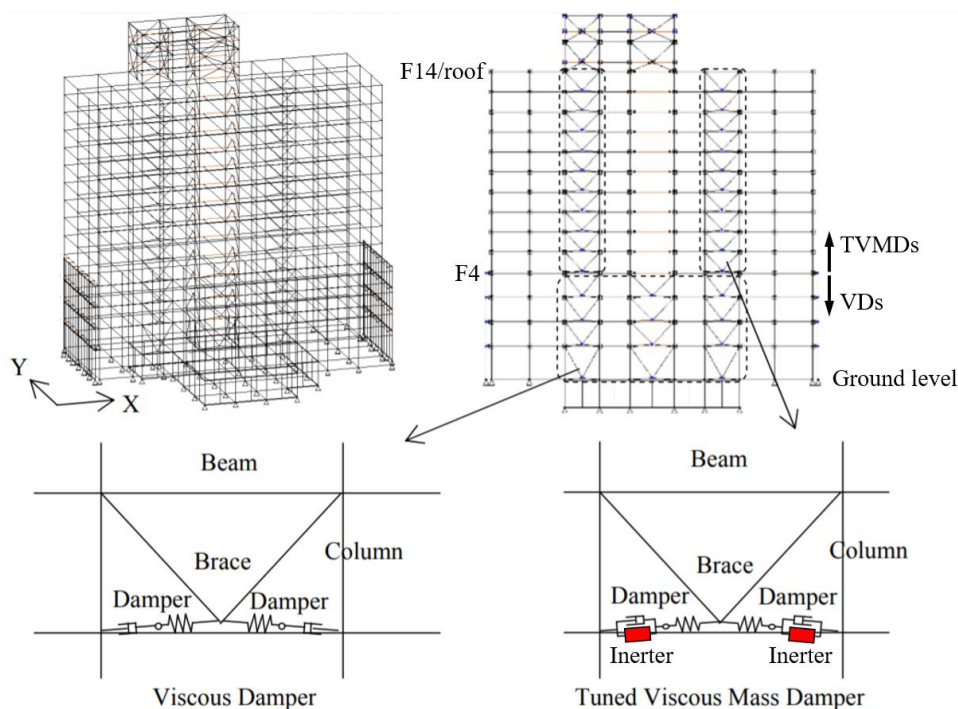


**Fig. 2.4.** a 14-storey MRF building in Tohoku Japan that utilises viscous dampers and tuned viscous mass dampers configured in conjunction with V-shaped bracing systems for seismic control (Sugimura et al. 2012).

For application, figure 2.4 shows a 14-storey MRF building in Tohoku, Japan, that incorporates conventional VD's (in the first four stories) and TVMD's (from the 4th floor above) in conjunction with V-shaped steel bracing systems for seismic protection of the building through simultaneous mass and damping enhancements. Sugimura et al. (2012) reported that an apparent mass of 5,400 tonnes, accounting for 7% of the total building mass, can be obtained by a physical mass of 560 kg only, thus achieving a mass amplifying factor of 9,643. Further, the modal damping ratio of the fundamental mode, which dominates the seismic response of the building, is increased to 14% through the inclusion of the VD's and TVMD's.

### 2.3.2 The tuned inerter damper (TID)

Another representative inerter-based vibration control configuration, proposed by Lazar et al. (2014) for seismic protection of multi-storey buildings, is the so-called tuned inerter damper (TID). The latter can be installed either on the top floor (connecting the roof and penultimate floor) to replace the conventional TMD or on the first floor (connecting the first floor and ground) of the buildings (see Fig. 1.6(c)) in which case the inerter is grounded and acts as a mass element equal to  $b$ . In both cases, the inclusion of the inerter element creates an additional lateral degree-of-freedom (DOF), denoted by  $x_{TID}$  in Fig. 1.6 (c), which, in the case of the ground-level installation, makes the TID to be dynamically equivalent to a TMD hung from the first floor but without an attached mass. The main advantage of TID's is that a high level of vibration suppression can be achieved with a much reduced weight through scaling up the

inertance by gearing (Lazar et al. 2014). Compared to the TMDI, the TID has a simpler configuration as the entire attached mass is substituted with a single inerter element (Radu et al. 2019), which connects the parallelly arranged spring and damper elements directly to the floor underneath. Through algebraic solution, Lazar et al. (2014) found that, in addition to the two well-known fixed points on the FRF of TMD-equipped undamped SDOF oscillators, there exists a third fixed point on the FRF curve of TID-equipped SDOF system at a higher frequency. By extending the fixed-points technique (Den Hartog 1956), the TID tuning strategy was established analytically for undamped SDOF systems subjected to sinusoidal ground motion. Four different control strategies with the same apparent mass, namely, the top-floor and ground-floor TMD and TID, were studied numerically in an undamped 3-storey planar frame model subjected to seismic excitation. The numerical results show that the ground-floor TID achieved better control performance than the top-floor counterpart with the same inertance value, whereas, in the case of TMDs, the opposite was true. Further, optimally-tuned TID and TMD installed on the same floor exhibit similar control performance, though the former required a much smaller weight. Finally, for the ground-floor TID to perform equally well as top-floor TMD, the inertance value needs to be five times larger than the attached mass of the TMD for the frame model considered therein.

### 2.3.3 The tuned mass damper inerter (TMDI): a generalization of TMD and TID

Independently of the TID, Marian and Giaralis (2013) proposed a DVA, called tuned mass damper inerter (TMDI), for passive protection of seismically excited multi-storey buildings combining the inerter with the classical TMD as depicted in Fig. 1.6 (b). In this configuration, the inerter device connects the TMD attached mass to a lower floor of the building, with the TMDI stiffness and damping properties,  $k_{TMDI}$  and  $c_{TMDI}$ , tuned to control the fundamental vibration mode of the primary structure for given attached mass,  $m_{TMD}$ , and inertance constant,  $b$  (cf. Fig. 1.6 (b)). Notably, in the absence of the inerter, the TMDI in Fig. 1.6 (b) reduces to a classical TMD with a free-to-oscillate mass in Fig. 1.6 (a), whereas when the inerter substitutes the attached mass entirely, the TID configuration in Fig. 1.6 (c) is retrieved. In this respect, the TMDI can be viewed as a generalization of the TMD and the TID (Marian and Giaralis 2017). Pertinent analytical and numerical data, reported in Marian and Giaralis (2014) for damped SDOF and MDOF primary structures base-excited by stationary stochastic processes, evidenced that using the inerter in the proposed configuration can either replace a considerable part of the TMD vibrating mass to achieve a significantly lighter passive vibration absorber for fixed performance or improve the TMD performance for a fixed attached mass. These advantages of the TMDI were attributed, on the one hand, to the mass-amplification and higher-mode damping effects endowed by the inerter and, on the other hand, to more efficient usage of the damper with a much higher damping coefficient compared to a same-mass TMD. In this regard, the TMDI was shown to outperform the TMD for the seismic protection of fixed-based buildings (Giaralis and Marian 2016, Pietrosanti et al. 2017, Giaralis and Taflanidis 2018,



Ruiz et al. 2018, De Domenico et al. 2020, Kaveh et al. 2020) and based-isolated buildings (De Domenico and Ricciardi 2018, De Angelis et al. 2019), as well as for serviceability performance enhancement of wind-excited high-rises (Giaralis and Petrini 2017, Dai et al. 2019) and vibration control of wind turbine towers (Sarkar and Fitzgerald 2019).

In detail, Pietrosanti et al. (2017) investigated the effects of different TMDI optimisation strategies on optimal TMDI tuning properties, i.e., stiffness and damping coefficients, employing a white-noise base-excited damped SDOF primary structure system with the inerter connecting the secondary mass to the ground. Three optimisation criteria were adopted to design the TMDI, i.e., minimising displacement and acceleration of the primary system, as well as maximising dissipated energy by TMDI over total input energy. Numerical results show that the tuning parameters obtained by the three criteria were similar for the same TMDI attached mass and inertance value, whereas the optimal solutions found by the third criteria always lie between the corresponding values determined by the first and second strategies. To this effect, the authors concluded that the third criterion forms a "middle ground" for optimal TMDI design under simultaneous displacement and acceleration constraints on the primary system. Furthermore, Giaralis and Taflanidis (2018) considered an optimum TMDI design framework accommodating the mass-amplification and higher-mode-damping benefits while accounting for parametric uncertainties to the host structure properties and seismic excitation. Numerical results pertinent to a 10-storey building under stationary Kanai - Tajimi stochastic excitation evidence that the TMDI achieves enhanced structural performance and robustness to building and excitation uncertainties compared to same mass/weight TMDs. In particular, parametric uncertainty to the excitation was shown to have a minor impact on TMDs, TIDs, and TMDIs, whereas structural uncertainties only had a noticeable impact on the first two but not on the TMDI.

More recently, Pietrosanti et al. (2020a) demonstrated that the relative modal coordinate of the hosting structure between the two terminals of the TMDI influences the TMDI effectiveness significantly in seismically excited buildings represented by lumped-mass models. In this regard, the work of Pietrosanti et al. (2020a) points to the fact that the stiffness and/or mass properties of the primary structure can affect the motion control efficacy of the TMDI, which is not the case for classical TMDs. Further, Pietrosanti et al. (2020b) conducted a campaign employing shaking table testing to assess the TMDI vibration suppression attributes in harmonically excited SDOF structures under combined effects of structural and inerter nonlinearity. Experimental data show that the main advantages of the TMDI established in the literature for ideal inerter elements (e.g., improved vibration suppression through increasing inertance without increasing physical mass) is maintained for non-ideal inerter devices. More importantly, the dynamic response of the SDOF structure in terms of displacement, acceleration, and base reaction force is insignificantly influenced by the nonlinear attributes of the inerter device.

## 2.4 Applications of TMDI to benchmark building structures

### 2.4.1 Earthquake engineering applications

In several previous studies (see, e.g., [Marian and Giaralis 2014](#), [Giaralis and Taflanidis 2018](#), [Pietrosanti et al. 2017](#)), optimally tuned TMDIs were shown to outperform TMDs in mitigating earthquake-induced vibrations in building structures for the same secondary mass, especially, if it is relatively small. Nevertheless, all these TMDI seismic application studies involved simplified modelling assumptions, such as considering shear-type frame building models, adopting a single performance objective, and/or representing seismic excitation as a stationary stochastic process). Recognising the above limitations, [Ruiz et al. \(2018\)](#) extended these efforts by examining a risk-informed TMDI optimisation, adopting multiple objectives for TMDI design and employing probabilistic life-cycle criteria to quantify performance using time-history analysis while assuming linear structural behaviour. Emphasis of the work was placed on TMDI applications for seismic protection of tall buildings in the region of Chile, which was motivated by the fact that mass/inertia dampers had been shown particularly efficient in reducing structural damage potential of earthquakes in the Chilean seismo-tectonic environment ([Ruiz et al. 2015](#)). Three performance criteria were used in the design optimisation including the life-cycle cost of the integrated system composed of the device upfront cost and anticipated seismic losses over the structure lifetime, the repair cost with a specific return of period, and the inerter force magnitude affecting the inerter size and upfront cost. A case study was presented employing a specific 76.2m-tall 21-storey building with an unsymmetrical tapered elliptical floorplan located in Santiago, Chile. Seven different inerter topological configurations were examined with the TMDI mass attached either to the top floor or the 18th floor and the inerter connecting the secondary mass to the floor either one, two, or three stories above or below. Numerical results show that optimal TMDI configurations can accomplish simultaneous reduction of life-cycle and repair costs, though at the expense of larger inerter forces and, thus, increased inerter size and cost. Further, it was shown that connecting the inerter to a lower floor provides considerable benefits across all examined performance criteria as the inerter is engaged in a more efficient way for the same inerter coefficient and attached mass ratios.

Furthermore, [De Domenico et al. \(2020\)](#) recently explored the potential of using multiple TMDIs, integrated into the aerial walkway connecting two adjacent high-rise buildings, as an unconventional control strategy for enhancing structural safety and serviceability of near located tall buildings or twin towers subject to seismic hazards. The idea was to utilise the uncorrelated relative motion between the buildings to maximise the TMDI efficiency in suppressing earthquake-borne vibrations in both structures. A case study was presented involving a real project in China that has two closely located buildings coupled by an aerial corridor connecting the 46th floor of the taller tower to the roof/55th floor of the lower. One TMDI system was installed in each building with the second terminal of the inerter device connected to the other building via the aerial passage. For optimal TMDI designs, performance-



based optimisations were performed to determine the optimal values of attached mass, inertance, stiffness and damping coefficients of both TMDIs that minimise the averaged floor displacement, inter-storey drift, *or* floor acceleration of two buildings simultaneously by employing Nondominated Sorting Genetic Algorithm II for 44 ground motions from the FEMA P695 far-field record set. It was found that the frequency contents of the seismic input have a strong impact on the TMDI control performance. Considering reasonable constraints imposed on the TMDI inertial properties and location, the optimally designed dual TMDI system was shown to outperform both the conventional multiple TMD system and single TMDI and to be very efficient in acceleration and inter-storey control but not in displacement suppression.

#### 2.4.2 Wind engineering applications

Turning attention to wind engineering applications, [Giaralis and Petrini \(2017\)](#) explored for the first time the idea of using a top-floor TMDI in various inerter topologies to suppress excessive crosswind-induced oscillations compromising occupant comfort in super-tall buildings. A parametric numerical study was undertaken involving a TMDI-equipped planar low-order model, defined in terms of lumped mass, damping, and stiffness matrices, that accurately captured the in-plane dynamic behaviour of a 74-storey benchmark building exposed to a quasi-stationary spatially correlated wind force field accounting for VS effects in the crosswind direction. The TMDI frequency and damping ratios were determined using closed-form solutions yielding optimal tuning parameters for the classical TMD that minimise the displacement response variance of white noise force-excited undamped SDOF primary structures ([Warburton 1982](#)). To this effect, the tuning parameters used in this study did not **aim to** achieve optimal TMDI design for the considered wind-excited primary structure against any particular optimisation criterion, but only yielded reasonable yet suboptimal values of tuning parameters. Still, it was found that the inerter incorporation to the TMD reduces the peak top floor acceleration supporting improved occupant comfort beyond a same-weight TMD more effectively by adopting smaller attached mass together with TMDI connectivity in which the inerter spans more storeys in linking the attached mass to the host structure. These findings were attributed to the mass-amplification and higher-mode damping effects of the TMDI previously discussed (see also Figure 1.5), which become more prominent for smaller TMD masses and larger inerter topologies. In this context, it was numerically shown that the TMDI can meet code-prescribed serviceability design requirements by considering significantly smaller attached mass (depending on the TMDI connectivity and inertance coefficient) compared to the TMD and (ii) the inerter device can be used to upgrade existing TMD-equipped tall buildings, without changing the attached mass, to meet more stringent serviceability design requirements than those considered in the initial design due to site-specific climate change effects or changes to the surrounding built environment (i.e., increased wind exposure).

Moreover, [Wang et al. \(2019\)](#) extended the above efforts by considering a performance-

based numerical optimisation that aims to minimise either peak floor displacement or acceleration in wind-excited tall buildings. The optimisation formulation treated explicitly the device's location, i.e., on which floor the TMDI is deployed, as an active/primary design variables alongside the TMDI stiffness and damping coefficients. However, given the inherent complexity of wind excitation models, the therein proposed TMDI optimisation approach, which relies on repetitive time-domain analysis through complex mode superposition, becomes computationally overly demanding, as the number of the primary structure DOFs increases. In this context, it is deemed necessary to develop a computationally efficient tuning strategy for wind-excited TMDI-equipped tall buildings to meet the relevant serviceability requirements.

## 2.5 Research gaps

The existing body of research on TMDI vibration control for tall buildings (Giaralis and Petrini 2017, Giaralis and Taflanidis 2018, Ruiz et al. 2018, Dai et al. 2019, Domenico et al. 2020) has well established the beneficial effects of inerter incorporation in conventional TMDs for improved control efficacy and robustness. These improvements are achieved by means of increasing the inertance and/or inerter connectivity. Nevertheless, most of these studies have been undertaken to investigate the TMDI control performance in earthquake-excited building structures, while limited work has been undertaken to address the efficient optimal TMDI design for wind-induced vibration suppression (research gap #1). At the same time, no relevant work has been conducted to systematically quantify the influence of elastic and mass properties of the primary structure on the TMDI control efficacy (research gap #2). Moreover, for typical mid-rise buildings and certain cantilever-like structures, spanning the inerter over several floors in linking the attached mass to the host structure may not be physically possible or cost-effective. In these circumstances, alternative strategies are needed to extend the applicability of TMDI for routine mid-to-high-rise wind-sensitive buildings and, more generally, slender cantilevered structures (research gap #3). Last but not least, no prior research has utilised inerter-based DVAs to achieve material-efficient design of the lateral wind load resisting structural systems of tall buildings commonly governed by serviceability (occupant comfort) requirements through simultaneous optimisation of the primary structural system and of the vibration absorber in an integrated manner (research gap #4). The above four identified research gaps are addressed in this PhD thesis by pursuing the four research objectives, respectively, listed in Section 1.2. In the following Chapter, the focus is placed on developing a computationally efficient optimal TMDI tuning strategy for wind-borne motion control of tall buildings, and then on quantifying numerically various gains achieved by TMDIs *optimally tuned* for occupant comfort performance in tall buildings subject to VS effects. Thus, next chapter addresses research gap #1 by pursuing objective (I).

---

## Chapter 3

---

### Optimal TMDI Tuning for Wind Excited Buildings

Note: Part of this Chapter has been published in

Petrini, F., Giaralis, A., and Wang, Z. (2020). “Optimal tuned mass-damper-inerter (TMDI) design in wind-excited tall buildings for occupants’ comfort serviceability performance and energy harvesting.” *Eng. Struct.*, 204: 109904.

Herein, material corresponding only to the Candidate contribution to the paper is presented. This includes the formulation of a novel optimal TMDI design problem with a numerically efficient tuning algorithm for minimising floor accelerations in wind-excited tall buildings through optimal TMDI tuning, but with no energy harvesting considerations. All the numerical data presented in this Chapter have been obtained by the candidate using own-developed computer code. Further, Appendix B.5 includes verification of frequency-domain analysis results against time-domain analyses conducted by the Candidate using wind tunnel force data made available to the Candidate.

#### 3.1 Preliminary remarks

Design of any DVA for motion control of a primary structure involves determining optimal properties of the absorber to maximise its effectiveness (Ghosh and Basu 2007). To this aim, this Chapter extends the work of Giaralis and Petrini (2017) to explore the full potential of *optimally tuned* TMDI with different inertial properties and inerter connectivities for vibration control and occupant comfort in wind-excited tall buildings susceptible to VS effects. In this respect, the Chapter addresses directly research gap #1 in Section 2.5 by pursuing objective (I) of Section 1.2. Specifically, the investigation is supported by formulating a novel TMDI optimisation problem (OP) and by considering a numerical solution strategy, aiming to minimise building floor accelerations under specified wind action. The approach is illustrated by application to the 74-storey benchmark structure equipped with a top-floor TMDI considered previously in Giaralis and Petrini (2017) *without* optimal TMDI tuning. The optimal TMDI properties are determined using a numerically efficient algorithm for a wide range of TMDI inertial properties and various inerter connectivities. The tuning process requires a structural analysis step to be undertaken assuming the same wind-excited primary structure but different TMDI stiffness and damping properties, which can be computationally intensive if applied to a detailed finite element (FE) model. To this effect, simplified low-order models that can accurately represent the detailed FE model (of the building) are necessary to meet the objective in a computationally efficient manner. Therefore, the planar low-order model derived in Giaralis and Petrini (2017), which was found dynamically equivalent to the FE model of the benchmark building, is adopted in this Chapter as the testbed/case-study structure for validating

the herein proposed tuning algorithm and for investigating the TMDI control effectiveness. The low-order model is excited by a well-established stochastic wind force model accounting for VS effects calibrated against wind tunnel tests (Liang et al. 2002). Notably, the OP formulation and numerical solution strategy presented herein are applicable to the optimal design of *any* inerter-based DVA for maximising occupant comfort in slender structures and are, thus, employed in later Chapters, with necessary modifications, for optimal TMD, TID, and TMDI design in various dynamically excited cantilevered structures.

### 3.2 Optimal TMDI design for occupant comfort in wind excited structures

In this section, a novel TMDI tuning problem is formulated alongside a custom-coded pattern search algorithm with iteratively narrowing search range to efficiently design/tune the TMDI primary design variables (DVs) for floor acceleration minimisation under a given design wind.

#### 3.2.1 Optimal design problem formulation

The proposed optimal TMDI tuning for a  $n$ -storey building aims to minimise either the peak or RMS acceleration of the  $k$ -th floor. In most cases, the  $k$ -th floor is chosen to be the top floor as this is where the floor acceleration reaches its maximum value in the crosswind direction of typical building structures. With reference to Figure 1.6(b), the considered OP involves five dimensionless design parameters in total. These include the TMDI frequency and damping ratios defined as

$$v_{TMDI} = \frac{\sqrt{k_{TMDI}/(m_{TMDI} + b)}}{\omega_1} \quad \text{and} \quad \xi_{TMDI} = \frac{c_{TMDI}}{2\sqrt{(m_{TMDI} + b)k_{TMDI}}}, \quad (3.1)$$

respectively. They are grouped in the vector  $\mathbf{x}_1 = [v_{TMDI}, \xi_{TMDI}]^T$  and are treated as primary DVs throughout this thesis. Additionally, the OP involves three secondary DVs, namely the TMDI attached mass and inertance ratios defined as

$$\mu = \frac{m_{TMDI}}{M} \quad \text{and} \quad \beta = \frac{b}{M}, \quad (3.2)$$

respectively, plus the TMDI connectivity  $1 \leq p \leq n$ , grouped in the vector  $\mathbf{x}_2 = [\mu, \beta, p]^T$ . In Eq.(3.2),  $M$  is a characteristic mass property of the primary structure (e.g., total building mass). Then, optimal design parameters in  $\mathbf{x}_1$  (primary DVs) are sought within a prespecified search range  $[\mathbf{x}_1^{\min}, \mathbf{x}_1^{\max}]$  to minimise the objective function (OF), i.e.,  $\text{peak}\{\ddot{x}_k\}$  or  $\text{RMS}\{\ddot{x}_k\}$ , given values of the parameters in  $\mathbf{x}_2$  (secondary design parameters). The problem can be mathematically expressed as

$$\begin{aligned} & \min_{\mathbf{x}_1} [\text{OF}(\mathbf{x}_1 | \mathbf{x}_2)], \text{ where } \text{OF} = \text{peak}\{\ddot{x}_k\} \text{ or } \text{RMS}\{\ddot{x}_k\}, \\ & \text{subjected to } \mathbf{x}_1^{\min} \leq \mathbf{x}_1 \leq \mathbf{x}_1^{\max} \end{aligned} \quad (3.3)$$

For a given building structure subjected to crosswind excitation, the OF can be efficiently computed following the frequency-domain random vibration analysis approach detailed in Appendix A.

Purposely, the optimal design formulation in Eq. (3.3) allows for considering explicitly any desired combination of TMDI inertial properties (through  $\mu$  and  $\beta$ ) and TMDI connectivity  $p$  (i.e., number of floors spanned by the inerter element). In this manner, the special cases of TMD and TID can be examined by taking  $\beta=0$  and  $\mu=0$ , respectively. The performance in terms of occupants comfort can be verified by comparing either the hourly peak or RMS acceleration of the highest occupied floor under a design wind having a particular annual return period with the code-prescribed threshold values depending on the first natural frequency of the building (i.e.,  $\text{peak}\{\ddot{x}_k\} \leq \ddot{x}_{\text{threshold}}$  or  $\text{RMS}\{\ddot{x}_k\} \leq \ddot{x}_{\text{threshold}}$ ).

### 3.2.2 Numerical solution strategy

The solution to the OP in Eq. (3.3) for a TMDI-equipped tall building represented by a damped MDOF system excited by complex wind excitation model is mathematically intractable and non-trivial. Therefore, a numerical pattern search solution strategy (Charles and Dennis 2003) with iteratively updated search range of the primary DVs for efficiency is herein employed for the task and coded in MATLAB®. Specifically, a Cartesian three-dimensional coordinate system ( $v_{TMDI}$ ,  $\zeta_{TMDI}$ ,  $\text{peak}\{\ddot{x}_k\}$  or  $\text{RMS}\{\ddot{x}_k\}$ ) is first created, with the vertical axis representing the peak or RMS crosswind acceleration on the selected floor  $k$ . The horizontal  $v_{TMDI}$ - $\zeta_{TMDI}$  plane is discretised into an orthogonal mesh grid with upper and lower boundaries specified by  $\mathbf{x}_1^{\max}$  and  $\mathbf{x}_1^{\min}$ , respectively. The performance is evaluated at all points of the mesh grid for fixed TMDI inertial properties defined by  $\mu$  and  $\beta$ , and connectivity  $p$ . Subsequently, the minimal performance, i.e.,  $\min\{\text{peak}\{\ddot{x}_k\}\}$  or  $\min\{\text{RMS}\{\ddot{x}_k\}\}$ , within the search range is returned, with the corresponding  $v_{TMDI}$  and  $\zeta_{TMDI}$  coordinates stored as the optimal tuning parameters,  $v_{opt}$  and  $\zeta_{opt}$ , at the *current* iterative step for the pre-selected TMDI inertial properties and connectivity. Based on the convergence criterion against the optimal performance, the boundaries/search range for  $v_{TMDI}$  and  $\zeta_{TMDI}$  are narrowed in the next iteration, using the optimal tuning values found in the current iteration. The iterations stop when the ratio of the absolute performance difference (between current iteration  $i$  and previous iteration  $i-1$ ) to the current performance becomes smaller than a pre-specified tolerance, in which case convergence is assumed and the global minimum is returned. The algorithm is illustrated in the flowchart of Fig. 3.1. The TMDI tuning approach presented here is illustrated in section 3.5 using the TMDI-equipped benchmark structure and wind excitation discussed in the following

two section.

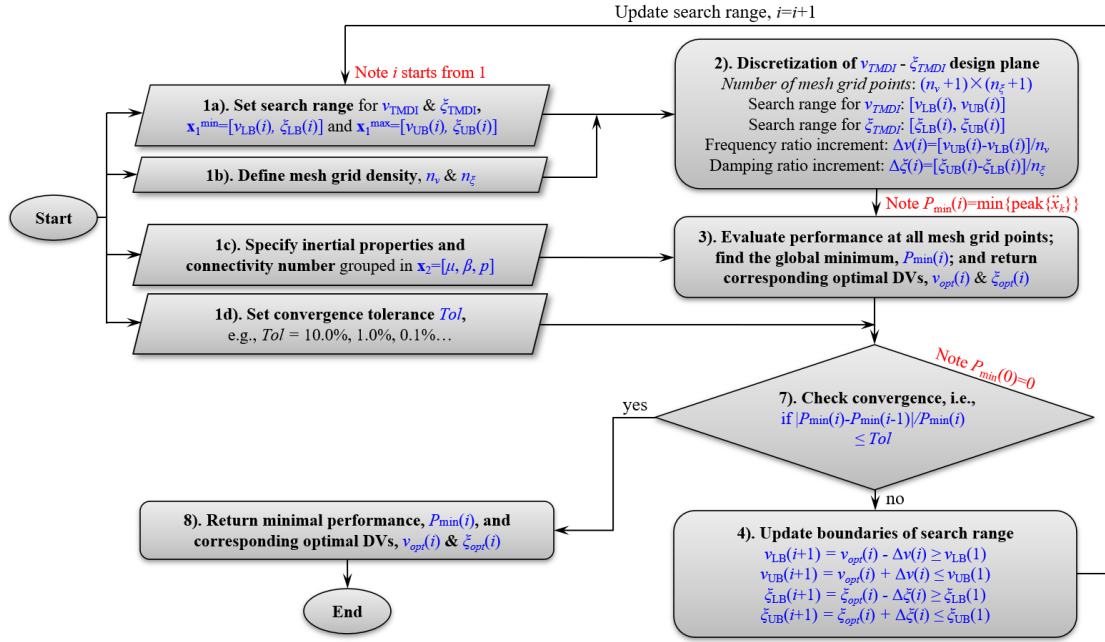


Fig. 3.1. Flowchart of the pattern search algorithm with adapted search range for optimal TMDI design.

### 3.3 Modelling of case-study building structure and wind force excitation

#### 3.3.1 Benchmark building description and finite element modelling

A slender crosswind-excited 74-storey steel building with height-to-width aspect ratio of more than 6 is used as a case-study structure for assessing performance and advantages of *optimally tuned* TMDIs throughout this chapter. The building has rectangular 50m  $\times$  50m footprint and is 305.9 m tall: typical floor height is 4 m, while ground and last floor height is 13 m and 4.9 m, respectively. The adopted structure is sensitive to VS induced vibrations compromising occupant comfort and has been previously considered as benchmark for the development of performance-based wind engineering approaches (Ciampoli and Petrini 2012, Petrini and Ciampoli 2012, Spence and Giofrè 2012). The lateral load bearing system of the case-study structure is double-symmetric along two horizontal perpendicular principal axes. It comprises an inner and an outer spatial steel frame having 12 and 28 columns, respectively, which are all pinned at the base. The two frames are connected by three steel truss outriggers spaced approximately 100 m apart. All columns have hollow square sections, with varying dimensions and thickness along the building height ranging between 1.20 m  $\times$  1.20 m to 0.50 m  $\times$  0.50 m, and 0.06 m to 0.025 m, respectively. Beams are of various standard double-T steel profiles while outriggers consist of double-T horizontal and hollow-square diagonal members. A linear FE model of the considered structural system is developed in SAP2000® software package as shown in Fig. 3.2. The FE model comprises 7592 linear Euler-Bernoulli beam elements with all beam-to-column connections taken as rigid. Horizontal rigid diaphragm constraints are imposed at the height of each floor to account for the effect of the slabs in the



model. The total mass of the structure accounting for dead, superimposed, and live loads is 92830 Mg and is uniformly distributed at each floor level except for the last floor to which half of the typical floor mass is assigned.

Due to the presence of VS effects, the direction of the wind field which maximises lateral wind-induced vibrations (floor accelerations) in the crosswind direction coincides with any of the two principal axes of the adopted structure (Petrini and Ciampoli 2012). Therefore, only the uncoupled purely translational vibration modes of the FE model along a principal building axis are required for the assessment of structural performance in terms of occupant comfort serviceability limit state. For illustration, the first three translational mode shapes along a horizontal principal building axis are plotted in Fig. 3.2 tracing nodal displacements of the master node of each floor. They are obtained from standard linear modal/eigenvector analysis in SAP2000® upon constraining all rotational DOFs about the gravitational axis and all translational DOFs along the perpendicular horizontal principal axis of the building. The first three natural frequencies of these modes and the corresponding modal participating mass ratios in parentheses are 0.185 Hz (0.6233), 0.563 Hz (0.1900), and 1.052 Hz (0.0745).

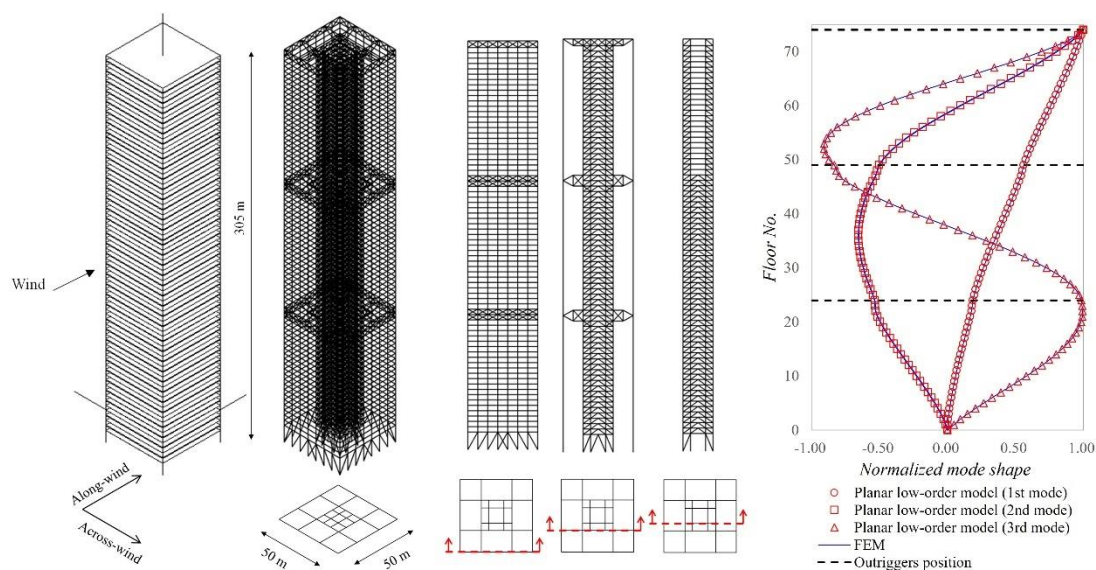


**Fig. 3.2.** Detailed FE model of the adopted benchmark case-study tall building structure and in-plan lateral translational mode shapes.

Furthermore, the first six natural frequencies and respective modal participating mass ratios of the same building model in Fig. 3.2, with *all* DOFs activated (i.e., six DOFs per node), are summarised in Table 3.1 to demonstrate the influence of out-of-plane DOF deactivation on the modal properties of the model. In the Table,  $U_x$ ,  $U_y$ , and  $U_z$  denote the global translational directions, X, Y, and Z, respectively, and  $R_x$ ,  $R_y$ , and  $R_z$  denote the rotational directions about the X, Y, and Z axes, separately. Evidently, besides the symmetry of translational/flexural vibration modes in the two principal directions, no coupling is noted between any two flexural

modes or within any combination of flexural and torsional modes by viewing the pertinent modal participating mass ratios. To this end, it is reasonable to model the building as a planar dynamic system within any of the principal planes. As an extra precaution, it has been numerically verified that floor accelerations of the case-study building under the wind excitation introduced in section 3.3.3 are dominated by the fundamental vibration mode *only*, as the acceleration response is found insensitive to variation of the higher modal damping ratios.

**Table 3.1.** The first six natural frequencies and corresponding modal participating mass ratios of the building FE model in Fig. 3.2 with all degrees-of-freedom activated.

Mode	Frequency [Hz]	Modal participating mass ratio					
		Ux	Uy	Uz	Rx	Ry	Rz
1	0.185	0.6233	0.0000	0.0000	0.0000	0.3921	0.0000
2	0.185	0.0000	0.6233	0.0000	0.3922	0.0000	0.0000
3	0.323	0.0000	0.0000	0.0000	0.0000	0.0000	0.7481
4	0.563	0.1901	0.0000	0.0000	0.0000	0.2138	0.0000
5	0.564	0.0000	0.1901	0.0000	0.2137	0.0000	0.0000
6	0.867	0.0000	0.0000	0.0000	0.0000	0.0000	0.1219
Sum		0.8134	0.8134	0.0000	0.6059	0.6059	0.8699

### 3.3.2 Low-order planar frame model

The fact that the critical response of the adopted case-study building to wind excitation lies along any one structural principal axis motivates the consideration of a surrogate planar (two-dimensional) dynamical model capturing faithfully the in-plane lateral vibrational behaviour along a principal axis of the high-fidelity three-dimensional FE model of Fig. 3.2. The considered model has  $N = 74$  DOFs corresponding to the lateral translational displacements of the 74 rigid diaphragms, one at each floor, along a principal horizontal axis of symmetry of the case-study building. It, therefore, can be viewed as a 74-storey planar frame supporting, in later sections, the physical tractability of different TMDI topologies involving different floor connectivity.

Mathematically, the adopted planar model is defined in terms of mass,  $\mathbf{M}_s \in \mathbb{R}^{74 \times 74}$ , damping,  $\mathbf{C}_s \in \mathbb{R}^{74 \times 74}$ , and stiffness,  $\mathbf{K}_s \in \mathbb{R}^{74 \times 74}$  matrices such that: (i) its undamped 74 modes of vibration match the 74 lateral uncoupled translational modes of the FE model of the case-study structure in Fig. 3.2, and (ii) it attains mode-dependent damping properties specified based on recorded measurements from real-life tall buildings reported in the literature (Spence and Kareem 2014). Notably, the definition of the planar frame model through  $\mathbf{M}_s$ ,  $\mathbf{C}_s$ , and  $\mathbf{K}_s$  matrices enables, later, the incorporation of the TMDI through straightforward matrix manipulations rather than modifications to the detailed FE model.

Following Giaralis and Petrini (2017), condition (i) is met by first defining a diagonal mass matrix  $\mathbf{M}_s$  with diagonal elements equal to the floor masses assumed by the FE model. That is,  $\mathbf{M}_s[k, k] = 1263$  tonne ( $k = 1, 2, \dots, 73$ ) and  $\mathbf{M}_s[74, 74] = 631$  tonne. Next, a full stiffness



matrix  $\mathbf{K}_s$  is obtained by satisfying the modal analysis equations

$$\left[ \mathbf{K}_s - \omega_{(\text{FE})j}^2 \mathbf{M}_s \right] \boldsymbol{\varphi}_{(\text{FE})j} = 0; j = 1, 2, \dots, 74, \quad (3.4)$$

where  $\boldsymbol{\varphi}_{(\text{FE})j} \in \mathbb{R}^{74 \times 1}$  is the  $j$ -th uncoupled translational mode shape along a principal building axis obtained from the detailed FE model as previously discussed and  $\omega_{(\text{FE})j}$  is the corresponding natural frequency. Excellent mode shape matching is achieved as illustrated in the rightmost panel of Fig. 3.2 in which the first three normalised mode shapes obtained from the FE model,  $\boldsymbol{\varphi}_{(\text{FE})j}$  ( $j = 1, 2, 3$ ) and from the planar frame model,  $\boldsymbol{\varphi}_j$  ( $j = 1, 2, 3$ ), are superposed plotted as continuous lines and circle-shaped dots, respectively. Further, a full damping matrix is obtained by the expression

$$\mathbf{C}_s = (\boldsymbol{\Phi}^T)^{-1} \mathbf{C}_{\text{mod}} (\boldsymbol{\Phi})^{-1}, \quad (3.5)$$

where  $\boldsymbol{\Phi} \in \mathbb{R}^{74 \times 74}$  is the modal matrix collecting all 74  $\boldsymbol{\varphi}_j$  mode shapes, the superscript “-1” denotes matrix inversion, and  $\mathbf{C}_{\text{mod}} \in \mathbb{R}^{74 \times 74}$  is a diagonal matrix defined as

$$\mathbf{C}_{\text{mod}}(j, j) = 2\omega_j \xi_j (\boldsymbol{\varphi}_j^T \mathbf{M}_s \boldsymbol{\varphi}_j); j = 1, 2, \dots, 74 \quad (3.6)$$

In the last equation,  $\omega_j$  and  $\xi_j$  are the  $j$ -th natural frequency and modal damping ratio, respectively, of the planar frame model. In meeting condition (ii) above, modal damping ratios are taken equal to the values summarised in Table 3.2. Specifically, damping ratios in the frequency range of 0-7Hz are specified to match experimentally identified damping ratios from full-scale field measurements in tall steel framed buildings reported in [Spence and Kareem \(2014\)](#) and references therein. For natural frequencies above this range, increasing damping ratios with natural frequency are assumed to converge asymptotically to an arbitrary 18% damping ratio. The assumed increase in damping with frequency accounts for the anticipated greater participation of non-structural components in the inherent damping of the structure for oscillations dominated by the higher vibration modes (see [Spence and Kareem 2014](#) and references therein). Notably, it has been numerically verified that the floor accelerations of the case-study building are solely dominated by the fundamental vibration mode in the sense that modal damping ratios of higher modes do not affect the response practically.

**Table 3.2** Modal damping ratios for all 74 translational vibration modes of the planar low-order FE model representing the case-study building structure in Fig. 3.2.

Mode number, $j$	1 to 3	4 to 6	7 to 10	11 to 20	21 to 40	41 to 60	61 to 74
Modal damping, $\xi_j$	2%	4%	6%	9%	12%	15%	18%

### 3.3.3 Wind force excitation model

The input wind action to the 74-storey planar frame model derived in the previous section is herein represented by the stochastic crosswind force model developed in [Liang et al. \(2002\)](#) for tall buildings with rectangular footprint. The adopted model is based on experimental data from a comprehensive wind tunnel testing campaign and accounts for both the turbulence and the VS components of the crosswind force, the latter being critical for occupant comfort in the case-study building ([Petrini and Ciampoli 2012](#)). It is defined by a zero-mean Gaussian ergodic spatially correlated random field expressed in the domain of circular frequencies  $\omega$  analytically through a PSD matrix. Upon spatial discretisation of the wind force random field at each floor slab of the case-study 74-storey building, a PSD  $\mathbf{S}_{FF}^{74} \in \mathbb{R}^{74 \times 74}$  wind force matrix is specified. For the case-study building with total height 305.9m and square footprint the diagonal elements of the PSD wind force matrix, are given as [Liang et al. \(2002\)](#)

$$\mathbf{S}_{FF}^{74}[k, k] = \frac{\sigma_k^2}{\omega} \left[ \frac{0.1032(\omega/\omega_k)^2}{\left(1 - (\omega/\omega_k)^2\right)^2 + 0.031(\omega/\omega_k)^2} + \frac{0.1278(\omega/\omega_k)^3}{\left(1 - (\omega/\omega_k)^2\right)^2 + 2(\omega/\omega_k)^2} \right], \quad k = 1, 2, \dots, 74 \quad (3.7)$$

which specify the PSD of the wind force acting at the  $k$ -th floor slab located at height  $z_k$  from the ground. In the previous expression,  $\sigma_k$  is the RMS of the crosswind force at the  $k$ -th floor slab and  $\omega_k$  is the frequency of VS at  $z_k$  height. The RMS of the crosswind force is herein computed as

$$\sigma_k = \frac{1}{2} \rho V_m^2(z_k) \bar{C}_L B \Delta z_k, \quad (3.8)$$

where  $\rho$  is the air mass density taken equal to 1.25kg/m<sup>3</sup>;  $\bar{C}_L$  is the mean RMS lift coefficient which is equal to 0.404 for square footprint buildings according to [Liang et al. \(2002\)](#);  $B=50$ m is the width of the building in the crosswind direction;  $\Delta z_k$  is the tributary height of the  $k$ -th floor taken as half the storey height above floor  $k$  plus half the storey height below floor  $k$ ; and  $V_m(z_k)$  is the mean wind velocity at  $z_k$  height. The latter can be determined through the power law expression ([Simiu and Scanlan 1996](#))

$$V_m(z) = V_{ref} \left( \frac{z}{H_{ref}} \right)^a, \quad (3.9)$$

where  $V_{ref}$  is a reference gradient wind velocity controlling the intensity of the wind action at

$H_{ref}$  above the ground, and  $\alpha$  is a dimensionless parameter dependent on the site terrain roughness. In the numerical part of this chapter, the  $\alpha$  parameter is taken equal to 0.35 which is consistent with large cities terrain type (Simiu and Scanlan 1996), while  $H_{ref}$  is pinned to 810m assumed as a characteristic height of the atmospheric boundary layer in congested urban environments. Notably, selection of the reference height,  $H_{ref}$ , in the power law expression given by Eq. (3.9) for estimating the mean wind profile,  $V_m(z)$ , within the atmospheric boundary is arbitrary so long as the reference wind speed,  $V_{ref}$ , is calibrated/adjusted to that height accordingly (Simiu and Scanlan 1996). Further, the VS frequency in Eq. (3.7) is determined by

$$\omega_k = \frac{2\pi S_t V_m(z_k)}{B}, \quad (3.10)$$

in which  $S_t$  is the Strouhal number taken equal to 0.084 as experimentally determined in Liang et al. (2002) for square footprint tall buildings.

For illustration, the PSDs of wind force acting at four different floor slab heights are plotted in Fig. 3.3 for  $V_{ref}=30\text{m/s}$  at  $H_{ref}=810\text{m}$ , which corresponds to a mean wind velocity of 21.3m/s at the building top (i.e., 305m above the ground). This particular speed corresponds to relatively weak, frequently occurring wind events. For stronger winds, the logarithmic law is currently considered by meteorologists as a superior representation of wind profile in the lower atmosphere (Owen 1974). It is seen that the dominant VS frequency increases with floor height as can be inferred by Eqs. (3.9) and (3.10). The same happens for the wind force amplitude except from the first and last floors whose tributary heights are different from the rest of the building floors, i.e., 8.5m and 2.45m, respectively as opposed to 4m for typical floor.

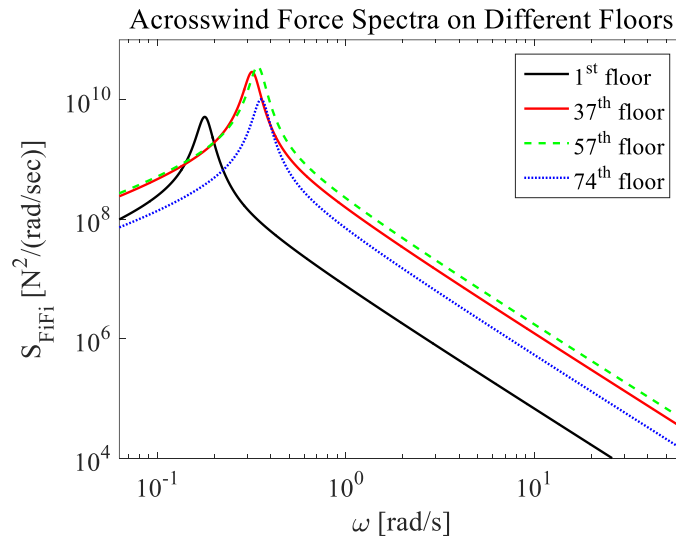


**Fig. 3.3.** Power spectral density functions of cross-wind forces acting at different floor levels of the case-study structure.

Lastly, the off-diagonal terms of the  $\mathbf{S}_{FF}^{74}$  PSD matrix modelling the spatial correlation of wind forces acting at floor slabs  $k$  and  $l$  are given as (Liang et al. 2002)

$$\mathbf{S}_{FF}^{74}[k,l] = \exp\left[-\left(\frac{z_k - z_l}{5.56B}\right)^2\right] \sqrt{S_k(\omega)S_l(\omega)}, \quad (3.11)$$

for the case-study building. In Section B.5 of the Appendix, the accuracy of the considered crosswind load modelling is verified against wind tunnel force data by examining the response of the benchmark building in Figure 3.3 (see Fig.B.7).

### 3.4 TMDI-equipped tall building modelling and structural analysis for crosswind excitation

Following Giaralis and Petrini (2017), a TMDI is herein considered to mitigate wind-induced accelerations in the crosswind direction of the benchmark structure. The modelling of the TMDI and its incorporation to the adopted structure is graphically shown in Fig. 3.4 depicting the 74-DOF surrogate model derived in section 3.3.2 as a planar 74-storey frame-like building with lumped floor masses  $m_k = \mathbf{M}_s(k,k)$ ;  $k=1,2,\dots,74$ . The TMDI consists of a conventional TMD comprising a secondary  $m_{TMDI}$  mass attached to the top floor via a stiffener, modelled as a linear spring with  $k_{TMDI}$  stiffness, in parallel with a linear viscous damper, modelled as a dashpot with damping coefficient  $c_{TMDI}$ , and an inerter device, highlighted in red in Fig. 3.4, connecting the secondary mass to  $p$  floors below the top floor. The inerter device is modelled through an ideal massless/weightless mechanical element resisting the relative acceleration developing at its two ends/terminals through the inertance coefficient  $b$  (Smith 2002). In this regard, following Eq. (2.1), the inerter element force reads as  $F_b = b(\ddot{x}_{TMDI} - \ddot{x}_{74-p})$ , where  $x_{TMDI}$  is the lateral displacement of the secondary mass,  $x_{74-p}$  is the lateral displacement of the floor which the inerter connects the secondary mass to and a dot over a symbol signifies differentiation with respect to time. Therefore, in the TMDI configuration the inerter exerts an additional, compared to the conventional TMD, control force,  $F_b$ , to the host structure whose amplitude depends on the relative acceleration of the inerter terminals and on the inertance  $b$ . In this regard, the potentially improved vibration suppression capability of the TMDI compared to the TMD depends on the inerter connectivity “- $p$ ”, as well as on the inertance  $b$ .

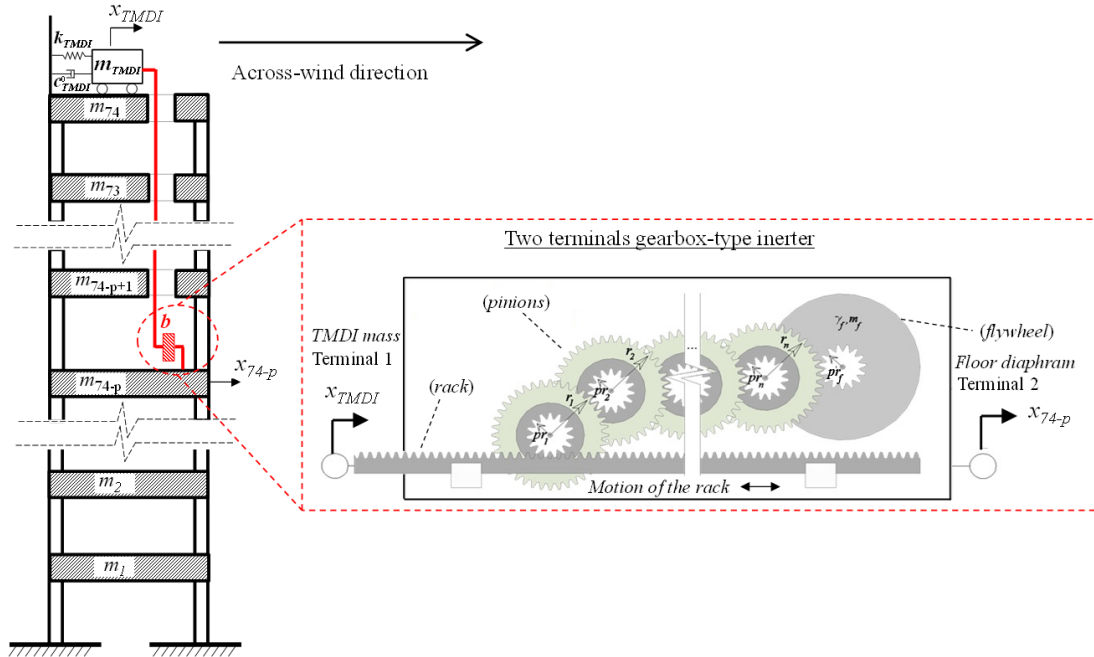


**Fig. 3.4.** TMDI equipped lumped-mass surrogate planar frame model of the wind-excited case-study building with “p” connectivity and typical rack-and-pinion flywheel inerter device with n gears.

With regards to TMDI connectivity, the cases  $p=1, 2,$  and  $3$  are examined in Section 3.5 taken to be mostly appealing to potential practical implementations involving a pendulum-like TMDI accommodated within a central atrium spanning up to three highest building floors (see e.g., Taipei 101 building). Further, turning the attention to the inertance property,  $b$ , it is important to note it is readily scalable and independent of the physical mass/weight of the inerter device in a similar manner to the scalability of the damping coefficient  $c_{TMDI}$  of the TMDI viscous damper. Indeed, supplemental damping devices for seismic protection of building structures incorporating inerters with several hundred thousand tonnes of inertance have been prototyped and experimentally verified in recent years (Watanabe et al. 2012, Nakamura et al. 2014). To shed further light on this issue, consider a commonly used inerter device embodiment employing a rack-and-pinion mechanism to transform the translational motion into rotational motion of a flywheel (i.e., a solid spinning disk) through a gearbox shown in Fig. 3.4. It can be readily shown the inertance of this device is given by Eq. (2.2). Clearly, the inertance can be scaled by orders of magnitude through changing the gearing ratios and/or the number of the gears with immaterial change to the mass/weight of the device. Along these lines, Brzeski et al. (2017) demonstrated experimentally the feasibility of inerter devices with continuously varying transmission gearbox, rather than stepped gearing changes, leading to inerters that may achieve any desired inertance value, within the gearbox effective range of transmission.

Mathematically, the mass,  $\mathbf{M}$ , the damping,  $\mathbf{C}$ , and the stiffness,  $\mathbf{K}$ , matrices of a surrogate  $n$ -storey building model equipped with a top-storey TMDI configured in “ $-p$  connectivity” are concisely written as (Giaralis and Petrini 2017)

$$\begin{aligned}
\mathbf{M} &= \mathbf{M}_s^+ + (m_{TMDI} + b)\mathbf{1}_{n+1}\mathbf{1}_{n+1}^T + b\mathbf{1}_{n-p}\mathbf{1}_{n-p}^T - b(\mathbf{1}_{n+1}\mathbf{1}_{n-p}^T + \mathbf{1}_{n-p}\mathbf{1}_{n+1}^T) \\
\mathbf{C} &= \mathbf{C}_s^+ + c_{TMDI}(\mathbf{1}_{n+1}\mathbf{1}_{n+1}^T + \mathbf{1}_n\mathbf{1}_n^T - \mathbf{1}_{n+1}\mathbf{1}_n^T - \mathbf{1}_n\mathbf{1}_{n+1}^T) \\
\mathbf{K} &= \mathbf{K}_s^+ + k_{TMDI}(\mathbf{1}_{n+1}\mathbf{1}_{n+1}^T + \mathbf{1}_n\mathbf{1}_n^T - \mathbf{1}_{n+1}\mathbf{1}_n^T - \mathbf{1}_n\mathbf{1}_{n+1}^T)
\end{aligned} \tag{3.12}$$

where  $n = 74$  for the herein considered benchmark structure. Further, in the above expressions,  $\mathbf{M}_s^+ \in \mathbb{R}^{75 \times 75}$ ,  $\mathbf{C}_s^+ \in \mathbb{R}^{75 \times 75}$ , and  $\mathbf{K}_s^+ \in \mathbb{R}^{75 \times 75}$  are the mass,  $\mathbf{M}_s \in \mathbb{R}^{74 \times 74}$ , the damping,  $\mathbf{C}_s \in \mathbb{R}^{74 \times 74}$ , and the stiffness,  $\mathbf{K}_s \in \mathbb{R}^{74 \times 74}$ , matrices of the surrogate planar frame model defined in section 3.3.2, respectively, augmented by one last (bottom) row with zero entries and by one last (rightmost) column with zero entries. Further, the vector  $\mathbf{1}_u \in \mathbb{R}^{75 \times 1}$  has zero elements except from the  $u$ -th entry which is equal to one, and the superscript “ $T$ ” denotes matrix transposition. Note that the inclusion of the inerter influences only the mass matrix  $\mathbf{M}$  of the controlled surrogate building model in Eq. (3.12), that is, matrices  $\mathbf{C}$  and  $\mathbf{K}$  are the same for the TMD and for the TMDI. More importantly, note that for  $b=0$  (no inerter), Eq. (3.12) represents the surrogate building model with a conventional TMD attached to its top, 74-th, floor, which is the most widely considered TMD connectivity for vibration suppression in wind-excited tall buildings (see e.g. [Kareem et al. 1999](#), [Tse et al. 2012](#), [Ierimonti et al. 2018](#)). Therefore, in the following numerical work, the TMD is treated as a special case of the TMDI by setting  $b=0$ . Finally, the frequency-domain crosswind response analysis of the TMDI-equipped low-order benchmark building model is performed following the steps detailed in Appendix A.

### 3.5 Optimal TMDI design for occupant comfort

To explore the full potential of TMDI for motion control in wind-excited tall buildings susceptible to VS effects, the OP in Section 3.2.1 is herein solved numerically using the solution strategy in Section 3.2.2 to find the optimal TMDI DVs,  $v_{TMDI}$  and  $\zeta_{TMDI}$ , for different sets of secondary parameters,  $\mu$ ,  $\beta$ , and  $p$ , to maximise occupant comfort in the benchmark building structure in Section 3.3.1. Since the largest wind-induced peak floor acceleration is always reached at the roof level of the case-study building, the proposed optimal TMDI design problem essentially aims to minimise the peak top-floor acceleration  $\text{peak}\{\ddot{x}_{74}\}$  in Eq. (A.5) (by setting  $k=74$ ), attained within one hour of excitation under the wind force PSD matrix  $\mathbf{S}_{FF}$  in Eq. (3.11) specified for a given design reference wind speed  $V_{ref}$  in Eq. (3.9). Under the common assumption of gaussian (stochastic) input/output processes being stationary, ergodic, and time-limited, the peak instantaneous floor accelerations can be estimated from the corresponding RMS values through the widely used peak factor due to [Davenport \(1964\)](#) given in Eq. (A.7) of Appendix A. For the case-study building, this peak factor is equal to 3.77, which is evaluated by setting the effective structural response frequency  $\eta$  in Eq. (A.7) to the building’s uncontrolled fundamental frequency, i.e.,  $\eta=0.185\text{Hz}$ , and by taking the duration of

exposure  $T_{\text{wind}}$  to one hour, i.e.,  $T_{\text{wind}} = 3600\text{s}$ .

Purposely, application of the optimal design formulation in Eq. (3.3) to the herein considered case-study building allows considering explicitly any desired combination of TMDI inertial properties, that is, attached mass and inertance, through the secondary design parameters  $\mu$  and  $\beta$ , respectively, and inerter floor connectivity through the connectivity number  $p$ . In this manner, the special case of the TMD can be examined by setting  $\beta = 0$ . Further, the bounds of  $\mu$  value are set to  $[0.1\%, 1\%]$  based on real-life TMD installations tuned to the first/fundamental mode shape of high-rise buildings, whereas the  $\beta$  value is confined within the range  $[0.0, 0.8]$  to avoid unrealistically high inertance for the considered structure throughout the rest of this Chapter. The search range for the primary DVs of TMDI,  $v_{TMDI}$  and  $\zeta_{TMDI}$ , used in solving Eq. (3.3) is taken as  $\mathbf{x}_1^{\min} = [0.0, 0.0]^T$  and  $\mathbf{x}_1^{\max} = [2.0, 2.0]^T$ . This range was proved sufficient for the adopted structure, TMDI inertial properties spanning  $0.1\% \leq \mu \leq 1\%$  and  $0 \leq \beta \leq 0.8$ , practically relevant TMDI connectivities  $p = 1, 2, 3$ , and for  $V_{ref}$  up to 50 m/s.

First, for numerical illustration of the tuning strategy in section 3.2.2, Fig. 3.5 plots the peak top-floor acceleration/OF surfaces in three successive iterations on the primary DV ( $v_{TMDI} - \zeta_{TMDI}$ ) plane, obtained by applying the preceding iterative pattern search algorithm to the benchmark building in Fig. 3.2 subjected to the crosswind force excitation in Fig. 3.3 and equipped with a top-floor TMDI with  $\mu=0.5\%$ ,  $\beta=20\%$ , and  $p=3$ . Numerical results pertaining to optimal TMDI design parameters and structural response of the TMDI-controlled structure considered previously in Giaralis and Petrini 2017 are first presented with the focus placed on exhibiting the convergence behaviour of the algorithm.

The optimal TMDI design in this example involves finding the primary DVs in  $\mathbf{x}_1=[v_{TMDI}, \zeta_{TMDI}]^T$  for given secondary design parameters,  $\mathbf{x}_2=[\mu=0.5\%, \beta=20\%, p=3]$ , and reference wind velocity,  $V_{ref}=30\text{m/s}$ , to minimise the peak crosswind acceleration on the 74<sup>th</sup> floor/top floor of the benchmark structure. The initial lower and upper bounds of the search range for the primary DVs is set to  $\mathbf{x}_1^{\min} = [0.0, 0.0]^T$  and  $\mathbf{x}_1^{\max} = [2.0, 2.0]^T$ , respectively. The global minimum point ( $v_{opt}(i), \zeta_{opt}(i), P_{\min}(i)$ ) for iteration  $i$  where  $P_{\min}(i)=\min\{\text{peak}\{\ddot{x}_{74}\}\}(i)$  is reported on Fig. 3.5. The convergence tolerance is set to 1.0%. In this particular example, convergence is reached after three iterations in which the initial search range narrows down to  $\mathbf{x}_1^{\min}=[0.9, 0.1]^T$  and  $\mathbf{x}_1^{\max}=[1.1, 0.3]^T$  in the second iteration, and ultimately to  $\mathbf{x}_1^{\min}=[0.97, 0.13]^T$  and  $\mathbf{x}_1^{\max}=[0.99, 0.15]^T$  in the final iteration, with the same discretisation density of the adaptive search domain and with a logarithmic increase of precision/resolution by which optimal parameters are determined.

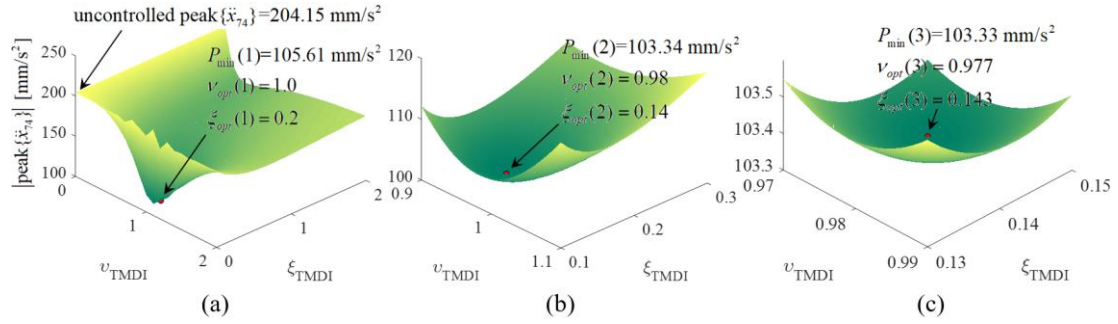


**Fig. 3.5.** Iterative optimal TMDI design with  $\mu=0.5\%$ ,  $\beta=20\%$ , and  $p=3$  for a benchmark with  $V_{ref}=30$  m/s (a) 1<sup>st</sup> iteration; (b) 2<sup>nd</sup> iteration; and (c) 3<sup>rd</sup> iteration.

### 3.5.1 Convexity and optimality of the TMDI design problem

In this sub-section, the performance surfaces of peak top-floor acceleration of TMDI-controlled benchmark structure on the primary DV ( $v_{TMDI}$ - $\zeta_{TMDI}$ ) plane are demonstrated in the vicinity of the optimal solution point for different combinations of TMDI inertial properties and inerter connectivities. From a computational viewpoint, strong convex behaviour of the objective function  $OF = \text{peak}\{\ddot{x}_{74}\}$  on the  $v_{TMDI}$ - $\zeta_{TMDI}$  plane is noted with a single prominent global optimal design point being observed for all TMDI cases considered. For illustration, Figs. 3.6(a)-3.6(c) plot the  $\text{peak}\{\ddot{x}_{74}\}$  as a function of the primary DVs for fixed  $\mu=0.5\%$ ,  $\beta=20\%$ , and  $V_{ref}=30\text{m/s}$  as considered in Fig. 3.5, and for three different TMDI connectivity numbers, i.e.,  $p=1, 2, 3$  demonstrating that convexity of the OP in Eq. (3.3) is maintained for all TMDI topologies herein examined. Moreover, Figs. 3.6(c) and 3.6(d) plot the  $\text{peak}\{\ddot{x}_{74}\}$  response surface on the primary DV plane for fixed  $\mu=0.5\%$ , TMDI connectivity “-3” or  $p=3$ , and  $V_{ref}=30\text{m/s}$  and for two different inertance ratio values illustrating that the problem in Eq. (3.3) is convex irrespective of the assumed inertance value.



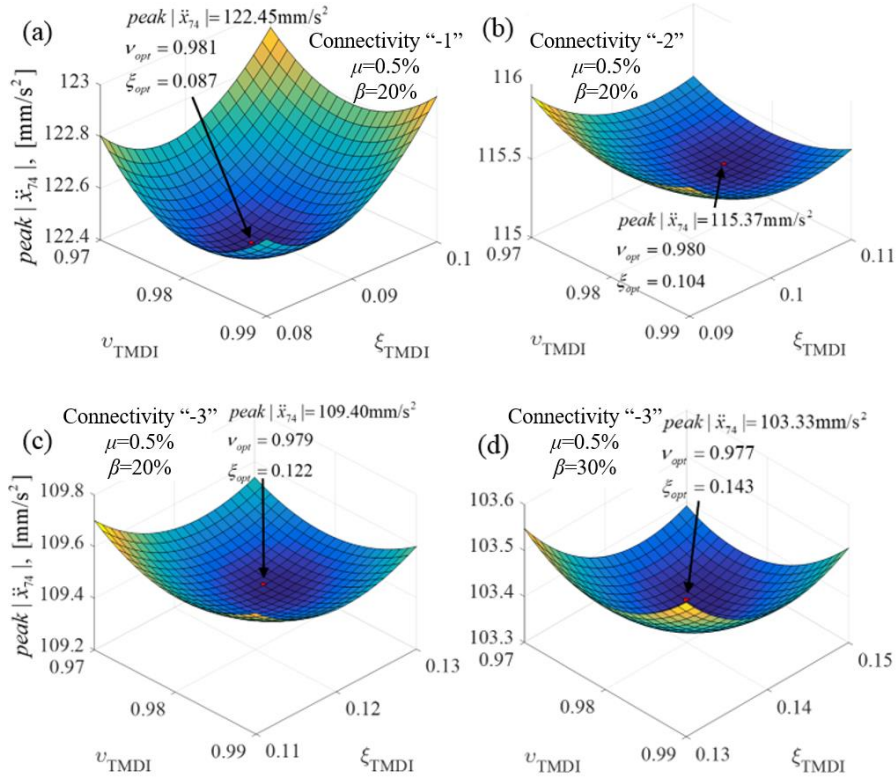


**Fig. 3.6.** Objective function and design point of the optimisation problem in Eq.(3.3) for  $\mu=0.5\%$ ,  $V_{ref}=30m/s$  and for different TMDI connectivities and inrtance ratios.

To shed light on the nature of the motion control achieved through solving Eq. (3.3), Fig. 3.7 plots FRFs of top floor acceleration of the adopted benchmark structure for  $V_{ref}=30m/s$  equipped with optimally designed TMDIs for various connectivity number,  $p$ , and inrtance ratios,  $\beta$ , including the limiting case of  $\beta=0$  (TMD). All inertial dampers considered have the same attached mass  $\mu=0.5\%$ , while the FRF of the uncontrolled model is also superposed. The left column panels of Fig. 3.7 focuses on the FRFs behaviour within a narrow frequency range around the first/fundamental natural frequency of the uncontrolled structure and the two lowest natural frequencies of the TMD(I) controlled structures. It is seen in Fig. 3.7(a), considering TMDIs with fixed connectivity ( $p=3$  or “-3”) and varying inrtance, that the solution of the proposed optimal TMDI design formulation yields a “Den Hartog” style of optimality at least for  $\beta \leq 20\%$  in the sense that the two resonant peaks of the controlled structure attain almost equal FRF values (Den Hartog 1956). This type of optimality is mostly efficient for suppressing narrow-band excitations characterised by a dominant frequency (see also Marian and Giaralis 2017) and, therefore, relevant to the problem at hand. Nevertheless, as the inrtance increases above 20% the right-most peak value in the FRFs becomes lower than the left-most peak value. Further, a shift of the first resonant frequency to lower frequencies is observed as inrtance increases for fixed  $\mu$  and inrteter connectivity in the FRFs of TMDI-controlled structure, while the second resonant frequency is attained at higher frequencies. Overall, the FRF value at the fundamental natural frequency of the uncontrolled structure reduces considerably with

increasing inertance, however, the controlled structure attains larger FRF values compared to the uncontrolled structure at a relatively narrow band of frequencies lower than the fundamental natural frequency of the uncontrolled structure. Interestingly, all the previous trends in the FRFs of optimal TMDI-equipped case-study structure with increasing inertance are true for the case of TMDI-equipped structure with fixed attached mass  $\mu=0.5\%$  and inertance  $\beta=30\%$  as the inerter spans more floors, that is, as TMDI topologies with increasing  $p$  are considered shown in Fig. 3.7(c). The latter observation suggests that increasing the number of floors spanned by the inerter has a similar effect to the FRFs of optimal TMDI-equipped structures as the increase of the inertance for fixed TMDI connectivity. More importantly, the FRFs in the right column panels of Fig. 3.7, plotted for a wider frequency range to include the first three natural frequencies of the uncontrolled structure, demonstrate that TMDIs optimally designed through the problem formulation in Eq. (3.3) suppress higher modes of vibration. Notably, this is not the case for the TMD. Specifically, appreciable reductions to peak FRF values corresponding to higher vibration modes for optimal TMDI-equipped structures are achieved as the inertance increases for fixed TMDI connectivity, Fig. 3.7(b), and as the inerter device spans more floors for fixed inertance, Figs. 3.7(d). To this end, it is established that increasing inertance for fixed TMDI connectivity and secondary mass affect qualitatively the FRF of peak  $\{\ddot{x}_{74}\}$  in the same manner as by increasing the number of floors spanned by the inerter in TMDIs with fixed inertance and secondary mass.

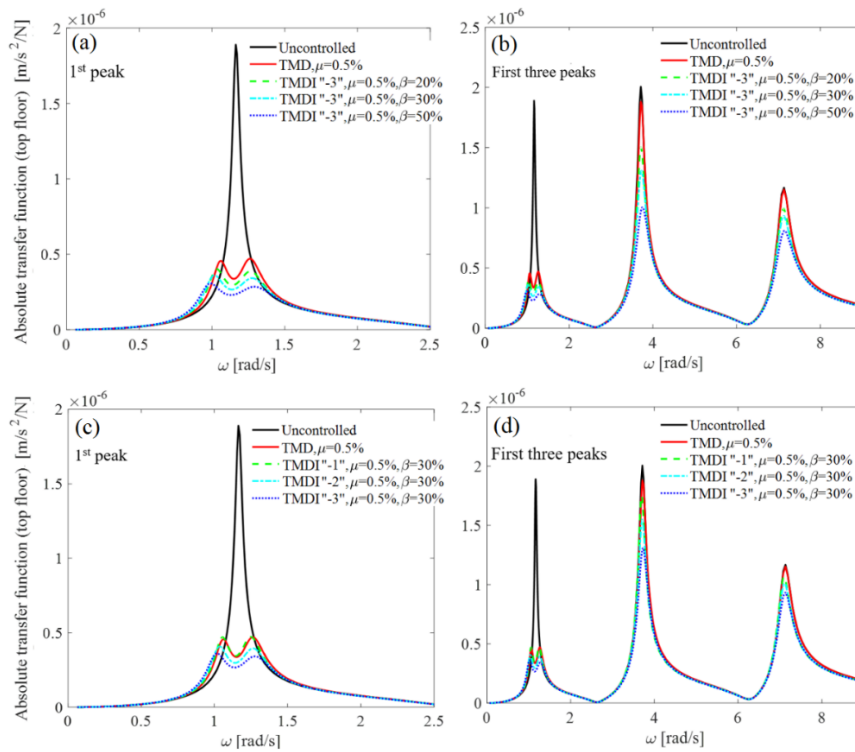


**Fig. 3.7.** Frequency response functions of top floor acceleration of the case-study structure for  $V_{\text{ref}}=30\text{m/s}$  with no motion control (uncontrolled), controlled with optimal TMD ( $\mu=0.5\%$ ), and controlled with optimal TMDIs for fixed  $\mu=0.5\%$  and different TMDI topologies and inertance ratios.

### 3.5.2 Sensitivity of primary optimal design parameters to secondary parameters and to wind velocity

Turning the attention to the TMDI primary design variables in  $\mathbf{x}_1$ , Fig. 3.8 plots iso-value curves of the optimal parameters  $v_{opt}$  and  $\zeta_{opt}$ , related to the TMDI stiffness and damping properties respectively, on the plane of the secondary design parameters in  $\mathbf{x}_2$  (i.e., the  $\mu$ - $\beta$  TMDI *inertial design plane*) obtained by solving Eq.(3.3) for  $V_{ref}=30\text{m/s}$  and TMDI topologies “-1” to “-3”. Note that the y-axis of the graphs in Fig. 3.8 correspond to TMD optimal designs ( $\beta=0$ ), while the x-axis corresponds to lightweight TMDIs with relatively low physical mass. It is seen in Fig. 3.8 (a) that  $v_{opt}$  decreases with increasing inertance ratio for fixed secondary mass as well as with increasing mass ratio for fixed inertance for all considered TMDI topologies. Further, increasing the inerter connectivity results in faster changes of  $v_{opt}$  with  $\beta$ , that is, iso-value  $v_{opt}$  curves of the “-3” TMDI connectivity are steeper than of the “-2”. Still, deviations of TMDI  $v_{opt}$  values from those obtained for TMD cases are relatively small. Nevertheless, the variation of  $\zeta_{opt}$  on the TMDI inertial design plane in Fig. 3.8 (b) is more significant. In particular,  $\zeta_{opt}$  increases monotonically with increasing  $\mu$  for fixed  $\beta$ . Further, it increases monotonically with  $\beta$  for fixed  $\mu$  for all the considered TMDI topologies only for  $\beta > 15\%$ , while  $\zeta_{opt}$  is more sensitive to differences in TMDI connectivity compared to  $v_{opt}$ .

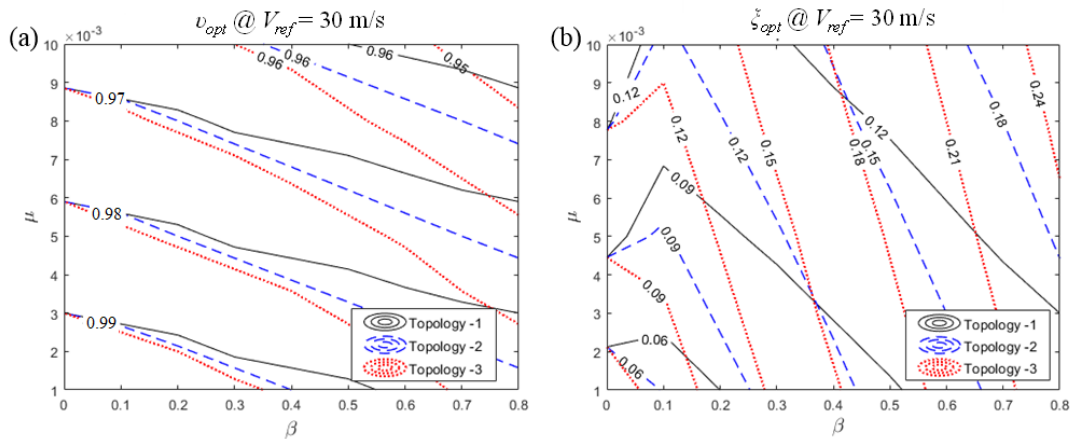


**Fig. 3.8.** Optimal values of the primary design variables in  $\mathbf{x}_1$  on the secondary design parameters plane.

Finally, the sensitivity of the optimal design values in  $\mathbf{x}_1$  is further quantified against changes to the reference wind velocity,  $V_{ref}$ , in Fig. 3.9, for the three considered TMDI topologies, one low inertance ratio value,  $\beta=0.1$  and one very high inertance value,  $\beta=0.8$ , for fixed mass ratio  $\mu=0.5\%$ . Such changes to  $V_{ref}$  may be due to new high-rise buildings being erected nearby the benchmark structure bringing about changes to wind field exposure and/or due to climate change effects predicted to increase  $V_{ref}$  at a given location in the foreseen future as discussed in [Steenbergen et al. \(2012\)](#). It is important to note that changes to  $V_{ref}$  not only change the intensity of wind exciting forces, but also the dominant excitation VS frequency (see Eqs. (3.9) and (3.10)). It is seen that optimal  $\mathbf{x}_1$  values are at large insensitive and, therefore,

robust to  $V_{ref}$  variations. In particular,  $\zeta_{opt}$  remains practically constant with  $V_{ref}$ , while  $v_{opt}$  decreases only slightly with  $V_{ref}$  and only for the high  $\beta$  value considered.

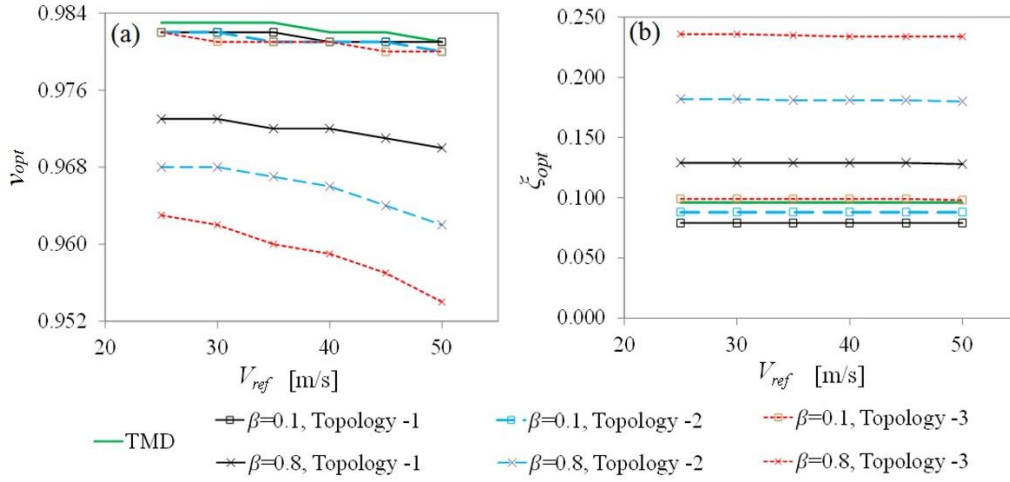


**Fig. 3.9.** Sensitivity of the optimal values of the DVs to the variation of the wind speed. Case  $\mu=0.5\%$ .

### 3.6 Performance-based assessment and design in optimally tuned TMDI-equipped structures

#### 3.6.1 Peak top floor acceleration, secondary mass stroke, and inertance force

The efficiency of TMDIs designed/tuned through the OP in Eq. (3.3) to contain VS induced vibrations causing occupant discomfort in tall, slender structures can be quantified in a practically useful manner by evaluating the OF in Eq. (3.3), i.e., peak top floor acceleration of the case-study structure, for optimal parameters in  $\mathbf{x}_1$  determined for various TMDI topologies and inertial properties in  $\mathbf{x}_2$ . To this aim, Fig. 3.10 plots three different families of iso-value curves of peak  $\{\ddot{x}_{74}\}$  achieved by optimally tuned TMDIs in three different topologies on the  $\beta$ - $\mu$  plane. These curves are obtained by using optimal values for the TMDI primary design parameters,  $v_{opt}$  and  $\zeta_{opt}$ , reported in Fig. 3.8 for  $V_{ref}=30\text{m/s}$ . It is seen that improved structural performance in terms of peak floor acceleration can be achieved by increasing the secondary TMDI mass for fixed inertance across the board. Further, improved structural performance is monotonically achieved with increasing inertance for the “-3” TMDI connectivity for fixed mass ratio as long as  $\mu < 0.6\%$ . This is readily explained by examining the FRFs plotted in Fig. 3.7(b) whose peak values are reduced as inertance increases at all structural natural frequencies and not just the first/fundamental one and by noting that response acceleration are sensitive to high frequency dynamics. Interestingly, TMDs with  $\mu > 0.3\%$  perform better than TMDIs in “-1” and “-2” topologies with relatively low inertance ratios  $\beta < 15\%$ . However, as the inertance ratio increases above 15%, all TMDIs outperform TMDs for any fixed attached mass ratio providing improved performance with increasing inertance verifying trends reported in [Giaralis and Petrini \(2007\)](#) for the case of non-optimal TMDIs. Importantly, it is deduced by comparing the slopes of the different families of the iso-value curves that the more floors the inerter spans, the faster is the rate of improved performance with

increasing inertance. Consequently, better performance is achieved for sufficiently large fixed inertance ratio as the inerter spans more floors (see also FRFs in Fig. 3.7(d)).

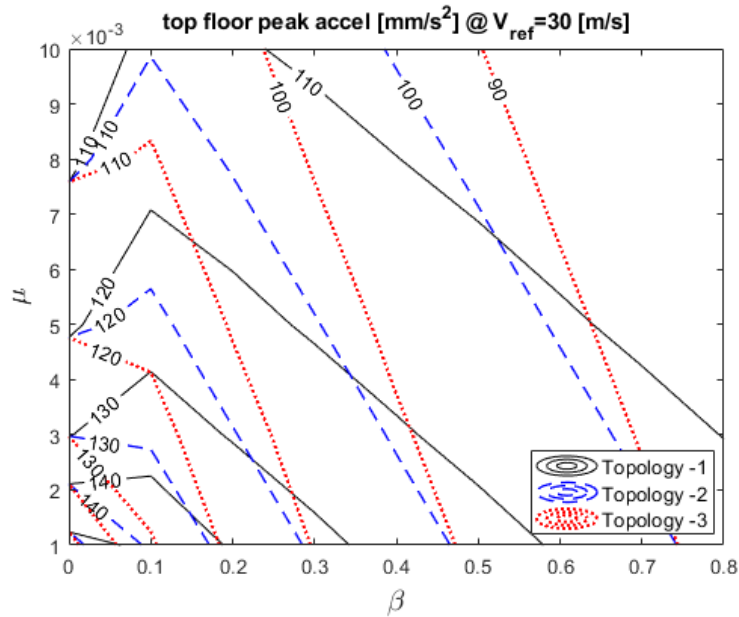


**Fig. 3.10.** Peak top floor acceleration in  $\text{mm/s}^2$  achieved with optimally designed TMDIs in different topologies and inertial properties: secondary mass ratio  $\mu$  and inertance ratio  $\beta$ .

Apart from the improvement to host structural performance, an important response quantity of interest to the practical design of mass/inertial dampers is the so-called peak stroke of the secondary mass, that is the peak relative displacement of the TMD(I) mass with respect to the floor that the mass is attached to. This is because increased TMD(I) stroke demands require larger clearance in housing safely a TMDI within the host structure such that no local pounding/collision occurs. Further, the cost of energy dissipation devices/dampers increases with the stroke. For the case-study structure, the peak stroke is computed by setting  $k=74$  and  $l=75$  (i.e., DOF corresponding to the  $x_{TMDI}$  displacement in Fig. 3.4) in peak  $\{x_{kl}\}$  expression in Eq.(A.6). Peak TMDI stroke values obtained for optimal TMDIs in three different topologies for the case-study structure for  $V_{ref}=30\text{m/s}$  are plotted in Fig. 3.11 as functions of TMDI inertial properties within the ranges  $0.1\% \leq \mu \leq 0.55\%$  and  $0 \leq \beta \leq 10\%$ . A considerable stroke demand reduction is observed with increasing inertance for any fixed mass ration value as has been also the case for non-optimal TMDIs in Giaralis and Petrini (2017). For example, as illustrated in Fig. 3.11, a ten-fold reduction of the peak stroke (from 600mm to 60mm) is achieved by increasing the inertance from 0.5% to 9.5% for fixed mass ratio  $\mu=0.2\%$ . Interestingly, appreciable stroke reduction is achieved with increased mass ratio for only relatively small inertance ratios as the iso-value peak stroke curves in Fig. 3.11 tend to become parallel to the y-axis with increasing  $\beta$ . Further, it is seen that stroke is insensitive to TMDI connectivity.



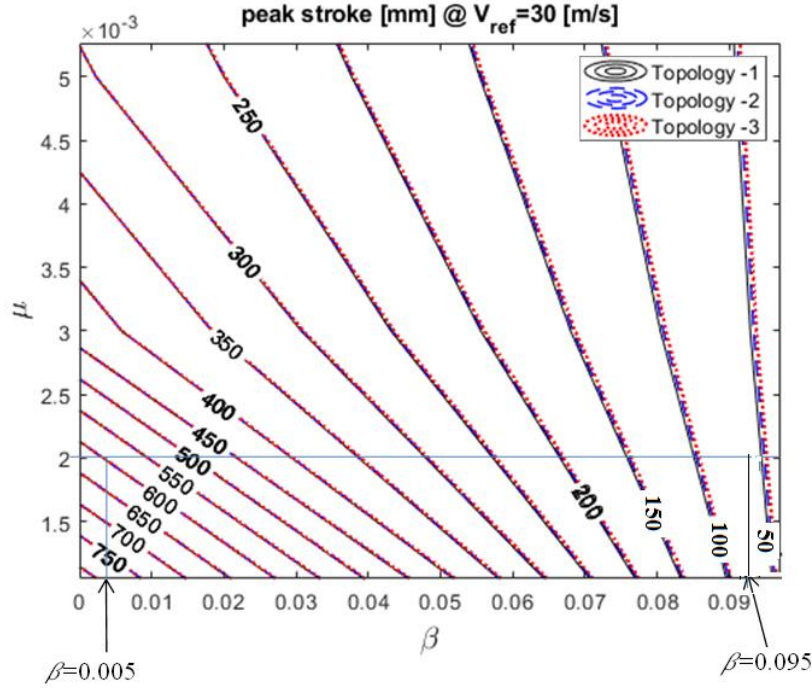


Fig. 3.11. Peak stroke of optimally designed TMDI in the secondary design parameters plane.

Having established that TMDI achieves better motion control with respect to TMD through increase of inertance and/or through considering TMDI topologies in which the inerter spans more floors, it is deemed useful to examine the peak inerter force  $F_b$  (note  $F_b = b(\ddot{x}_{TMDI} - \ddot{x}_{74-p})$ ) developing for optimal TMDIs of different topologies as  $\beta$  increases. Figure 3.12 serves this purpose by plotting iso-value curves on the  $\beta$ - $\mu$  plane of peak inerter force developing in the case-study structure for different TMDI topologies under  $V_{ref}=30\text{m/s}$ . These curves are determined by setting  $k=74-p$  and  $l=75$  in  $\text{peak}\{\ddot{x}_{kl}\}$  expression in Eq.(A.6) in conjunction with  $F_b = b(\ddot{x}_{TMDI} - \ddot{x}_{74-p})$ . Trivially, inerter force is zero for  $\beta=0$ . Then, inerter force demands increase monotonically with inertance but at a gradually reduced rate. It is further observed that for  $\beta>10\%$ , the inerter force increases for fixed inertance as the inerter spans more floors while variations to the inerter force among different TMDI topologies become more significant with decreasing attached mass. These observations verify that the key to the efficacy of the TMDI for motion control is the inerter force. Indeed, larger inerter forces correlate well with more significant peak floor acceleration reductions as can be inferred by comparing iso-value curves in Figs. 3.10 and 3.12. Still, it is seen that even for very large inertance ratios and for “-3” connectivity, the peak developing inerter force, at least for  $V_{ref}=30\text{m/s}$ , is not excessively large, as is the case for the use of TMDIs for seismic protection of buildings structures (Ruiz et al. 2018), and can be accommodated locally by the structure with some appropriate local detailing.

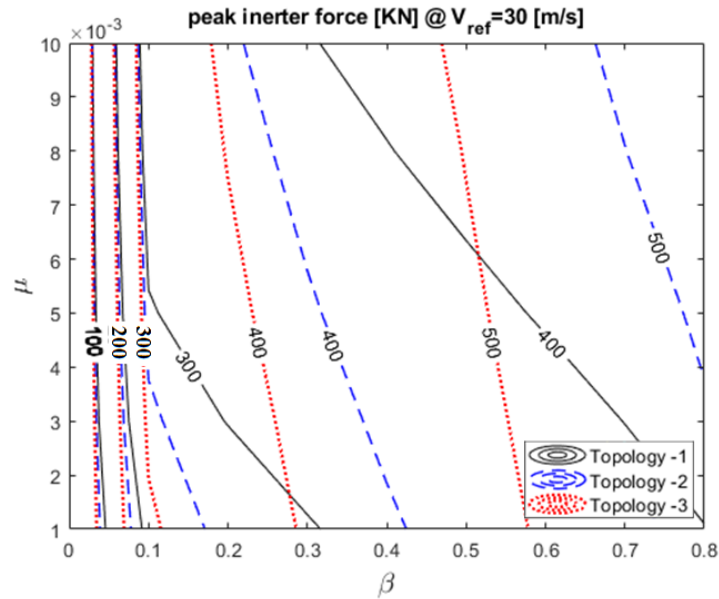
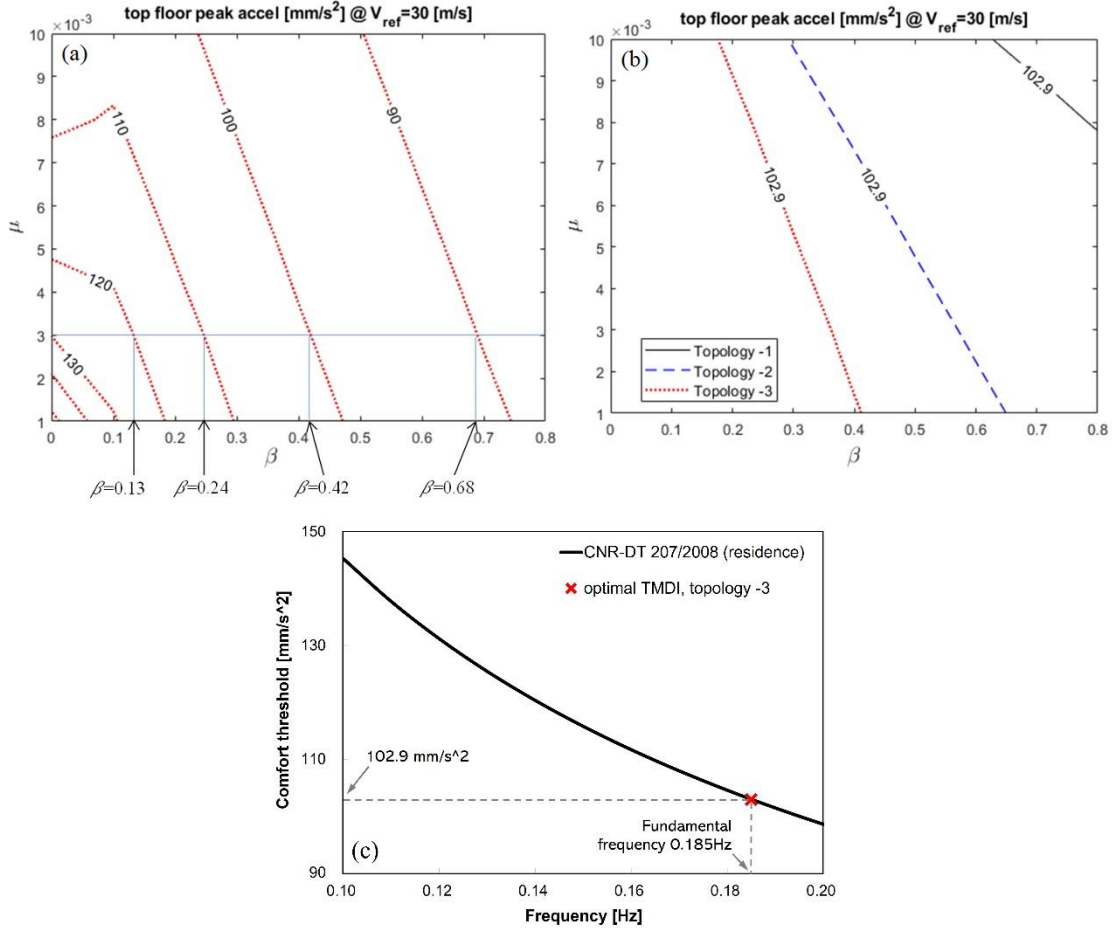


Fig. 3.12. Peak inerter force of optimally designed TMDI in the secondary design parameters plane.

### 3.6.2 Trading secondary mass to inertance

In the previous section, Fig. 3.10 was used for comparative quantitative assessment of the potential of optimal TMDIs with different inertial properties and connectivities to reduce floor accelerations in the case-study structure. Herein, the iso-value curves of Fig. 3.10 are interpreted as TMDI design charts *from a PBD perspective* to demonstrate that attached mass and, therefore weight, can be effectively traded with inertance for a desired pre-specified/target structural performance level in terms of peak floor acceleration related to occupant comfort criteria (Tamura et al. 2006, Kwok et al. 2009). To this aim, Fig. 3.13(a) plots the data of Fig. 3.10 pertaining to TMDI connectivity “-3” which was arbitrarily chosen for the sake of exemplification. Treating Fig. 3.13(a) as a design chart, it is seen that different levels of peak floor acceleration can be achieved by optimal TMDIs with different sets of inertial properties  $\mu$  and  $\beta$  for fixed inerter connectivity. Importantly, it is seen that in most cases the iso-value curves have negative slope on the  $\beta$ - $\mu$  plane. Therefore, optimised TMDIs with reduced secondary mass can achieve the same performance through increased inertance. This establishes a direct mass reduction/substitution effect endowed by the inerter to the TMDI and leading to overall more lightweight inertial dampers: *an important advantage in designing new slender minimal-weight tall buildings*. To further illustrate this point, Fig. 3.13(b) plots iso-value curves for different TMDI topologies for peak top-floor acceleration equal to the occupants comfort threshold,  $102.9\text{mm/s}^2$ , applicable to the case-study structure assuming residential occupancy according to guidelines effective in Italy (see Guidelines CNR-DT 207/2008, also Petrini and Ciampoli 2012). The serviceability comfort threshold curve from the guideline is plotted in Fig. 3.13(c) as a function of the building vibration frequency, together with the performance of the adopted case-study structure equipped with an optimal TMDI with connectivity “-3”. Evidently, it is seen in Fig. 3.13(b) that the more floors the inerter spans the more significant the weight

reduction effect becomes with increasing inertance as the iso-value curves become steeper going from “-1” to “-3” topologies, and, at the same time, inertance demands are reduced for fixed mass ratio in achieving the targeted performance.



**Fig. 3.13.** Performance-based design charts of TMDI for the case-study structure (a) Connectivity “-3”; (b) Various topologies for case-study structure occupants’ comfort threshold 102.9 $\text{mm/s}^2$ ; (c) Code-prescribed serviceability design threshold and performance of the adopted primary structure equipped with optimal TMDI with connectivity “-3”.

Further to the case of new structures, the incorporation of an inerter, alongside retuning to achieve optimal parameters  $v_{opt}$  and  $\zeta_{opt}$ , is also applicable as a *retrofitting strategy in existing TMD-equipped tall buildings* to enhance their performance against wind excitation required by change of use/occupancy (e.g., from office to residential building) or by increasing  $V_{ref}$  (e.g., due to changes to wind exposure (Simiu and Scanlan 1996) or due to climate change effects (Steenbergen et al. 2012)). Along these lines, an illustrative example is shown in Fig. 3.13(a) which assumes the scenario that the case-study building has a TMD with  $\mu=0.3\%$  already installed achieving 130 $\text{mm/s}^2$  peak top floor acceleration under  $V_{ref}=30\text{m/s}$ . By incorporating an inerter with  $\beta=13\%$ , 24%, 42%, or 68% at TMDI connectivity “-3”, performance increases through reduction of peak top floor acceleration by 7.7%, 15.4%, 23.1%, or 30.8% respectively



upon optimal retuning.

### 3.7 Performance assessment of non-optimally designed TMDI structure

#### 3.7.1 Robustness to detuning due to changes of benchmark structure properties

Numerical data reported in previous section concerns optimally designed TMDIs for a pre-specified reference wind velocity assuming perfectly known structural properties of the case-study structure. Nevertheless, as discussed in the introduction, TMD(I)s may be “detuned” either over time due to changes to the properties of the host building structure, or due to inaccurate knowledge of structural properties. In this respect, it is deemed useful to gauge the sensitivity of TMDIs (with different inertance ratios and inerter connectivities) in mitigating wind-induced floor accelerations to changes to primary structure properties in case the actual structure has different properties from those assumed in optimal TMDI tuning. To this aim, the mass and damping matrices of the case-study structure defined in section 3.3.2 are perturbed by uniformly scaling them down by 10% and 20% of their original values, respectively. Mass perturbation consideration is related to uncertainty in mass density of materials as well as its occupancy and live loads during its service life, while damping perturbation consideration is motivated by large uncertainty in estimating inherent damping of tall buildings influenced, phenomenologically, by several parameters as discussed in [Spence and Kareem \(2014\)](#) and references therein.

Figure 3.14 plots peak top-floor acceleration versus inertance ratio for the case-study structure with perturbed mass and damping properties, respectively, and equipped with TMD(I)s optimally tuned to the original structure. In all cases,  $V_{ref}=30\text{m/s}$  for the incident wind is assumed, and TMDIs with  $\mu=0.2\%$  and  $0.5\%$ , connectivities “-1” and “-3”, and inertance ratios  $\beta$  ranging from 0% (TMD) to 70% are considered. Further, to facilitate a comparison, the obtained accelerations are normalised by peak top-floor acceleration of the original structure with optimal TMD(I)s. In this setting, the closer the ordinates of the graphs in Figs. 3.14(a) and 3.14(b) to unity is, the less sensitive the TMD(I) is to mass and damping property perturbations, respectively. In all the cases considered, it is seen that the TMDI is more sensitive than the same-mass TMD for inertance ratios smaller than a relatively low critical value which depends on TMDI connectivity and attached mass ratio. These critical inertance ratios are reported in Table 3.3. It is found that the more floors spanned by the inerter and/or the smaller the mass ratio, the lower the critical inertance ratios above which the TMDI becomes less sensitive than the TMD to the structural property perturbations. Then, as the inertance increases above the critical inertance ratios of Table 3.3, the TMDI becomes more “robust” to structural uncertainties at a rate that, again, depends on TMDI connectivity and mass ratio: the more floors are spanned by the inerter and/or the smaller the mass ratio is, the faster decreases the level of sensitivity with increasing inertance. In fact, the relatively lightweight TMDIs ( $\mu=0.2\%$ ) with connectivities “-2” and “-3” appear to be less sensitive than the “heavy” TMD ( $\mu=0.5\%$ ) for inertance ratios higher than 25% and 20%, respectively, to considered

perturbations/uncertainties in the mass and damping properties. As a general comment, one concludes through inerters spanning more floors and through sufficiently large inertance the TMDI outperforms TMDs in terms of sensitivity to structural properties perturbation.

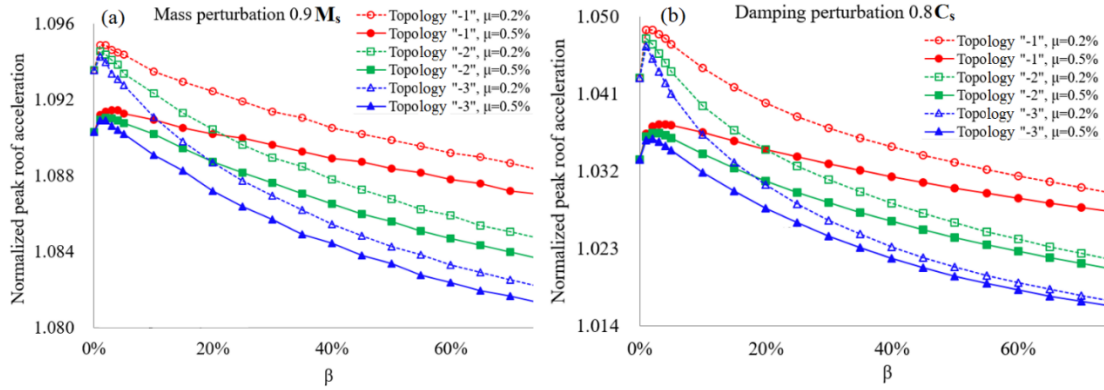


**Fig. 3.14.** Robustness of optimally tuned TMDI to mass and damping properties perturbations of the case-study primary structure for  $V_{ref}=30\text{m/s}$ .

**Table 3.3.** Critical inertance values (%) above which the TMDI is less sensitive than the TMD

	Connectivity	$\mu=0.2\%$	$\mu=0.5\%$
Mass perturbation $0.9M_s$	-1	10.0%	20.0%
	-2	4.5%	9.5%
	-3	2.7%	4.8%
Damping perturbation $0.8C_s$	-1	14.0%	27.5%
	-2	5.5%	11.0%
	-3	3.5%	6.5%

### 3.7.2 Performance for increased reference wind velocity, $V_{ref}$

In Fig. 3.9 (section 3.5.2), it was found that optimal TMDI tuning parameters are quite insensitive to increasing reference wind velocity resulting in increasing amplitude and dominant frequency of the wind forcing field. This observation motivates investigating the potential of incorporating an inerter device to retrofit an existing structure equipped with a TMD optimally tuned to a particular  $V_{ref}$ , such that improved performance is achieved for a significantly higher  $V_{ref}$ . In doing so, it is assumed that no retuning takes place to the TMD which results in a non-optimal TMDI as opposed to optimal TMDIs for retrofitting of existing TMD-equipped structures discussed in section 3.6.2 (Fig. 3.13(a)). In this regard, the herein considered retrofitting scenario for existing TMD-equipped structures involves only adding an inerter, with no replacement/adjustment of any other TMD(I) device components. This is a quite appealing retrofitting scenario from a practical viewpoint due to its simplicity as well as in view of inerter devices with varying inertance through gearing (see e.g., Brzeski et al. 2017).

Figure 3.15 plots peak top floor acceleration for the case-study building equipped with an

optimally designed TMD at  $V_{ref} = 30\text{m/s}$  with  $\mu=0.5\%$  subjected to wind force field with  $V_{ref} = 45\text{m/s}$  (i.e., 50% above the design one) and provided with an inerter with varying inertance (without any variation of other parameters) and for three TMDI connectivities. Reported top floor acceleration is normalised to the peak top floor acceleration for the TMD equipped structure at the increased  $V_{ref} = 45\text{m/s}$ . Therefore, ordinates below unity in Fig. 3.15 indicate improved TMDI performance compared to TMD for  $V_{ref} = 45\text{m/s}$ . Similar to Fig. 3.14, it is seen that there is a critical inertance value, different for each TMDI connectivity, below which the TMD performs better than the TMDI, ranging from  $\beta=3.1\%$ , for “-3” connectivity, to  $\beta=8.5\%$ , for “-1” connectivity. To this effect, incorporating an inerter with larger inertance from this critical value will result in an increasingly better performance compared to the original TMD of the existing structure. Therefore, the proposed retrofitting strategy is effective as long as sufficient inertance is considered together with an appropriate TMDI connectivity.

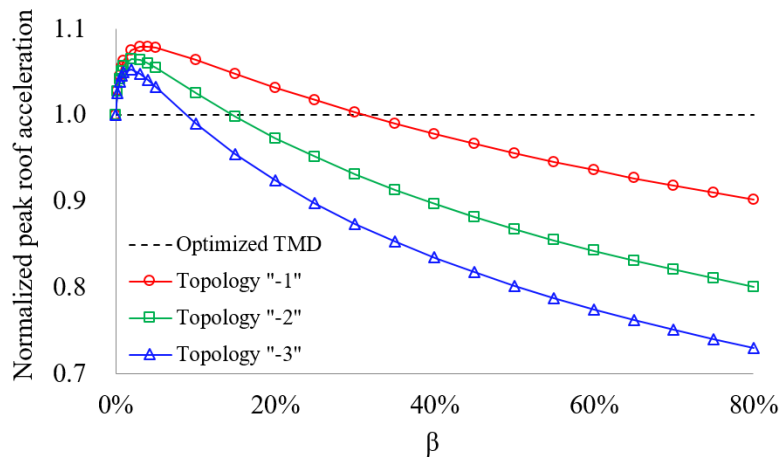


**Fig. 3.15.** Comparative performance of non-optimal TMDI under  $V_{ref}=45\text{m/s}$  for retrofitting the case-study structure equipped with a TMD with  $\mu=0.5\%$  optimally tuned for  $V_{ref}=30\text{m/s}$ .

As a closure of Section 3.7, the non-monotonic performance trends in Figs. 3.14 and 3.15 correspond to non-optimal TMD(I) designs with a non-uniform level of lack of optimality. In other words, the TMD (no inertance) and the various TMDIs (with different inertance) are not detuned to the same extent for the same perturbation of the structure or of the excitation intensity. The physical interpretation is that, under these non-uniformly non-optimal conditions, it requires large inertance for the TMDI to outperform the TMD. This is because the TMD is attached to one floor of the structure while the TMDI to two floors. So the TMDI performance is affected more than the TMD when excitation or structural property change for relatively small inertance. However, as inertance increases, the TMDI becomes eventually less sensitive to detuning than the TMD because of the increased inertial property (inertance). Trends here confirm numerical data for earthquake excitations (Giaralis and Taflanidis 2018).

### 3.8 Closure

In this chapter, a novel optimal TMDI design problem has been formulated to determine

the tunable properties (i.e., stiffness and damping properties) of TMDI such that the crosswind floor acceleration, critical to buildings' occupant comfort, is minimised for pre-specified TMDI inertial properties and connectivity. The OP was solved efficiently using a custom-made pattern search algorithm with an adaptive DV search domain that is iteratively narrowed within the bounded solution region based on the optimal solution found in the previous step. Novel numerical results on optimal TMDI design parameters and structural response of a 305.9 m tall 74-storey benchmark structure considered previously in the literature are presented to showcase the effectiveness and convergence behaviour of the proposed TMDI tuning algorithm.

Further, the efficacy of the TMDI to achieve occupant comfort performance in wind-excited slender tall buildings susceptible to VS effects has been numerically established for the 74-storey case-study building with more than 6 height-to-width ratio. Attention has been focused on exploring the influence and potential benefits of TMDIs with different inertial properties (i.e., secondary mass/weight and inertance) configured in different topologies defined by the number of floors spanned by the inerter device to connect the secondary mass to the building structure. Optimally designed TMDIs for a wide range of inertial properties and three different topologies have been obtained through numerical solution of the underlying OP for the benchmark structure subjected to experimentally calibrated spatially-correlated crosswind force field accounting for VS effects in tall buildings with rectangular footprint. Computational work has been expedited by considering a surrogate low-order planar dynamical model of the benchmark building capturing faithfully structural dynamic behaviour along the critical wind direction as well as by performing frequency domain structural analysis.

High level of convexity in solving the OP for all cases considered has been noted as well as robustness to TMDI optimal design parameters to varying reference wind velocity. Additionally, peak top floor acceleration FRFs for optimal TMDI-equipped structures demonstrated that TMDIs with fixed secondary mass/weight reduce FRF coordinates for all modes of vibration as opposed to solely mitigating the first/fundamental one in the case of the TMD. This wideband mode-dampening effect was shown to be more significant as the inertance coefficient and/or as the number of floors spanned by the inerter increases. More importantly, innovative PBD graphs on the TMDI inertial (mass-inertance) plane have been furnished demonstrating that any fixed structural performance level in terms of occupant comfort (i.e., peak top floor acceleration) may be achieved through replacing secondary mass by inertance as long as sufficiently large inertance, above a relatively low critical value, are considered. Further, the same graphs demonstrate that the more floors the inerter spans, the more significant mass reductions are achieved for same inertance. In this respect, it is concluded that more lightweight TMDIs for fixed performance are achieved through inerters spanning more floors and/or through increased inertance within an optimal TMDI design setting. Meanwhile, it was further shown that the stroke of the secondary TMDI mass is considerably reduced with increasing inertance, while peak inerter forces exerted to the host structure were shown to be of reasonable magnitude in all cases considered. To this end, the applicability of the reported PBD graphs to

design new TMDI-equipped buildings as well as to retrofit existing TMD-equipped tall buildings has been established. The latter case involves adding inerters spanning one or more floors to already installed TMDs with no changes to secondary mass to address increased requirements for occupants comfort and/or climate change effects expected to increase design reference wind velocity.

Robustness of optimally designed TMDIs to changes to the building structural properties, namely to total mass and inherent damping attributes, as well as to increased wind velocity, either due to increased wind exposure of the building and/or to climate change effects, was also explored. It was found that optimally tuned TMDIs become more robust than TMDs for same secondary mass as long as inertance above a certain limiting value is provided. This value depends on the secondary mass and on the number of floors spanned by the inerter: the lower the secondary mass and/or the more floors are spanned by the inerter, the lower the critical inertance value is.

Overall, the evidenced numerical data suggest that the proposed optimal TMDI design formulation yields practically meaningful PBD charts for occupant comfort, while sufficiently large inertance values and/or TMDI topologies in which the inerter spans more floors are beneficial for occupant comfort in VS-prone tall buildings, for reducing secondary mass stroke, and for increasing robustness to building structural properties and wind intensity. Nevertheless, these benefits come at the cost of larger inerter force exerted to the building for increased inertance and/or for TMDI topologies spanning more floors (Giaralis and Petrini 2017). In the upcoming chapter, the focus is directed towards the influence of the elastic and mass properties of the primary structure to the optimal TMDI performance.

## Chapter 4

---

### Analytical and Numerical Investigation of TMDI Connectivity and Primary Structure Influence

Note: This Chapter has been submitted for publication and is currently under review:

Wang, Z. and Giaralis, A. (2020) “Enhanced motion control performance of the tuned mass damper inerter (TMDI) through primary structure shaping.” Manuscript submitted to *Struct. Control Health Monit.* for publication (accepted pending on minor revisions).

#### 4.1 Preliminary remarks

As stated in the introduction, upward tapering of tall buildings along the building height is a practical and efficient technique to alleviate the wind-induced accelerations. In the crosswind direction, this shape modification technique renders formation and shedding of vortices irregular and spatially incoherent (Kim and Kanda 2013), hence reducing the dynamic wind effects and ultimately the acceleration response (see, e.g., Kim and You 2002, You et al. 2008). Recently, Khodaie (2020) investigated the potential of using an optimal TMD system, attached to the free-end of cantilever structures with a square footprint, in conjunction with upward tapering of the primary structure for enhanced wind-borne performance in terms of displacement and acceleration. Numerical results evidenced that using the TMD system collaboratively with the proposed shape modification can efficiently reduce the wind-induced vibration through simultaneously increasing the energy dissipation capability and reducing the dynamic wind loads at source. Nevertheless, the TMD effectiveness is known to be only influenced by the attached mass but not by the properties of the host structure, meaning that the improved performance reported in Khodaie (2020) was an additive outcome. On the contrary, for the TMDI configuration, Pietrosanti et al. (2020a) recently demonstrated that the modal coordinate difference (of the primary structure) between the two terminals of the TMDI influences its effectiveness significantly in suppressing vibrations in earthquake-excited lumped-mass models. This finding points to the fact that the stiffness and mass properties of the host structure influence the motion control efficacy of the TMDI and warrants further investigation into the influences of the host structural properties on TMDI performance. Notably, the quantification of this influence has not been systematically pursued to date as all previous works have focused on leveraging the TMDI inertial properties (i.e., secondary mass and inertance) and inerter connectivity to mitigate the response of TMDI-equipped structures to dynamic excitations.

In this context, this Chapter aims to address the above gap in the literature by investigating the influence of the elastic and mass properties of the primary structure on the TMDI motion

control performance. This is pursued through an innovative parametric study involving a wide range of tapered beam-like cantilevered primary structures with different geometrical shapes (and, hence, different continuously varying flexural rigidity and mass distributions), equipped with TMDIs optimally tuned for minimising the steady-state peak and RMS free-end/tip displacements of the primary structure under harmonic resonant and white noise excitation, respectively. Optimal TMDI tuning and performance assessment are facilitated through a simplified 2-DOF dynamic model, which accounts for the properties of the primary structure as well as the influence of its uncontrolled mode shape at the location where the inerter connects the secondary mass to the host structure through a generalised SDOF oscillator. The accuracy of the 2-DOF model for optimal TMDI design and for structural performance assessment is verified against detailed finite element (FE) models for a wide range of TMDI parameters and primary structure shapes.

## 4.2 Two-DOF modelling and analysis of TMDI-equipped continuous flexural cantilever structures

### 4.2.1 System description and equations of motion in time domain

Consider a fixed-base structure amenable to be modelled as a continuous cantilevered beam with height  $h$  and with distributed flexural rigidity  $EI(x)$  and mass per unit length  $m(x)$  where  $0 \leq x \leq h$  as depicted in Fig. 4.1(a). This generic beam model can well represent slender tall buildings, industrial chimneys, wind turbine towers, as well as solar towers. Further, let a TMDI be attached to the free-end/tip of the considered beam (primary structure) to control the beam lateral motion due to a horizontal distributed dynamic load  $p(x, t)$  as shown in Fig. 4.1 (b). The TMDI comprises a secondary mass  $m_{TMDI}$  attached to the primary structure through a linear spring with stiffness  $k_{TMDI}$  in parallel with a dashpot with damping coefficient  $c_{TMDI}$ . The secondary mass is further connected to the primary structure at height  $\chi$  from the ground (fixed end) through an inerter element with inertance  $b$ .

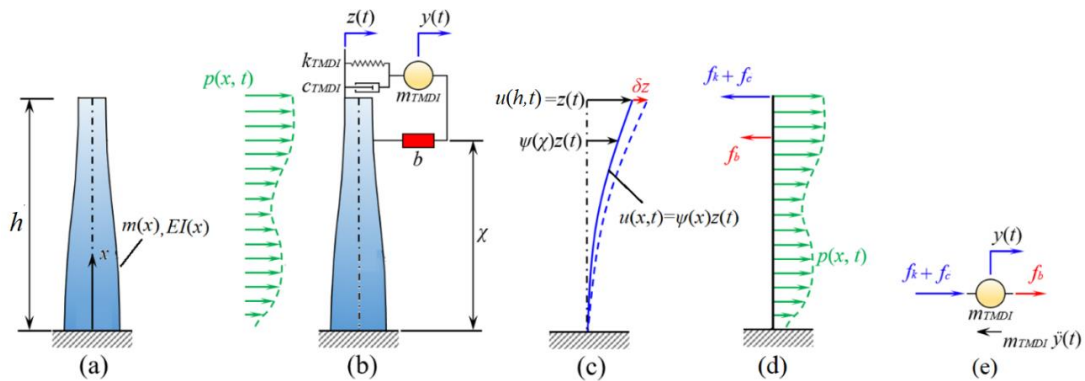


**Fig. 4.1.** (a) Continuous flexural cantilevered uncontrolled (primary) structure; (b) TMDI-controlled structure; (c) Assumed deflected shape and virtually displaced deflected shape; (d) External loads acting on the primary structure; and (e) External loads acting on the TMDI mass.

Next, assume that under the external load  $p(x, t)$ , the lateral response of the uncontrolled

primary structure can be faithfully approximated by a single deflected time-invariant shape  $\psi(x)$ . Under this assumption, the response displacement of the primary structure can be written as (Clough and Penzien 1995)

$$u(x,t) = \psi(x)z(t), \quad (4.1)$$

where  $z(t)$  is the free-end displacement of the cantilever and  $\psi(x)$  satisfies the fixed-end boundary conditions and is normalized such that  $\psi(h)=1$  (Fig. 4.1(c)). In this setting, the continuous beam can be represented by a generalised SDOF oscillator whose equation of motion is readily derived using the principle of virtual work (Clough and Penzien 1995). Specifically, the virtual work done by the inertial resistance and the external forces acting onto the primary structure shown in Fig. 4.1(d) due to some virtual displacement  $\delta z$  at the free-end of the primary structure is given as

$$\delta W_E = \int_0^h p \delta u(x) dx - \int_0^h f_i \delta u(x) dx - f_b \delta u(\chi) - (f_c + f_k) \delta u(h), \quad (4.2)$$

where  $\delta u(x) = \psi(x) \delta z$ . In the above equation,  $f_i$  is the distributed inertial resistance of the primary structure,  $f_b$  is the force of the TMDI inerter element acting at  $x=\chi$  height, and  $f_c$  and  $f_k$  are the forces of the TMDI damper (dashpot) and spring elements, respectively, acting at  $x=h$  (free-end). These forces are given as

$$f_i = m(x)\ddot{u}(x,t), \quad f_b = b[\psi(\chi)\ddot{z} - \ddot{y}], \quad f_c = c_{TMDI}(\dot{z} - \dot{y}), \quad \text{and} \quad f_k = k_{TMDI}(z - y), \quad (4.3)$$

where a dot over a symbol signifies differentiation with time and  $y(t)$  is the displacement of the secondary mass (Fig. 4.1(b)). Further, the virtual work done by the internal flexural and damping forces of the primary structure due to the same virtual displacement  $\delta z$  is given as

$$\delta W_I(t) = \int_0^h EI(x) \left[ \frac{\partial^2 u(x,t)}{\partial x^2} + a_c \frac{\partial^2 \dot{u}(x,t)}{\partial x^2} \right] \frac{d^2 \psi}{dx^2} \delta z dx, \quad (4.4)$$

assuming that stresses due to inherent damping of the primary structure are proportional to the strain velocity by a constant  $a_c$ .

By setting  $\delta W_E = \delta W_I$  and manipulating algebraically Eqs. (4.2-4.4), the following equation of motion is reached



$$\left(m^* + b\psi(\chi)^2\right)\ddot{z} - b\psi(\chi)\ddot{y} + \left(c^* + c_{TMDI}\right)\dot{z} - c_{TMDI}\dot{y} + \left(k^* + k_{TMDI}\right)z - k_{TMDI}y = p^*(t), \quad (4.5)$$

written in terms of the free-end displacement  $z(t)$  of the primary structure and the TMDI secondary mass displacement  $y(t)$ . In the above equation,  $p^*(t)$ ,  $m^*$ ,  $c^*$ , and  $k^*$  are the generalised load, mass, damping, and stiffness, respectively, of an underlying generalised SDOF system which represents the primary structure in the considered simplified model. These generalised quantities are defined as

$$\begin{aligned} p^*(t) &= \int_0^h p(x,t)\psi(x)dx \\ m^* &= \int_0^h m(x)(\psi(x))^2 dx \\ c^* &= a_c \int_0^h EI(x) \left(\frac{d^2\psi}{dx^2}\right)^2 dx = a_c k^* \\ k^* &= \int_0^h EI(x) \left(\frac{d^2\psi}{dx^2}\right)^2 dx \end{aligned} \quad (4.6)$$

Further to Eq. (4.5), an additional independent equation of motion can be written in terms of the displacements  $z(t)$  and  $y(t)$  by taking equilibrium of the external forces acting on the secondary mass and making use of d'Alembert's principle as follows (Fig. 4.1(e))

$$\begin{aligned} f_k + f_c + f_b &= m_{TMDI}\ddot{y} \quad \text{or} \\ b\psi(\chi)\ddot{z} - (m_{TMDI} + b)\ddot{y} + c_{TMDI}(\dot{z} - \dot{y}) + k_{TMDI}(z - y) &= 0. \end{aligned} \quad (4.7)$$

Next, the two equations of motion, Eqs. (4.5) and (4.7), are re-written as

$$\begin{cases} \left(1 + \beta\psi(\chi)^2\right)\ddot{z} - \beta\psi(\chi)\ddot{y} + 2\xi_1\omega_1\dot{z} + 2\nu\xi(\mu + \beta)\omega_1(\dot{z} - \dot{y}) + \omega_1^2 z + \nu^2\omega_1^2(\mu + \beta)(z - y) = \frac{p^*(t)}{m^*} \\ \beta\psi(\chi)\ddot{z} - (\mu + \beta)\ddot{y} + 2\nu\xi(\mu + \beta)\omega_1(\dot{z} - \dot{y}) + \nu^2(\mu + \beta)\omega_1^2(z - y) = 0 \end{cases} \quad (4.8)$$

with the aid of the circular natural frequency of the generalised SDOF primary structure representation,  $\omega_1 = (k^*/m^*)^{1/2}$ , and of five non-dimensional parameters, namely, the mass ratio,  $\mu$ , the inertance ratio,  $\beta$ , the TMDI frequency ratio,  $\nu$ , the TMDI damping ratio,  $\xi$ , and the primary structure inherent damping ratio  $\xi_1$ . These parameters are defined in terms of the generalised primary structure properties and the TMDI properties as

$$\mu = \frac{m_{TMDI}}{m^*}, \beta = \frac{b}{m^*}, \nu = \frac{\sqrt{k_{TMDI}/(m_{TMDI} + b)}}{\omega_1}, \xi = \frac{c_{TMDI}}{2\sqrt{(m_{TMDI} + b)k_{TMDI}}}, \text{ and } \xi_1 = \frac{c^*}{2\sqrt{m^*k^*}}. \quad (4.9)$$

Clearly, the equations of motion in Eq. (4.8) define a 2-DOF dynamical model which approximates the response of the TMDI-equipped cantilevered continuous beam of Fig. 4.1(b) in terms of the free-end displacement  $z(t)$  and the secondary TMDI mass displacement  $y(t)$ . Importantly, the properties of the herein derived 2-DOF model depend explicitly on the flexural stiffness and mass distribution of the primary cantilevered beam structure as well as on the assumed deflected shape (mode)  $\psi(x)$  through the generalised SDOF properties in Eq. (4.6). Further, the 2-DOF model accounts for the location  $x=\chi$  that the inerter connects the secondary mass to the primary structure through the modal coordinate  $\psi(\chi)$ . In this regard, the considered 2-DOF model encompasses the special case of a TMDI with grounded inerter (i.e., the inerter connects the TMDI mass to the ground) by setting  $\chi=0$  in Eq. (4.8) for which  $\psi(0)=0$ . The latter TMDI arrangement (with grounded inerter) has been widely studied in the literature (Marian and Giaralis 2014, Marian and Giaralis 2017, Pietrosanti et al. 2017, De Domenico and Riciardi 2018) and corresponds to a TMD with secondary mass equal to  $b+m_{TMDI}$  for force-excited primary structure. To this end, it is deemed convenient to define the non-dimensional inerter connectivity ratio

$$CR = 1 - \frac{\chi}{h}, \quad (4.10)$$

which will be seen to be a critical parameter for TMDI motion control performance taking values between  $CR=0$  (inerter in parallel to TMDI spring and dashpot) and  $CR=1$  (grounded inerter). Further to the TMDI with grounded inerter, the 2-DOF model can also approximate the special case of a conventional TMD with secondary mass  $m_{TMDI}$  attached to the free-end of the primary structure by setting  $b=\beta=0$  in Eq. (4.8).

#### 4.2.2 Frequency response functions

To expedite numerical work in subsequent sections, a set of non-dimensional FRFs corresponding to response quantities of practical interest are herein derived analytically. To this end, the equations of motion in Eq. (8) are first written in the domain of circular frequency,  $\omega$ , as

$$\begin{cases} [1 - g^2(1 + \beta\psi(\chi)^2) + (\nu^2 + i2g\nu\xi)(\mu + \beta) + i2g\xi_1]Z(\omega) + [g^2\beta\psi(\chi) - (\nu^2 + i2g\nu\xi)(\mu + \beta)]Y(\omega) = \frac{P^*(\omega)}{k^*}, \\ [g^2\beta\psi(\chi) - (\nu^2 + i2g\nu\xi)(\mu + \beta)]Z(\omega) + (\nu^2 - g^2 + i2g\nu\xi)(\mu + \beta)Y(\omega) = 0, \end{cases} \quad (4.11)$$

in which  $i = \sqrt{-1}$ ,  $g$  is the normalized frequency  $\omega/\omega_1$ ,  $Z(\omega)$  and  $Y(\omega)$  are the Fourier transformed displacements  $z(t)$  and  $y(t)$ , respectively, and  $P^*(\omega)$  is the Fourier transform of the generalised load  $p^*(t)$  in Eq. (4.6). Then, by eliminating  $Y(\omega)$  from Eq. (4.11), one obtains the non-dimensional FRF relating the primary structure free-end displacement to the static free-end displacement  $P^*(\omega)/k^*$  given as

$$H(\omega) = \frac{Z(\omega)}{P^*(\omega)/k^*} = \frac{(v^2 - g^2 + i2gv\xi)(\mu + \beta)}{\{1 - g^2[1 + \beta\psi(\chi)^2] + (v^2 + i2gv\xi)(\mu + \beta) + i2g\xi_1\}(v^2 - g^2 + i2gv\xi)(\mu + \beta) - [(v^2 + i2gv\xi)(\mu + \beta) - g^2\beta\psi(\chi)]^2}$$
(4.12)

In subsequent sections, the above analytical FRF is used to facilitate optimal TMDI design (tuning). Further, the non-dimensional FRF of the relative displacement of the TMDI secondary mass with respect to the primary structure free-end displacement, commonly termed as TMDI stroke, is given as

$$G(\omega) = \frac{Z(\omega) - Y(\omega)}{P^*(\omega)/k^*} = \frac{g^2[\beta\psi(\chi) - (\mu + \beta)]}{\{1 - g^2[1 + \beta\psi(\chi)^2] + (v^2 + i2gv\xi)(\mu + \beta) + i2g\xi_1\}(v^2 - g^2 + i2gv\xi)(\mu + \beta) - [(v^2 + i2gv\xi)(\mu + \beta) - g^2\beta\psi(\chi)]^2}$$
(4.13)

while the non-dimensional FRF of the relative acceleration between the secondary mass and the primary structure at height  $x=\chi$ , that is  $\psi(\chi)\ddot{z}(t) - \ddot{y}(t)$ , is given as

$$B(\omega) = \frac{[Z(\omega)\psi(\chi) - Y(\omega)]\omega^2}{P^*(\omega)/m^*} = \frac{\{\psi(\chi)[(v^2 - g^2 + i2gv\xi)(\mu + \beta)] - [(v^2 + i2gv\xi)(\mu + \beta) - g^2\beta\psi(\chi)]\}g^2}{\{1 - g^2[1 + \beta\psi(\chi)^2] + (v^2 + i2gv\xi)(\mu + \beta) + i2g\xi_1\}(v^2 - g^2 + i2gv\xi)(\mu + \beta) - [(v^2 + i2gv\xi)(\mu + \beta) - g^2\beta\psi(\chi)]^2}$$
(4.14)

The analytical FRFs in Eqs. (4.13) and (4.14) are used in the numerical part of this work for efficient calculation of the TMDI stroke, damping force, and inerter force under random excitation. This is achieved through frequency domain random vibration analysis as detailed in the next sub-section.

### 4.2.3 Random vibration analysis for white noise excitation

For the case of stochastically excited primary structure, the previous analytically derived

FRFs can be readily used to calculate RMS response statistics through standard random vibration analysis in frequency domain. Specifically, consider the case of zero-mean uniformly distributed in space white noise excitation. For this excitation, response PSD functions of practical interest are computed with the aid of the FRFs in Eqs. (4.12)-(4.14) as

$$S_z(\omega) = \frac{|H(\omega)|^2 S_p(\omega)}{(k^*)^2}, S_{stroke}(\omega) = \frac{|G(\omega)|^2 S_p(\omega)}{(k^*)^2}, S_v(\omega) = \frac{|\omega G(\omega)|^2 S_p(\omega)}{(k^*)^2}, \text{ and } S_a(\omega) = \frac{|B(\omega)|^2 S_p(\omega)}{(m^*)^2}, \quad (4.15)$$

where  $S_z(\omega)$  is the PSD of the free-end displacement of the primary structure,  $S_{stroke}(\omega)$  is the PSD of the TMDI stroke,  $S_v(\omega)$  is the PSD of the relative velocity between the attached mass and the cantilever free-end, and  $S_a(\omega)$  is the PSD of the relative acceleration between the attached mass and cantilever structure at height  $\chi$ . In the above expressions,  $S_p(\omega)$  is the excitation PSD given as

$$S_p(\omega) = \left( \int_0^h \psi(x) dx \right)^2 W_0, \quad (4.16)$$

where  $W_0$  is the constant PSD amplitude of the white noise excitation. Then, the RMS values of the free-end displacement of the primary structure,  $z(t)$ , attached mass stroke,  $z(t)-y(t)$ , damping force,  $f_c(t)$ , and inerter force,  $f_b(t)$ , are obtained using the expressions

$$\sigma_z = \sqrt{\int_0^{\omega_{max}} S_z(\omega) d\omega}, \sigma_{stroke} = \sqrt{\int_0^{\omega_{max}} S_{stroke}(\omega) d\omega}, \sigma_{f_c} = c_{TMDI} \sqrt{\int_0^{\omega_{max}} S_v(\omega) d\omega}, \text{ and } \sigma_{f_b} = b \sqrt{\int_0^{\omega_{max}} S_a(\omega) d\omega}, \quad (4.17)$$

respectively, where  $\omega_{max}$  is a cut-off frequency above which the PSDs in Eq. (4.15) attain negligible values.

### 4.3 Optimal TMDI design using the two-DOF simplified model

#### 4.3.1 Optimal TMDI design for resonant harmonic loading

Consider the case of a harmonic generalised load applied to the 2-DOF model defined in the previous section with frequency equal to  $\omega_1$ , that is, the natural frequency of the generalised SDOF system representing the primary structure. Arguably, this is a worse-case scenario excitation based on resonance considerations (Cacciola et al. 2020). In this respect, it is deemed useful to examine the effectiveness of the TMDI to mitigate the free-end displacement  $z(t)$  under resonant harmonic loading. To this aim, the magnitude of the FRF in Eq.(4.12) at  $\omega=\omega_1$  (i.e.,  $g=1$ ) given as

$$H(\omega_1) = \frac{(v^2 - 1 + i2v\xi)(\mu + \beta)}{[(v^2 + i2v\xi)(\mu + \beta) - \beta\psi(\chi)^2 + i2\xi_1](v^2 - 1 + i2v\xi)(\mu + \beta) - [\beta\psi(\chi) - (v^2 + i2v\xi)(\mu + \beta)]^2}, \quad (4.18)$$

is adopted to gauge TMDI motion control effectiveness. This is because  $|H(\omega_1)|$  provides the ratio of the peak steady-state free-end displacement over the static displacement for resonant harmonic excitation. To ensure meaningful performance comparison for different TMDI properties, an optimal TMDI tuning problem is formulated to determine TMDI frequency,  $v$ , and damping,  $\xi$ , properties which minimise  $|H(\omega_1)|$  given mass ratio,  $\mu$ , inertance ratio,  $\beta$ , and inerter connectivity ratio,  $CR$ , for a primary structure with assumed deflected shape  $\psi$  and damping ratio  $\zeta^*$ . In this setting, the primary TMDI design variables (DVs) can be collected in the vector  $\mathbf{x}_1 = [v, \xi]^T$  and the secondary TMDI DVs in the vector  $\mathbf{x}_2 = [\beta, \mu, CR]^T$  so that the optimal TMDI tuning problem is mathematically written as

$$\min_{\mathbf{x}_1} \{|H(\omega_1)| | \mathbf{x}_2\} \text{ subjected to } \mathbf{x}_1^{\min} \leq \mathbf{x}_1 \leq \mathbf{x}_1^{\max}, \quad (4.19)$$

where the vectors  $\mathbf{x}_1^{\min}$  and  $\mathbf{x}_1^{\max}$  specify the lower and the upper bounds, respectively, of the search range of the two primary DVs. Note that the TMDI tuning problem in Eq.(19) allows for explicit treatment of the TMD and of the TMDI with grounded inerter as special cases by taking  $\beta=0$  and  $CR=0$ , respectively.

The solution of the optimisation problem in Eq.(4.19) is straightforward as the numerator of the FRF in Eq.(4.18) becomes zero for  $v=1$  and  $\xi=0$ , for every  $\mathbf{x}_2$ ,  $\psi$ , and  $\zeta^*$ . Still, given that in practical applications some TMDI damping will always be present in anticipation of wide-band excitations (see also next sub-section), it is instructive to study the behaviour of  $|H(\omega_1)|$  as function of the primary design variables for different TMDI inertial and connectivity properties. To this end, Fig. 4.2 plots  $|H(\omega_1)|$  on the  $v$ - $\xi$  plane for TMD ( $\beta=0$ ) and for TMDI with  $\beta=40\%$  and different CR values. In all cases, the mass ratio is taken as  $\mu=0.1\%$ , the inherent damping ratio is taken as  $\zeta^*=2\%$ , and the deflected shape of the primary structure is assumed to be

$$\psi(x) = 1 - \cos\left(\frac{\pi x}{2h}\right), \quad (4.20)$$

which is commonly adopted to approximate single-mode dynamic behaviour of cantilevered structures whose response is dominated by their first mode shape (Chopra 2000). It is seen that the global  $|H(\omega_1)|$  minimum is reached at  $v=1$  as  $\xi \rightarrow 0$  and that the TMDI becomes more effective than TMD throughout the primary variables design plane as  $CR$  increases. The latter observation is practically important as it suggests that connecting the inerter further away from

the free-end of the primary structure enhances TMDI motion control for resonant harmonic loading even for non-optimal (i.e.,  $\zeta > 0$ ) TMDI damping ratios.

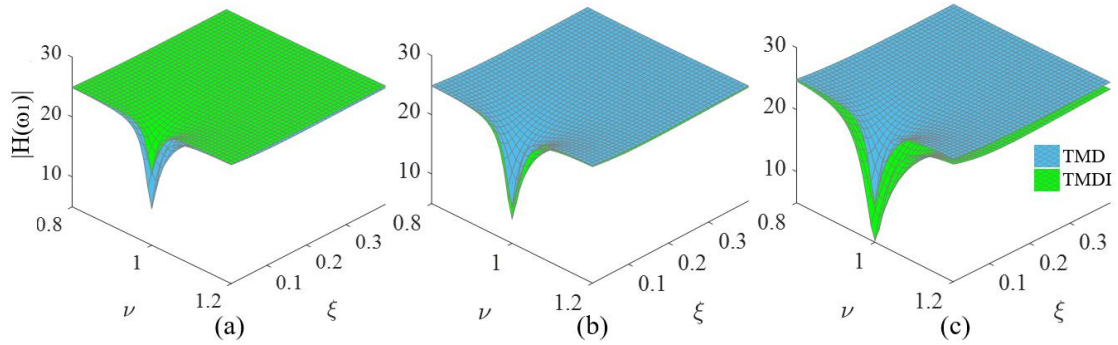


**Fig. 4.2.** Magnitude of the non-dimensional FRF,  $H(\omega_1)$ , in Eq. (18) versus TMDI frequency ratio,  $\nu$ , and damping ratio,  $\zeta$ , for attached mass ratio  $\mu=0.1\%$ , inertance ratios,  $\beta=0$  (TMD) and  $\beta=40\%$ , and connectivity ratios, (a) 2.5%; (b) 5.0%; and (c) 7.5%.

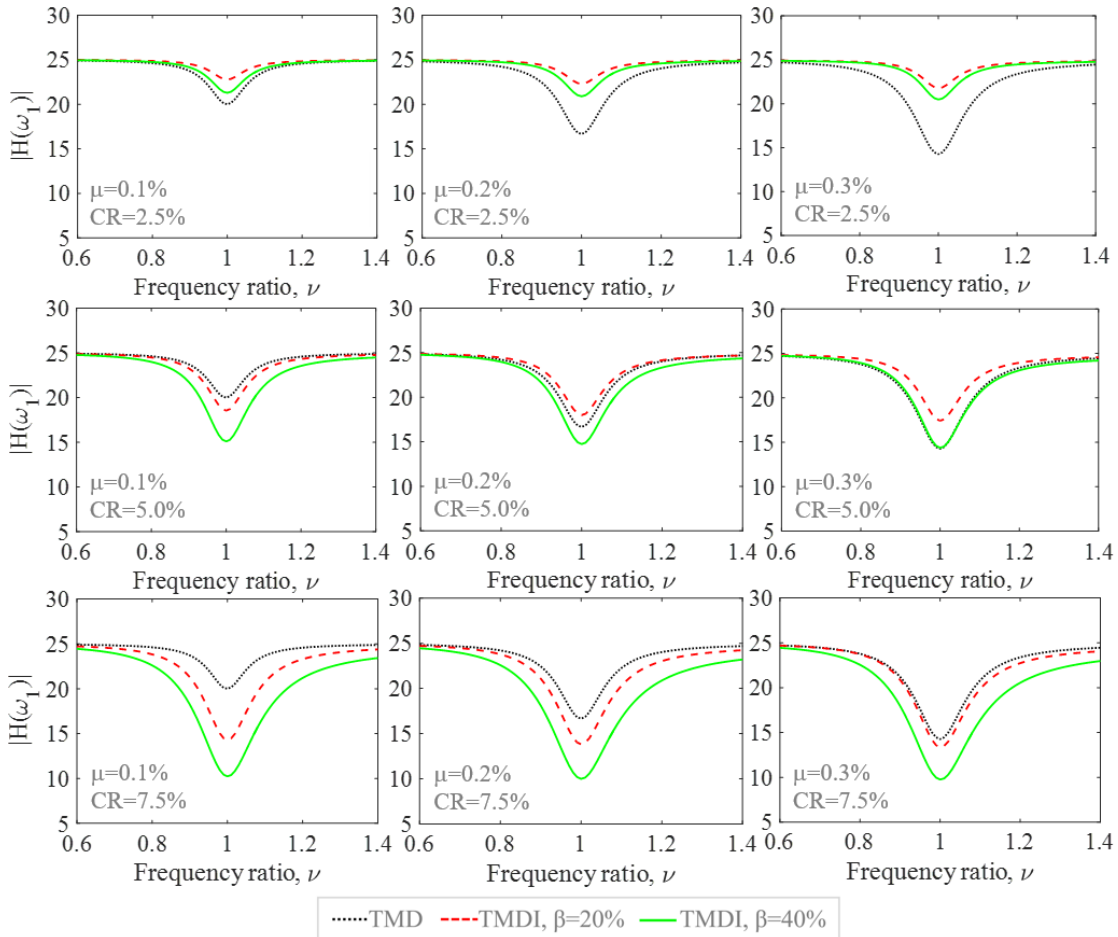


**Fig. 4.3.** Magnitude of the non-dimensional FRF,  $H(\omega_1)$ , in Eq. (4.18) versus TMDI frequency ratio for various secondary mass ratios,  $\mu$ , inertance ratios,  $\beta$ , and connectivity ratios,  $CR$ .

Further light on the optimal TMDI design for resonant harmonic loading is shed by examining numerical data in Fig. 4.3 where  $|H(\omega)|$  is plotted against TMDI frequency  $\nu$  for

three different secondary mass ratios  $\mu = [0.1\%, 0.2\%, 0.3\%]$ , inertance ratios  $\beta = [0, 20\%, 40\%]$ , and connectivity ratios  $CR = [2.5\%, 5.0\%, 7.5\%]$ . A fixed arbitrarily taken value of TMDI damping ratio  $\zeta = 5\%$  is taken, while  $\zeta^*$  is taken equal to 2% and the deflected shape of Eq.(4.20) is assumed. It is seen that improved free-end displacement reduction at a wider band of frequencies around the optimal value  $\nu=1$  is achieved as the inertance ratio  $\beta$  and/or the connectivity ratio  $CR$  increase. On the contrary, the increase of the secondary mass has negligible effect to the motion control performance of the TMDI, though it is significant (beneficial) for the TMD. Notably, similar trends on motion control performance of optimally designed TMDI have been reported in previous works which considered lumped-mass primary structures under earthquake and wind excitations (see e.g., [Giaralis and Taflanidis 2018](#), [Petrini et al. 2020](#)). These similarities indicate the capability of the simplified 2-DOF model of section 4.2.1, derived from a primary structure with continuously distributed mass and stiffness properties, to capture the salient dynamics of TMDI-equipped cantilevered structures as well as to facilitate optimal TMDI tuning.

### 4.3.2 Optimal TMDI design for white noise excitation

Turning the attention to mitigating primary structure motion to white noise excitation (uniformly distributed and spatially correlated), TMDI optimal tuning is sought in the second norm,  $H_2$ , sense. Specifically, the primary DVs in vector  $\mathbf{x}_1$  are determined to minimise the area under the square magnitude of the non-dimensional FRF in Eq. (4.12) (OF) for given secondary DVs in vector  $\mathbf{x}_2$  and for assumed primary structure deflected shape  $\psi$  and damping ratio  $\zeta_j$ . The underlying optimisation problem is mathematically written as

$$A_{\min} = \min_{\mathbf{x}_1} \left\{ \underbrace{\int_0^{\omega_{\max}} |H(\omega)|^2 d\omega}_{\text{objective function (OF)}} \right\} \text{ subjected to } \mathbf{x}_1^{\min} \leq \mathbf{x}_1 \leq \mathbf{x}_1^{\max}. \quad (4.21)$$

The solution to the above problem is non-trivial and, herein, pattern search ([Charles and Dennis 2003](#)) is employed to find numerically  $\mathbf{x}_1$  that yields the minimum,  $A_{\min}$ , value of the objective function. For computational efficiency, a custom-made pattern search algorithm with iteratively narrowing search range in a step-wise manner is hard-coded in MATLAB®. In all the ensuing numerical work, the initial search range in solving the optimisation problem in Eq. (4.21) is taken as  $\mathbf{x}_1^{\min} = [0.0, 0.0]^T$  and  $\mathbf{x}_1^{\max} = [2.0, 2.0]^T$ . This initial search range is iteratively narrowed around the  $\nu$  and  $\zeta$  values which minimise the OF in the previous step, until the difference of  $A_{\min}$  between two successive steps becomes smaller than a pre-specified tolerance set equal to  $10^{-2}$ .

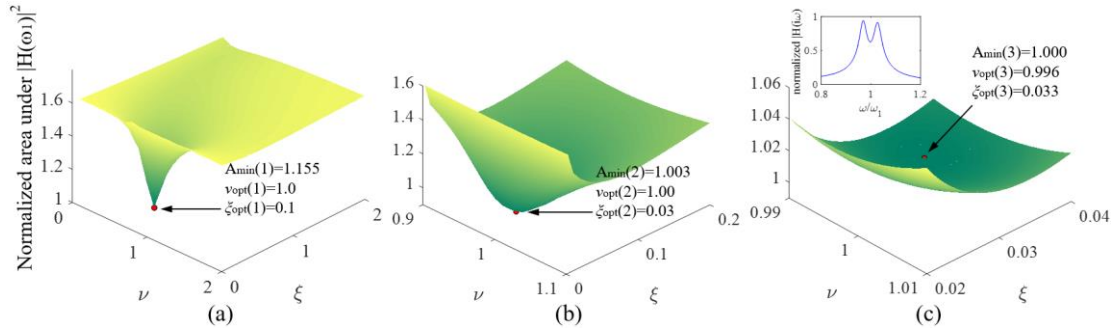


**Fig. 4.4.** Iterative pattern search algorithm illustration for solving the optimisation problem in Eq.(4.21) for TMDI with mass ratio  $\mu=0.1\%$ , inertance ratio  $\beta=40\%$ , and connectivity ratio  $CR=7.5\%$ , and primary structure with  $\zeta^* = 2\%$  and deflected shape in Eq.(20): (a) 1<sup>st</sup> iteration; (b) 2<sup>nd</sup> iteration; and (c) 3<sup>rd</sup> iteration.

For numerical illustration, Fig. 4.4 plots the OF in Eq.(4.21) on the primary DV plane computed in three different successive steps/iterations of the pattern search algorithm for  $\mathbf{x}_2=[40\%, 0.1\%, 7.5\%]^T$ ,  $\xi_l=2\%$ , and primary structure deflected shape in Eq.(4.20). Optimal values  $\nu(j)$ ,  $\zeta(j)$  and  $A_{\min}(j)$  for  $j=1,2,3$  iterations are indicated in the plots. It is seen that the algorithm converges fast and that the OF is convex exhibiting a single (global) minimum. The same behavior is noted in all cases examined later in this work. Moreover, in the inset of Fig. 4.4(c), the magnitude of the normalized FRF in Eq. (4.12) for the optimally designed TMDI is plotted to demonstrate the nature of the achieved optimality. It is seen that the free-end displacement FRF exhibits two distinct peaks of almost equal height with a local minimum (valley) attained roughly at the uncontrolled fundamental frequency. These two peaks correspond to the shifted vibration mode of the primary structure and the TMDI mode.

Further to Fig. 4.4(c), Fig. 4.5 plots the magnitude of the FRF in Eq. (4.12),  $|H(\omega)|$ , for optimally designed TMDIs to white noise excitation for the same  $\mathbf{x}_2$  properties and primary structure considered in Fig. 4.3. Evidently, increased inerter and connectivity ratios are beneficial to the TMDI capability to mitigate primary structure motion for white noise excitation just as for resonant harmonic excitation, while the mass ratio has negligible effect.



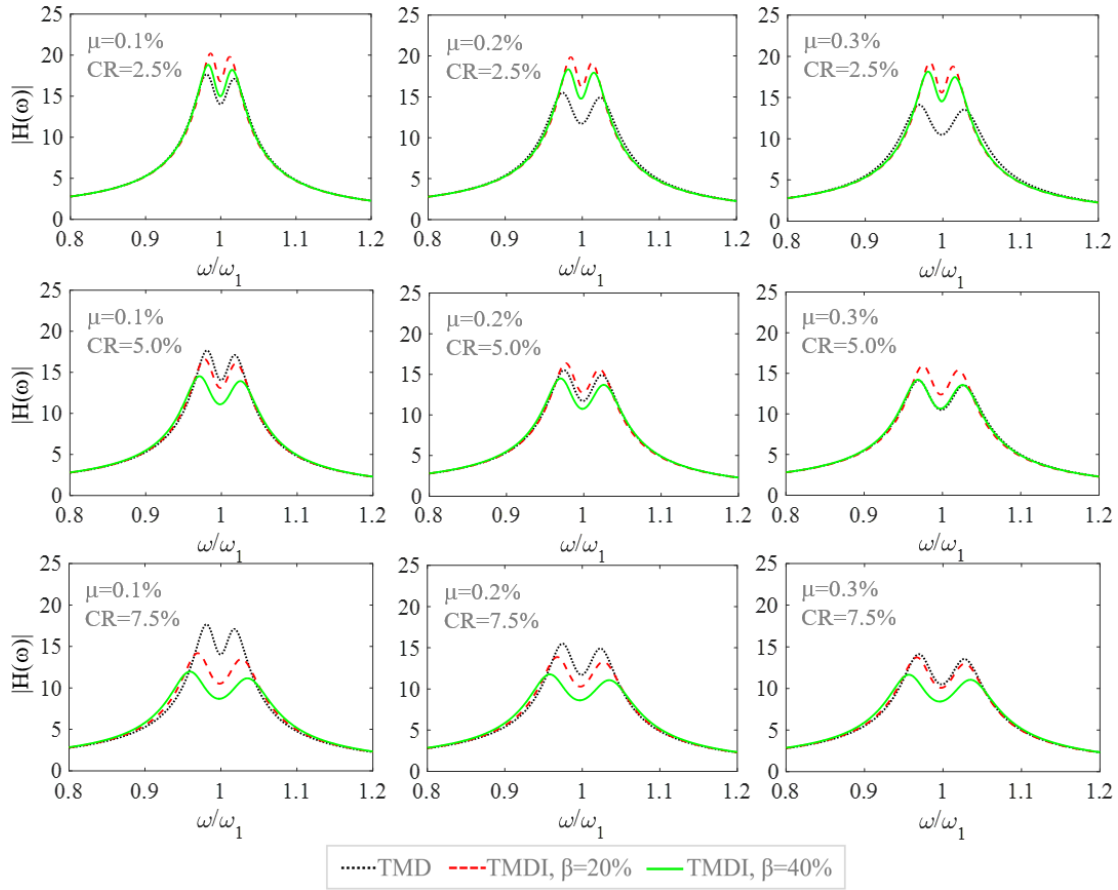


**Fig. 4.5.** Magnitude of the non-dimensional FRF,  $H(\omega)$ , in Eq. (12) for optimally designed TMDIs to white noise excitation for various secondary mass ratios,  $\mu$ , inertance ratios,  $\beta$ , and connectivity ratios,  $CR$ .

#### 4.4 Geometric shape variation of primary structure

##### 4.4.1 Geometric shape definition and derivation of fundamental mode shapes

Having established the applicability and usefulness of the simplified 2-DOF model presented in section 4.2 to support optimal TMDI tuning for motion control of cantilevered primary structures, the attention is turned to leveraging this model for investigating the influence of the primary structure geometry to the TMDI vibration suppression effectiveness. To this aim, cantilevered beams with solid rectangular cross-section, height  $h$ , constant width  $L$ , and varying depth  $D(x)$  with height are considered as shown in Fig. 4.6. The continuously varying depth allows to define beams with different smoothly tapered shapes inspired by real-life structures such as industrial chimneys (e.g., [Brownjohn et al. 2009](#)), slender towers supporting renewable energy generation (e.g., [Zhao et al. 2018](#), [Li et al. 2018](#)), and tall buildings (e.g., [Li et al. 2011](#), [Lu et al. 2017](#)). Specifically, beams with five different geometric shapes shown in Fig. 4.6 are defined through the analytical expressions of the depth profiles,  $D(x)$ , reported in Table 4.1. The uniform shape “I” has constant depth profile assuming a square cross-section. The non-constant depth profiles of the other four geometric shapes are specified with the aid of the depth ratio  $R=D(0)/D(h)$  (i.e. base depth over free-end depth). Purposely, the

base depth,  $D(0)$ , is defined as a function of  $R$  (see Table 1) such that all shapes have the same total volume for any value of  $R$ . This consideration allows for establishing beams with different height-wise mass and flexural rigidity distributions expressed as

$$m(x) = \rho L D(x) \quad \text{and} \quad EI(x) = \frac{ELD^3(x)}{12}, \quad (4.22)$$

respectively, but with the same total mass equal to  $\rho h L^2$ , where  $\rho$  is the mass density. In this regard, these beams constitute a practically meaningful set of parametrically defined primary structures for the purpose of assessing comparatively the TMDI motion control effectiveness. This is because they attain different dynamic/modal properties, which do influence TMDI efficacy, but have equal total weight and material usage which are directly linked to sustainability considerations in construction (Cabeza et al. 2013).

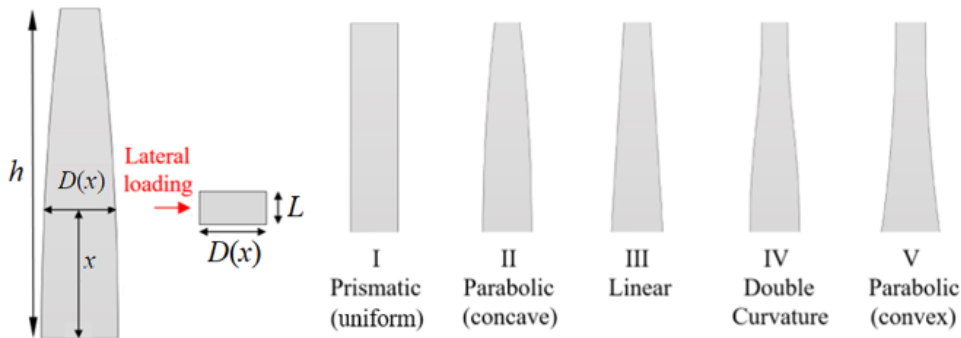


**Fig. 4.6.** Considered geometric shapes of cantilevered beam-like primary structures.

**Table 4.1.** Analytical definition of primary structure geometric shapes in Fig.6(b) through the depth  $D(x)$  and the depth ratio  $R=D(0)/D(h)$ .

Shape	Description	Depth at the base $D(0)=D_o$	Depth at height $x$ $D(x)$	Depth at the tip $D(h)$
I	Uniform	$L$	$L$	$L$
II	Parabolic (concave)	$3L/(2+1/R)$	$D_o + D_o(1/R-1)(x/h)^2$	$D_o/R$
III	Linear	$2L/(1+1/R)$	$D_o + D_o(1/R-1)x/h$	
IV	Double curvature	$2L/(1+1/R)$	$D_o + 1/2 D_o(1/R-1)[1 - \cos(\pi x/h)]$	
V	Parabolic (convex)	$3L/(1+2/R)$	$D_o + D_o(1-1/R)[(x/h)^2 - 2(x/h)]$	

To provide an insight into the relative variation of mass and flexural rigidity distributions of the primary structures in Fig. 4.6, Fig. 4.7 plots the ratio  $EI(x)/m(x)$  (i.e., flexural rigidity over mass) for different values of the depth ratio  $R$  and for all four non-uniform geometric shapes. These plots are normalized by the constant ratio  $EI/m=EL^2/12\rho$  of the uniform shape. In all the panels of Fig. 4.7, the same reference continuous curve corresponding to the uniform

shape ( $R=1$ ) is included to facilitate comparisons. It is seen that for all shapes (depth profiles  $D(x)$ ), an increase in the depth ratio  $R$  results in higher values of  $EI(x)/m(x)$  towards the base of the structure and lower values towards the free-end of the structure. Therefore, an increase of  $R$  defines primary structures that become increasingly more flexible with height. Further, as shapes evolve from “II” to “V” the rate of change of  $EI(x)/m(x)$  with height reduces faster, that is, the primary structure becomes more flexible with height at a faster rate while the value  $[EI(h)/m(h)]/[EI(0)/m(0)]$  reduces. In fact, for shapes “IV” and “V” the ratio  $EI(x)/m(x)$  becomes practically constant  $x/h>0.80$  and  $x/h>0.75$ , respectively. Notably, these differences in the distribution of  $EI(x)/m(x)$  with height affects the properties of the primary structure mode shapes as discussed later in this section.

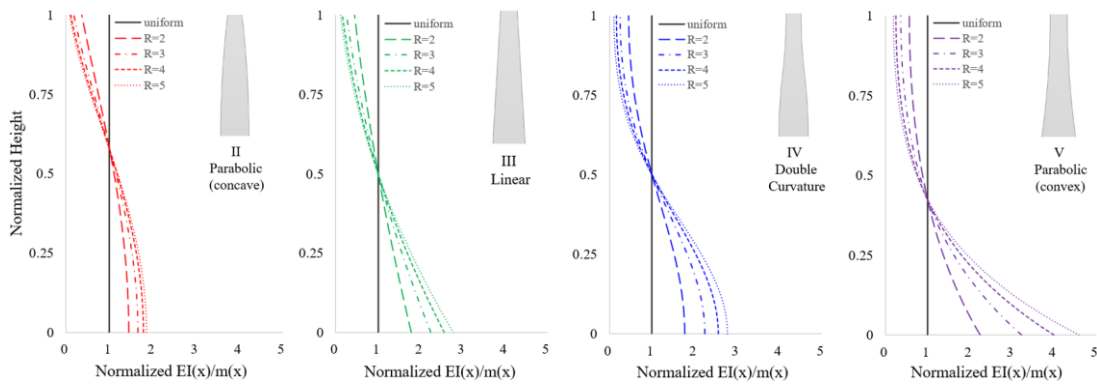


**Fig. 4.7.** Rigidity over mass distribution plots for all considered geometric shapes (depth profiles in Table 1) and for various depth ratios  $R$  of cantilevered beam-like primary structures.

Regardless of their geometric shape, the assumption that the dynamic response of the primary structure is dominated by the first/fundamental mode shape,  $\varphi_1(x)$ , is made which is reasonable for slender structures. In this respect, the simplified 2-DOF model of section 4.2 can be used in conjunction with the primary structures in Fig. 4.6 by using the mass and flexural rigidity distributions of Eq.(4.22) in Eq.(4.6) and by setting  $\psi(x)=\varphi_1(x)$ . For the purposes of this work, the fundamental mode shape  $\varphi_1(x)$  of the uncontrolled primary structures is numerically approximated using a FE approach. This is achieved by discretising the primary structure using 40 tapered equal-length linear Euler-Bernoulli beam elements. Then, a 41-DOF planar dynamic model is derived involving only one lateral translational DOF per FE node grid along the horizontal load direction in terms of a diagonal mass matrix and a full stiffness matrix. The mass matrix is formed by lumping the own mass of the elements at the nodes while the stiffness matrix is constructed using standard static condensation to eliminate vertical and rotational DOFs at each FE node. Next, standard modal analysis is conducted to obtain the fundamental mode shape vector  $\varphi_1 \in \mathbb{R}^{41 \times 1}$ . The central difference method is used to obtain numerically the second derivative of the mode shape vector (modal curvature) and the standard trapezoid quadrature rule is used to determine the integrals in defining the generalised primary structure properties in Eq. (4.6).

The influence of the geometric shape of the primary structure to its fundamental mode is qualitatively seen in Figs. 4.8(a) and 4.8(b). In Fig. 4.8(a), numerically derived fundamental modes are plotted for all five geometric shapes of Fig. 4.6 and for the same ratio  $R=3$  (except for the uniform shaped structure which can only attain  $R=1$ ), while in Fig. 4.8(b) fundamental modes for shapes “I” and “V” with different depth ratios  $R=2,3,4$ , and 5 are plotted. It is observed that as geometric shapes vary from “II” towards “V” for fixed  $R$  and as the ratio  $R$  increases for fixed shape, the convexity of the modes increases. This is readily justified by the fact that the ratio  $EI(x)/m(x)$  takes on higher values (i.e., is always heavier distributed) towards the base of the primary structure and reduces faster with height as  $R$  increases and/or as shapes vary from “II” to “V” as previously discussed in view of Fig. 4.7. In this work, the average modal curvature along the height of the structure is used as an intuitive scalar quantitative metric to measure the convexity of the fundamental modal shape. The variation of this novel metric for the four non-uniform primary structures and for  $R=2,3,4$ , and 5 is reported in Fig. 4.8(c) in which ordinates are normalized by the average curvature of the uniform primary structure. This is an important consideration for the purposes of this work as it will be seen, in subsequent sections, that the average modal curvature of the primary structure correlates well with the TMDI motion control potential.

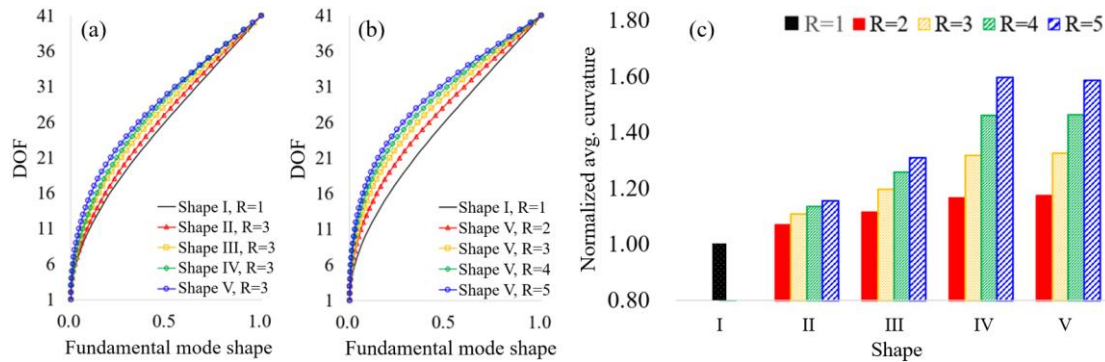


**Fig. 4.8.** Numerically derived fundamental mode shapes and average modal curvature for primary structures with different depth profiles (shapes) and depth ratios  $R$ .

Furthermore, [Pietrosanti et al. \(2020a\)](#) showed that the TMDI control effectiveness (in suppressing earthquake-induced vibrations in lumped-mass models) correlates positively with the modal coordinate difference (of the primary structure) between the two connecting locations of the TMDI, i.e.,  $\Psi(h)-\Psi(\chi)$ . To examine the influences of primary structure tapering on the latter quantity, Fig. 4.9 plots the modal coordinate difference of the fundamental modes, values normalized by the corresponding difference of the uniform cantilever (i.e., the shape I) with  $CR=2.5\%$ , for all five geometric shapes in Fig. 4.6, four depth ratios in Fig. 4.7, and three  $CR$  in Fig. 4.5. It is seen that, as the depth profile varies from “II” towards “V” for fixed  $R$ , or as  $R$  increases for fixed shape, or as  $CR$  increases for fixed shape and  $R$ , the modal coordinate difference between the two TMDI terminals increases, which, as will be seen later, correlates

well with the TMDI control effectiveness.

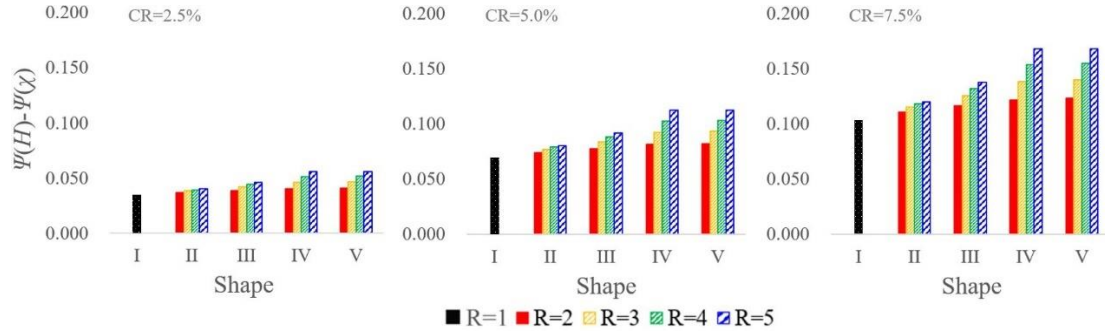


**Fig. 4.9.** Normalized mode coordinate difference between the free end and the inerter connecting location of primary structures,  $\Psi(H) - \Psi(\chi)$ , with different depth profiles (shapes), depth ratios,  $R$ , and inerter connectivity ratios,  $CR$ .

#### 4.4.2 Verification of the simplified 2-DOF model for optimal TMDI design and performance assessment

Besides approximating the dynamic response of the primary structure via a single mode shape through modal truncation, another simplifying assumption made in the 2-DOF model defined in section 4.2 is that the TMDI-controlled primary structure would have the same fundamental mode shape as the uncontrolled. Indeed, the inclusion of the TMDI alters locally the fundamental mode shape of the primary structure which, in turn, may affect the effectiveness of the optimal TMDI tuning if using the simplified 2-DOF model for the task. Thus, it is herein deemed important to verify the accuracy of the 2-DOF model for optimal TMDI tuning vis-à-vis a more detailed model that can capture the structure-TMDI coupling as well as the effects of higher modes.

In this junction, note that the combination of large  $R$ ,  $\beta$ , and  $CR$  values leads to higher influence of the TMDI to mode shapes since a large  $R$  specifies primary structures with a more flexible upper part while large  $\beta$  and  $CR$  result in higher magnitude dashpot and inerter forces exerted to the primary structure (see Fig. 4.15 later in the chapter). Therefore, structures with high ratio  $R=5$  for shapes II-V and large TMDI inertance,  $\beta=40\%$ , and  $CR=7.5\%$  are used for the verification of the 2-DOF model tuning accuracy. For each structure, two different dynamic systems are considered to determine the FRF  $H(\omega)$  used in the objective function for optimal tuning. The first system is the 2-DOF model in section 4.2 in which  $\psi(x)$  is set equal to the fundamental mode shape of the uncontrolled primary structure. This mode shape is estimated through modal analysis using the 41-DOF FE model as detailed in section 4.4.1. For this system, the  $H(\omega)$  is determined using Eq. (4.12). The second system uses directly the 41-DOF FE modelling of the primary structure which is augmented by an additional DOF for the TMDI following the formulation of [Giaralis and Petrini \(2017\)](#). The resulting 42-DOF model accounts for primary structure-TMDI interaction explicitly while  $H(\omega)$  is determined using the frequency domain approach in [Giaralis and Petrini \(2017\)](#). Next, two different sets of optimal TMDI primary DV values,  $v_{opt}$  and  $\xi_{opt}$ , are computed by solving the  $H_2$  optimisation problem in Eq.

(4.21) using the  $H(\omega)$  from the two different systems (the 2-DOF and the 42-DOF).

Table 4.2 reports the percentage difference of the two sets of optimal TMDI tuning parameters for all structures considered. In the same Table, the deviation to the structural performance due to adopting different sets of TMDI tuning parameters for each structure is also reported, measured in terms of RMS free-end displacement percentage difference obtained from 42-DOF detailed models under white noise excitation. It is evidenced that the simplified 2-DOF model is sufficiently accurate to be used for TMDI optimal tuning since errors to the tuning parameters are less than 0.2% for all considered structures, causing deviations to structural performance of 1% or less. Moreover, Table 4.2 furnishes differences to structural performance obtained by using the simplified and the detailed models and adopting the corresponding sets of TMDI tuning parameters. It is seen that percentage differences are less than 2% across the board. In view of these small differences, the 2-DOF model is used for optimal TMDI tuning as well as for comparative performance assessment of optimal TMDI-equipped primary structures in all the ensuing numerical work. Note that this consideration expedites significantly the computational work given that the evaluation of  $H(\omega)$  for the 42-DOF model involves multiplications and inversion of 42-by-42 full matrices which are computationally much more demanding than the evaluation of  $H(\omega)$  through Eq. (4.12). Hence the practical merit of the model in section 4.2 is established for optimal TMDI tuning of generic cantilevered structures with dominant fundamental mode.

**Table 4.2** Absolute percentage differences of optimal TMDI tuning parameters and of RMS free-end displacements using 42-DOF detailed FE models and 2-DOF simplified models of TMDI-equipped primary structures. Optimal tuning for white noise excitation is considered.

Control device	TMDI ( $\mu=0.3\%$ , $\beta=40\%$ , $CR=7.5\%$ )				
	I ( $R=1$ )	II ( $R=5$ )	III ( $R=5$ )	IV ( $R=5$ )	V ( $R=5$ )
Primary structure					
$v_{opt}$	0.00%	0.05%	0.13%	0.09%	0.16%
$\zeta_{opt}$	0.00%	0.00%	0.00%	0.00%	0.00%
RMS free-end displacement deviation	0.01%	0.49%	0.61%	0.30%	1.05%
RMS free-end displacement performance	1.88%	1.15%	1.22%	1.42%	1.69%

#### 4.5 Performance assessment of TMDI-equipped structures with different geometric shapes

In this section, the influence of primary structure geometric shape to the motion control effectiveness of TMDI is assessed through a parametric numerical investigation, involving primary structures of different geometric shapes characterized by the depth ratio  $R=D(0)/D(h)$  and the depth profile  $D(x)$  in Table 4.1 and Fig. 4.6. To this aim, TMDIs with various  $\mu$ ,  $\beta$ , and  $CR$  properties are optimally tuned for resonant harmonic excitation or for white noise excitation (as indicated in the text and figure captions) by solving the optimisation problem in Eq. (4.19)

or (4.21), respectively. In all structures investigated,  $\zeta^*=2\%$  inherent structural damping is assumed. To expedite computations, the 2-DOF model of section 4.2 with deflected shape  $\psi(x)$  equal to the fundamental mode shape of the primary structure is used for TMD(I) tuning and for obtaining response quantities of interest throughout this section for the above excitations. Fundamental mode shapes are computed through modal analysis applied to FE models of the primary structures as detailed in section 4.4.1.

#### 4.5.1 Influence of depth ratio $R$ to free-end displacement

First, attention is focused on investigating the influence of the depth ratio  $R=D(0)/D(h)$  of the primary structure on the TMDI motion control efficacy. This is supported by plotting in Fig. 4.10 the RMS free-end displacement of optimal TMDI-equipped structures against  $CR$  for fixed depth ratios  $R=2,3,4$ , and 5 and for each of the geometric shapes II-V in Fig. 4.6, separately. The same TMDI mass and inertance are considered for all structures of each panel of Fig. 4.10, taken as  $m_{TMDI}=0.1\% \times m^*_{Avg}$  and  $b=40\% \times m^*_{Avg}$ , respectively, where  $m^*_{Avg}$  is the average generalized mass  $m^*$  in Eq. (4.6) of all the primary structures studied in Fig. 4.10. These assumed inertial values are representative of low mass/weight and high inertance TMDIs which were found to be quite effective and advantageous over TMDs in earthquake (Giaralis and Taflanidis 2017) and wind (Giaralis and Petrini 2017) engineering applications as they relax requirements for large secondary mass and reduce significantly the kinematics of the secondary mass. Both considerations are practically important: the former leads, ultimately, to more lightweight and, therefore, economic absorbers; the latter reduces needs for space/clearance to accommodate the absorber, as well as the cost of energy dissipation devices (dampers) whose cost increases with the stroke (relative displacement between primary structure and secondary mass). For each structure, TMDI is optimally tuned for white noise excitation using Eq.(4.21). Further, the reported RMS free-end displacements in Fig. 4.10 are normalised by the RMS free-end displacement of the same primary structure equipped with a same-mass TMD which is optimally tuned by solving Eq. (4.21) for  $b=0$ . In all the panels of Fig. 4.10, the same reference continuous curve corresponding to the uniform shape ( $R=1$ ) is included to facilitate comparisons.



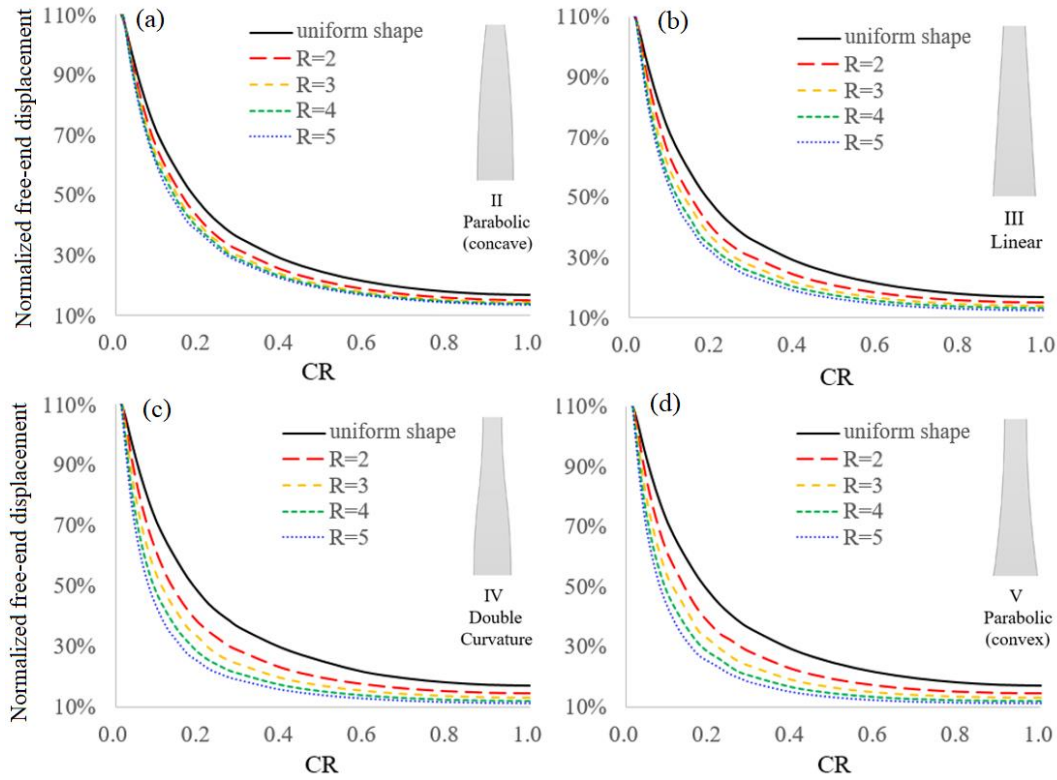


**Fig. 4.10.** RMS free-end displacements of white noise excited TMDI-equipped structures for attached mass  $m_{\text{TMDI}}=0.1\% \times m_{\text{Avg}}^*$  and inertance  $b=0.40 \times m_{\text{Avg}}^*$  for different geometric shapes and depth ratios normalized by the corresponding displacements of optimal TMD-equipped structures and plotted against  $CR$ .

It is seen that improved vibration suppression is achieved monotonically as  $CR$  increases (i.e., as the inerter links the secondary mass further away from the free-end) for all geometric shapes and  $R$  values and, thus, for all different primary structure mode shapes. In this regard, best performance is always achieved for grounded inerter ( $CR=100\%$ ). However, performance improvement saturates with  $CR$  fast for all structures and, in general, little improvement is demonstrated for  $CR>30\%$ . Further, for relatively small  $CR$  values (less than about 3%) the TMD outperforms the TMDI (normalized free-end displacement is higher than 100%). All the above trends agree with trends reported in previous numerical studies examining various TMDI-equipped lumped-mass models of different benchmark building structures exposed to wind or earthquake excitations (e.g., [Giaralis and Taflanidis 2018](#), [Ruiz et al. 2018](#), [Taflanidis et al. 2019](#), [Giaralis and Petrini 2017](#), [Petrini et al. 2020](#), [Kaveh et al. 2020](#)). Hence, it is safely concluded that these trends are applicable to any type of primary cantilevered structure which suggests that it is always beneficial to attach the inerter as further away from the free-end of the primary structure as structurally and economically feasible.

More importantly, reported data in Fig. 4.10 evidence that TMDI performance improves monotonically over a same-mass TMD as the depth ratio  $R$  increases for fixed  $CR$  value and for any geometric shape. This improvement is more substantial for lower  $CR$  values. This novel finding suggests that the TMDI becomes more effective as the upper part of cantilevered



primary structures becomes more flexible (see discussion in view of Fig. 4.7) for same total structural weight. In this regard, from the structural design viewpoint, the  $CR$  can be traded for tapering of the primary structure geometric shape in achieving a desired target structural performance for fixed inertial TMDI parameters (i.e., mass  $m_{TMDI}$  and inertance  $b$ ). For instance, for shape “V” in Fig. 4.10(d), the required  $CR$  for a TMDI with  $m_{TMDI}=0.1\% \times m_{Avg}^*$  and  $b=40\% \times m_{Avg}^*$  to achieve 50% better performance than a same-mass TMD reduces from 18% to 11% as the depth ratio increases from  $R=2$  to  $R=4$ . In the first instance, this consideration is useful for design engineers as it leads to more lightweight vibration absorbers and, thus, more economical since the attached mass is proportional to the upfront TMD(I) cost (e.g., Ruiz et al. 2018). This consideration is also beneficial in applications where connecting the inerter much below the top of the structure is practically challenging such as in the case of tall buildings discussed in Wang and Giaralis (2020) and Kaveh et al. (2020). In this respect, increasing the depth ratio  $R$  of the primary structure (or more generally, designing the primary structure such that the flexural rigidity over mass ratio,  $EI(x)/m(x)$ , reduces faster with height) widens the applicability of the TMDI over the TMD. As an example, note that for shape “IV” in Fig. 4.10(c), the critical  $CR$  value beyond which the TMDI outperforms the TMD are 7.4%, 5.1%, and 2.75% for depth ratios  $R=1$  (uniform),  $R=2$ , and  $R=5$ , respectively.

#### 4.5.2 Influence of depth profile (primary structure shaping) to free-end displacement and acceleration

In this section, the attention is turned to quantifying the influence of the depth profile,  $D(x)$ , of primary structures to the TMDI motion control potential. For this purpose, Figs. 4.11 and 4.12 plot peak steady-state displacement (under resonant harmonic excitation) and RMS free-end displacement (under white noise excitation) of primary structures with different geometric shapes equipped with TMDIs optimally tuned for resonant harmonic and white noise excitations, respectively. Displacement values are normalised by the corresponding displacement of optimally tuned TMD-equipped structures. In each panel of these figures, 17 different primary structures are considered with same TMDI mass and inertance (the upper/middle and bottom rows of panels actually use different  $\beta$  ratios) equal to  $m_{TMDI}=\mu \times m_{Avg}^*$  and  $b=\beta \times m_{Avg}^*$ , respectively, where  $m_{Avg}^*$  is the generalised mass in Eq. (4.6) across the 17 primary structures. The primary DVs of TMDI for resonant harmonic excitation are set as  $\nu=1$  and  $\zeta=5\%$ , while TMDI DVs for white noise excitation are determined numerically by solving Eq.(4.21).

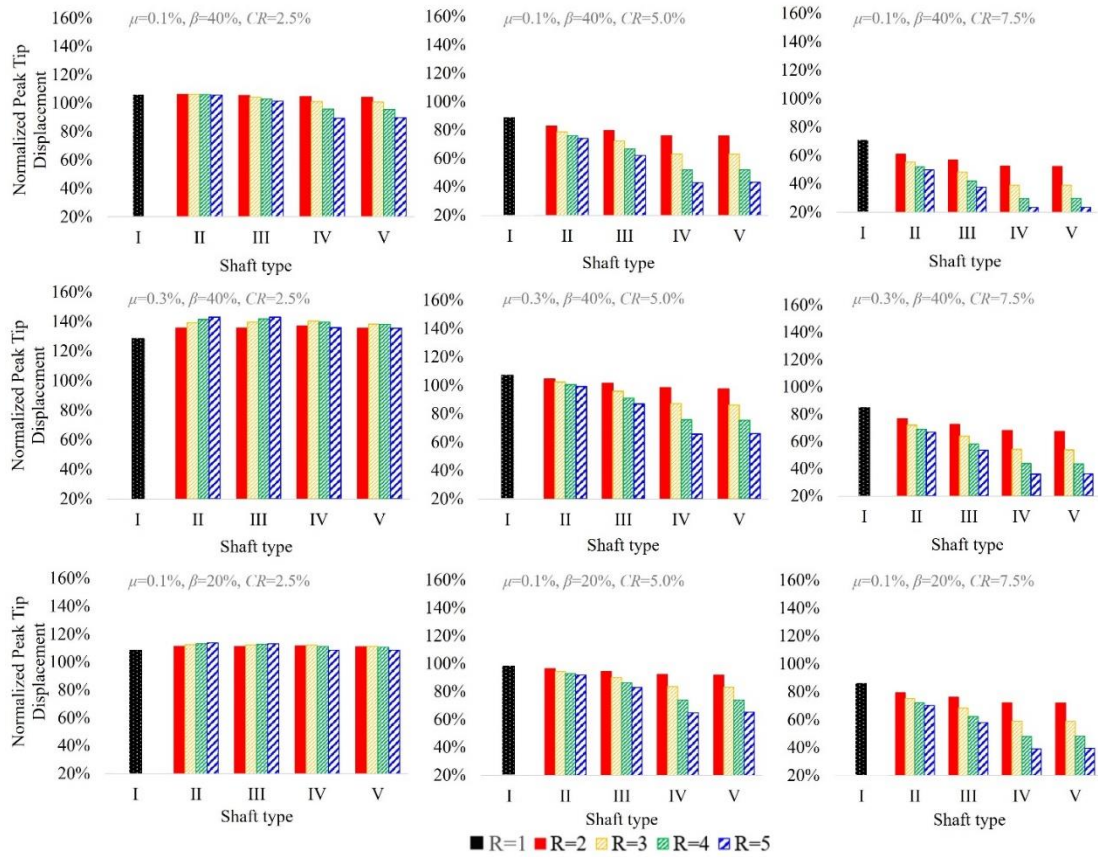


**Fig. 4.11.** Peak free-end displacement of TMDI-equipped structures under resonant harmonic excitation for attached mass  $m_{TMDI}=\mu \times m^*_{Avg}$ , inertance  $b=\beta \times m^*_{Avg}$ , and various interter connectivity ratios,  $CR$ , primary structure shapes, and depth ratios  $R$ . Values are normalised by the corresponding displacement of optimal TMD-equipped structures.

It is seen that, for sufficiently large  $CR$  values (5.0% and 7.5%), the TMDI motion control potential improves over the TMD as the depth profile (shape) of the primary structure changes from type “II” towards type “V” for any fixed  $R$  value and for both harmonic and white noise excitations. With reference to Fig. 4.8(c) and 4.9, this trend suggests that improved TMDI performance is achieved as the average modal curvature or the modal coordinate difference (i.e.,  $\Psi(h)-\Psi(\chi)$ ) of the uncontrolled primary structure increases. This can be achieved by shaping the primary structure such that its flexural rigidity over mass ratio,  $EI(x)/m(x)$ , reduces faster with height (see Fig. 4.7). To elaborate on this point, Fig. 4.13 plots RMS free-end displacement for white noise excited structures of the middle row of panels of Fig. 4.12 versus the average modal curvature of Fig. 4.8(c). It is seen that, for  $CR \geq 5.0$ , the TMDI performance improves linearly with the average modal curvature at a similar rate (slope) for all considered shapes and as  $R$  values increase, which establishes the beneficial effect of the average modal curvature in TMDI-equipped cantilevered structures.

At the same time, it is also evidenced that the improvement of the TMDI motion control effectiveness over the TMD due to a change to the depth profile becomes more substantial for

larger depth ratio  $R$  values. This is readily attributed to the fact that  $R$  influences the value of  $[EI(h)/m(h)]/[EI(0)/m(0)]$  in a direct manner. For example, the improvement of TMDI performance over TMD for harmonic excitation between primary structures with shape “II” and “V” for the case of  $CR= 5.0\%$ ,  $\mu=0.1\%$ , and  $\beta=40\%$  (Fig. 4.11) is only 7.0% (from 17.2% to 24.2%) for  $R=2$  compared to a much higher 24.0% (from 23.8% to 47.8%) for  $R=4$ . Moreover, TMDI performance benefits more significantly by an increase to  $R$  for depth profiles exhibiting faster reduction of the  $EI(x)/m(x)$  ratio with height (i.e., shapes “IV” and “V”). For instance, as  $R$  increases from 2 to 4 TMDI relative performance to TMD improves by only 6.6% (from 17.2% to 23.8%) for shape “II” as opposed to 23.6% (from 24.2% to 47.8%) for shape “V” for the previous TMDI case and harmonic resonant excitation.

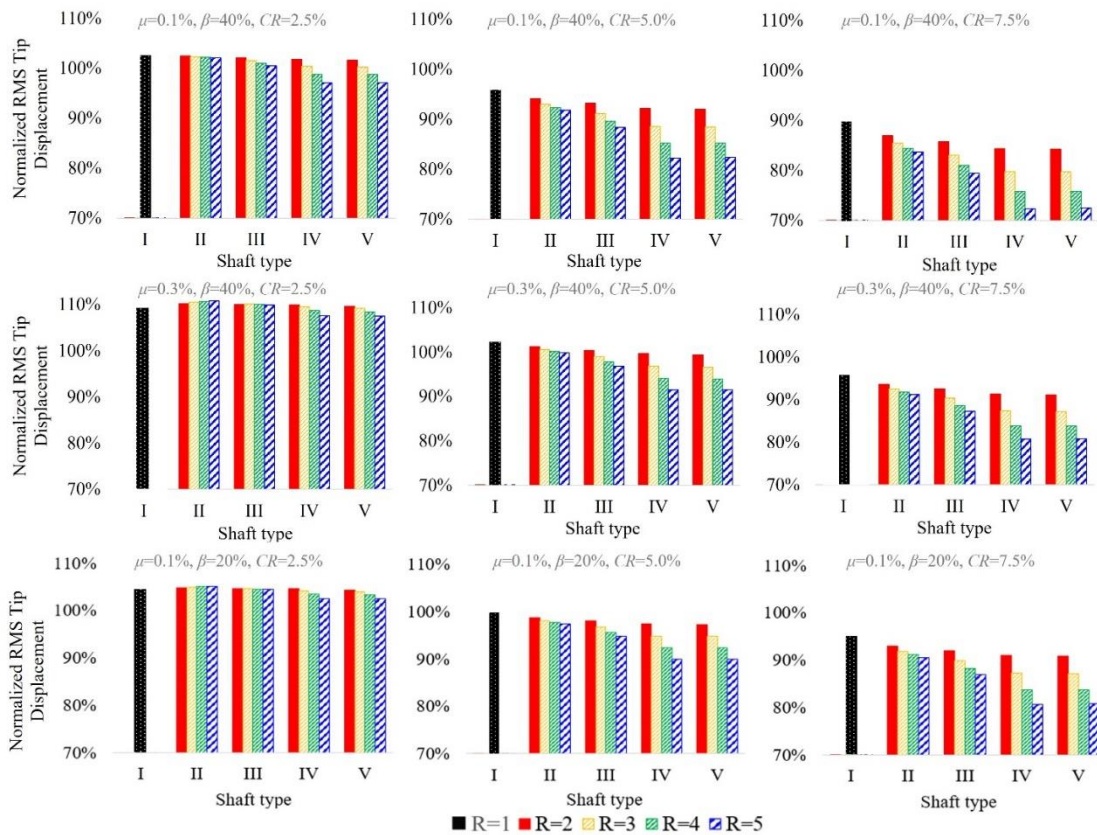


**Fig. 4.12.** RMS free-end displacement of TMDI-equipped structures under white noise excitation for attached mass  $m_{TMDI}=\mu \times m^*_{Avg}$ , inertance  $b=\beta \times m^*_{Avg}$ , and various interter connectivity ratios,  $CR$ , primary structure shapes, and depth ratios  $R$ . Values are normalized by the corresponding displacement of optimal TMD-equipped structures.

Still, for the relatively low  $CR=2.5\%$  value (first column of panels in Figs. 4.11 and 4.12), the TMD outperforms the TMDI except for shapes IV and V with  $R =4$  and 5 and for the combination of large inertance  $\beta=40\%$  and small secondary mass  $\mu=0.1\%$ . With regards to the spectral content of the excitation, a comparison between Figs. 4.11 and 4.12 shows that TMDI is more effective in suppressing primary structure free-end displacement due to harmonic

excitation than white noise excitation compared to the TMD. For example, the TMDI with  $\mu=0.1\%$ ,  $\beta=40\%$ , and  $CR=5.0\%$  achieves a 36.9% improvement in reducing the peak free-end displacement under harmonic excitation (Fig. 4.11) as opposed to a mere 11.5% improvement in reducing the RMS free-end displacement under white noise excitation (Fig. 4.12) for the primary structure shape “V” with  $R=3$ . As a remark, it is noted that for all shapes and depth ratios considered, the relative motion control effectiveness of TMDI over TMD improves significantly by increasing the inertance for both harmonic and white noise excitations, as seen by comparing the upper rows of panels with the bottom rows in Figs. 4.11 and 4.12. On the other hand, this improvement reduces by increasing the attached mass as seen by comparing the upper rows of panels with the middle rows in Figs. 4.11 and 4.12. These trends confirm that, irrespective of the primary structure shape, the TMDI attached mass can be traded off for inertance in order to achieve some prespecified target structural performance as has been exhaustively demonstrated and discussed in the literature (e.g., [Giaralis and Marian 2016](#), [Petriani et al. 2020](#)).

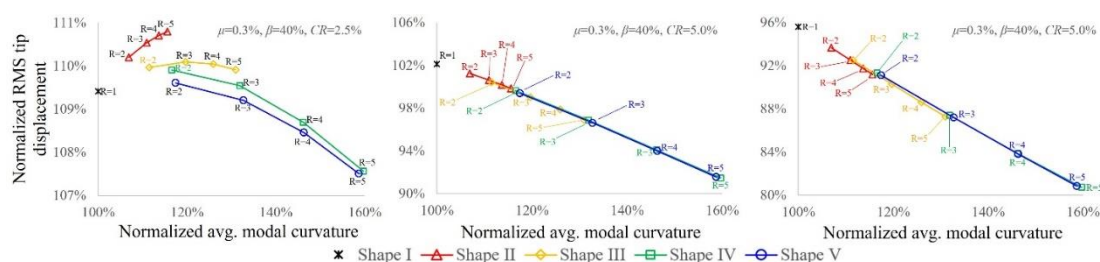


**Fig. 4.13.** RMS free-end displacement of TMDI-equipped structures under white noise excitation as function of normalised average modal curvature (Fig.4.8(c)) for attached mass  $m_{TMDI}=0.3\% \times m_{Avg}^*$ , inertance  $b=0.4 \times m_{Avg}^*$ , and various inerter connectivity ratios,  $CR$ , primary structure shapes, and depth ratios  $R$ . Values are normalized by the corresponding displacement of optimal TMD-equipped structures.

Notably, up to this point, the free-end displacement (not the acceleration) has been chosen and studied as the engineering demand parameter for assessing the structural performance under two worst-case scenario excitations. The reason for this selection is that the simplified 2-DOF model degenerates the primary structure as a SDOF system to the first vibration mode. To this effect, the 2-DOF model is not applicable to acceleration-response assessment under white noise excitation due to higher mode contributions to acceleration response. Still, it is deemed relevant to report the free-end acceleration of the primary structures, equipped with TMDI optimally tuned for minimising the tip displacements subject to white noise excitation. In this regard, Figure 4.14 plots the RMS acceleration of TMDI-equipped primary structures considered in the middle row of Fig. 4.12. Again, acceleration values are normalised by the corresponding value of optimal TMD-equipped structures. It is seen that the trends in Fig. 4.14 trivially follow the same, favourable trends as the free-end displacement evidenced in the



middle row of Fig. 4.12.

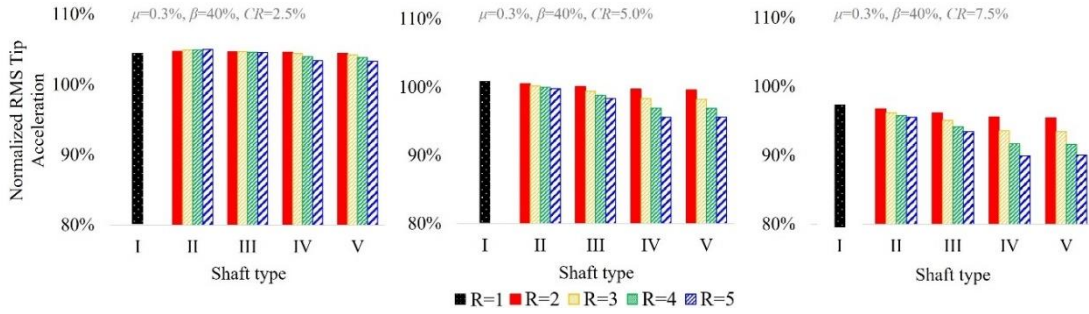


**Fig. 4.14.** RMS free-end acceleration of TMDI-equipped structures under white noise excitation for attached mass  $m_{TMDI}=0.3\% \times m^*_{Avg}$ , inertance  $b=0.4 \times m^*_{Avg}$ , and various interter connectivity ratios,  $CR$ , primary structure shapes, and depth ratios  $R$ . Values are normalised by the corresponding acceleration of optimal TMD-equipped structures. Optimal tuning is for white noise excitation.

### 4.5.3 Influence of primary structure shaping to TMDI stroke and control forces

Having quantified the influence of primary structure shaping to the performance of TMDI-equipped cantilevers in terms of free-end displacement suppression, its influence on the attached mass stroke (relative displacement to the free-end displacement), as well as on the damping and inerter forces, is now investigated. This is because these three quantities are important to the practical design of TMDI-equipped structures. Specifically, TMDI stroke demands relate to the required clearance in housing the attached mass to avoid collisions as well as to the cost of the damping device (see e.g., Ruiz et al. 2018). Further, the magnitude of the damping and the inerter forces relates as well to the cost of the devices and may necessitate special design provisions at the connections of the devices to the primary structure to safely accommodate locally the exerted forces (e.g., Giaralis and Petrini 2017).

The upper row of panels in Fig. 4.15 furnishes bar-plots of RMS stroke values  $\sigma_{stroke}$  in Eq. (4.17) for the same structures as the first row of panels in Figs. 4.11 and 4.12 normalised by the corresponding RMS stroke of optimal TMDs. This data confirms that, irrespective of the primary structure shape, the inclusion of the inerter to the TMD reduces dramatically the attached mass stroke (by more than 90% for all structures considered) as has been reported in several previous studies (e.g., Giaralis and Petrini 2017, Petrini et al., 2020). Nevertheless, it is seen that this relative reduction does not depend significantly on the variation of the primary structure shape due to different depth profile and/or depth ratio. However, the reduction of the RMS stroke with respect to the TMDI stroke for uniform primary structure with  $CR=2.5\%$  depends appreciably on the primary structure shape with more than 40% reduction observed for all the non-uniformly distributed shapes (bottom row of panels in Fig. 4.15), while it is insensitive to  $CR$ . The reduction trends of RMS stroke with respect to the primary structure shape are consistent with the free-end RMS displacement improvement in Figs. 4.11 and 4.12 and, therefore, very well correlated with the average modal curvature and the modal coordinate

difference of the primary structure mode shape in Fig. 4.8(c) and Fig. 4.9, respectively. This observation leads to the practically welcoming conclusion that appropriate primary structure shaping along the same lines discussed in the previous section achieves simultaneous gains both in terms of free-end displacement and TMDI secondary mass stroke.

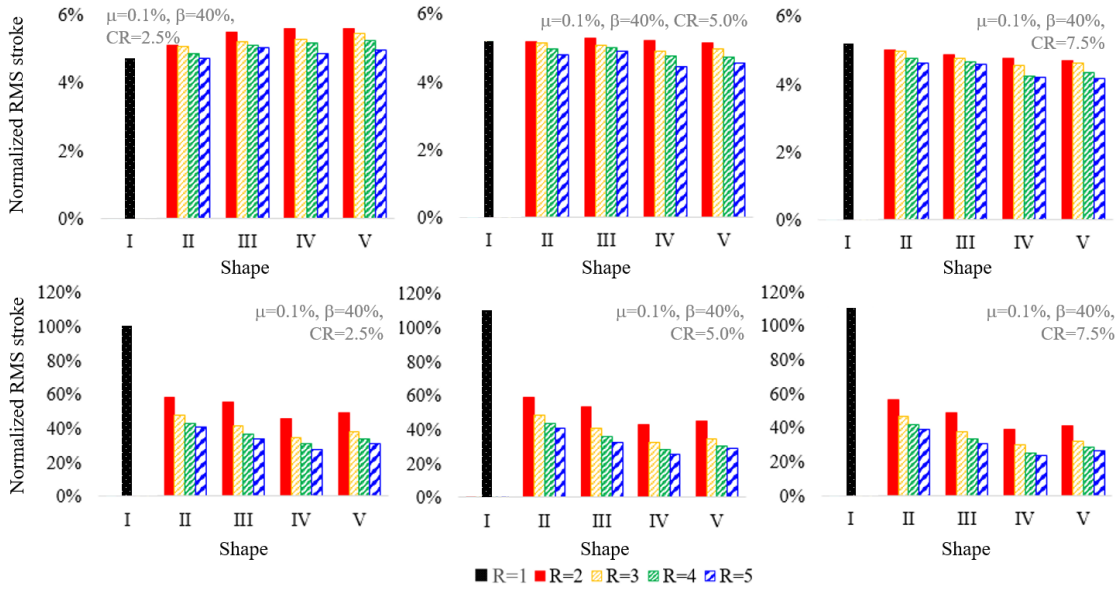


**Fig. 4.15.** RMS TMDI attached mass stroke for TMDI-equipped structures under white noise excitation for attached mass  $m_{\text{TMDI}}=0.1\% \times m_{\text{Avg}}^*$ , inertance  $b=0.4 \times m_{\text{Avg}}^*$ , and various interter connectivity ratios,  $CR$ , primary structure shapes, and depth ratios  $R$ . In the upper row of panels values are normalized by the corresponding stroke of TMD-equipped structures and in the bottom row of panels values are normalized by the stroke of TMDI uniform shaped structure with  $CR=2.5\%$ .

Further, Fig. 4.16 reports the RMS inerter force,  $\sigma_b$  (upper row of panels), and damping force,  $\sigma_c$  (bottom row of panels), in Eq.(4.17) for the same structures in the first row of panels in Figs. 4.11 and 4.12 normalised by the corresponding forces developing in the uniform primary structure for  $CR=2.5\%$ . For all shapes considered, damping forces are seen to increase appreciably with the depth ratio  $R$  for fixed depth profile and  $CR$ , whereas the increase in inerter forces is less significant. In this regard, there is a positive correlation between average modal curvature in Fig. 4.8(c) and developing inerter and damping forces as  $R$  changes for fixed primary structure shape. These trends are further visualised in Fig. 4.17, which plots curves of performance (RMS free-end displacement) versus inerter and damping forces for fixed primary structure shapes and different  $R$  values. It is seen that, for  $CR \geq 5.0\%$ , a positive correlation exists between the depth ratio  $R$  and the control forces (i.e., damping and inerter forces) within an optimal TMDI design setting. More importantly, structural performance improves almost linearly with the control forces as  $R$  increases with higher rate of improvement as the depth profile evolves from “II” towards “V”. From a structural design viewpoint, the significance of the above observed trend is that, in case of leveraging/exchanging  $R$  for improved structural performance, higher control forces are developed and need to be accommodated by the primary

structure.

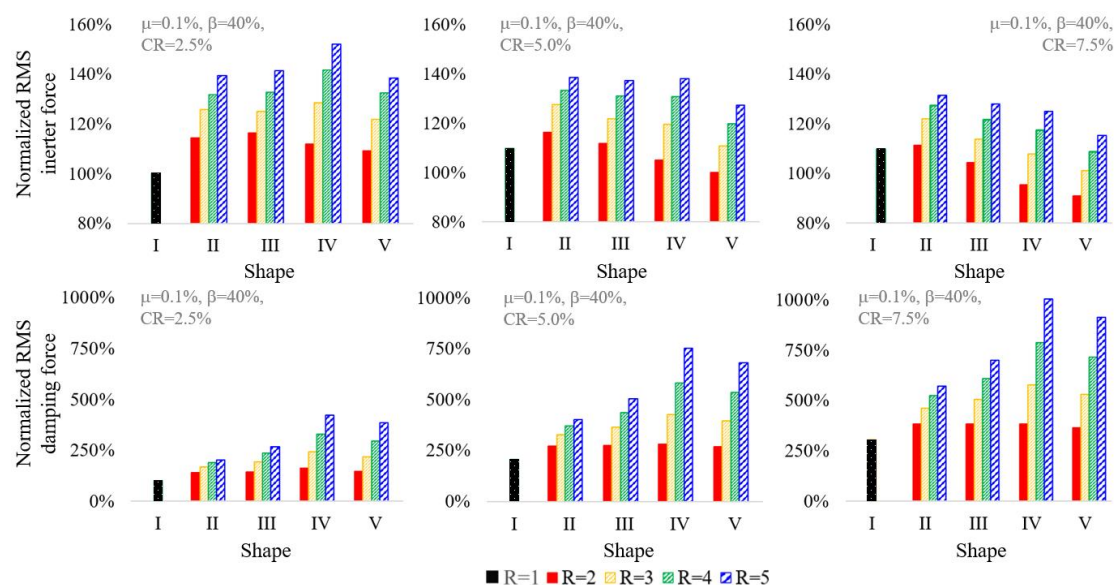


**Fig. 4.16.** RMS inverter resisting force (upper row of panels) and damping force (bottom row of panels) for attached mass,  $m_{TMDI}=0.1\% \times m^*_{Avg}$ , inertance  $b=0.4 \times m^*_{Avg}$ , and various interter connectivity ratios,  $CR$ , primary structure shapes, and depth ratios  $R$  normalized by the corresponding values of optimal TMDI for the uniform primary structure with the interter connectivity ratio,  $CR=2.5\%$ .

Meanwhile, for the cases that TMDI outperforms TMD ( $CR=5\%$  and  $7.5\%$ ), it is seen, in the first row of panels in Fig. 4.16, that the inverter force reduces as the depth profile varies from type “II” to type “V” and fixed  $R$ . This observation suggests that pursuing shaping of the primary structure (to achieve faster  $EI(x)/m(x)$  change with height) through appropriate selection of depth profile rather than increase of the depth ratio may be preferable for improving structural performance in applications where the magnitude of the inverter force is critical in design, as can be seen by examining the first row of panels in Fig. 4.17. At the same time, the magnitude of the damping force is influenced significantly by the depth profile, as evidenced in the second row of panels in Fig. 4.16. However, the damping force reduces slightly when going from shape “VI” and “V” for fixed  $R$ , while the structural performance remains almost the same as seen in Fig. 4.17. Collectively, the above observations and data in Figs. 4.16 and 4.17 suggest that TMDI damping and inverter force demands might be reduced through appropriate shaping of primary structure. This is an important practical consideration since the upfront cost of dampers and inverter devices is well-related to the force they need to be designed for.



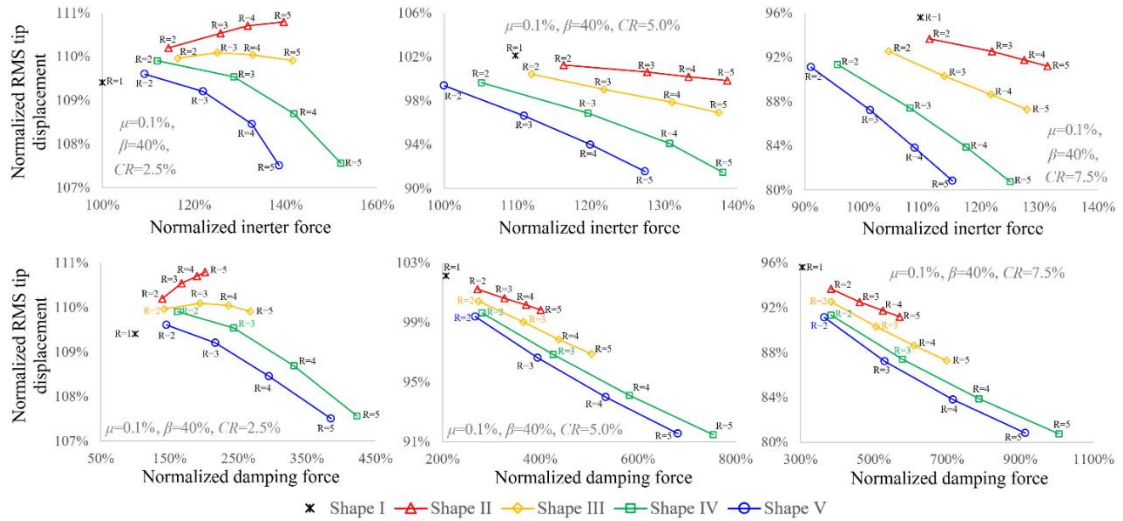


**Fig. 4.17.** RMS free-end displacement versus RMS inerter force (upper row of panels) and damping force (bottom row of panels) for attached mass,  $m_{\text{TMDI}}=0.1\% \times m^*_{\text{Avg}}$ , inertance  $b=0.4 \times m^*_{\text{Avg}}$ , and various inerter connectivity ratios,  $CR$ , primary structure shapes, and depth ratios  $R$ . All quantities are normalized by the corresponding values of optimal TMDI for the uniform primary structure ( $R=1$ ) with  $CR=2.5\%$ .

#### 4.6 Closure

In this chapter, the significance of the geometric shape of primary cantilevered structures to the motion control efficacy of the TMDI under resonant harmonic as well as white noise excitations has been herein established. This was achieved through an innovative parametric study involving a wide range of tapered beam-like primary structures with different continuously varying flexural rigidity,  $EI(x)$ , and mass,  $m(x)$ , properties but same total weight equipped with TMDIs optimally tuned for minimising the free-end displacement under resonant harmonic and white noise excitation. Optimal TMDI tuning and structural performance assessment was expedited through a novel simplified 2-DOF dynamic model in which the primary structure is represented by a generalised SDOF system to accounts for its flexural rigidity and mass distribution as well as its fundamental vibration mode,  $\psi(x)$ , and the location that the inerter connects to the primary structure ( $CR$ ). The accuracy of the simplified model for TMDI tuning and structural performance assessment have been numerically verified using detailed FE models of primary structures. Structural performance of optimal TMDI-equipped primary structures with different shapes was expressed in terms of peak and RMS free-end displacement for harmonic and white noise excitation, respectively. Further, RMS values of TMDI stroke, inerter force and damping force were also presented.

Numerical data demonstrated that TMDI motion control efficiency improves monotonically with increasing inertance and  $CR$  (distance of inerter connection to the primary structure from the free-end) irrespective of the primary structure shape at a reduced rate with best performance always achieved for grounded inerter (i.e.,  $CR=1.0$ ). More importantly, it was found that improved TMDI performance as well as reduced TMDI stroke are achieved for

primary structure shapes in which the ratio  $EI(x)/m(x)$  reduces faster with height (at the cost of increased damping force), rendering the upper part of the primary structure more flexible compared to its base. The beneficial effect of such geometric primary structure shaping was attributed to an increase in the convexity of the fundamental vibration mode of the primary structure (measured through the average along height modal curvature), which creates a larger modal coordinate difference between the two terminals of the TMDI, i.e.,  $\psi(H)-\psi(\chi)$ . This was showcased by demonstrating excellent correlation between structural performance improvement and increase of the average modal curvature. In this respect, the herein reported numerical results establish that shaping the uncontrolled primary structure for faster reduction of  $EI(x)/m(x)$  is beneficial from a performance-oriented structural design viewpoint as it relaxes requirements for attached mass and/or reduces requirements of  $CR$  which allows for the inerter to be connected closer to the free-end of the primary structure. The former is important as it leads to more lightweight vibration absorbers, the latter is important as it extends the applicability of TMDI to structures where connecting the inerter away from the free-end is practically challenging/prohibitive. Furthermore, it was also found that the primary structure shape influences significantly the TMDI inerter and damping control forces exerted to the primary structure and demonstrated that the magnitude of these forces may be contained through judicial shaping of the primary structure without compromising structural performance.

As a closing note, the fact that the TMDI motion control potential is heavily dependent on the primary structure elastic and mass properties and, ultimately, on the global modal shape of the uncontrolled structure suggests that tailored application-dependent structural design may be key for improved performance of TMDI-equipped structures to dynamic excitations, besides optimal TMDI tuning ( $v_{TMDI}$  and  $\zeta_{TMDI}$ ), inertial properties ( $\mu$  and  $\beta$ ), and inerter connectivity ( $CR$ ). In this regard, the numerical data furnished in this chapter motivates locally modifying the lateral stiffness of the primary structure for improved TMDI performance. To this end, in the next chapter, the applicability of TMDI is extended by leveraging judicious local primary structure modification to improve the performance of structures equipped with top-floor TMDIs spanning just one floor ( $p=1$ ).

## Chapter 5

---

### Extending the Use of TMDI to High-Rise Buildings: Soft Top Floor Modification

Note: This Chapter has been published in:

Wang, Z. and Giaralis, A. (2020). “Top-storey softening for enhanced mitigation of vortex shedding induced vibrations in wind-excited optimal tuned mass damper inerter (TMDI)-equipped tall buildings.” *J. Struct. Eng.*, DOI: 10.1061/(ASCE)ST.1943- 541X.0002838.

#### 5.1 Preliminary remarks

Numerical results in Chapter 3 demonstrated the efficacy of optimal top-storey TMDIs with adequate connectivities in mitigating wind-induced vibrations in ultra-tall, landmark building structures for enhanced occupant comfort performance. It was shown that optimally tuned TMDIs achieve appreciably larger peak top-floor acceleration reductions compared to the TMD for the same attached mass as the inertance increases and/or as TMDI connectivity with the inerter spanning more than one storey are considered. The latter consideration is graphically illustrated in Fig. 5.1 (b) and (c), which shows two different TMDI topologies in a  $n$ -storey building with the inerter spanning one (the top) storey ( $p=1$  or “-1” connectivity) and two (the top and the penultimate) storeys ( $p=2$  or “-2” connectivity), respectively. Moreover, Fig. 5.1(e) furnishes indicative numerical data (explained and discussed in detail later in the chapter) demonstrating, phenomenologically, that FRF ordinates of the  $n-2$  floor acceleration reduce for optimally designed TMDIs with connectivity “-2” vis-à-vis “-1” for the same attached mass and inertance (see also [Giaralis and Taflanidis 2015, 2018](#)). On the downside, however, it is also found that the improved floor acceleration performance through increasing inertance and/or inerter-floor connectivity came at the expense of larger inerter and damping forces exerted to the building structure (see also [Giaralis and Petrini 2017](#)). More importantly, whilst TMDI topologies with inerter spanning more than one floor may be economically feasible for landmark structures/skyscrapers with a large number of floors, it does not seem a practically sensible solution for the typical slender mid-to-high-rise buildings with 20-40 storeys. This is because sacrificing high-premium space across several upper floors of such structures for hosting a control device to suppress VS-induced floor accelerations is not cost-efficient.

To this end and in light of the conclusions in chapter 4, the idea of modifying the primary structure properties (i.e., lateral stiffness/flexibility distribution) *locally* to better engage the TMDI for enhanced vibration control and thus avoiding the inerter spanning more than one storey is investigated and pursued in this chapter. Specifically, for routine slender high-rise

buildings, a structural modification, namely top-storey softening, is proposed in conjunction with a top-storey TMDI in “-1” connectivity placement as graphically shown in Fig. 5.1(d) to mitigate crosswind floor accelerations in a cost-effective manner. Note that the case-study structure adopted in this chapter is a typical 34-storey, composite core-frame building that comprises a reinforced concrete (r/c) core coupled with perimeter steel MRFs, as depicted in Fig. 5.1(a). Then, top-storey softening can be readily implemented by discontinuing the r/c core beyond the penultimate floor/slab and, if required, by further reducing the top-storey lateral stiffness. The latter may be accomplished by increasing the top-storey height, as shown in Fig. 5.1(d), among other alternative means such as size reduction of top-storey structural members. From the structural dynamics viewpoint, consideration of top-storey softening is motivated by the fact that reducing the lateral stiffness of the storey equipped with the TMDI has, phenomenologically, similar effects to system FRF as letting the inerter of the TMDI span more floors while keeping in all cases TMDI weight and inertance fixed as evidenced in Fig. 5.1(e). This beneficial effect can be readily attributed to the fact that top-floor softening increases locally the curvature and the modal coordinate difference of the fundamental mode shape of the primary structure between the two TMDI terminals as discussed in Chapter 4.

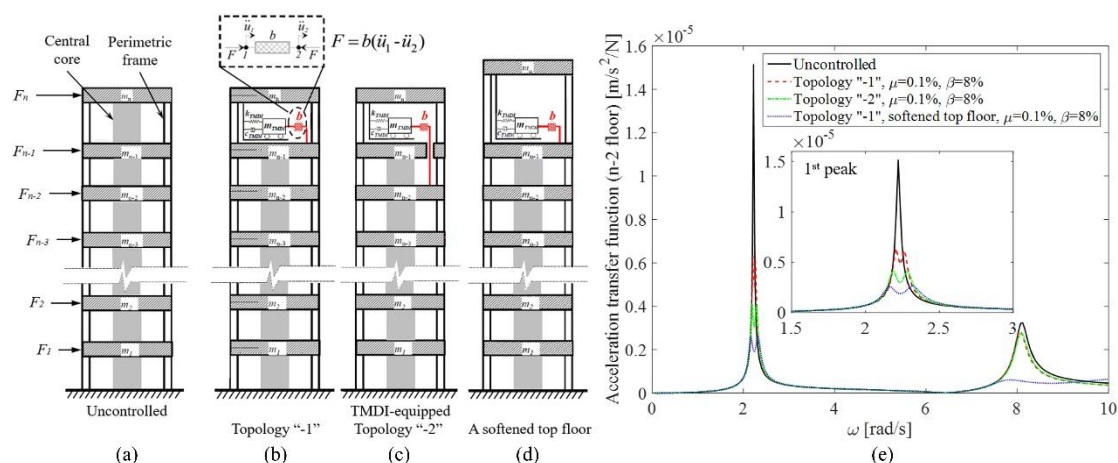


**Fig. 5.1.** (a) Planar graphical representation of a typical coupled core-frame building (primary structure); (b) and (c) Unmodified primary structure with different TMDI topologies; (d) Proposed structural modification with top-storey TMDI, (e) Floor acceleration transfer functions for uncontrolled and TMDI-controlled structures.

## 5.2 Case-study coupled core-frame building and FE modelling

The potential of top-storey softening for mitigating wind-induced vibrations in TMDI-equipped core-frame tall buildings is assessed throughout this work with reference to the 34-storey case-study structure shown in Fig. 5.2(a). The adopted structure is 110.6m tall and has a square 24m-by-24m footprint. The lateral load-resisting structural system is composite consisting of a perimeter steel MRF and a central reinforced concrete (r/c) core. The MRF has 12 equally-spaced columns in total and, therefore, three-bay frames with 8m opening are

formed along each side of the building as shown in Fig. 5.2(b). MRF members, columns and beams, are rigidly connected and have hollow rectangular sections with varying dimensions along the building height reported in Table 5.1. The r/c core has 8m-by-8m plan-view dimensions and comprises of outer and inner shear wall segments as seen in Fig. 5.2(c). The thickness of the outer r/c core walls decreases with building height as detailed in Table 5.1 while one large (door) opening is left within the y-z plane on each side of the core (Fig. 5.2(c)). The inner (stiffening) shear wall segments have uniform thickness with building height (Table 5.1). The MRF and core are coupled at each floor level through primary beams assumed to be hinged at both ends. Therefore, primary beams carry only gravitational loads: they do not participate in resisting lateral loads and do not transfer moments to the MRF and core. Slabs are taken as rigid diaphragms.

**Table 5.1** Member sections geometry of 34-storey composite core-frame case-study building.

floor	storey height [m]	Hollow square column	Hollow rectangular beam sections	r/c core outer wall thickness [mm]	r/c core inner wall thickness [mm]
		sections (a×t) [mm]	(a <sub>1</sub> ×a <sub>2</sub> ×t <sub>1</sub> ×t <sub>2</sub> ) [mm]		
1 <sup>st</sup> (ground)	5.0	700×40	700×400×36×20	400	150
2 <sup>nd</sup> - 7 <sup>th</sup>	3.2	700×40	700×400×36×20	400	150
8 <sup>th</sup> - 14 <sup>th</sup>	3.2	650×36	650×360×32×20	350	150
15 <sup>th</sup> - 21 <sup>st</sup>	3.2	600×32	600×320×28×20	300	150
22 <sup>nd</sup> -28 <sup>th</sup>	3.2	550×28	550×280×24×20	250	150
29 <sup>th</sup> - 34 <sup>th</sup>	3.2	500×24	500×240×20×20	200	150

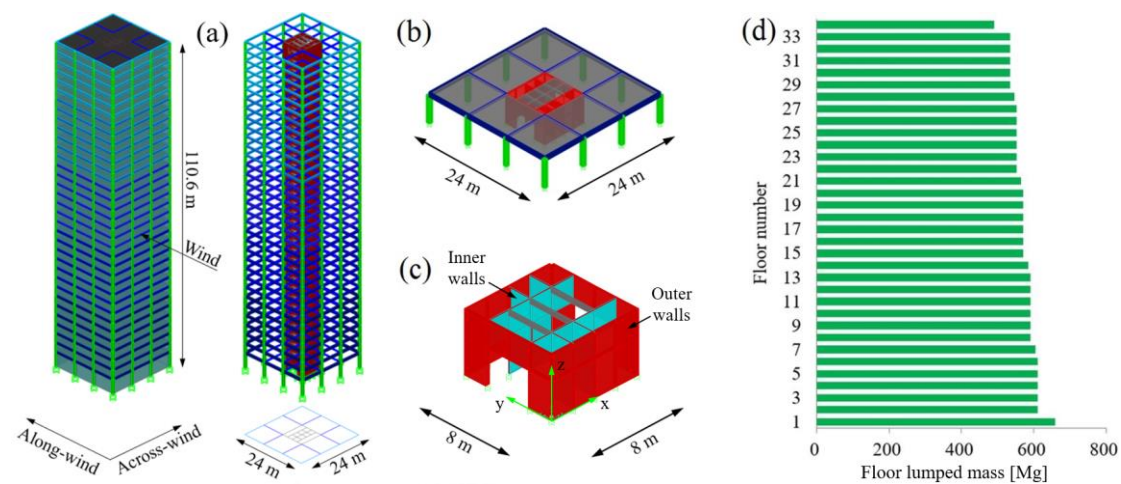


**Fig. 5.2.** (a) Case-study 34-storey building; (b) typical floor and core-frame lateral load-resisting system; (c) geometry of r/c core; (d) floor mass distribution.

A linear FE model of the building is developed in SAP2000® software package. The FE model comprises 552 membrane and 1564 shell elements, representing the slabs and r/c shear walls, respectively, as well as 1292 Euler-Bernoulli one-dimensional beam elements with rigid or hinged connections as appropriate. Horizontal perfectly rigid diaphragm constraints are imposed at the height of each floor. The total mass of the structure accounting for dead and live loads is 92830 Mg and is lumped at each floor level following the distribution shown in Fig. 5.2(d).

Due to the presence of the two large door openings in the r/c core shown in Fig. 5.2(c), the lateral-load resisting system of the case-study building is not doubly-symmetric in plan. It is found that for the particular wind excitation model adopted in all the ensuing numerical work and discussed later in the chapter, the critical (along-) wind field direction is along the y principal building axis inducing maximum lateral floor accelerations along the x principal building axis. Hence, only the in-plane translational vibration motion of the FE model along the x principal axis is required for studying structural performance for occupants' comfort serviceability limit state associated with floor response acceleration in the crosswind direction. To this end, in the next section, a low-order linear planar dynamical model is developed capturing faithfully in-plane structural response to dynamic excitation along x axis of the case-study building in Fig. 5.2.

### 5.3 Low-order planar model of uncoupled case-study structure and wind force excitation

To expedite computational work in later sections, herein, a low-order lumped-mass planar dynamic model with 34 DOFs corresponding to the uncoupled lateral in-plane translations of rigid slabs along the x axis of the case-study building in Fig. 5.2 is derived from the previously discussed detailed FE model. The reasons for using such a relatively large number of DOFs in the low-order model (i.e., one DOF per floor) is to capture accurately the effect of local changes, such as top-storey softening, to the global structural response of the building in support of optimal design and assessment of TMDI-equipped case-study structure as well as to facilitate a fine spatial discretisation of the wind loading. The 34-DOF model is defined in terms of a diagonal mass matrix,  $\mathbf{M}_s \in \mathbb{R}^{34 \times 34}$ , and full damping and stiffness matrices,  $\mathbf{C}_s \in \mathbb{R}^{34 \times 34}$  and  $\mathbf{K}_s \in \mathbb{R}^{34 \times 34}$ , respectively. Main diagonal of the  $\mathbf{M}_s$  matrix is populated with the lumped floor masses in Fig. 5.2(d) while  $\mathbf{K}_s$  and  $\mathbf{C}_s$  matrices are obtained as detailed in the following two sub-sections.

#### 5.3.1 Stiffness matrix derivation and verification based on modal properties

The lateral stiffness of the case-study building in Fig. 5.2 along principal axis x is primarily contributed by two planar perimeter three-bay rigid-jointed MRFs and by the r/c core acting along its “weak” axis due to the two openings (i.e., the contribution of the two out-of-plane MRFs is neglected). The MRFs and the core undergo the same lateral displacement at each floor being coupled through rigid diaphragms. In this setting, the coupled core-frame system is



modelled as a sum of two contributing cantilevered beam-like structural systems: one corresponding to the r/c core and one to the two same steel MRFs (e.g., [Dym and Williams 2007](#), [Cluni et al. 2013](#)). The r/c core contribution is represented by a  $\mathbf{K}_{core} \in \mathbb{R}^{34 \times 34}$  stiffness matrix derived from application of static condensation to a flexural Timoshenko beam as seen in Fig. 5.3(a). Further, each perimeteric MRF is represented by a  $\mathbf{K}_{frame} \in \mathbb{R}^{34 \times 34}$  stiffness matrix of an equivalent beam-like structure derived through static condensation as shown in Fig. 5.3(b). The stiffness matrix of the 34-DOF low-order model can thus be determined as

$$\mathbf{K}_s = \mathbf{K}_{core} + 2\mathbf{K}_{frame}, \quad (5.1)$$

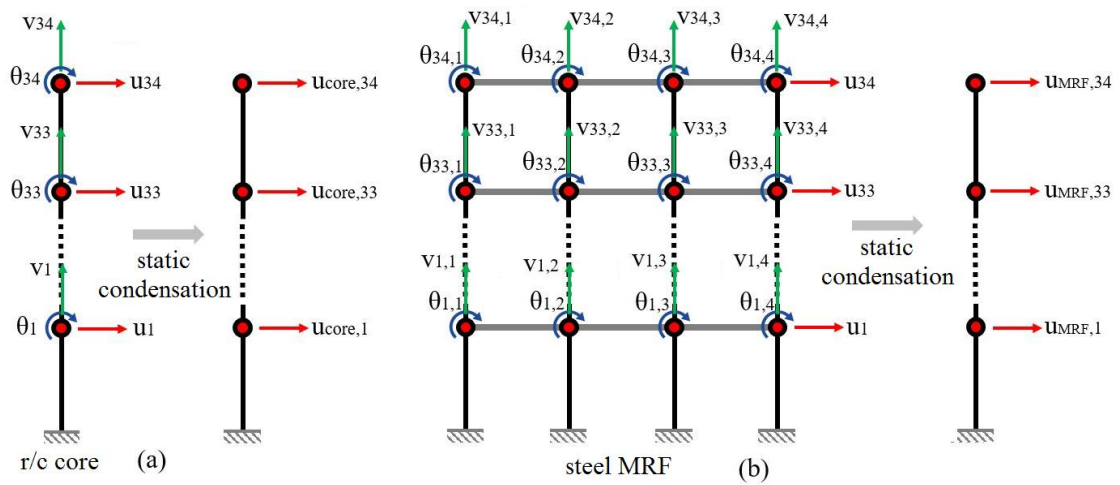


**Fig. 5.3.** Static condensation for stiffness matrix derivation of the low-order model: (a) for the central core; (b) for the perimeteric frame.

The properties of the uncondensed Timoshenko beam in Fig. 5.3(a) corresponding to the r/c core component are evaluated storey-wise. Effective shear area, cross-sectional area, and second moment of area of the core is determined by accounting for all inner and outer walls along the x principal building axis considering also properties reductions due to door openings. Moreover, the uncondensed stiffness matrix of the 3-bay 34-storey MRF in Fig. 5.3(b) is determined based on standard FE discretisation with Euler-Bernoulli beam elements using columns and beam member sections in Table 5.1. Importantly, the above approach for  $\mathbf{K}_s$  matrix specification allows for modifications to be made independently in any of the two contributing components to the lateral load resisting system (i.e., the MRFs and the r/c core), which facilitates pertinent parametric investigations to be undertaken to explore the performance of TMDI-equipped benchmark structure for different host structure configurations in the numerical part of this work.

The accuracy of the developed 34-DOF low-order model to capture accurately dynamic modal properties of the detailed FE model of the case-study building even for large local stiffness variations, as will be required in implementing top-storey softening in later sections,



is herein verified in terms of natural frequencies and mode shapes for two different r/c core configurations. In the first configuration (baseline uncontrolled structure) the core runs up to the roof (34<sup>th</sup> floor). In the second configuration, the core stops at the penultimate storey (33<sup>rd</sup> floor), thus creating a coreless (flexible) top-storey. The latter configuration is readily implemented in the developed coupled two-beam stiffness matrix derivation approach by setting cross-sectional area and the second moment of area properties of the last segment of the Timoshenko beam in Fig. 5.3(a) to zero. For both configurations, standard modal analysis is applied to the detailed FE model (Fig. 5.2) and to the low-order model to extract modal properties corresponding to the translational vibration modes along the x principal axis.

Table 5.2 reports differences of the lowest three vibration modes obtained from the FE model and the low-order model in terms of natural frequencies and mode shapes. Mode shape difference is quantified through the modal assurance criterion ( $MAC_j$ ) for the  $j$ -th mode which is a scalar measure of mode shape similarity defined as (Brincker and Ventura 2015)

$$MAC_j = \left( \frac{\boldsymbol{\Phi}_{j\ low\_order}^T \boldsymbol{\Phi}_{j\ FEM}}{\|\boldsymbol{\Phi}_{j\ low\_order}\| \|\boldsymbol{\Phi}_{j\ FEM}\|} \right)^2, \quad (5.2)$$

where  $\boldsymbol{\Phi}_{j\ low\_order}$  and  $\boldsymbol{\Phi}_{j\ FEM}$  are the  $j$ -th mode shape vectors obtained by the low-order and the detailed FE model, respectively, the superscript “ $T$ ” denotes matrix transposition and  $\|\mathbf{p}\|$  is the length of vector  $\mathbf{p}$ . Clearly,  $MAC_j$  value equal to unity means that  $\boldsymbol{\Phi}_{j\ low\_order}$  and  $\boldsymbol{\Phi}_{j\ FEM}$  mode shape vectors are identical. It is seen in Table 5.2 that, for both configurations, natural frequencies estimated by the low-order model are slightly lower than those computed from the FE model. This is because the contribution of the two out-of-plane MRFs are neglected in the lower-order model. Still, percentage error difference in natural frequencies is below 2% across the board, while  $MAC$  values indicate perfect agreement between mode shapes obtained by the two different models. This is further verified visually in Fig. 5.4, which plots the lowest three modes of the two building configurations obtained by the two computational models.

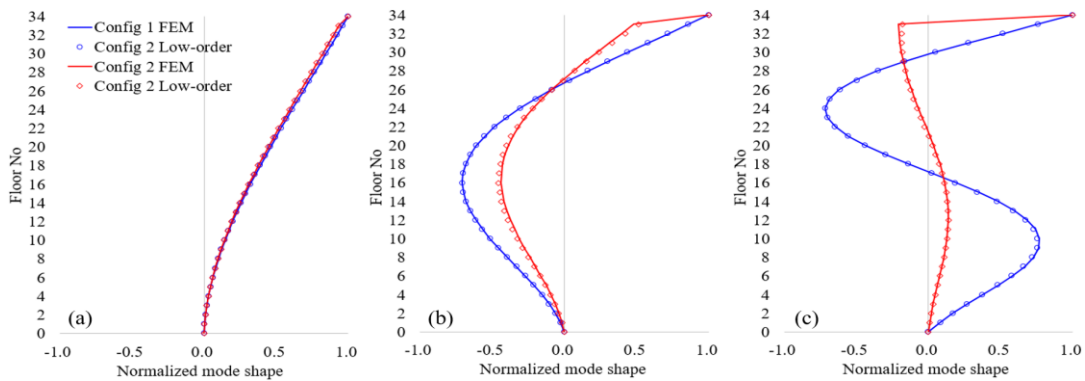


**Fig. 5.4.** Lowest three lateral mode shapes for the two different case-study building r/c core configurations of Table 5.2 obtained by the detailed FE and low-order model: (a) 1<sup>st</sup> mode; (b) 2<sup>nd</sup> mode; and (c) 3<sup>rd</sup> mode.

**Table 5.2** Comparison of modal properties of the lowest 3 translational vibration modes along principal axis y of the case-study building between the detailed FE model and the low-order model.

Core configuration	Mode	Frequency [Hz]			MAC	Mass participation factor
		FEM	Low-order	Error		
Core runs up to 34 <sup>th</sup> floor (baseline uncontrolled structure)	1 <sup>st</sup>	0.3409	0.3344	1.91%	1.000000	63.18%
	2 <sup>nd</sup>	1.3745	1.3537	1.51%	0.999994	18.77%
	3 <sup>rd</sup>	3.2010	3.1651	1.12%	0.999858	7.51%
Core runs up to 33 <sup>rd</sup> floor (coreless top-storey structure)	1 <sup>st</sup>	0.3398	0.3336	1.83%	0.999998	63.19%
	2 <sup>nd</sup>	1.3300	1.3140	1.20%	0.999542	18.82%
	3 <sup>rd</sup>	2.0979	2.0801	0.85%	0.998782	7.27%

Overall, matching quality of modal properties quantified in Table 5.2 and Fig. 5.4 verify that the herein derived 34-DOF low-order model is dynamically equivalent to the detailed FE model along the x principal direction and will be used henceforth to expedite numerical work.

### 5.3.2 Inherent damping modelling

The inherent structural damping of the case-study building is incorporated in the low-order model through a full damping matrix obtained by the expression (e.g., [Chopra 2000](#))

$$\mathbf{C}_s = (\mathbf{\Phi}^T)^{-1} \mathbf{C}_{\text{mod}} (\mathbf{\Phi})^{-1}, \quad (5.3)$$

where  $\mathbf{\Phi} \in \mathbb{R}^{34 \times 34}$  is the modal matrix collecting all  $\boldsymbol{\phi}_j$  low\_order,  $j=1,2,\dots,34$  mode shapes, the superscript “-1” denotes matrix inversion, and  $\mathbf{C}_{\text{mod}} \in \mathbb{R}^{34 \times 34}$  is a diagonal matrix defined as

$$\mathbf{C}_{\text{mod}} [j, j] = 2\omega_{n(j)} \xi_j \left( \boldsymbol{\phi}_{j \text{ low\_order}}^T \mathbf{M}_s \boldsymbol{\phi}_{j \text{ low\_order}} \right); j = 1, 2, \dots, 34 \quad (5.4)$$

In the last equation,  $\omega_{n(j)}$  and  $\xi_j$  are the  $j$ -th natural circular frequency and modal damping ratio, respectively, of the 34-DOF low-order model. In all the ensuing numerical work, unless otherwise specified, the modal damping ratio of the first mode,  $\xi_1$ , which dominates the crosswind response of the case-study building, is taken equal to 0.55%. This modal damping ratio value was estimated from field measurements for a similar to the herein considered case-study structure 120m-tall composite building with square floorplan studied in [Fang et al. \(1997\)](#). For higher vibration modes, gradually increasing modal damping ratios are assumed as follows  $\xi_j = 1\%$  for  $j = 2, 3, 4$ ;  $\xi_j = 2\%$  for  $j = 5, 6, 7$ ;  $\xi_j = 4\%$  for  $j = 8, 9, 10$ ;  $\xi_j = 8\%$  for  $j = 11, \dots, 20$ ; and  $\xi_j$

= 16% for  $j = 21, \dots, 34$ , following trends of frequency-dependent damping models for tall buildings proposed in the literature (see e.g., [Spence and Kareem 2014](#) and references therein).

### 5.3.3 Wind excitation model

Wind action to the low-order 34-DOF planar model derived in the previous section is represented by the stochastic crosswind force model developed by [Liang et al. \(2002\)](#) for tall buildings with rectangular footprint. Upon spatial discretisation of the wind force random field at each floor slab of the case-study 34-storey building, a PSD  $\mathbf{S}_{FF}^{34} \in \mathbb{R}^{34 \times 34}$  wind force matrix is specified. For the case-study building with total height 110.6m and square footprint the diagonal elements of the PSD wind force matrix, are given as ([Liang et al. 2002](#))

$$\mathbf{S}_{FF}^{34} [k, k] = \frac{\sigma_k^2}{\omega} \left[ \frac{0.1143(\omega/\omega_k)^2}{\left(1 - (\omega/\omega_k)^2\right)^2 + 0.041(\omega/\omega_k)^2} + \frac{0.1633(\omega/\omega_k)^3}{\left(1 - (\omega/\omega_k)^2\right)^2 + 2(\omega/\omega_k)^2} \right]; k = 1, 2, \dots, 34 \quad (5.5)$$

which specify the PSD of the wind force acting at the  $k$ -th floor slab located at height  $z_k$  from the ground. In the last expression,  $\sigma_k$  is the RMS of the crosswind force at the  $k$ -th floor slab and  $\omega_k$  is the frequency of VS at  $z_k$  height. The RMS of the crosswind force  $\sigma_k$  is computed by Eq. (5.5) by assuming the air mass density  $\rho = 1.25 \text{ kg/m}^3$ , the mean RMS lift coefficient  $\bar{C}_L = 0.404$  for square footprint buildings according to [Liang et al. \(2002\)](#), and the building breadth in the crosswind direction  $B = 24 \text{ m}$ . The tributary height of the  $k$ -th floor,  $\Delta z_k$  is still taken as half the storey height above floor  $k$  plus half the storey height below floor  $k$ . The mean wind velocity at  $z_k$  height,  $V_m(z)$ , is determined by Eurocode 1 ([EN 1991-1-4: 2005](#))

$$V_m(z) = c_r(z) c_o(z) V_b, \quad (5.6)$$

where  $V_b$  is the basic wind velocity (i.e., the 10 minute mean wind velocity at 10m above open flat country terrain) taken equal to 22 m/s throughout this work,  $c_o(z)$  is the orography factor assumed equal to 1.0, and  $c_r(z)$  is the roughness factor based on the Eurocode-compliant logarithmic law and terrain category IV ( i.e., area in which at least 15% of the surface is covered with buildings and their average height exceeds 15 m). Further, the VS frequency  $\omega_k$  is determined by Eq. (3.10) by assuming the Strouhal number  $S_t = 0.084$  as experimentally determined by [Liang et al. \(2002\)](#) for square footprint tall buildings.

For illustration, the PSDs of wind force acting at four different floor slab heights are plotted in Fig. 5.5 for  $V_b = 22 \text{ m/s}$ . It is seen that the dominant VS frequency increases with floor height as can be inferred by Eqs. (3.10) and (5.6). The same happens for the wind force

amplitude except from the last floor whose tributary height is different from the rest of the building floors, i.e., 1.6 m as opposed to 3.2 m applicable for the typical floor.

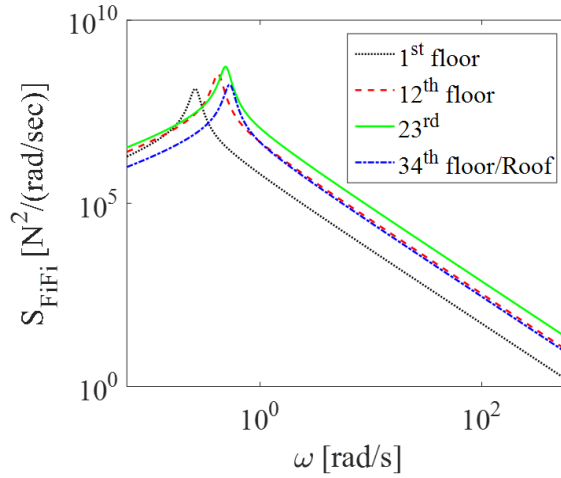


**Fig. 5.5.** Power spectral density functions of crosswind forces acting at different floor levels of the case-study building.

The off-diagonal terms of the  $\mathbf{S}_{FF}^{34}$  PSD matrix modelling the spatial correlation of wind forces acting at floor slabs  $k$  and  $l$  are given as (Liang et al., 2002)

$$\mathbf{S}_{FF}^{34} [k, l] = \exp \left[ - \left( \frac{z_k - z_l}{5.56B} \right)^2 \right] \sqrt{S_k(\omega) S_l(\omega)}, \quad (5.7)$$

for the case-study building, where  $B$  is the building breadth in the crosswind direction.

#### 5.4 Optimal TMDI design for serviceability performance accounting for top-storey stiffness reduction

To investigate the potential of top-storey softening for enhanced serviceability performance in TMDI-equipped wind-excited tall buildings subject to VS effects, it is essential to optimally tune the TMDI to minimise peak floor accelerations for pre-specified wind excitation and building structure properties. To this aim, the optimal TMDI tuning problem formulated in Section 3.2.1 is now adapted to include the top-storey height,  $H_{top}$ , as a secondary design parameter replacing the TMDI connectivity number  $p$ , as the inerter connectivity number of the proposed vibration control strategy is fixed to 1. As a remark, the increase of top-storey height (as an efficient means of increasing its lateral flexibility) was taken into account explicitly when evaluating the wind excitation model. In this way, a fair and meaningful comparison can be made between the original building structure and the locally modified one with a softened top floor. In this setting, the vector  $\mathbf{x}_2$  (see Section 3.2.1) collecting the secondary design parameters changes to  $\mathbf{x}_2 = [\mu, \beta, H_{top}]^T$ , while the numerical solution

strategy for obtaining the optimal tuning parameters,  $v_{opt}$  and  $\zeta_{opt}$ , for pre-specified TMDI inertial properties and top-storey height remains unchanged (see Section 3.3.2). For the adopted case-study building, the OF is evaluated by Eq.(B.5) on the 32<sup>nd</sup>/highest occupied floor by setting  $k=32$ , i.e.,  $OF = \text{peak}\{\ddot{x}_{32}\}$ . The adapted optimal TMDI problem is applied to the case-study structure in which top-storey stiffness is explicitly accounted for in the design.

Purposely, the above optimal design formulation allows for considering explicitly any desired combination of TMDI inertial properties (i.e., attached mass and inertance), and utilises a single geometric property, top-storey height, to leverage the level of top-storey softening or, equivalently, of top-storey lateral stiffness reduction in a straightforward manner. In an actual application, top-storey stiffness reduction may be implemented by one, or a combination of, several other local (top-storey) structural modifications apart from discontinuing the r/c core. These may include the reduction of flexural rigidity of beams and/or columns of the MRF and the increase of top-storey height. More importantly, the reason of including a host/building structure parameter to TMDI design is because the lateral stiffness of the top-storey (where the TMDI is installed) influences heavily TMDI (though not TMD) optimal primary design parameters as will be seen in view of numerical results.

#### 5.4.1 Convexity and nature of achieved optimality

The OP in Eq. (3.3) with the OF changed to  $\text{peak}\{\ddot{x}_{32}\}$  and  $\mathbf{x}_2$  to  $[\mu, \beta, H_{top}]^T$  is numerically solved for the case-study structure using the numerical solution strategy detailed in Section 3.2.2. A wide *initial* search range delimited by  $\mathbf{x}_1^{\min} = [0.0, 0.0]^T$  and  $\mathbf{x}_1^{\max} = [2.0, 2.0]^T$  is adopted since it is found that optimal TMDI tuning parameters move away from the commonly encountered values for building structures with smooth stiffness variation in elevation as top-storey stiffness reduces (e.g., optimal frequency ratios  $v_{TMDI}$  are much higher than unity corresponding to tuning to the first mode of the uncontrolled structure as seen later in Fig. 5.7). To expedite computations in solving Eq. (3.3), the custom-developed algorithm (see Section 3.2.2) applies the pattern search (see Charles and Dennis 2003) iteratively with progressively narrower search range in  $\mathbf{x}_1$  by “zooming-in” the neighbourhood of the optimal  $v_{TMDI}$  and  $\zeta_{TMDI}$  values found in the previous iteration. The stoppage criterion for the iterations checks the absolute difference between two successive optimal OF values against a pre-specified convergence tolerance.

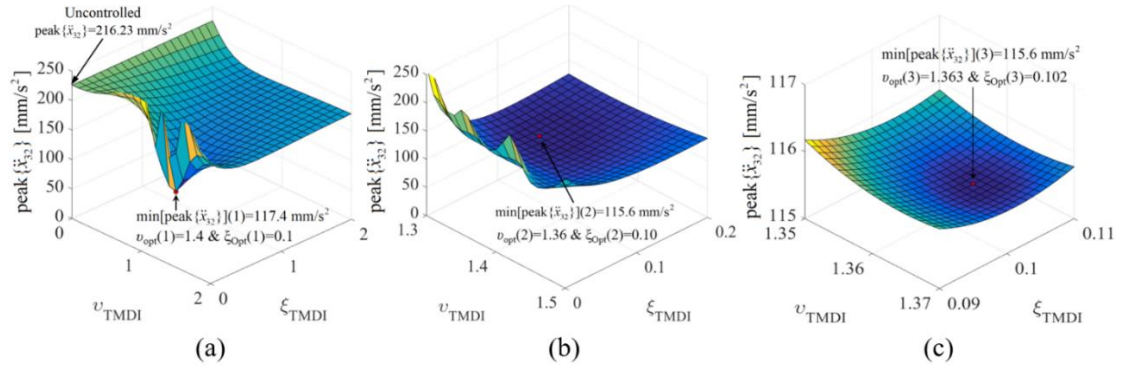


**Fig. 5.6.** Iterative optimal TMDI design with  $\mu=0.1\%$  and  $\beta=8\%$  for the adopted case-study structure with  $H_{top}=5\text{m}$  and discontinued r/c core (a) 1<sup>st</sup> iteration; (b) 2<sup>nd</sup> iteration; and (c) 3<sup>rd</sup> iteration.

For numerical illustration, Fig. 5.6 plots OF surfaces on the primary DV plane ( $v_{TMDI}$ ,  $\zeta_{TMDI}$ ) obtained from the iterative pattern search-based algorithm for the case-study structure with coreless top-storey for  $\mathbf{x}_2 = [\mu=0.1\%, \beta=8\%, H_{top}=5\text{m}]^T$  and for the wind excitation PSD  $\mathbf{S}_{FF}^{34}$ . The global minimum point  $(v_{opt}(p), \zeta_{opt}(p), peak\{\ddot{x}_{32}\}(p))$  for the  $p$ -th iteration is further reported in Fig. 5.6. The convergence tolerance is set to 1%. For this case, convergence is reached after three iterations in which the initial search range narrows down to  $\mathbf{x}_1^{\min} = [1.3, 0.0]^T$  and  $\mathbf{x}_1^{\max} = [1.5, 0.2]^T$  in the second iteration, and ultimately to  $\mathbf{x}_1^{\min} = [1.35, 0.09]^T$  and  $\mathbf{x}_1^{\max} = [1.37, 0.11]^T$  in the final iteration, with same discretisation density of the search domain and with logarithmic increase of precision/resolution by which optimal parameters are determined.

To shed light on the nature of optimality achieved through solving Eq. (3.3) for buildings with flexible top-storey, Fig. 5.1(e) plots the 32<sup>nd</sup> floor acceleration FRF of the optimal TMDI-equipped example structure treated in Fig. 5.6 (softened top-storey case) together with the FRFs for optimal TMDI-equipped structure with coreless top-storey modification (connectivity “-1” case) and for uncontrolled/unmodified structure. It is seen that the considered optimal TMDI design formulation yields a classical “Den Hartog” style of optimality (Den Hartog 1956): both FRFs of optimal TMDI-controlled structures show two local resonant peaks of almost equal height one to the left and one to the right of the fundamental natural frequency of the uncontrolled structure  $\omega_{n(1)}$ . Evidently, this type of optimality is maintained under the herein considered building modification (i.e., top-storey softening) since the latter does not change significantly  $\omega_{n(1)}$  (see Table 5.2). Notably, it is known that Den Hartog optimality is mostly efficient for suppressing narrow-band excitations characterised by a dominant frequency and, therefore, relevant to addressing VS effects (see Fig. 5.5). Moreover, the higher-natural-frequency (i.e., wideband) damping effect of TMDI, which is well-reported in the literature (Giaralis and Taflanidis 2015, 2018), becomes more prominent with top-storey softening Fig. 5.1(e): the second resonant peak in the FRF of the uncontrolled structure is slightly reduced in the FRF of TMDI-equipped unmodified structure, while it is practically non-visible in the FRF of the TMDI-equipped structure with top-storey softening.

### 5.4.2 Sensitivity of optimal primary design parameters to top-storey stiffness

The influence of top-storey stiffness to the optimal TMDI parameters in  $\mathbf{x}_1$  determined through solving Eq. (3.3) is parametrically investigated in Fig. 5.7 considering the cases of TMDI with  $\mu=0.1\%$ ,  $\beta=6\%$  and structures with coreless top-storey and with different top-storey heights  $H_{top} = 4\text{m}, 5\text{m}, \text{and } 6\text{m}$ . All panels of Fig. 5.7 plot the peak  $\{\ddot{x}_{32}\}$  of TMDI-controlled structures normalized by peak  $\{\ddot{x}_{32}\}$  of the uncontrolled and unmodified case-study building versus the frequency ratio  $\nu_{TMDI}$  and/or the damping ratio  $\zeta_{TMDI}$ . It is seen that, as top-storey stiffness reduces (i.e., top-storey height increases), optimal  $\nu_{TMDI}$  and  $\zeta_{TMDI}$  values increase appreciably. The fact that  $\zeta_{opt}$  increases with top-storey softening for fixed TMDI inertial properties (i.e., secondary mass and inertance) is quite welcoming as it has been shown to be well-associated with improved TMDI motion control capacity for seismically excited multi-storey buildings (Ruiz et al. 2018, Taflanidis et al. 2019). This trend is herein confirmed as the minimum achieved peak  $\{\ddot{x}_{32}\}$  value attained at the optimal TMDI design point reduces considerably as  $\zeta_{opt}$  increases driven by higher top-storey building height (last row of panels in Fig. 5.7).

From a structural dynamics viewpoint, it appears that TMDI stiffness is key to the improved TMDI motion control potential as top-storey becomes more flexible. Indeed,  $\nu_{opt}$  increases significantly with top-storey height (e.g., TMDI frequency becomes 60% higher from the first natural frequency of the uncontrolled structure  $\omega_{n(1)}$  for the case of  $H_{top} = 6\text{m}$ ) demonstrating that TMDI resonates with local top-storey dynamics associated with higher frequencies as the top-storey stiffness reduces (see e.g., mode shapes of uncontrolled case-study building structure with coreless top-storey in Fig. 5.4). Notably, such large  $\nu_{opt}$  values are not observed in optimal TMDI designs for regular in elevation structures in which  $\nu_{opt}$  ranges typically within  $[0.8 \text{ } 1.0]$  interval (Ruiz et al. 2018) even in the case of TMDI topologies with inerters spanning more than one storey (e.g., connectivity “-2” in Fig. 5.1). Even more important, from a practical viewpoint, is to observe in Fig. 5.7 that the optimal TMDI design/tuning becomes significantly less sensitive to the optimal TMDI parameters in  $\mathbf{x}_1$  as the top-storey becomes more flexible: perturbations to  $\nu_{opt}$  and/or  $\zeta_{opt}$  values have less impact to the achieved peak  $\{\ddot{x}_{32}\}$  performance as top-storey height increases. Therefore, top-storey softening increases TMDI robustness to design parameters and, ultimately, to uncertain or inaccurate knowledge of the fundamental natural frequency of the uncontrolled structure as well as to detuning effects which are major concerns in passive TMD applications (Elias and Matsagar 2018).



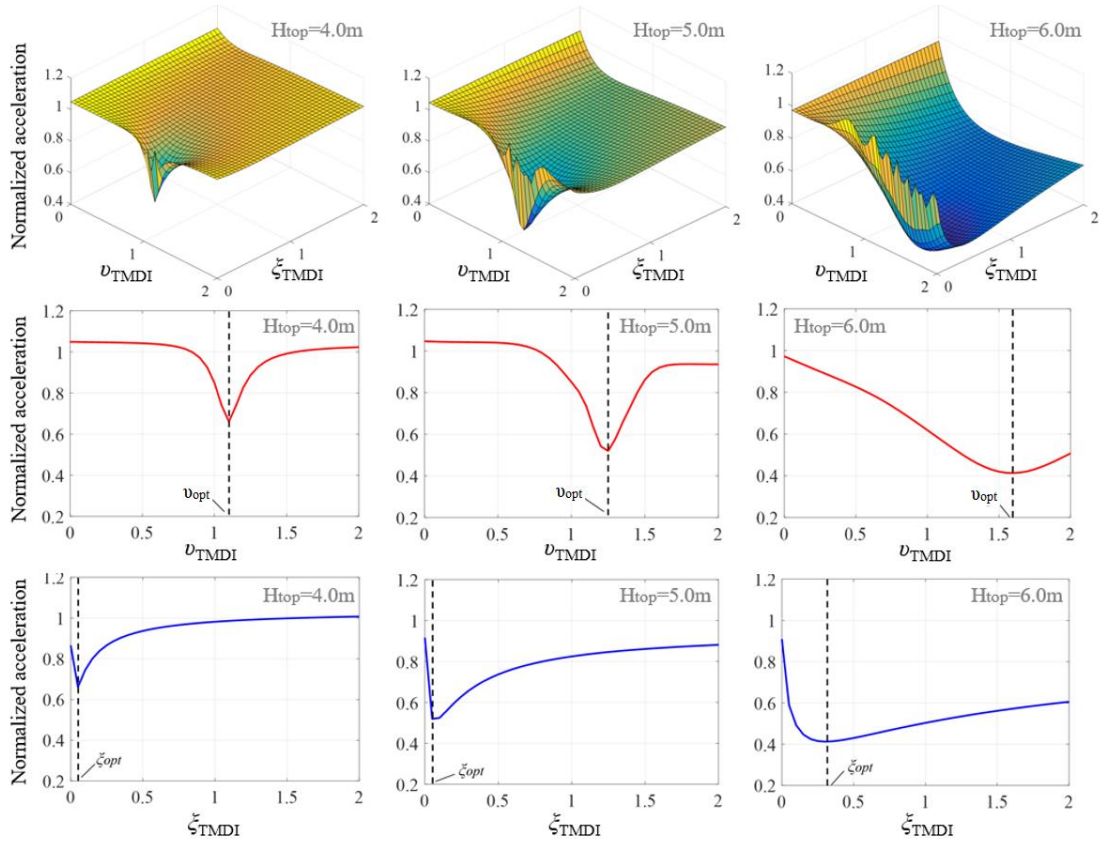


**Fig. 5.7.** Objective function surface on the primary design variables plane (upper row of panels) and surface cross-sections along  $\nu_{TMDI}$  at the optimal  $\zeta_{TMDI} = \zeta_{opt}$  value (middle row of panels), and along  $\zeta_{TMDI}$  at the optimal  $\nu_{TMDI} = \nu_{opt}$  value (lower row of panels) for  $\mu=0.1\%$ ,  $\beta=6\%$ , and various top storey heights  $H_{top}$ .

### 5.5 Performance assessment and design of optimal TMDI-equipped structure with reduced top-storey stiffness

In this section, comprehensive numerical results are furnished and discussed shedding light to the effectiveness of TMDI designed/tuned through the solution of the optimisation problem in Eq.(3.3) in containing VS induced vibrations in the case-study building exposed to the  $\mathbf{S}_{FF}^{34}(\omega)$  PSD wind force matrix. To this aim, TMDIs with different inertial properties (i.e., secondary mass and inertance) are examined while the top-storey of the case-study building is softened laterally by eliminating the r/c core and by varying its height within  $H_{top} = [4.0, 6.0]$  (m) interval. Firstly, performance in terms of peak floor acceleration of the 32<sup>nd</sup> floor as well as peak secondary mass stroke (relative displacement between secondary mass and 33<sup>rd</sup> floor) is presented and discussed. Next, peak developed damping and inerter forces are reported to gain an insight on their relative importance as TMDI properties vary. Lastly, attention is focused on quantifying the trade-offs among secondary mass, inertance and top-storey stiffness to explore the feasibility of more lightweight TMDIs achieving a pre-specified structural performance in terms of peak floor acceleration (i.e., performance-oriented design).



### 5.5.1 Floor acceleration and secondary mass stroke

The first row of panels in Fig. 5.8 reports percentage reduction factor (RF) of peak floor acceleration at the 32<sup>nd</sup> floor of optimal TMDI-equipped structure with respect to the uncontrolled case-study building with a coreless (flexible) top-storey (i.e., the core stops at the penultimate/33<sup>rd</sup> storey) for three different mass ratios and for several inertance ratios including the limiting case of  $\beta=0$  (TMD) as a function of top-storey lateral stiffness. The latter is given as a percentage of the top-storey stiffness of the case-study structure without r/c core at the 33<sup>rd</sup> storey and  $H_{top} = 3.2\text{m}$ . It is observed that optimal TMDI capability to suppress floor accelerations increases appreciably and monotonically as the top-storey stiffness reduces for fixed mass and inertance ratios (but for different TMDI stiffness and damping properties as determined through the solution of the optimisation problem in Eq. (3.3)). On the contrary, for the TMD case acceleration RFs remain practically constant with top-storey flexibility. These results demonstrate that the very presence of the inerter (i.e., as long as  $b>0$ ) enables improved TMDI vibration control potential as top-storey flexibility increases. This fact is attributed to the coupling of the acceleration of the secondary oscillating mass to the acceleration of the 33<sup>rd</sup> floor achieved by the inerter mathematically manifested through the non-diagonal terms in the mass matrix  $\mathbf{M}$  (refer to Eq. (3.12) by setting  $n=34$  and  $p=1$ ). And the herein advocated host-structure modification (i.e., top-storey softening) leverages the positive effect of this coupling in reducing floor accelerations *below the top-storey*. Nevertheless, when no such coupling exists (i.e., conventional TMD case in which  $\beta=b=0$  and  $\mathbf{M}$  is a diagonal matrix), top-storey flexibility has no effect to the overall motion control level achieved. In the latter case, the appended secondary mass does not “see” the local top-storey change of stiffness and, therefore, the TMD is trivially tuned to the first natural frequency of the host structure (note that  $v_{opt}=1$  across the board in the second row of panels in Fig. 5.8) which remains practically unchanged with top-storey stiffness (see e.g., first natural frequencies for unmodified and top-storey coreless uncontrolled building in Table 5.2).

In this regard, top-storey lateral stiffness becomes a critical TMDI design parameter (though not for TMD). For example, for TMDI with  $\mu=0.1\%$  and  $\beta=8\%$ , a reduction to top-storey stiffness from 53% to 18% (herein implemented by increasing top-storey height  $h$  from 4.0m to 5.8m) achieves 20% improvement in reducing peak 32<sup>nd</sup> floor acceleration *and* 10% better performance compared to the TMD with same attached mass. Moreover, it is seen that for given  $\mu$  and  $\beta$  there is a limiting top-storey stiffness reduction defined by the intersection of the (practically horizontal) TMD RF curves with the TMDI RF curves, above which the TMD outperforms TMDI. This limiting value increases (i.e., less severe top-storey softening is required for TMDI to outperform TMD) as inertance increases and secondary mass reduces.

Furthermore, for fixed top-storey stiffness, higher inertance improves floor acceleration control at a reduced rate with inertance. This improvement becomes more significant for increased top-storey flexibility and for reduced attached mass, that is, TMDI RF curves are

more spaced out as top-storey stiffness reduces and/or  $\mu$  decreases. Notably, these trends confirm results reported in the previous chapter for the case of a high-rise 74-storey wind-excited building as well as for seismically excited low-to-mid-rise buildings with optimal TMDIs (Giaralis and Taflanidis 2018, Ruiz et al. 2018).

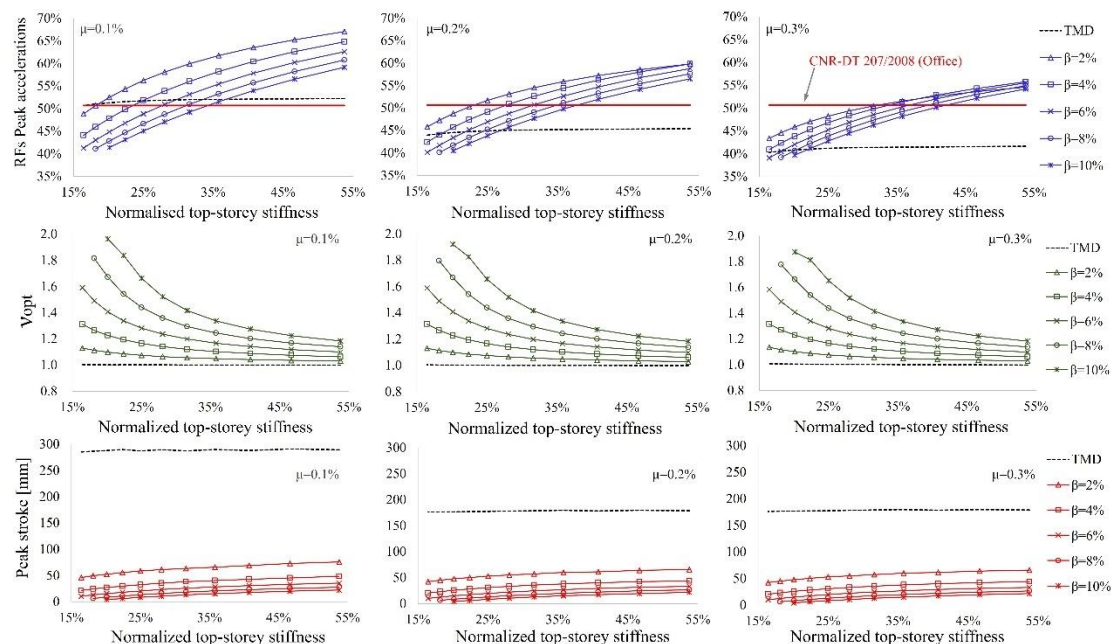


**Fig. 5.8.** Peak acceleration percentage reduction of 32<sup>nd</sup> floor (upper row of panels), optimal frequency ratio (middle row of panels), and secondary mass stroke (lower row of panels), in TMDI-equipped structure for various mass ratios,  $\mu$ , and inertia ratios,  $\beta$ , against lateral top-storey stiffness reduction.

Finally, in the upper panels of Fig. 5.8, a horizontal red solid line has been added to each subplot to indicate the comfort threshold by CNR-DT 207/2008 (used previously in Chapter 3), assuming office occupancy and based on the uncontrolled fundamental frequency of the original case-study building, i.e.,  $f_1=0.341\text{Hz}$ . Notably, the slight decrease in the fundamental frequency of the primary structure due to top-storey softening is not considered when evaluating the comfort threshold value, as the proposed structural modification is local (i.e., only at the top floor) and should not be used to ease the comfort requirement considered in the original design. It is seen that, for TMDI with  $\mu=0.1\%$ , optimal TMDIs are unable to suppress the peak floor acceleration below the codified threshold. For the TMDI, as the inertia ratio increases, the required (normalised) top-storey stiffness for the structural performance to satisfy the criterion also increases, whereas as the top storey softens, the required inertia ratio for meeting the considered comfort criterion is reduced. Importantly, the intersections of the comfort threshold line with the acceleration RF curves of TMDI indicate a series of feasible/code-compliant design in terms of habitability under given wind action, achieved by different combinations of top-storey stiffness and inertia values.

Apart from peak floor acceleration, which is the critical building performance index for

serviceability limit state design in the crosswind direction, an important quantity of interest to practical design of mass/inertial dampers is the so-called peak stroke of the secondary mass, that is, the peak relative displacement of the TMD(I) mass with respect to the floor that the mass is attached to. This is because increased TMD(I) stroke demands require larger clearance in housing safely a TMDI within the host structure such that no local pounding/collision occurs. Further, the cost of damper device increases with stroke. For the case-study structure, the peak stroke is computed by setting  $k=34$  and  $l=35$  (i.e., DOF corresponding to the secondary mass displacement) in  $\text{peak}\{x_{kl}\}$  expression in Eq. (A.6). The bottom row of panels in Fig. 5.8 plots peak TMD(I) stroke for the same inertial properties versus top-storey stiffness reduction. It is seen that the inclusion of the inerter reduces considerably secondary mass stroke demands, as also by [Giaralis and Petrini \(2017\)](#) for non-optimally tuned TMDIs, and that peak stroke reduces with increasing inertance at a reduced rate. The gains in stroke demand of the TMDI compared to TMD reduce as secondary mass increases but remain significant (almost 6-fold stroke reduction for  $\mu=0.1$  reducing to almost 4-fold reduction for  $\mu=0.2$  and  $0.3$ ). More importantly, stroke demand is positively (though insignificantly) affected by top-storey stiffness reduction. This is quite welcoming result suggesting that the favourable effect of increasing top-storey flexibility to the TMDI effectiveness for mitigating floor accelerations does not come with any increasing cost/demand related to the stroke of the damping device or to the clearance of the secondary mass.

### 5.5.2 Inerter force and damping force

To gain further insight to the effect of top-storey stiffness reduction to TMDI motion control capacity, attention is herein focused on quantifying the peak forces developing at the inerter and at the damping device of optimally designed TMDIs according to Eq. (3.3). The quantification of peak inerter and damping forces is also deemed essential to check that they are not excessive and, thus, can be economically accommodated locally by the host structure as this is found to be critical for TMDIs used in seismic protection of building structures (see e.g., [Ruiz et al. 2018](#) and [Taflanidis et al. 2019](#)). In this respect, the upper two rows of panels in Fig. 6.9 report peak inerter and damping device forces for the same optimal TMDI designs examined in Fig. 5.8. The peak relative acceleration required in determining the peak inerter force in Eq. (2.1), is computed by setting  $k=33$  and  $l=35$  in  $\text{peak}\{\ddot{x}_{kl}\}$  expression in Eq. (A.6), while the peak damping force is computed by the product of the peak relative velocity between the secondary mass and last floor found by setting  $k=34$  and  $l=35$  in  $\text{peak}\{\dot{x}_{kl}\}$  expression in Eq. (A.6) and the damping coefficient,  $c_{opt}$ , determined by

$$c_{opt} = 2\xi_{opt}v_{opt}(m_{TMDI} + b)\omega_{n(1)}, \quad (5.8)$$

The latter expression is obtained by setting  $v_{TMDI}$  and  $\xi_{TMDI}$  equal to  $v_{opt}$  and  $\xi_{opt}$ , respectively,

in Eq. (3.1) and manipulating. Results evidence that secondary mass has negligible effect to the inerter and damping forces, while these forces increase monotonically with inertance for fixed mass ratio and top-storey stiffness. The effect of the inertance to the inerter force is readily deduced from Eq.(2.1) and confirms trends reported by [Giaralis and Petrini \(2017\)](#) for non-optimal TMDIs for VS-induced vibrations mitigation in tall buildings. Further, the positive relationship between inertance and damping force, also seen in TMDIs optimised for seismic protection of multi-storey buildings ([Ruiz et al. 2018](#)), is attributed to the fact that  $c_{opt}$  in Eq.(5.8) increases with inertance since  $\xi_{opt}$  (reported in the bottom row of panels in Fig. 5.9) as well as  $v_{opt}$  in Fig. 5.8 increase with  $\beta$ . Effectively, higher inertance not only enables higher inerter force but also supports the use of damping devices with higher damping coefficients which, ultimately, increases damping force leading to overall improved motion control.

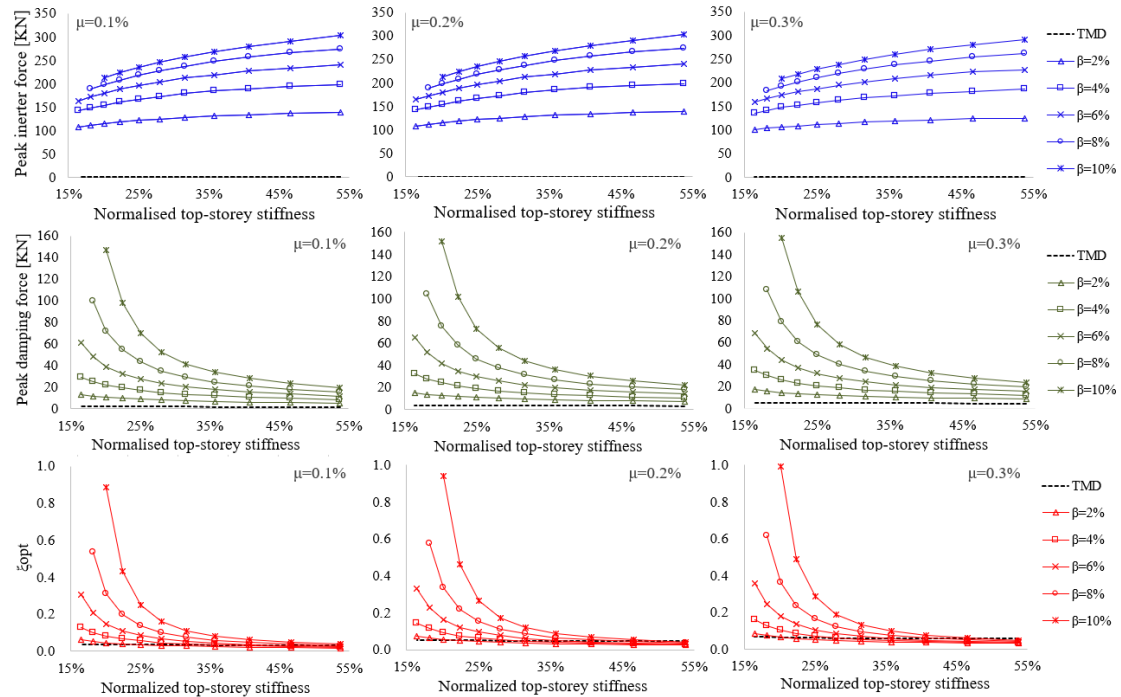


**Fig. 5.9.** Peak inerter force (upper row of panels), peak damping force (middle row of panels), and optimal damping ratios (lower row of panels) of TMDI-equipped structure for various mass ratios,  $\mu$ , and inertance ratios,  $\beta$ , against lateral top-storey stiffness reduction.

Nevertheless, top-storey stiffness reduction has a prominently different effect between the inerter force and the damping force. Peak inerter force decreases as the top-storey softens at an increasing rate. On the contrary, damping force increases as the top-storey softens at a rate that becomes exponential for  $\beta \geq 6\%$ . These trends indicate that top-storey stiffness reduction improves TMDI motion control performance through significant increase of the damping force, but not of the inerter force. Notably, the achieved increase in damping force via top-storey softening does not come from an increase to the relative velocity at the ends of the damper, but from an increase of  $c_{opt}$  in Eq. (5.8). This can be appreciated by noting that the variation trends

of  $\zeta_{opt}$  with top-storey stiffness reduction in Fig. 5.9 are similar to those of  $v_{opt}$  in Fig. 6.8 and to peak damping force trends in Fig. 5.9. In this respect, top-storey stiffness reduction affects TMDI damping force in a similar manner as the increasing of inertance.

With regards to the actual values of peak TMDI forces attained for the case-study structure under the assumed wind intensity, it is seen that the inerter force is always larger than the damping force (for the herein considered  $\beta$  and  $\mu$  inertial properties) and this difference is higher for larger inertance values and/or stiffer top-storey. The highest inerter force observed is of the order of 320kN (for  $\beta=10\%$  and  $H_{top}=4.0\text{m}$ ) which can be readily transferred to the host structure without requiring any out-of-ordinary connection and be safely accommodated by an adequately designed inerter device. Yet, top-storey stiffness reduction tends to balance off the difference between peak inerter and damping forces for fixed inertance resulting in a reduction of the peak inerter force. For instance, the peak inerter force of 320kN drops to 225kN for  $\beta=10\%$  through stiffness reduction by 35%. In this regard, top-storey softening is beneficial in containing peak inerter force.

### 5.5.3 Trading secondary mass to inertance and/or top-storey stiffness in performance-oriented design

Numerical results reported in Fig. 5.8 suggest that the same structural performance, in terms of peak floor acceleration, can be achieved by using different sets of secondary design variables in  $\mathbf{x}_2$  (i.e., secondary mass, inertance, and top-storey height). This is an important consideration from the designer's viewpoint as it enables exchanging secondary mass (attached weight) to inertance and/or to top-storey stiffness within a performance-oriented design context (i.e., aiming to achieve a pre-set performance level). To illustrate this point and to quantify potential practical benefits, Fig. 5.10(a) and 5.10(b) plot optimal iso-performance curves on the TMDI inertial  $\mu$ - $\beta$  plane for fixed top-storey stiffness and for fixed performance, respectively.

Optimal damping coefficient,  $c_{opt}$ , and peak inerter force,  $F_b$ , and damping force,  $F_c$ , are reported for all optimal designs considered in the graphs. It is seen that all iso-performance curves have negative slope on the  $\mu$ - $\beta$  plane establishing the direct mass reduction/substitution effect endowed by the inerter to the TMDI and leading to overall more lightweight inertial dampers: a practically important advantage in designing new slender minimal-weight tall buildings. Nevertheless, trading mass to inertance for fixed top-storey stiffness, Fig. 5.10(a), comes at the cost of increased damping coefficient and force as well as increased inerter force. Further, significant increase to the inertance and to damping coefficient and force are required to achieve small performance improvements for fixed mass. Quantitatively, for  $\mu=0.1\%$  it takes, on average, increases of about 15% in inertance and 72% in damping coefficient, leading to an average increase of 31% of peak damping force, for every 1% of improvement of peak floor acceleration. Conveniently, these arduous requirements can be relaxed through minute top-storey softening as seen in Fig. 5.10(b). For  $\mu=0.1\%$ , the same performance can be achieved

with reduced average required inertance, damping coefficient, and damping force by approximately 18%, 28%, and 25%, respectively, for every 2% reduction to the top-storey stiffness. As a final remark, top-storey softening further leads to attached mass reduction for fixed inertance to achieve a pre-set performance: Fig. 5.10(b) shows that 2% reduction of top-storey stiffness reduces the required mass ratio by about 0.1% corresponding to a 20 tonne TMDI weight reduction for the case-study building.

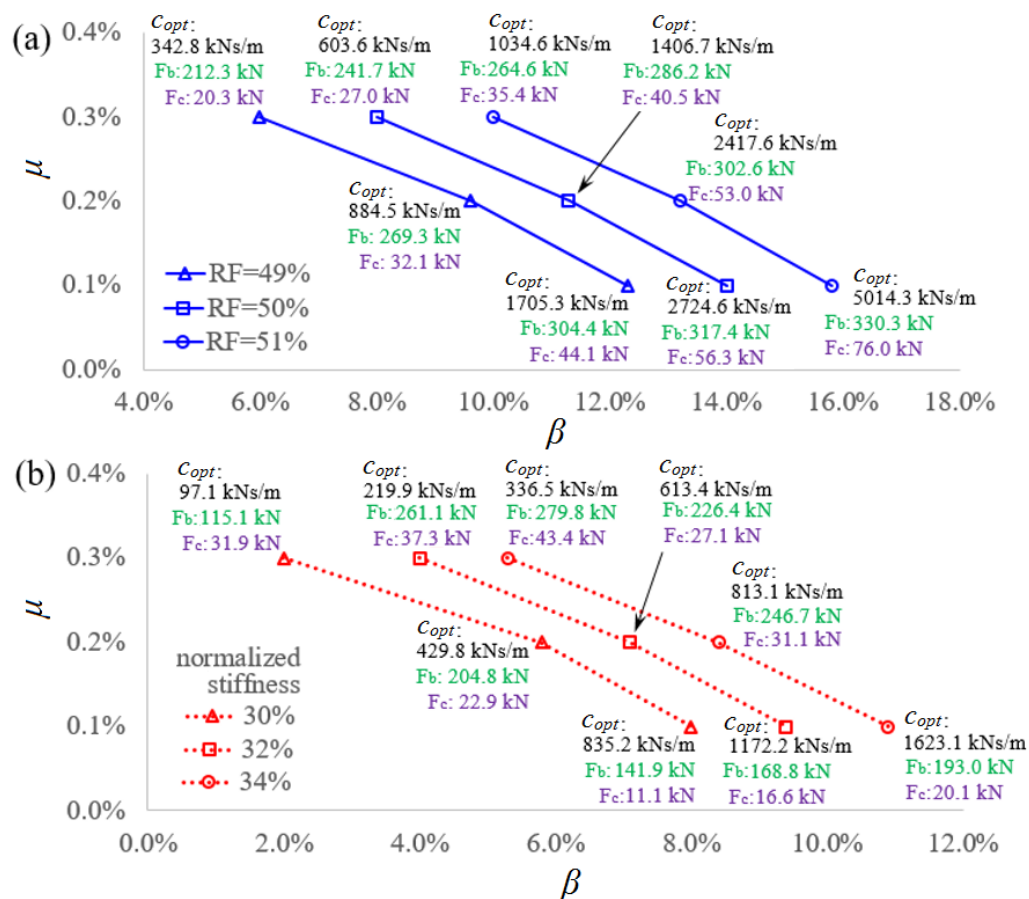


Fig. 5.10. Quantification of mass-inertance-damping coefficient trade-off for (a) fixed normalized stiffness 38%; and (b) fixed performance RF=50%.

### 5.6 Influence of building properties to floor acceleration performance

In this final section the influence of the inherent damping and r/c core stiffness of the case-study building to the performance of optimal-TMDI equipped structure is quantified, separately, through parametric analyses. The influence of these two building properties was deemed important to assess since: (a) accurate estimation of the inherent damping properties in tall buildings is a quite challenging task involving uncertainty (e.g., Spence and Kareem 2014) while it is known to affect significantly their response to wind excitation, (b) lateral r/c core stiffness is primarily defined from along-wind direction ultimate limit state design (e.g., Huang 2017) and, therefore, may vary independently from serviceability limit state design in the crosswind direction.



### 5.6.1 Influence of inherent structural damping modelling

The amount of inherent damping present in the dominant vibration modes of an uncontrolled system can heavily affect its response to dynamic loading. At the design stage, damping characteristics of building structures are usually assumed as constant and independent of response magnitudes in the dynamic analysis because as yet there is no widely accepted method available for accurately predicting damping ratios of a structure before construction (Li et al. 2003). As such, to explore the influence of the inherent structural damping, the first modal damping ratio,  $\zeta_1$ , of the case-study building is herein estimated using the following three different damping models proposed in the literature:  $\zeta_1 = 0.01f_1$  (Jeary 1986),  $\zeta_1 = 0.002884/f_1 + 0.012856 f_1$  (Lagomarsino 1993), and  $\zeta_1 = 0.0231f_1$  (Satake et al. 2003), where  $f_1$  is the first structural natural frequency in Hz. Damping ratios for higher modes are taken the same as before as it is found that their influence is insignificant to structural performance. The normalised standard deviation of peak 32<sup>nd</sup> floor accelerations of optimal TMDI-equipped case-study structure with different first modal damping ratios,  $\zeta_1$ , computed from the above damping estimators is plotted in the upper panels of Fig. 5.11 as a function of the inertance  $\beta$  and for various mass ratio  $\mu$  and top-storey height  $H_{top}$  values. Further, each standard deviation is normalised by the corresponding average value of the same peak floor accelerations used in computing that standard deviation. Therefore, the curves in the upper panels of Fig. 5.11 measure directly the structural performance dispersion of the TMDI-equipped case-study building due to different inherent damping ratios for various sets of  $\mu$ ,  $\beta$ , and  $H_{top}$ .

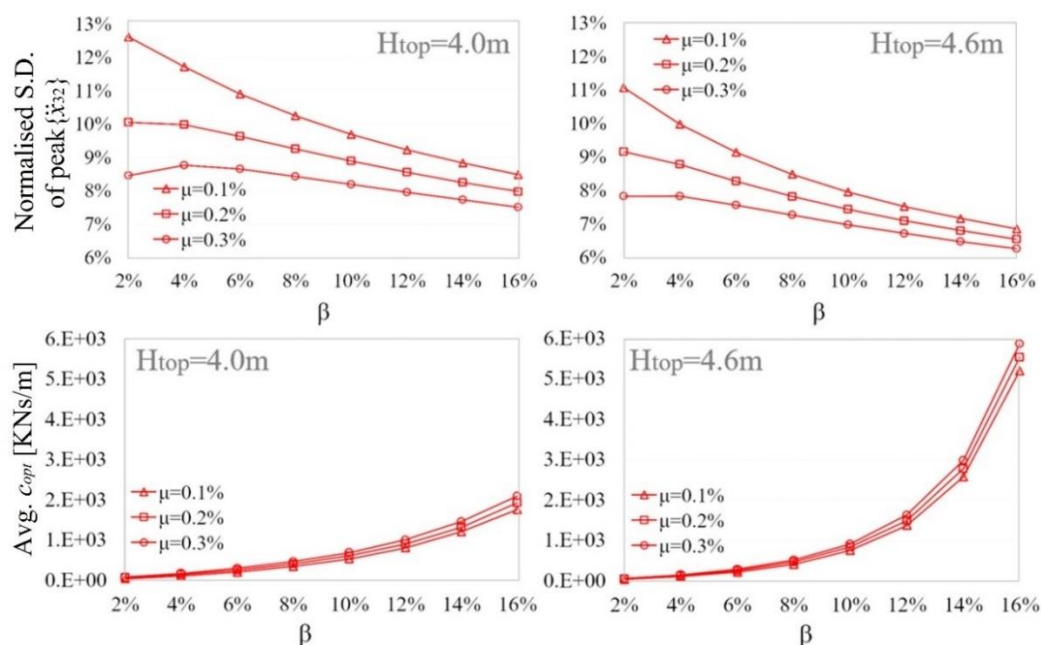


**Fig. 5.11.** Normalised standard deviation of peak crosswind acceleration at 32<sup>nd</sup> floor (upper panels) and average TMDI damping coefficient  $c_{opt}$  (lower panels) as functions of inertance ratio for three inherent damping models, various mass ratios, and two top-storey heights.



It is observed that the significance of the influence of the assumed/estimated  $\zeta_l$  value to structural performance dispersion reduces with increased inertance and attached mass. Interestingly, it is further seen that the influence of the inherent damping is less important as the top-storey softens, that is, as the top-storey height increases from 4.0m to 4.6m. Finally, as  $\beta$  and  $H_{top}$  increase, the normalised standard deviation of structural performance for different mass ratios converge. All the above trends can be readily attributed to the fact that the average value of optimal TMDI damping coefficients (i.e.,  $c_{opt}$ ), determined by assuming different inherent damping ratios for the case-study building, increase with inertance and top-storey softening as shown in the lower panels of Fig. 5.11. In this regard, the effect of the assumed  $\zeta_l$  value becomes less important in optimal TMDI-equipped tall buildings as inertance increases and/or top-storey softens due to the increased TMDI supplementary damping rendering the inherent damping modelling less critical in tall buildings design.

### 5.6.2 Influence of r/c core stiffness

Treating the structure in Fig. 5.2 as the base-case, two variants of the case-study structure with r/c core lateral stiffness contribution uniformly reduced by 10% and 20% are considered. This is readily achieved through the low-order model of the structure by multiplying the  $\mathbf{K}_{core}$  term in Eq. (5.1) with reduction factors 0.9 and 0.8, respectively, while the perimeteric MRF stiffness contribution remains the same. Figure 5.12 plots percentage RF of peak 32<sup>nd</sup> floor acceleration of optimal TMDI-equipped structures over optimal TMD-equipped structures ( $\beta=0$ ) with different core stiffness as function of top-storey stiffness reduction for  $\mu=0.1\%$  and for different  $\beta$  values.

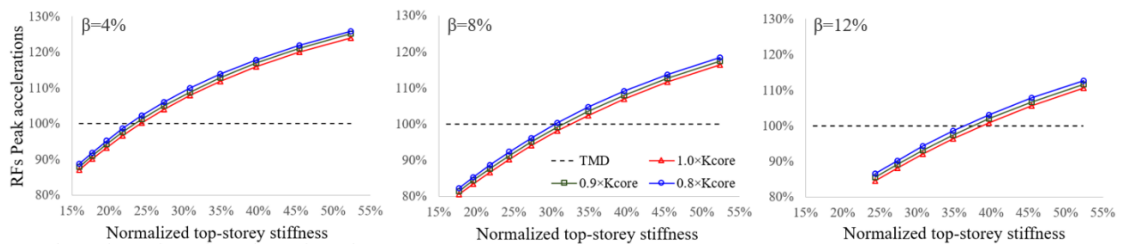


**Fig. 5.12** Peak acceleration percentage reduction of 32<sup>nd</sup> floor for optimal TMDI-equipped versus optimal TMD-equipped structures with different r/c core contributions against lateral top-storey stiffness reduction for attached mass ratio  $\mu=0.1\%$ , and various inertance ratios.

It is seen that TMDI peak floor acceleration control capability deteriorates slightly compared to TMD capability as the relative stiffness contribution of the core reduces by about 1% for 10% r/c core stiffness reduction. Notably, this deterioration is independent of top-storey stiffness. These findings suggest that top floor optimal TMDIs are more efficient for tall buildings behaving closer to a flexural cantilever. It is, therefore, concluded that increasing lateral stiffness contribution of the r/c core as opposed to the MRFs to contain deformation demands in the along-wind direction facilitates controlling floor accelerations in the crosswind

direction by means of TMDI.

## 5.7 Closure

The effectiveness and advantages of using optimally tuned top-storey TMDIs in conjunction with an innovative local structural modification, i.e., top-storey lateral stiffness reduction, have been numerically explored for mitigating floor accelerations in the crosswind direction of slender core-frame high-rise buildings critical for serviceability design (occupants' comfort criteria). This has been accomplished by furnishing pertinent numerical data for a low-order top-storey-TMDI-equipped dynamical system capturing faithfully in-plane modal properties (mode shapes and natural frequencies) of a 34-storey square-plan core-frame benchmark building with softened top-floor through discontinuing the central r/c core and increasing the top-floor height. A novel optimal TMDI tuning problem has been formulated and numerically solved treating TMDI properties and top-floor height as design parameters aiming to minimise peak floor acceleration demands under crosswind excitation forces. These forces were modelled as a stationary spatially-correlated random field accounting for vortex shedding effects.

Numerical results obtained for different TMDI inertial properties (mass and inertance) and top-storey height have shown that improved structural performance in terms of peak floor acceleration and attached mass stroke are achieved by increasing inertance and/or by reducing top-storey stiffness for fixed TMDI attached mass, while no improved performance is achieved by the classical TMD (no inertance) with top-storey softening. In this regard, it was demonstrated, through the consideration of optimal TMDI design charts for fixed floor acceleration performance, that the required TMDI mass/weight can be reduced either by increasing inertance or by softening the top storey. This is deemed a rather advantageous consideration in the design of new structures. Still, it was found that mass reduction achieved through increased inertance *for a fixed target performance* increases the required damping and inerter forces exerted to the structure. However, these forces reduce for fixed attached mass and structural performance by exchanging inertance to top-storey softening. Thus, by leveraging inertance and top-storey stiffness, the proposed motion control solution can be judiciously designed to exert overall balanced and relatively small amplitude additional forces in new structures in the gravitational (small added weight) and the horizontal directions. Additionally, it was shown that increase of the top-storey height lead to increased robustness of structural performance (floor acceleration) with respect to the optimal TMDI properties and as well as to the assumed inherent structural damping. Therefore, top-storey softening yields more robust TMDI designs to detuning effects as well as to inaccurate knowledge of structural properties. Lastly, it was seen that response acceleration performance of optimal TMDI-controlled structures improves by increasing the flexural contribution in coupled core-frame lateral load-resisting suggesting that increasing the core vis-à-vis frame resistance in meeting ultimate limit design criteria in the along-wind direction favours meeting serviceability design criteria in the

crosswind direction.

Looking further into the case of existing tall/slender buildings, the reported numerical data suggest that the addition of a relatively soft top-storey housing a properly tuned lightweight TMDI is a potent retrofitting measure to enhance serviceability performance. In this manner, more stringent serviceability design requirements than those considered in the initial design due to site-specific climate change effects or changes to the surrounding built environment (i.e., increased wind exposure) can be achieved. Overall, the numerical data furnished in this chapter demonstrate the great potential of improving the performance of TMDI-equipped structures to crosswind excitations through appropriate design of the primary structure. Thus, there is scope to pursue optimal primary structure design in lieu with the use of inerter-based vibration control. These aspects are explored in the following two chapters.

## Chapter 6

---

### A Novel Sizing Optimisation Method for Minimal-Weight Skeletal Structures

#### 6.1 Preliminary remarks

Numerical results presented in previous chapters demonstrated that there is scope in pursuing integrated optimal DVA (achieved in Chapter 3) and primary structure design. To support this task, this chapter proposes a novel automated sizing optimisation algorithm/routine for addressing the material efficiency issue in wind-excited, occupant comfort-governed tall buildings through increasing the lateral stiffness (and thus the fundamental frequency) without the aid of any vibration suppression device. This task can be straightforwardly introduced in the structural design of tall buildings by requiring self-weight minimisation of the load-bearing systems through finding optimal cross-section sizes of structural members (DVs) while satisfying certain performance objectives, such as the requirement that wind-induced floor accelerations be below codified thresholds (Spence 2018). For wind-excited buildings subject to habitability criteria, their weight-minimisation problem can be conveniently converted to a sizing OP of elastic structures under a behavioural constraint (BC) on its fundamental frequency. This is owing to the fact that wind-induced floor accelerations in both along-wind and crosswind directions are, in general, inversely related to the building's fundamental frequency within the frequency range for serviceability check, i.e., from 0.1 - 1.0 Hz (Tallin and Ellingwd 1983, Griffis 1993, Chan and Chui 2006). Two numerical approaches are currently available for sizing optimisation under a frequency constraint: mathematical programming techniques and optimality criteria (OC) methods (Lógó 2005). Notwithstanding the rigorous basis and generality, the former approach can be computationally costly for design problems with a large number of DVs (Kirsch 1993), which is typically the case for tall buildings. Therefore, the (discrete) OC methods, developed by Venkayya et al. (1968) and generalised by Berke (1970), Gellatly and Berke (1972), and Venkayya et al. (1973), are widely considered as a more efficient alternative for solving large-scale OPs whose BCs are many fewer than the DVs (Yin and Yang, 2001).

In general, the OC methods rely on first characterising the optimal structure through some necessary conditions that are believed to hold at the optimum, and then applying an iterative algorithm to gradually modify/resize the current non-optimal design for satisfying the conditions in the continuous design space until convergence, and hence indirectly optimising the structure. These criteria can be mathematically defined statements (known as rigorous OC) derived by the Karush-Kuhn-Tucker approach, or more intuitive one (known as intuitive OC) such as the requirement that the strain energy density (SED) averaged per unit volume must be

uniform throughout the structure (Prager and Shield 1968, Prager and Taylor 1968, Venkayya et al. 1968). Although the recursive relations (for updating the DVs) involving nonlinear and implicit BC functions are inherently iterative, fast convergence to a practically meaningful solution is still shared across many applications for at least well-understood structural behaviours, especially if the behaviours approximate those of statically determinate systems (Patnaik et al. 1995).

Whilst the intuitive OC methods based on the uniform SED criterion are quite attractive owing to their engineering intuition and efficiency, two issues not addressed by the current approaches exist. Firstly, a systematic approach, capable of handling different element types (i.e., bar, beam, frame) and various structural BCs (i.e., on frequency, buckling, or displacements) in a unified and stable manner, is lacking. Indeed, when only displacement constraints are present, the current OC methods appear to be satisfactory even for large systems with many DVs. However, the methods can become *erratic* in obtaining a solution for eigenvalue-constrained OPs or for structures whose behaviours do not resemble those of determinate systems (Patnaik et al. 1995). Secondly, the successful implementation of intuitive OC methods requires the OF (i.e., structural self-weight) as well as the BCs to be separable explicitly. That is, both functions need to be written as a sum of contributions of different structural elements, each one being a function of one DV only (Berke and Khot 1987). For indeterminate structures, uncoupling/separability does not hold because BCs contain internal forces that are implicit functions of some or all DVs. Thus, in the current energy-based OC approaches, the required separability is assumed either explicitly or implicitly for hyperstatic systems (see, e.g., Kiusalaas 1973, Khot 1983, Berke and Khot 1987, Canfield et al. 1989, Levy 1994, Makris and Provatidis 2002, Chan and Chui 2006, Makris et al. 2006).

To this end, this chapter proposes a novel strain energy-based OC that takes into account the coupling between the DVs in the indeterminate system, together with a rigorous resizing algorithm, for the automated minimum-weight design of frame structures with fixed layout subject to a single (natural) frequency constraint. The novel OC is derived through a Lagrangian Multiplier (LM) formulation which adjoins the nonlinear frequency constraint, expressed in terms of *modal* strain energy, to the linear OF representing the total material volume. The optimal structure is characterised through a set of differential equations whose solution defines the optimality without heuristically suggesting uniform SED distribution across all structural members adopted by current energy-based OC methods. Further, the numerical algorithm used for solving the proposed OC-based optimal sizing formulation relies on updating of the DVs and the LM using recursive closed-form formulae. Conveniently, the algorithm is readily amendable to parallel computing programming which reduces significantly computational time requirements.

## 6.2 Formulation of the structural sizing optimisation problem subject to frequency constraint

For linear elastic skeletal structures with fixed layout, the considered sizing optimisation seeks to minimise the structural self-weight while satisfying a frequency constraint of a chosen mode restated in modal strain energy. This is achieved by a novel OC derived herein and a compatible iterative algorithm adapted from [Chan and Chui \(2006\)](#) to optimally reallocate the material within the (fixed) layout while ensuring the target strain energy (and target frequency) is met by the structure. The considered OP for a structure comprising  $n$  frame elements and, hence,  $n$  independent DVs can be mathematically expressed as

$$\begin{aligned} \mathbf{a}^* &= \arg \min_{\mathbf{a}^{\min} \leq \mathbf{a} \leq \mathbf{a}^{\max}} \left\{ V(\mathbf{a}) = \sum_{i=1}^n l_i \cdot a_i \right\} \\ \text{s.t. } U_{\text{total}}(\mathbf{a}) - U_{\text{target}} &= 0, \end{aligned} \quad (6.1)$$

where  $V(\mathbf{a}): \mathbb{R}^n \rightarrow \mathbb{R}$  is the OF measuring the total volume of structural material to be minimised, while  $l_i$  and  $a_i$  ( $i=1, \dots, n$ ) denote the length and cross-sectional area of element  $i$ , respectively. The length of structural elements are taken as fixed, while the  $n$  areas of the elements are *continuous* DVs grouped in the vector  $\mathbf{a} \in \mathbb{R}^{1 \times n}$  and bounded by the box constraint  $\mathbf{a}^{\min} \leq \mathbf{a} \leq \mathbf{a}^{\max}$ . The equality BC requires that the total strain energy,  $U_{\text{total}}(\mathbf{a}): \mathbb{R}^n \rightarrow \mathbb{R}$ , induced by some external loading is equal to a target strain energy  $U_{\text{target}}$ . The feasible solution set  $S$  of the OP can be therefore obtained by intersecting the convex solution set  $A = \{\mathbf{a} \mid \mathbf{a}^{\min} \leq \mathbf{a} \leq \mathbf{a}^{\max}\}$  with the set  $C = \{\mathbf{a} \mid U_{\text{total}}(\mathbf{a}) = U_{\text{target}}\}$ , where  $A, C, S \subset \mathbb{R}^n$ . Additional equal size constraints to enforce that the size of certain members is the same in support of design practicality and structural buildability, may be additionally imposed on the DVs. In this setting, the herein formulated OP involves finding the optimal point  $\mathbf{a}^*$  or a set of optimal cross-sections within the feasible solution set  $S = A \cap C$ , at which the self-weight is minimised. Geometrically, the optimal solution  $\mathbf{a}^*$  corresponds to the minimum point of the projection of the BC curve/surface onto the OF plane/hyperplane passing through the origin of the  $N+1$  dimensional design space and normal to the vector  $(l_1, \dots, l_n)$ .

To facilitate a solution of the above OP, the LM approach is employed to convert the constrained OP in Eq. (6.1) into an unconstrained OP in which the first derivative test is applicable. Specifically, the auxiliary Lagrangian,  $L: \mathbb{R}^n \times \mathbb{R} \rightarrow \mathbb{R}$ , that adjoins the nonlinear BC to the linear OF is formed as

$$L(\mathbf{a}, \lambda) = V(\mathbf{a}) - \lambda \left[ U_{\text{total}}(\mathbf{a}) - U_{\text{target}} \right], \quad (6.2)$$

where  $\lambda$  is the LM. Assuming  $U_{\text{total}}(\mathbf{a})$  is differentiable on the feasible set  $S$ , the stationary condition of the Lagrangian with respect to DVs,  $\nabla_{\mathbf{a}} L(\mathbf{a}, \lambda) = 0$ , yields

$$l_j = \lambda \frac{\partial U_{\text{total}}(\mathbf{a})}{\partial a_j} \quad (j=1, \dots, n). \quad (6.3)$$

Further, the stationary condition with respect to the LM,  $\nabla_{\lambda} L(\mathbf{a}, \lambda) = 0$ , yields the BC in Eq. (6.1), i.e.,

$$U_{\text{total}}(\mathbf{a}) - U_{\text{target}} = 0, \quad (6.4)$$

which is independent of the multiplier. Therefore, Eqs. (6.3) and (6.4) define a system of  $n+1$  coupled equations for  $n+1$  unknowns. These are the  $n$  DVs (areas  $a_i$ ) plus the LM  $\lambda$ . Moreover, the total strain energy,  $U_{\text{total}}(\mathbf{a})$ , may be written explicitly as a summation of element strain energies as

$$U_{\text{total}}(\mathbf{a}) = \sum_{i=1}^n \bar{u}_i(\mathbf{a}) \cdot l_i \cdot a_i, \quad (6.5)$$

where  $\bar{u}_i(\mathbf{a})$  denotes the average SED over the respective volume of element  $i$ .

According to the standard LM approach, at any stationary point of the OF evaluated under a single equality BC, the gradient of the OF can be expressed as a product of the gradient of the BC with the LM acting as a constant coefficient (Luenberger 1969). Note, however, that a stationary point may not be the global minimum as it could equally well be a local extremum or a turning point. Furthermore, the global minimum may not be a stationary point since the optimum could be achieved on the boundaries of the feasible set. At this point, it is shown analytically in Section 6.3 that for an appropriately formulated strain-energy equality constraint associated with natural frequency, the set  $C$  always forms a convex/concave curve/surface within the DV plane/hyperplane such that there exists at most one (stationary) point in the feasible set  $S$  for which Eq. (6.3) holds. It is further shown that if such a stationary point exists in  $S$ , it must be the global minimum  $\mathbf{a}^*$  to the OP. Assured by this fact, Eq. (6.3), which gives the necessary conditions at the optimum, can be manipulated by using Eq. (6.5) to give

$$\frac{1}{\lambda} = \bar{u}_j + \frac{1}{l_j} \sum_{i=1}^n \frac{\partial \bar{u}_i}{\partial a_j} \cdot l_i \cdot a_i \quad (j = 1, \dots, n). \quad (6.6)$$

The above expressions define the necessary OC for all structural elements in an optimally sized structure via  $n$  differential equations involving the SED of each element. According to the uniform SED criterion derived in Prager and Taylor (1968) and Venkayya et al. (1968), the



average SED of each structural element at the optimum (i.e., the first term on the right hand side of Eq. (6.6)) must be equal to a same constant, i.e.,

$$\bar{u}_j(\mathbf{a}^*) = \frac{U_{\text{total}}(\mathbf{a}^*)}{V(\mathbf{a}^*)} \quad (j = 1, \dots, n), \quad (6.7)$$

Based on Eq. (6.7), it is evident that the following condition

$$\frac{1}{l_j} \sum_{i=1}^n \frac{\partial \bar{u}_i(\mathbf{a}^*)}{\partial a_j} \cdot l_i \cdot a_i = \frac{1}{l_k} \sum_{i=1}^n \frac{\partial \bar{u}_i(\mathbf{a}^*)}{\partial a_k} \cdot l_i \cdot a_i \quad (j, k = 1, \dots, n \text{ and } j \neq k), \quad (6.8)$$

must also be true at the optimum for Eq. (6.6) to hold.

In this setting, Eq. (6.7) describes the intuitive uniform SED criterion considered in [Prager and Taylor \(1968\)](#) and [Venkayya et al. \(1968\)](#) and will be referred as the first OC hereafter. As stated previously, it heuristically suggests that the average SED of all structural elements,  $\bar{u}_j$  ( $j = 1, \dots, n$ ), of the optimal structure to be equal to the same constant,  $U_{\text{total}}(\mathbf{a}^*)/V(\mathbf{a}^*)$ . More importantly, the *novel* second OC in Eq. (6.8) reveals that, for every element of the optimal structure, say element  $j$ , the weighted sum of partial derivatives of all SEDs with respect to the DV of that element,  $a^j$ , over the corresponding element length,  $l_j$ , must be constant. Therefore, Eqs. (6.7) and (6.8) together constitute a novel OC-based optimisation formulation. To satisfy the second OC, two possibilities exist depending on the static determinacy of the structure. In the case of statically determinate structures, the SED of element  $j$  depends only on the size of element  $j$ ,  $a_j$ , such that its partial derivatives with respect to all other DVs,  $a_k$  ( $k=1, \dots, n$  and  $k \neq j$ ), vanish and the summation on  $i$  in Eq. (6.8) drops. In the case of statically indeterminate structures, the element SEDs become multivariate functions of more than one DV. Thus, not all partial derivatives in Eq. (6.8) are zero such that Eq. (6.8) holds exactly with no decoupling between the DVs occurs.

Using the equality given in Eq. (6.8), the OC given in Eq. (6.6) can be rewritten in a more compact form as

$$\lambda[\bar{u}_j(\mathbf{a}^*) + d_j] = 1 \quad (j = 1, \dots, n). \quad (6.9)$$

For statically determinate structures,  $d_j$  in Eq.(6.9) is given by

$$d_j = \frac{d\bar{u}_j(\mathbf{a}^*)}{da_j} \cdot a_j^*, \quad (6.10)$$

while for statically indeterminate structures  $d_j$  is given as

$$d_j = \frac{1}{l_j} \sum_{i=1}^n \frac{\partial \bar{u}_i(\mathbf{a}^*)}{\partial a_j} \cdot l_i \cdot a_i^*. \quad (6.11)$$

It is worth noting that Eq. (6.9) expresses the novel OC-based formulation in terms of  $n$  equations involving  $n$  SED-related quantities and the unknown LM. By setting  $d_j=0$  in Eq. (6.9), the herein proposed OC-based formulation degenerates to the standard OC problem developed by [Prager and Taylor \(1968\)](#) and [Venkayya et al. \(1968\)](#) which assumes uniform SED across all members. In this respect, the proposed OC-based formulation constitutes a generalisation of the standard OC formulation with uniform SED. Importantly, it will be seen in section 6.5, in view of pertinent numerical results, that the generalised OC formulation, which additionally considers the OC in Eq. (6.8), improves the convergence rate of the resizing algorithm significantly.

### 6.3 Numerical solution strategy of the optimal sizing problem

#### 6.3.1 Iterative algorithm for resizing design variables

Based on the novel OC in Eq. (6.9), a numerical resizing routine, adapted from the linear recursive relation in [Chan and Chui \(2006\)](#), is herein presented for updating the DVs and LM (OP unknowns). The linear recursive relation for updating the DVs at the  $p$ -th iteration attains the form

$$a_j^{(p+1)} = \begin{cases} a_j^{\min} & \text{if } c_j^{(p)} \cdot a_j^{(p)} \leq a_j^{\min} \\ c_j^{(p)} \cdot a_j^{(p)} & \text{if } a_j^{\min} \leq c_j^{(p)} \cdot a_j^{(p)} \leq a_j^{\max} \\ a_j^{\max} & \text{if } c_j^{(p)} \cdot a_j^{(p)} \geq a_j^{\max} \end{cases} \quad (6.12)$$

where  $c_j^{(p)}$  is a scaling factor at iteration  $p$  for modifying the  $j$ -th DV based on Eq. (6.9) and is given by

$$c_j^{(p)} = 1 + 1/\eta[\lambda^{(p)}(\bar{u}_j^{(p)} + d_j^{(p)}) - 1], \quad (6.13)$$

In the last equation, the relaxation parameter  $\eta$  controls the convergence rate of the recursive process: as  $\eta$  becomes smaller, the value of  $a_j^{(p)}$  is modified to a larger extent, and vice versa. The SED of the  $j$ -th element,  $\bar{u}_j^{(p)}$ , and total strain energy,  $U_{\text{total}}^{(p)}$ , caused by the applied loads at iteration  $p$  are numerically evaluated by

$$\bar{u}_j^{(p)} = \frac{1}{2} \left( \frac{\delta_{e,j}^T \mathbf{k}_{e,j} \delta_{e,j}}{l_j \cdot a_j} \right)^{(p)}, \quad (6.14)$$

$$U_{\text{total}}^{(p)} = \frac{1}{2} (\delta^T \mathbf{K} \delta)^{(p)}, \quad (6.15)$$

respectively, in which  $(\mathbf{k}_{e,j})^{(p)}$  and  $(\delta_{e,j})^{(p)}$  are the element stiffness matrix and element displacement vector, separately, while  $(\mathbf{K})^{(p)}$  and  $(\delta)^{(p)}$  are the structure stiffness matrix and global displacement vector due to the applied loads at iteration  $p$  respectively.

The application of Eq. (6.12) to update the DVs require determining first the  $d_j$  terms in Eq. (6.13). To this aim, the following expressions

$$d_j^{(p)} = \frac{\bar{u}_j^{(p)} - \bar{u}_j^{(p)}(a_j^{(p-1)})}{a_j^{(p)} - a_j^{(p-1)}} \cdot a_j^{(p)}, \quad (6.16)$$

$$d_j^{(p)} = \frac{1}{l_j} \sum_{i=1}^n \frac{\bar{u}_i^{(p)} - \bar{u}_i^{(p)}(a_j^{(p-1)})}{a_j^{(p)} - a_j^{(p-1)}} \cdot l_i \cdot a_i^{(p)}, \quad (6.17)$$

can be used for the numerical approximation of  $d_j$  at the  $p$ -th iteration for statically determinate and indeterminate structures, respectively. The above expressions derive in a straightforward manner from the analytical expressions in Eqs. (6.10) and (6.11), respectively. Specifically, in these two equations,  $\bar{u}_i^{(p)}(a_j^{(p-1)})$  denotes the updated SED for element  $i$  at iteration  $p$ , which is evaluated by forcing the  $i$ -th DV to the corresponding value in the previous iteration  $p-1$  while keeping all other DV values in the current iteration  $p$ . Therefore, Eqs. (6.16) and (6.17) serve as estimations of Eqs. (6.10) and (6.11), respectively, through finite difference approximation. From a computational standpoint, the evaluation of  $d_j^{(p)}$  ( $j = 1, \dots, n$ ) according to Eq. (6.16) or (6.17) at iterative step  $p$  requires  $n$  *additional* analyses (compared to the current energy-based OC methods assuming static determinacy and uncoupled relations for updating the DVs) per structural element, as the quantities  $\bar{u}_i^{(p)}(a_j^{(p-1)})$  entails DVs from two successive iterative steps (i.e.,  $a_1^{(p)}, \dots, a_{j-1}^{(p)}, a_j^{(p-1)}, a_{j+1}^{(p)}, \dots, a_n^{(p)}$ ). For large structural systems, the evaluation of  $d_j^{(p)}$  as per these two equations may thus become computationally intensive and costly. Nevertheless, it should be recognised that computation of  $d_j$  values for different structural elements at one iterative step are independent of each other and thus need not be performed sequentially. With a high-performance computer with multiple processors/cores, it is possible to perform the computation of  $d_j$  values (for all  $n$  structural elements) in parallel on different cores (e.g., by switching from serial execution to parallel execution) at each iteration step, and hence expediting the resizing process by roughly  $m$  times

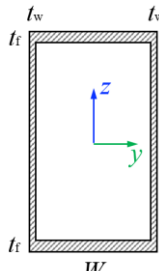
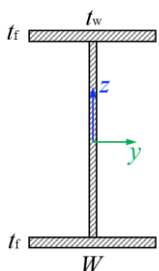
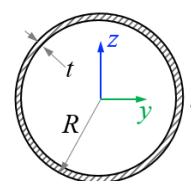
where  $m$  denotes the number of cores available for the task.

Next, to construct the element stiffness matrix  $\mathbf{k}_{e,j}$  for Euler-Bernoulli beams, it is necessary to express all moments of inertia, i.e.,  $I_{yy,j}$ ,  $I_{zz,j}$ , and  $J_{t,j}$ , as functions of the cross-section area  $a_j$  for each beam element. Previous studies by Chan (1992) showed that sectional properties can be expressed as reciprocal functions of cross-section areas through regression analysis. In addition, the well-known simple relationship  $I_j = ca_j^r$  covers many practical cases where “ $c$ ” and “ $r$ ” are constants (Berke and Khot 1987). In this work, however, it is assumed the skeletal structure to be optimised only consists of cross-sections with fixed dimension ratios defined in Table 6.1 (cf.  $r_1$ ,  $r_2$ ,  $r_3$ , and  $r_4$ ). For common arbitrary steel sections shown in Table 6.1, the sectional properties can be related to the cross-section area in an exact manner by introducing following relations

$$\begin{aligned} I_{yy,j} &= \alpha \cdot a_j^2, \\ I_{zz,j} &= \beta \cdot a_j^2, \\ J_{t,j} &= \gamma \cdot a_j^2 \quad (j = 1, \dots, n), \end{aligned} \quad (6.18)$$

where  $\alpha$ ,  $\beta$ , and  $\gamma$  are non-dimensional constants relating the moments of inertia to the cross-section area, and are derived for arbitrary hollow box, flange, and tubular sections in the table below

**Table 6.1.** Non-dimensional constants relating section properties to cross-section area.

	Hollow box	Flange section	Tubular section
Section illustration	 <p style="text-align: center;"><math>W/H = r_1</math> <math>t/H = r_2</math> <math>t_w/H = r_3</math></p>	 <p style="text-align: center;"><math>W/H = r_1</math> <math>t/H = r_2</math> <math>t_w/H = r_3</math></p>	 <p style="text-align: center;"><math>t/R = r_4</math></p>
$\alpha$	$\frac{1}{12} \cdot \frac{r_1 - (r_1 - 2r_3)(1 - 2r_2)^3}{[r_1 - (1 - 2r_2)(r_1 - 2r_3)]^2}$	$\frac{1}{12} \cdot \frac{r_1 - (r_1 - r_3)(1 - 2r_2)^3}{[2r_1r_2 + (1 - 2r_2)r_3]^2}$	$\frac{1}{4\pi} \cdot \frac{1 - (1 - r_4)^4}{[1 - (1 - r_4)^2]^2}$
$\beta$	$\frac{1}{12} \cdot \frac{r_1^3 - (1 - 2r_2)(r_1 - 2r_3)^3}{[r_1 - (1 - 2r_2)(r_1 - 2r_3)]^2}$	$\frac{1}{12} \cdot \frac{2r_1^3r_2 + (1 - 2r_2)r_3^3}{[2r_1r_2 + (1 - 2r_2)r_3]^2}$	
$\gamma$	$\frac{(1 - r_2)(r_1 - r_3)^2(r_2 + r_3)}{(1 + r_1 - r_2 - r_3)[r_1 - (1 - 2r_2)(r_1 - 2r_3)]^2}$	$\frac{1}{3} \cdot \frac{2r_1r_2^3 + (1 - r_2)r_3^3}{[2r_1r_2 + (1 - 2r_2)r_3]^2}$	$\frac{1}{2\pi} \cdot \frac{1 - (1 - r_4)^4}{[1 - (1 - r_4)^2]^2}$

Before utilising Eq. (6.12) to update the current design, it is necessary for the unknown

LM at the current iteration  $\lambda^{(p)}$  to be known. To this aim, the change in the total strain energy between two successive iterations can be expressed by the approximation to a first-order Taylor series expansion about the DVs as

$$U_{\text{total}}^{(p+1)} - U_{\text{total}}^{(p)} = \sum_{i=1}^n (\partial U_{\text{total}} / \partial a_i)^{(p)} (a_i^{(p+1)} - a_i^{(p)}). \quad (6.19)$$

Using Eq. (6.5) for  $U_{\text{total}}$  in conjunction with Eq. (6.11), the partial derivative  $(\partial U_{\text{total}} / \partial a_j)^{(p)}$  can be written as

$$\left( \frac{\partial U_{\text{total}}}{\partial a_j} \right)^{(p)} = (\bar{u}_j^{(p)} + d_j^{(p)}) \cdot l_j. \quad (6.20)$$

Upon substitution of Eqs. (6.12) and (6.20) into Eq. (6.19) (assuming all DVs are active, i.e.,  $a_j^{(p+1)} - a_j^{(p)} = a_j^{(p)} / \eta [\lambda^{(p)} (\bar{u}_j^{(p)} + d_j^{(p)}) - 1]$ ), the following relation is established after some algebraic manipulation

$$\lambda^{(p)} \sum_{j=1}^N [(\bar{u}_j^{(p)} + d_j^{(p)})^2 \cdot l_j \cdot a_j^{(p)}] = \sum_{j=1}^N [(\bar{u}_j^{(p)} + d_j^{(p)}) \cdot l_j \cdot a_j^{(p)}] + \eta (U_{\text{total}}^{(p+1)} - U_{\text{total}}^{(p)}), \quad (6.21)$$

where  $U_{\text{total}}^{(p+1)}$  and  $U_{\text{total}}^{(p)}$  represents the total strain energies of the structure due to the applied loads at two successive iterations. The latter quantity at iteration  $p$  can be evaluated by Eq. (6.15).

Let the equality energy constraint in Eq. (6.1) be satisfied after  $p$  iterations such that  $U_{\text{total}}^{(p+1)} = U_{\text{target}}$ . By substituting this equality into Eq. (6.21), one obtains

$$\lambda^{(p)} = \frac{\sum_{j=1}^N [(\bar{u}_j^{(p)} + d_j^{(p)}) \cdot l_j \cdot a_j^{(p)}] + \eta (U_{\text{target}} - U_{\text{total}}^{(p)})}{\sum_{j=1}^N [(\bar{u}_j^{(p)} + d_j^{(p)})^2 \cdot l_j \cdot a_j^{(p)}]}, \quad (6.22)$$

which can be used for computing the LM at the current iteration  $p$ .

At this junction, the iterative application of Eq. (6.12) for  $a_j^{(p+1)}$  and Eq. (6.22) for  $\lambda^{(p)}$  until convergence of the self-weight and the LM, the optimal solution  $\mathbf{a}^*$  of the sizing OP subject to the equality strain energy constraint is achieved. Note that in using Eq. (6.22), it is necessary to select a proper initial value for the LM at  $p = 1$  which influences the rate of convergence of

the proposed method. Experience shows that the initial value can be estimated using Eq. (6.22) by neglecting the contributions of  $d_j$  terms, i.e.,  $d_j = 0$ . The above sizing optimisation process is explained graphically in the algorithmic flowchart shown in Fig. 6.1.

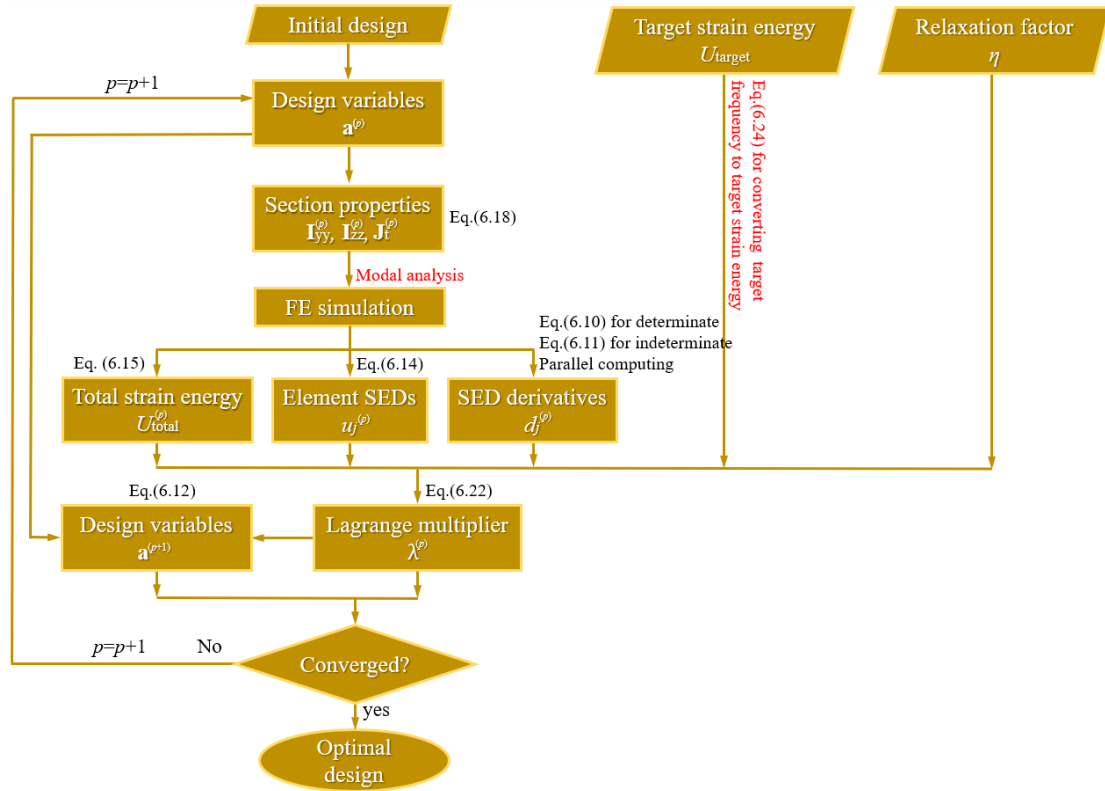


**Fig. 6.1.** Flowchart of sizing optimisation process for minimising material usage while satisfying the total strain energy constraint.

### 6.3.2 Expressing target frequency in terms of modal strain energy

In formulating the sizing OP in Eq. (6.1), the total strain energy is adopted as the state variable of the OP. It is therefore necessary to express the constraint on the natural frequency of a chosen mode in terms of modal strain energy. To this aim, consider the equation of motion for a discrete structural system with  $n$  elements and  $m$  DOFs in undamped free vibration give as

$$\frac{1}{2} \boldsymbol{\phi}_k^T \mathbf{K} \boldsymbol{\phi}_k = \frac{1}{2} \omega_k^2 \boldsymbol{\phi}_k^T \mathbf{M} \boldsymbol{\phi}_k \quad (k = 1, \dots, m), \quad (6.23)$$

where  $\mathbf{K} \in \mathbb{R}^{m \times m}$  and  $\mathbf{M} \in \mathbb{R}^{m \times m}$  are the elastic stiffness matrix and mass matrix of the structure, while  $\omega_k$  and  $\boldsymbol{\phi}_k \in \mathbb{R}^{m \times 1}$  are the circular frequency and mode shape vector for mode  $k$  respectively. The product  $\omega_k^2 \mathbf{M} \boldsymbol{\phi}_k$  on the right-hand side of Eq. (6.23) represents the applied-inertia load vector  $\mathbf{f}_{l,k} \in \mathbb{R}^{m \times 1}$  for mode  $k$ , whereas the entire left-hand side gives the modal strain energy  $U_k$  of the structure due to the applied-inertia load  $\mathbf{f}_{l,k}$ . Thus, the free-vibration motion may be

considered to involve deflections produced by inertial forces acting as applied loads. If the mode shape vector is normalized such that  $\boldsymbol{\phi}_k^T \mathbf{M} \boldsymbol{\phi}_k = 1$ , the modal strain energy  $U_k$  can be then expressed in terms of  $\omega_k$  as

$$U_k = \frac{1}{2} \omega_k^2 = \frac{1}{2} \boldsymbol{\phi}_k^T \mathbf{K} \boldsymbol{\phi}_k \quad (k = 1, \dots, m), \quad (6.24)$$

Based on Eq.(6.24), the constraint on the structure's  $k$ -th natural frequency can be converted to an equivalent constraint on the respective modal strain energy. The latter can be used as the target strain energy  $U_{\text{target}}$  in Eq. (6.1). In conjunction with the sizing optimisation algorithm presented in the last section, a FE-based optimal design procedure can be implemented as illustrated by the flowchart in Fig. 6.1 to refine the DVs iteratively towards the optimal solution  $\mathbf{a}^*$  that minimises the structural weight while meeting the target natural frequency for *any* chosen vibration mode.

#### 6.4 Convexity of the frequency-constrained sizing optimisation problem

The OP formulated in section 6.2 is that of minimising the structural volume/weight of a skeletal structure subject to a single equality constraint on the natural frequency of a chosen eigenmode. The latter BC is restated in terms of modal strain energy first before it enters the OP formulation in Eq. (6.1). It is assumed that the structure to be optimised has a fixed topology, and cross-section areas of the members are the DVs. This implies that the OF, i.e., the volume, depends linearly on the DVs and is therefore strictly convex. However, the nonlinear BC functions may give rise to a nonconvex feasible region/set in the design space (Svanberg 1984). Then, there is a risk that a local, but not global, minimum is attained when the derived OC (see Eqs. (6.7) and (6.8)) is satisfied through applying the numerical resizing procedure detailed in section 6.3 to the structure. Therefore, it is important to ensure the strict convexity of the OP (i.e., the OF is strictly convex over a convex and compact feasible set) so that, due to the linearity of the OF, each local optimum is also a global one (Christensen and Klarbring 2009). For the herein considered OP, the convexity of the feasible solution set  $S$  relies on the set  $C$  (where  $C = \{\mathbf{a} \mid U_{\text{total}}(\mathbf{a}) = U_{\text{target}}\}$ ) since the intersection of any two convex sets (say  $A = \{\mathbf{a} \mid \mathbf{a}_{\min} \leq \mathbf{a} \leq \mathbf{a}_{\max}\}$  and  $C$ ) is also a convex set. For this reason, the convexity of  $C$  is examined hereafter for the frequency constraint considered in section 6.3.2.

To this aim, the set  $C$  is first rewritten as  $C = \{\mathbf{a} \mid 1/2 \omega_k(\mathbf{a})^2 = U_{\text{target}}\}$  by using Eq. (6.24), where  $\omega_k$  denotes the target frequency value for mode  $k$ , and  $U_{\text{target}}$  is the corresponding modal strain energy. It is proved in Svanberg (1984) that, for any vibration mode (say  $k$ ), let  $\Omega = \{\mathbf{a} \mid \omega_k(\mathbf{a}) = \omega\}$  where  $\omega$  is a given real positive number and  $\omega_k(\mathbf{a}): \Omega \rightarrow \mathbb{R}$  ( $k=1, \dots, m$ ), the natural frequency  $\omega_k(\mathbf{a})$  and the feasible solution set  $\Omega$  are both convex. This means that the Hessian matrix of the  $k$ -th natural frequency,  $\mathbf{H}(\omega_k) \in \mathbb{R}^{n \times n}$ , must be positive semidefinite assuming  $\omega_k(\mathbf{a})$  is twice continuously differentiable on  $\Omega$  (Christensen and Klarbring 2009), i.e.,  $\mathbf{y}^T \mathbf{H}(\omega_k) \mathbf{y} \geq 0$



for all  $\mathbf{y} \in \mathbb{R}^{n \times 1}$  and  $\mathbf{y} \neq \mathbf{0}$ . Then,  $C$  must also be convex as the Hessian matrix of the natural frequency squared, i.e.,

$$\mathbf{H}(\omega_k^2) = 2(\nabla \omega_k)^T (\nabla \omega_k) + 2\omega_k \mathbf{H}(\omega_k), \quad (6.25)$$

is also positive semidefinite due to following inequality

$$\begin{aligned} \mathbf{y}^T \mathbf{H}(\omega_k^2) \mathbf{y} &= 2\mathbf{y}^T \left[ (\nabla \omega_k)^T (\nabla \omega_k) \right] \mathbf{y} + 2\omega_k \mathbf{y}^T \mathbf{H}(\omega_k) \mathbf{y} \\ &= 2 \left( \sum_{i=1}^n \frac{\partial \omega_k}{\partial a_i} y_i \right)^2 + 2\omega_k \mathbf{y}^T \mathbf{H}(\omega_k) \mathbf{y} \geq \mathbf{0}, \end{aligned} \quad (6.26)$$

since  $\mathbf{y}^T \mathbf{H}(\omega_k) \mathbf{y} \geq 0$  and  $\omega_k > 0$ , and the squared term in Eq. (6.26) is always nonnegative. Therefore,  $C = \{\mathbf{a} \mid 1/2\omega_k(\mathbf{a})^2 = U_{\text{target}}\}$  gives a convex set within the DV plane. Since  $S = A \cap C$ , the feasible set  $S$  is convex and compact (because of the box constraint  $A$ ), and there exists only one local/global optimum to the OP under the frequency constraint.

## 6.5 Illustrative application and validation of sizing optimisation method

The proposed sizing OP and its LM-based numerical solution method relies on the intuition that at the optimal design point  $\mathbf{a}^*$ , the OF  $V(\mathbf{a})$  cannot decrease in the direction of any such neighbouring point of  $\mathbf{a}^*$  that also satisfies the BC,  $U_{\text{total}}(\mathbf{a}) = U_{\text{target}}$ . Moreover, at the optimum, the contour line of the OF must be tangential to the BC curve; otherwise, one could “walk” along the constraint curve to descend, meaning that the point is not the minimum. In this section, this geometric interpretation for minimum weight design of skeletal structures is adopted to illustrate and validate the proposed OP and its numerical solution. To this aim, a simple structure with only two DVs is considered which can be readily solved graphically using the above geometric interpretation. The structure is a planar portal frame consisting of three structural elements and two DVs (one for the girder and one for the columns), as depicted in Fig. 6.2 (a). The OP involves determining optimal cross-sectional areas of the girder and columns,  $[a_1^*, a_2^*]$ , that minimise the structural volume while satisfying a constraint on the structural fundamental frequency. The two DVs are bounded by the side constraint  $\mathbf{a} \in [\mathbf{a}^{\min}, \mathbf{a}^{\max}]$ , where  $\mathbf{a}^{\min} = [1.0a_{1,o}, 1.0a_{2,o}]$  and  $\mathbf{a}^{\max} = [2.0a_{1,o}, 2.0a_{2,o}]$  with the subscript “o” denoting the initial design. The target fundamental frequency  $\omega_{\text{target}}$  is arbitrarily set to 1.5 times that of the initial structure, i.e.,  $\omega_{\text{target}} = 1.5\omega_{1,o}$ . The corresponding target value in terms of modal strain energy is  $U_{\text{target}} = 2.25U_{1,o}$  derived by using Eq. (6.24).

The problem is initially solved graphically using MATLAB, as shown in Fig. 6.2 (b) and (c). Specifically, Fig. 6.2 (b) plots the modal strain energy surface  $U_{\text{total}}(\mathbf{a})$  caused by the first modal inertia load vector  $\mathbf{f}_{1,1}$  defined in last section, and target energy plane  $U_{\text{target}}$  on the DV

plane  $(a_1, a_2)$ . Both surfaces are normalized by the modal strain energy of initial structure  $U_{1,o}$  such that  $U_{total}(a_{1,o}, a_{2,o})=1.0$  and  $U_{target}=2.25$ . Figure 6.2 (b) shows that the two surfaces intersect at the red dotted curve, which defines the BC for the DVs to satisfy. This curve is then projected onto the normalized OF surface  $V(\mathbf{a})$  (by the volume of initial structure) plotted in the  $a_1$ - $a_2$ - $V(a_1, a_2)$  design space to form another red dotted curve in Fig. 6.2 (c). Evidently, the lowest point on this curve corresponds to the minimum-weight design that satisfies the considered frequency constraint. Quantitatively, Fig. 6.2 (c) reveals that the two DVs need to increase to  $[1.6700a_{1,o}, 1.2227a_{2,o}]$  respectively for the MRF to see an increase in its fundamental frequency from  $\omega_{1,o}$  to  $1.5\omega_{1,o}$ . Accordingly, the volume of material required for this increase is about 44.64% of the initial design, i.e.,  $V(\mathbf{a}^*)=1.4464V(\mathbf{a}_o)$ . Evidently, this solution is exact for the problem at hand and can thus be used as a testbed to validate the numerical scheme in Fig. 6.1.

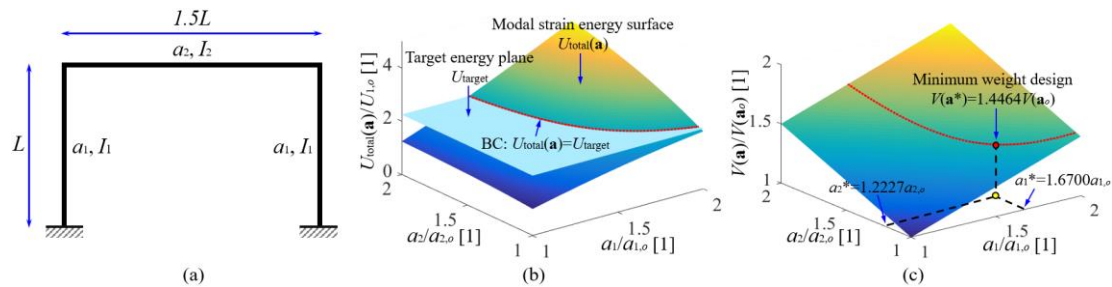


**Fig. 6.2.** (a) The planar cantilever system consisting of two beam elements and six DOFs; (b) modal strain energy surface versus target energy plane; and (c) surface of objective function and optimal solution point.

Next, the same OP is solved numerically using the iterative sizing algorithm presented in the previous sections. Variations of fundamental frequency, material volume, and LM value are plotted in Figs. 6.3 (a), (b), and (c), respectively, throughout the iterative optimisation process. Results from two independent solutions of the optimal design problem are plotted together in Fig. 6.3 to demonstrate the influence of different OC on the convergence of the iterative process and on the accuracy of the optimal solutions reached. In the first optimisation solution (denoted by 1OC), only the first OC in Eq. (6.7) requiring all structural elements to be equal in terms of SED is adopted by setting  $d_j = 0$  in Eq. (6.12), (6.17), and (6.22) for the three elements. As discussed previously, by setting  $d_j$  in these equations to zero, the uniform SED-based OC approach is retrieved. In the second optimisation solution (denoted by 2OC), both the OCs in Eqs. (6.7) and (6.8) are fulfilled simultaneously, which constitutes the main novelty of the herein presented optimal sizing approach, by following the numerical procedure detailed in Fig.6.1. The latter requires the evaluation of  $d_j$  for all elements at every iteration. Results in Fig. 6.3 (a) and (b) evidence that both the OC approaches are able to closely resolve the optimal DVs which minimise the self-weight as the exact (graphical) method presented above. Specifically, the 1OC converged after 183 iterations, giving a slightly heavier design by about 2.60% than the graphical method, while the second 2OC approach with two simultaneous OC

converged much faster after 19 iterations, giving a near-optimal overdensity by 1.62% only. In this regard, it is evident that the herein proposed OC approach is more accurate from the standard approach found in the literature, while it converges much faster.

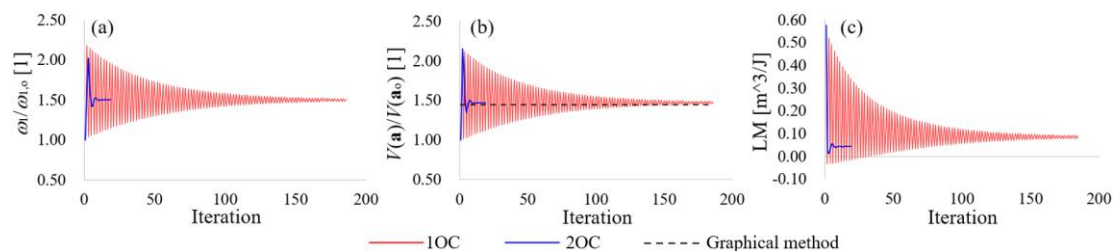


**Fig. 6.3.** variations of (a) fundamental frequency and (b) volume of structural material of the planar MRF, values normalized by corresponding values of the initial structure; and (c) Lagrangian multiplier throughout the sizing optimisation process.

## 6.6 Closure

In this chapter, a formulaic yet rigorously valid resizing algorithm, based on a novel OC concerning volume-averaged SEDs of structural elements (e.g., bars, beams, and frames), is developed for the minimum-weight design of skeletal structures with fixed layout under a frequency constraint on any chosen vibration mode. Through mathematical argument, the strict convexity of the OP is proved so that, if a stationary point exists in the feasible design set, it is guaranteed to be the global optimum to the frequency-constrained weight-minimisation problem. The method is exemplified by a planar portal frame with two active DVs only and validated/verified against a graphical method applying the geometric interpretation of the LM theorem. Numerical results show that the convergence behaviour of the resizing process, with coupled relations (for updating the DVs) derived from the herein proposed OC, is improved significantly compared to the conventional OC methods based on the uniform SED criterion and conjectured separability/uncoupled relations. As a remark, the formulation can be easily extended/generalised to tackle displacement- or buckling/stability-constrained sizing OPs of skeletal structures by restating all performance constraints (i.e., upper displacement limits, lowest buckling load factor of a chosen eigenmode) in terms of strain energy of the structures. To this end, the OP formulation in Eq. (6.1) and the corresponding numerical routines in Eq. (6.12) for updating the DVs and Eq. (6.24) for evaluating the LM can be applied directly to solve buckling- or displacements-constrained OPs.

In the following Chapter, the herein proposed sizing algorithm is used in conjunction with the TMDI tuning method detailed in Chapter 3 for the integrated tall building-plus-TMDI optimal design to meet the code-prescribed comfort requirement while minimising material usage of the primary structural system.

## Chapter 7

---

### Integrated Optimal Design of DVA-Equipped Wind Excited Buildings for Weight Minimisation and Occupant Comfort

#### 7.1 Preliminary remarks

As discussed in Chapter 1, lateral stiffening of VS-prone tall buildings (by increasing member sizes without changing the structural system) cannot efficiently address the serviceability occupant comfort requirement associated with floor accelerations (Simiu and Scanlan 1996, Ricciardelli et al. 2003). This strategy may lead to a feasible/code-compliant but heavy design that is neither material-efficient nor cost-effective (cf. the illustrative example in Chan and Chui 2005). In this regard, Chapters 3 and 5 explored the use of optimally tuned inerter-based DVAs for efficient vibration mitigation of wind-excited ultra-tall and high-rise buildings to meet occupant comfort criteria without the need of any structural modification/stiffening. Nevertheless, the therein considered TMD(I)s are designed independently from the primary/host structure which is taken as fixed. In this regard, no effort has been undertaken so far to design the tall building-plus-TMDI structural system in an integrated manner for structural efficiency and code-compliance.

In this context, this chapter proposes a novel framework for the optimal design of inerter-based DVA-equipped tall buildings governed by comfort criteria to achieve the *concurrent* self-weight reduction of the primary structural system and optimal vibration control of the absorber through a *two-staged, sequential* optimisation. Specifically, in the first stage, a sizing optimisation is performed using the OC-based resizing approach detailed in Chapter 6 and applied to the detailed FE model of an uncontrolled building to minimise its structural self-weight while satisfying a specified target fundamental frequency. In the second stage, the optimised minimum-weight structure is equipped with an optimally tuned TMDI (with fixed inertial properties and connectivity) to minimise its crosswind floor accelerations using the tuning method elaborated in Chapter 3. A low-order model, capturing the detailed (building) model's dynamic attributes accurately (see Section 3.3.2), is used to facilitate an efficient solution for optimal TMDI tuning and performance assessment of the optimally controlled building. Wind excitation is modelled as a spatially-correlated crosswind force field accounting for VS effects. This integrated design framework, involving sizing optimisation of the host structure, optimal TMDI design/tuning, and performance assessment of optimal TMDI-controlled minimum-weight structure, is iterative and seek for the size-optimal primary structure with an adequate fundamental frequency. In this respect, it is repeatedly executed until the building's critical fundamental frequency is determined. The latter is the minimum value of the fundamental frequency, below which the optimally controlled floor accelerations would no

longer satisfy the serviceability comfort constraint. In this regard, the proposed design framework utilises the fact that the crosswind-induced floor accelerations are inversely related to the primary structure's fundamental frequency within the frequency range (i.e., from 0.1Hz to 1.0Hz) for serviceability check (Chan and Chui 2006). At this point, it needs to be emphasised that this optimisation methodology/strategy is sequential, that is, it does not optimise the primary structural system and the vibration controller simultaneously. In this regard it might miss the theoretical optimum of the integrated system. Notwithstanding this pitfall, it provides a practical way of achieving concurrent self-weight reduction and optimal vibration control, thus paving the way towards material-efficient, wind-resilient tall building design.

As a case-study, a 15-storey steel MRF structure equipped with a ground-floor TID is adopted as the case-study structure to demonstrate the applicability and usefulness of the proposed design framework. Importantly, the consideration of a ground-floor TID is inspired by several studies (Lazar et al. 2014, Zhang et al. 2017, Giaralis and Taflanidis 2018) demonstrating the high efficiency of this DVA in controlling earthquake-induced vibrations in multi-storey buildings. Its rationale is supported by the fact that top-floor DVA placement sacrifices high premium space in the upper floor(s) which may not be applicable in routine mid-to-high-rise structures. Addressing such structures becomes a priority in this Chapter to demonstrate the potential impact of the proposed design framework together with employment of inerter-based DVAs in everyday engineering practice and the resulting material savings in routine structures.

## **7.2 A novel framework for minimal-weight design of inerter-based DVA-equipped tall buildings to meet cross-wind serviceability criteria**

This section presents a novel structure-plus-inerter-based DVA optimal design framework for simultaneous material use reduction and vibration mitigation of wind-excited building structures governed by serviceability occupant comfort criteria in the cross-wind direction. To date, in the scientific literature and practical design of DVA-equipped tall buildings, the control device has been designed and treated as a retrofitting measure to improve the habitability of wind-excited, inherently deficient buildings. Herein, it is proposed to optimise the building's lateral load resisting structural system and the DVA in an integrated manner to achieve optimal DVA-equipped building structures for own-weight minimisation based on material efficiency considerations. To this end, an integrated design cycle, entailing a two-staged optimisation (first for the host structure and then for the control device) followed by a performance assessment (of the optimal DVA-equipped building), is executed iteratively for the DVA-controlled host structure to find its critical fundamental frequency for given wind action. The latter frequency is the threshold value below which the optimal DVA-equipped building would no longer meet the code-prescribed comfort requirement without changing/increasing the secondary design parameters of the control device (e.g., attached mass, inertance, inerter connectivity). For

elaboration, this design strategy is broken down into three steps detailed below and graphically illustrated in the flowchart of Fig. 7.1.

- (1) First, a series of sizing optimisation runs are conducted, targeting different gradually increasing fundamental frequencies starting from the initial frequency  $f_i$  and at an increment of  $\Delta f$ . These runs are executed in parallel for numerical efficiency making use of the sizing algorithm developed in Chapter 6. The goal is to ensure minimum material consumption for the primary structural system under the same side constraints on the member sizes.
- (2) Next, the series of the above derived optimal designs, all with minimum self-weights but different fundamental frequencies, are retrofitted with a same inerter-based DVA whose stiffness and damping properties are optimally determined for given secondary DVs using the generic TMDI tuning method presented in section 3.2. The aim is to minimise the floor acceleration under the design wind excitation at the top-most occupied storey. Performance assessment is conducted for *each* optimal DVA-controlled structure to plot the optimally controlled performance curve in terms of the selected floor acceleration. The latter curve is compared against the performance demand curve generated by relevant building codes/guidelines to interpolate the critical fundamental frequency  $f_c$ .
- (3) Finally, the critical frequency determined in step (2) is now used as the *target* fundamental frequency for the sizing optimisation of the primary structure, after which the DVA is optimally tuned for the optimally designed host structure and considered wind action to generate the ultimate integrated optimal design.

Notably, the above strategy is based on the following two facts. Firstly, wind-induced floor accelerations of tall buildings in both along-wind and crosswind directions are, in general, inversely related to their fundamental frequencies within the frequency range of 0.1 – 1.0 Hz (Tallin and Ellingwd 1983, Griffis 1993). Within this range, the dynamic wind forces and corresponding acceleration response of tall buildings can generally be reduced by increasing the building's fundamental frequency (Chan and Chui 2006). This provision shifts the resonant frequency away from the VS frequency, therefore reducing the excitation at the source. Indeed, for most tall buildings, the PSD function of wind force throughout the building height attenuate *rapidly* with the loading frequency increasing when the reduced frequency, i.e.,  $\omega B/(2\pi VH)$ , is larger than 0.1, where  $B$  is the building breadth in the crosswind direction, and  $VH$  denotes the hourly mean design wind speed at the building top (Islam et al. 1990). Secondly, the fundamental frequency of the *optimised* structure (with fixed layout) is inversely related to its self-weight, that is, the lower the fundamental frequency is, the less structural material is required for the *optimised* structure to achieve that target frequency. To facilitate computations, the proposed framework utilises a low-order model with one DOF per floor to facilitate an efficient solution for optimal DVA tuning and performance assessment of the



optimal DVA-equipped structure. However, consideration of the detailed FE model of the uncontrolled building is required for sizing optimisation of the primary structural system.

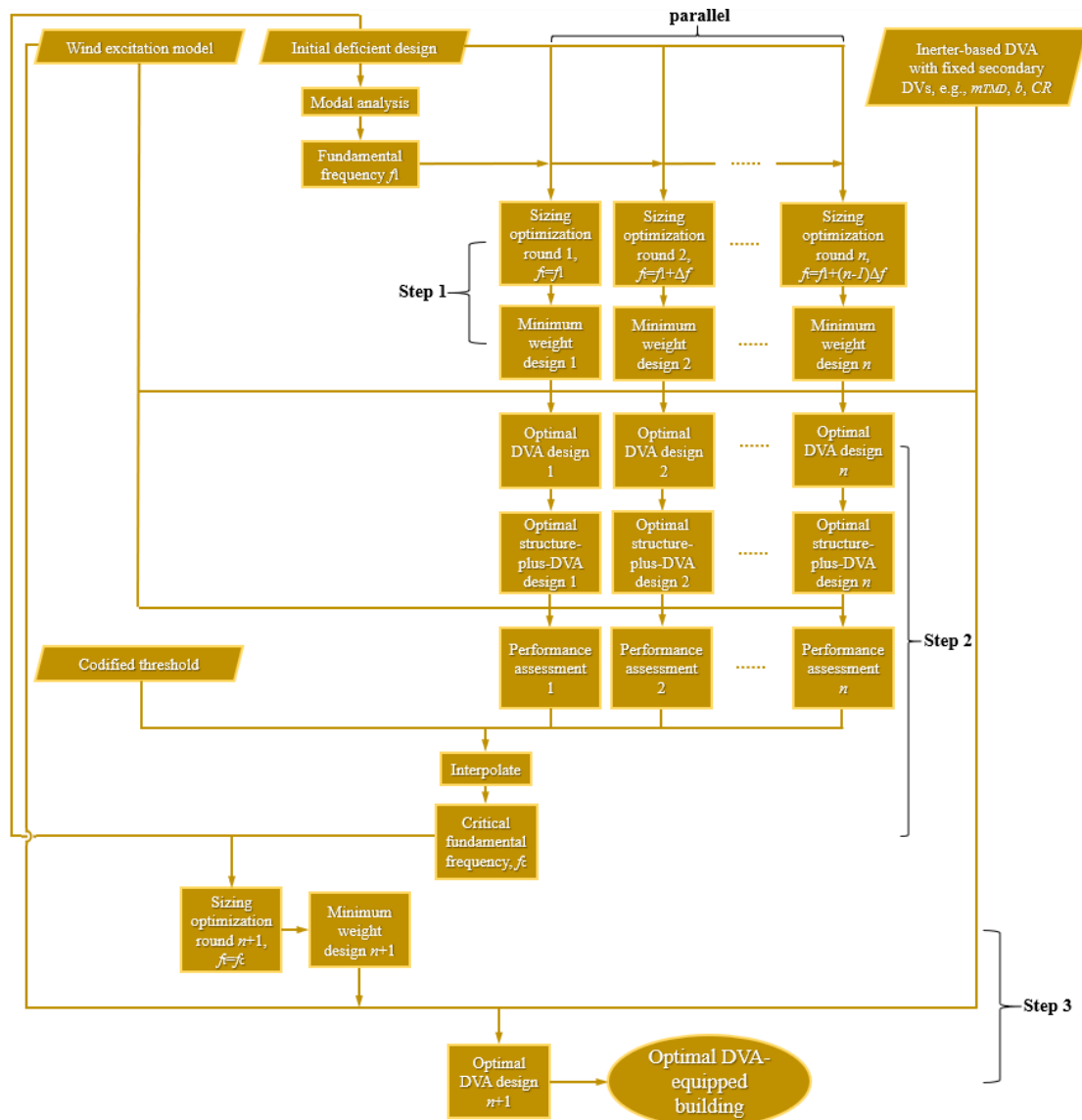


**Fig. 7.1.** Flowchart of novel framework for minimal-weight design of inerter-based DVA-equipped tall buildings to meet cross-wind serviceability criteria.

### 7.3 Modelling of case-study building structure and wind force excitation model

#### 7.3.1 Case-study building description and surrogate planar frame model

The case-study building considered for numerical demonstration of the proposed optimal integrated design framework is a doubly symmetric, 15-storey, 3-bay steel MRF building with 16.5m-by-16.5m footprint. It totals 49.8m of height: ground floor is 5.0m high, while the rest of the floors are 3.2m high. The structure comprises four parallel planar MRFs along each principal axis with all beam-to-column joints taken as rigid as shown in Fig. 7.2(a). Columns have hollow square sections with varying outer dimensions and thickness along the building height ranging between 0.48m and 0.32m, and 0.024m to 0.016m respectively. Beams are of



various welded wide flange sections with section height and flange width varying between 0.5m and 0.3m, and 0.3m and 0.18m, respectively. Horizontal perfectly rigid diaphragm constraints are imposed at the height of each floor in developing a detailed FE linear model of the structure in SAP2000® software package. By deactivating the out-of-plane DOFs, the first three natural frequencies of the building and corresponding modal mass participating ratios in parentheses are 0.548Hz (0.7118), 1.391Hz (0.1675), and 2.342Hz (0.0593). The building is designed to all serviceability and ultimate limit state requirements for static design load combinations including gravitational loads and mean wind component forces acting in the along-wind direction according to the relevant Eurocodes. The required steel tonnage (MRFs self-mass) is 471 tonnes.

To expedite computational work in later sections, a low-order planar dynamic model with 15 DOFs corresponding to the lateral in-plane translations of the rigid slabs is derived from the detailed FE model of the benchmark building using the modal-based procedure detailed in [Giarelis and Petrini \(2017\)](#). The 15-DOF model is defined in terms of a diagonal mass matrix, and full damping matrix and stiffness matrices. Building mass including nominal gravitational loads is lumped at each floor as shown in Fig. 7.1(b), while modal damping ratios for the  $j$ -th mode are taken as:  $\zeta_j=1\%$ , for  $j= 1,2,3$ ;  $\zeta_j= 2\%$  for  $j= 4,5,6$ ;  $\zeta_j= 4\%$  for  $j= 7,8,9$ ;  $\zeta_j=8\%$  for  $j= 10,11,12$ ; and  $\zeta_j=16\%$  for  $j= 13,14,15$ . The first three mode shapes obtained by the detailed FE model and the 15-DOF system match very well as shown in Fig. 7.2(c).

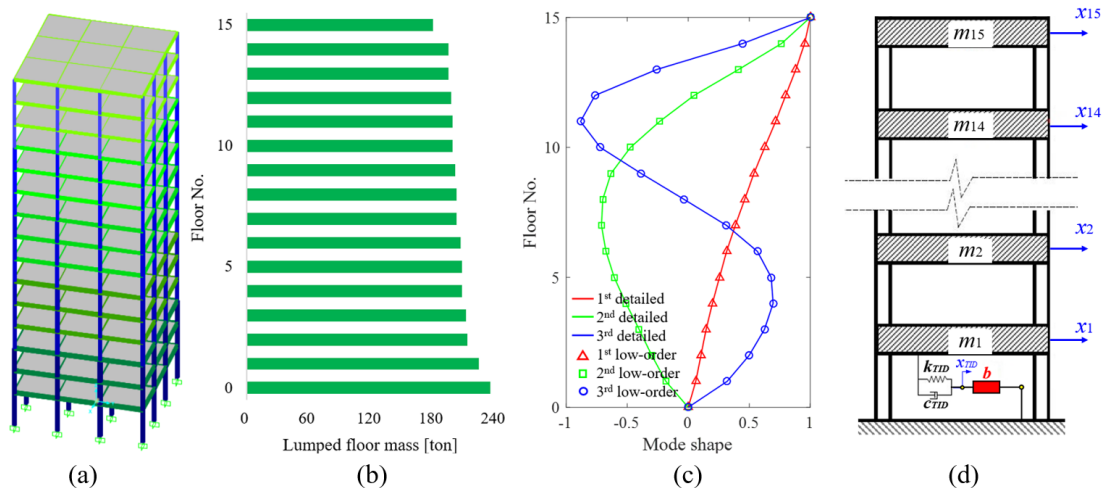


**Fig. 7.2.** Benchmark building structure: (a) detailed FE model; (b) lumped floor mass distribution along building height; (c) first three mode shapes obtained by the detailed FE and by the low-order models; and (d) ground-floor TID-equipped lumped-mass planar frame model of the benchmark building structure.

### 7.3.2 Crosswind force excitation model

The input wind action to the 15-storey (15-DOF) low-order model is herein represented by the stochastic crosswind force model developed in [Liang et al. \(2002\)](#) for buildings with rectangular footprint (refer also to Appendix B). This wind forcing model is based on

experimental data from a comprehensive wind tunnel testing campaign and accounts for both the turbulence and the VS components of the wind force in the crosswind direction, the latter being critical for occupants' comfort. It is defined by a zero-mean stationary Gaussian spatially correlated random field represented in frequency domain by a full PSD matrix. For the 15-DOF dynamic model, a  $\mathbf{S}_{FF}^{15} \in \mathbb{R}^{15 \times 15}$  wind force PSD matrix is determined upon spatial discretisation of the wind random field at each building floor. Herein, the logarithmic mean wind velocity profile of Eurocode 1 (EN 1991-1-4: 2005) is assumed for rough/urban terrain and for a (moderate) basic wind speed of 20m/s (i.e., 10mins mean wind velocity at 10m height above open flat terrain) plotted in Fig. 7.3(a). For this wind profile, wind force PSDs at three different floor slab heights are plotted in Fig. 7.3(b) following Liang et al. (2002). It is seen that the dominant VS frequency increases with floor height. The same happens for the wind force amplitude except from the last floor whose tributary height is only 1.6m. That is, half of the tributary height of typical floors.

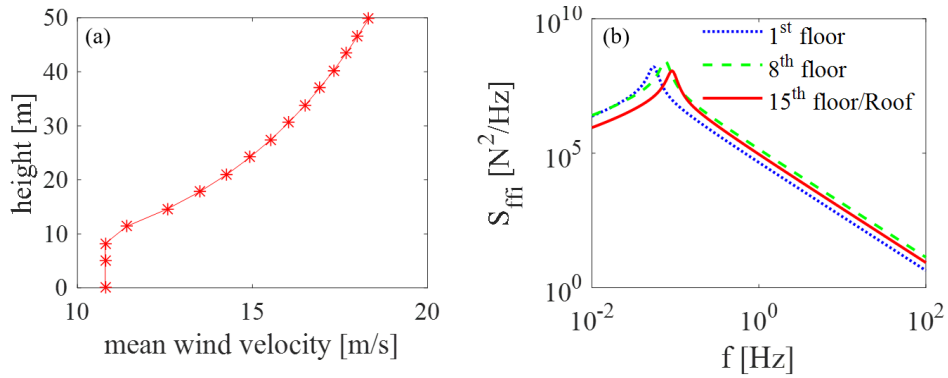


**Fig. 7.3.** Assumed wind excitation model: (a) mean wind velocity profile; (b) power spectral density functions of crosswind forces acting at different floor levels of the benchmark structure.

### 7.3.3 Assessment for occupant comfort criteria in the crosswind direction

Occupant comfort for the case study building is assessed against the [ISO Standard 6897 criterion which is based on the RMS floor acceleration defined as](#)

$$\ddot{\sigma}_a = \exp(-3.65 - 0.41 \ln f_1). \quad (7.1)$$

The above comfort threshold value,  $\ddot{\sigma}_a$ , is frequency-dependent: the higher the building's fundamental frequency  $f_1$  is, the more stringent the threshold becomes. To this end, increasing the lateral stiffness of VS-prone buildings cannot efficiently address the comfort deficiency as the code requirement would also tighten as the fundamental frequency increases. The reason for adopting the ISO 6897:1984 standard (as opposed to CNR-DT 207/2008 in Chapters 3 and 5) in the current chapter is that, here, the building's fundamental frequency,  $f_1$ , changes significantly (see Section 7.4.1) due to sizing optimisation for different target frequencies,

which is not the case in previous chapters where the buildings’ fundamental frequencies stay practically constant. Then, the peak factor,  $g$  (see Eq. (A.7)), for converting the RMS response to peak response will also change with  $f_1$  even though the time of exposure,  $T_{wind}$ , remains the same. In this setting, it is more straightforward to gauge the building habitability in terms of RMS floor accelerations instead of the peak ones, as evaluation of the latter requires further conversions through different peak factors.

Whilst the case-study building in Fig. 7.2(a) satisfies all requirements for *static* design load combinations, it is found to be deficient for the occupant comfort criterion in Eq. (7.1) under the moderate wind action defined in Fig. 7.3. To demonstrate the inadequacy of the case-study building, Fig. 7.4(a) reports the RMS accelerations developed at each floor of the initial building structure (solid orange curve) along the building height under the wind action shown in Fig. 7.3, together with the comfort threshold value for initial fundamental frequency 0.548 Hz (black dashed line). It is seen that the RMS acceleration is over the limit value at the last two occupied floors (excluding the unoccupied roof), indicating the code-deficiency of the case-study building.

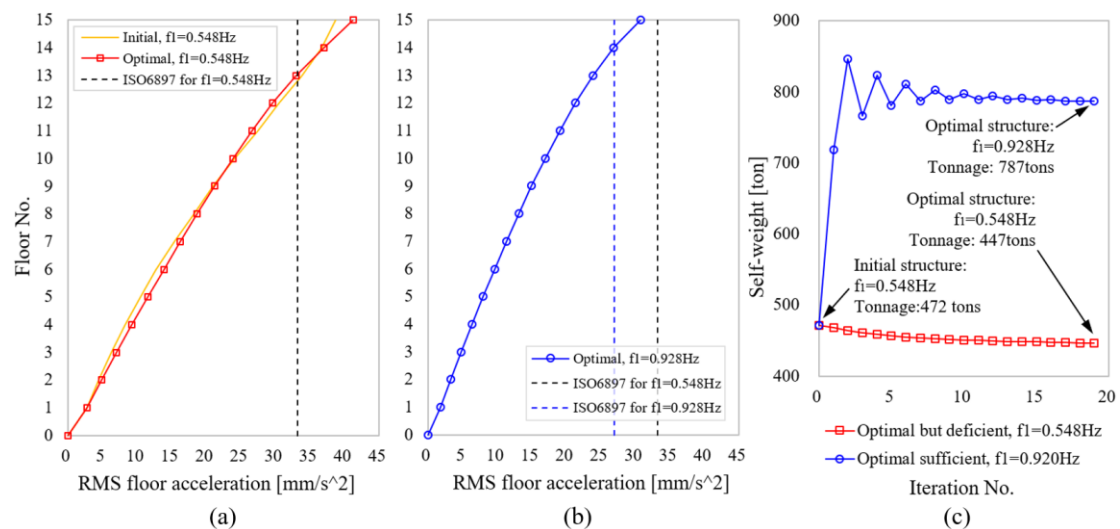


**Fig. 7.4.** RMS floor accelerations of (a) initial non-optimal structure and optimally re-designed structure with target fundamental frequency 0.548 Hz and of (b) optimally re-designed structure with target fundamental frequency 0.928 Hz, together with respective ISO6897 occupant comfort thresholds; (c) variation of total weight of structure throughout the optimal re-design process.

## 7.4 Re-design of uncontrolled case-study building and optimal TID tuning for occupant comfort

### 7.4.1 Re-design of uncontrolled benchmark structure for occupant comfort

The uncontrolled building in Fig. 7.2(a) is herein re-designed to satisfy the [ISO 6897](#) standard while minimising its own-weight. This is achieved by applying the optimally sizing OC-based approach developed in Chapter 6 to the initial structure which involves increasing its fundamental frequency to such a critical value that the uncontrolled RMS floor accelerations

at all floors (except the roof) drop below the [ISO 6897](#) limit value. This critical frequency, which also serves as the target frequency for the uncontrolled structure, is found to be 0.928Hz by interpolation. To shed further light on this resizing process, Fig. 7.4(c) traces the MRF self-weight variation throughout the iterative application of the OC-based algorithm, starting with the initial deficient design. The latter has a total self-mass of 472 tonnes and fundamental frequency 0.548Hz. The iterative process converged at 787tons with the fundamental frequency increased to the target value (i.e., 0.928Hz) after 19 iterations. Consideration of further iterations improves neither the self-weight nor the structural performance, i.e.,  $\text{RMS}\{\ddot{x}_{14}\}$ . The RMS floor accelerations of the optimally re-designed structure with  $f_1=0.928\text{Hz}$  are plotted in Fig. 7.4(b) (solid blue line with circular markers), together with the corresponding [ISO 6897](#) threshold (blue dashed line). The latter has decreased (i.e., became more stringent) since the re-designed structure has a higher fundamental frequency. It is seen that the code-prescribed requirement is satisfied at all occupied floors, and the floor accelerations have reduced noticeably compared to those of the initial design. However, this is achieved at the expense of 315tonnes of additional steel (i.e., 67% increase of steel tonnage).

To further demonstrate the effectiveness of the resizing algorithm in section 6.2, the initial deficient building is optimised again for the *original* fundamental frequency of 0.548Hz. The performance of the optimal, though deficient, design (solid red curve with square markers) is added in Fig. 7.4(a) with the corresponding self-weight variation plotted in Fig. 7.4(c). It is seen in Fig. 7.4 that, although the primary structure is optimised to have a reduced self-weight (from 472tonnes to 447tonnes) while still achieves the same fundamental frequency (0.548Hz), the overall acceleration performance does not improve noticeably as the fundamental frequency remains the same. In this context, in the following section, an optimally designed ground-floor TMDI with no secondary mass (i.e., a TID) is considered for this optimal but infeasible design to meet the occupant comfort requirement without demanding any additional steel to stiffen the lateral load-resisting system.

#### **7.4.2 TID-equipped tall building modelling and structural analysis for crosswind excitation**

The modelling of the TID and its incorporation to the case-study building is schematically shown in Fig. 7.2(d) depicting a low-order 15-DOF model as a planar 15-storey frame-like building with lumped floor masses  $m_k$  and lateral floor displacements  $x_k$  ( $k=1,2,\dots,15$ ). The low-order model is derived from the detailed FE model of the benchmark structure following the same approach as in Section 3.3.2 (see also [Giaralis and Petrini 2017](#)). The TID consists of a visco-elastic link, modelled as a linear spring with  $k_{TID}$  stiffness in parallel with a dashpot with damping coefficient  $c_{TID}$ , which connects one terminal of the inerter element, highlighted in red in Fig. 7.2(d), with the first-floor slab. The second inerter terminal is fixed to the ground. In this regard, the inerter element force reads as

$$F_b = b\dot{x}_{TID}, \quad (7.2)$$

where  $x_{TID}$  is the lateral TID displacement shown in Fig. 7.2(d) and a dot over a symbol signifies differentiation with respect to time.

Mathematically, the mass,  $\mathbf{M}$ , damping,  $\mathbf{C}$ , and stiffness,  $\mathbf{K}$ , matrices of the TID-equipped lumped-mass 15-DOF model in Fig. 7.2(d) are given as

$$\mathbf{M} = \begin{bmatrix} b & 0 & 0 & \cdots & 0 & 0 \\ & m_1 & 0 & \cdots & 0 & 0 \\ & & m_2 & \cdots & 0 & 0 \\ & & & \ddots & \vdots & \vdots \\ & SYM & & & m_{14} & 0 \\ & & & & & m_{15} \end{bmatrix}, \quad \mathbf{C} = \begin{bmatrix} c_{TID} & -c_{TID} & 0 & \cdots & 0 & 0 \\ & c_{1,1} + c_{TID} & c_{1,2} & \cdots & c_{1,14} & c_{1,15} \\ & & c_{2,2} & \cdots & c_{2,14} & c_{2,15} \\ & & & \ddots & \vdots & \vdots \\ & SYM & & & c_{14,14} & c_{14,15} \\ & & & & & c_{15,15} \end{bmatrix},$$

$$\text{and } \mathbf{K} = \begin{bmatrix} k_{TID} & -k_{TID} & 0 & \cdots & 0 & 0 \\ & k_{1,1} + k_{TID} & k_{1,2} & \cdots & k_{1,14} & k_{1,15} \\ & & k_{2,2} & \cdots & k_{2,14} & k_{2,15} \\ & & & \ddots & \vdots & \vdots \\ & SYM & & & k_{14,14} & k_{14,15} \\ & & & & & k_{15,15} \end{bmatrix}, \quad (7.3)$$

respectively, where  $c_{k,p}$  and  $k_{k,p}$  with  $k=1,\dots,15$  and  $p=1,\dots,15$  are the damping and stiffness coefficients of the low-order 15DOF system representing the uncontrolled optimised benchmark building. Response displacement, velocity, and acceleration PSD matrices, as well as corresponding RMS responses, of the TID-equipped structure subject to the wind force PSD matrix,  $\mathbf{S}_{FF}^{15} \in \mathbb{R}^{15 \times 15}$ , defined in section 7.3.2 can be obtained following the frequency domain analysis approach detailed in Appendix A.

### 7.4.3 Optimal TID design for minimum-weight host structure subject to occupant comfort requirement

In this section, a ground-floor TID is considered to mitigate crosswind-induced accelerations of the optimised but deficient structure with  $f_1=0.548\text{Hz}$  considered in Fig. 7.4(a) subject to VS effects associated with occupant comfort. To this aim, the optimal tuning problem in section 3.2 is adapted aiming to minimise the RMS floor acceleration at the highest occupied floor, i.e.,  $OF = \text{RMS}\{\ddot{x}_{14}\}$ . This is because RMS acceleration increases monotonically with building height in the crosswind direction of typical multi-storey buildings prone to VS effects

(see e.g. Fig. 7.4(a) and (b)). The problem DVs are the non-dimensional TID parameters defined as

$$\beta = \frac{b}{M}, \quad v_{TID} = \frac{\sqrt{k_{TID}/b}}{\omega_1}, \quad \text{and} \quad \xi_{TID} = \frac{c_{TID}}{2\sqrt{k_{TID}b}}, \quad (7.4)$$

namely, inertance ratio, frequency ratio, and damping ratio, respectively. In the last equation,  $M$  can be either the total building mass, the structural self-mass, or the generalised mass of the fundamental mode as before, while  $\omega_1$  is the first circular natural frequency of the uncontrolled (no TID-equipped) structure. Herein,  $M$  is taken as the self-weight of the primary structural system. The OP is solved numerically using the pattern search approach presented in section 3.2.2 with an evolving search domain. In this manner, optimal primary DVs, i.e., frequency ratio,  $v_{TID}$ , and damping ratio,  $\xi_{TID}$ , are determined to minimise the OF for the minimal-weight host structure, same wind excitation model, and fixed inertance ratio  $\beta$  treated as secondary DV.

To illustrate the above TID optimal design problem, Fig. 7.5 furnishes results from the application of the TMDI tuning method to the optimised but deficient structure under the wind force PSD matrix in section 7.3.2 to minimise  $\text{RMS}\{\ddot{x}_{14}\}$  or  $\sigma_{\ddot{x}_{14}}$ . The latter response is computed using Eq. (A.3) by setting  $k=14$  and then taking the square root of the corresponding acceleration variance. In doing so, practically meaningful range of values for the primary DVs are searched:  $v_{TID}$  is bounded in the [0.99, 1.01] range based on real-life TMD installations in high-rise buildings tuned to the first natural frequency  $\omega_1$ , while  $\xi_{TID}$  is bounded in the [0.00, 0.03] range to ensure realistic viscous damping coefficients. Strong convex behaviour of the OF on the primary DVs,  $v_{TID}$ - $\xi_{TID}$ , plane is noted with a single global optimal design point readily identified for inertance ratios  $\beta$  ranging within [0, 1] interval. It is found that the *required inertance ratio* in order for the optimised but deficient building with  $f_1=0.548\text{Hz}$  to be occupant-comfort adequate is 18.5% of the self-weight of the initial design (or  $b=87.27$  tonnes). The corresponding performance surface of the TID-equipped optimised structure, normalized by  $\text{RMS}\{\ddot{x}_{14}\}$  of the initial uncontrolled structure, is plotted in Fig. 7.5(a) on the  $v_{TID}$ - $\xi_{TID}$  plane for  $\beta=18.5\%$ . As seen, the optimal RMS acceleration at  $v_{opt}=1.004$  and  $\xi_{opt}=0.008$  is just below the codified threshold value of  $33.30 \text{ mm/s}^2$ , and hence confirming the feasibility of the integrated design. Further, optimal values of the primary DVs of the TID for the optimised structure are plotted in Fig. 7.5(b) as functions of  $\beta$  ranging within [0, 1]. It is seen that both DVs increase steadily with the inertance ratio except around  $\beta=0.20$ . Further, for all  $\beta$  ratios considered, the optimal frequency ratio  $v_{TID}$  is always between 0.99 and 1.01, while the optimal damping ratio  $\xi_{TID}$  is between 0.00 and 0.03.

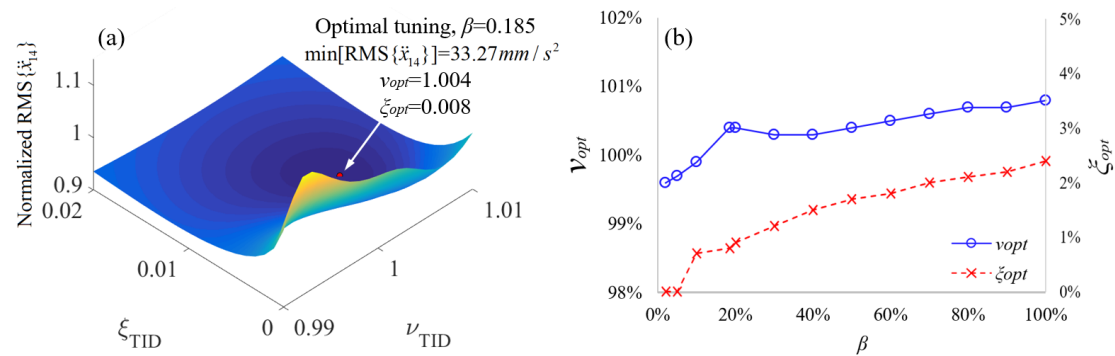


**Fig. 7.5.** Optimal TID design for optimised deficient structure in Figure 7.3 subject to wind excitation in Figure 7.2: (a) Objective function and optimal design point for  $\beta=0.185$ ; and (b) optimal primary DV values with  $\beta$ .

## 7.5 Application of the integrated optimal design framework to the TID-equipped MRF 15-storey benchmark building

### 7.5.1 Performance curve of optimal TID-equipped host structure in relation to ISO6897 occupant comfort demand curve

Herein, the three-step design framework of Fig. 7.1 is applied to the TID-controlled 15-storey case-study building (represented by the low-order model in section 7.4.2) to derive the performance curve of the optimal TID-equipped minimum-weight structure against the fundamental frequency. To this aim, the benchmark structure with the fixed layout is firstly optimised for a series of gradually increasing fundamental frequencies ranging between 0.548Hz and 1.100Hz at an increment of  $\Delta f=0.050\text{Hz}$ , that is, 12 parallel sizing optimisation rounds in total. Next, a ground-floor TID with fixed inertance ratio  $\beta=10\%$  (or inertance constant  $b=87.28$  tonnes) is incorporated to every optimised structure and optimally tuned for the wind model defined in section 7.3.2. Notably, the inertance ratio  $\beta$  herein is defined as the ratio of inertance value to the self-weight of initial, non-optimal host structure to avoid the change of inertance value as the host structure becomes stiffer/heavier such that a fair and meaningful comparison can be made. Performance assessment is then conducted for each optimal TID-equipped minimum-weight structure to generate the integrated performance curve in terms of the RMS acceleration on the 14<sup>th</sup> floor. The latter is compared against the demand curve computed by Eq. (7.1) to interpolate the critical fundamental frequency  $f_c$ , as shown in Fig. 7.6 (a). It is seen in Fig. 7.6(a) that the performance curve of the optimal TID-equipped structure (blue dashed line) intersects the demand curve at the fundamental frequency  $f_1=0.706\text{Hz}$ , corresponding to a self-mass of 576 tonnes. The RMS floor accelerations of this design along the building height can be found in Fig. 7.4(b) (the solid blue curve with circular markers). For comparison, the corresponding performance curve of the *uncontrolled* optimised structure is also added in Fig. 7.6(a) (solid red curve), which is found intersecting the demand curve at the increased frequency  $f_1=0.928\text{Hz}$ , corresponding to a self-mass of 787 tonnes as established in section 7.4.1. In this setting, a 26.8% (or 211 tonnes)



reduction in the steel consumption is achieved for the primary structural system through deploying a ground-floor TID with inertance  $b=87.28$  tonnes. Finally, the self-weight variation of the optimised structure is plotted in Fig. 7.5(b) as a function of the target fundamental frequency. As seen for this particular case-study building, the required self-weight to achieve a prescribed frequency follows a linear relation with the target frequency with a positive slope of 914.7 tonnes/Hz.

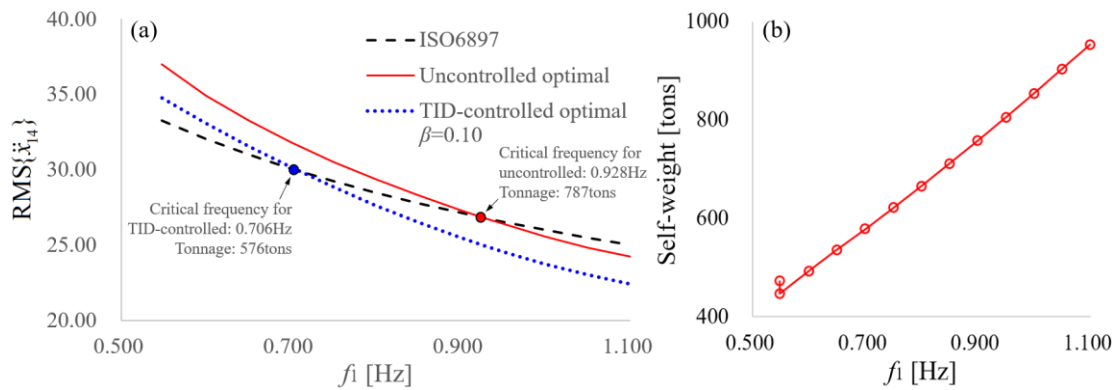


**Fig. 7.6.** (a) Performance curves of uncontrolled optimised structure and of optimal TID-equipped optimised structure for inertance ratio 0.10, together with the performance demand curve by ISO6897 standard; and (b) self-weight of optimised case-study structure against fundamental frequency.

### 7.5.2 Trading inertance to primary structure weight in optimally designed DVA-equipped structures for minimal weight

This section investigates numerically the potential of optimal ground-floor TIDs to suppress wind-induced vibration in VS-prone multi-storey buildings that were optimised for minimum self-weight while satisfying a fundamental frequency constraint. Attention is focused on demonstrating performance improvement of the optimally designed integrated system (i.e., optimal TID plus optimised host structure) as the fundamental frequency of the host structure increases for fixed inertance, as well as on enhanced vibration control of optimal TIDs as inertance increases for a given primary structure. To this aim, the occupant comfort deficient 15-storey case-study structure in Fig. 7.2(a) is optimised using the sizing optimisation method of Chapter 6 for the series of fundamental frequencies considered in Fig. 7.6. Then, optimal TIDs with various inertance ratios ranging between 10% and 100% at 10% interval are considered for the optimised structures with different fundamental frequencies and self-weights.

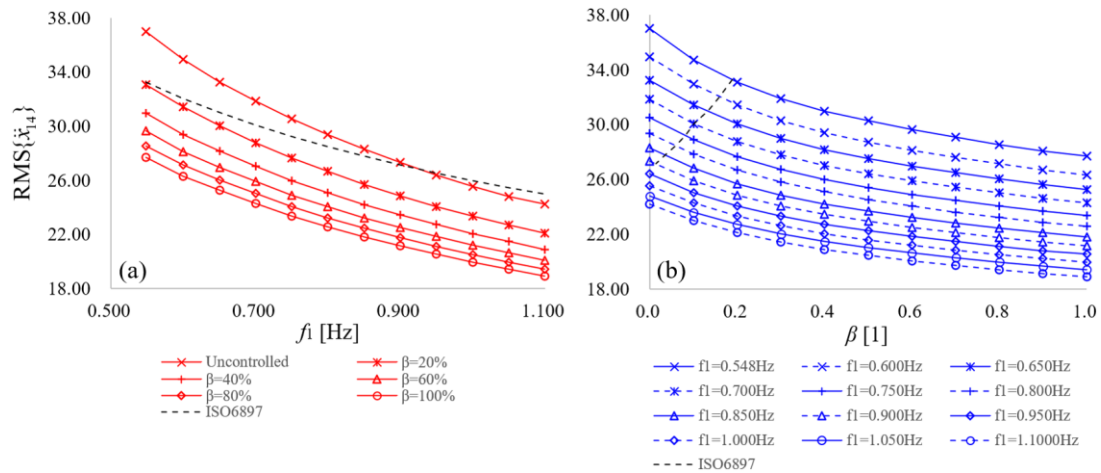


**Fig. 7.7.** (a) Performance curves of uncontrolled optimised structure and of optimal TID-equipped optimised structure for inertia ratio 0.10, together with the performance demand curve by ISO6897 standard; and (b) self-weight of optimised case-study structure against fundamental frequency.

Figures 7.7 (a) and (b) plot the RMS acceleration at the penultimate floor of optimally designed TID-equipped case-study structures as a function of the fundamental frequency for various inertia ratios and as a function of inertia ratio for different fundamental frequencies, respectively. The data evidence that the RMS floor acceleration reduces monotonically with the fundamental frequency for any inertia ratio considered or with the inertia ratio for any fundamental frequency, both at a reducing rate. The implications behind the graphs are therefore two-fold: first, stiffening the host-structure laterally is not cost-effective to address typical occupant comfort criteria because the beneficial effect of increasing lateral stiffness tends to saturate as the fundamental frequency increases; similarly, performance improvement of TID is more sensitive to inertia for lower inertia ratios and gradually reduces as  $\beta$  ratio increases. As seen in Fig. 7.7(a), an optimal TID with  $\beta=20\%$  is sufficient to achieve code-compliant floor accelerations for the optimised building with the original frequency without any modification to the primary structural system. Specifically, only a 10.6% reduction in the 14th floor RMS acceleration is required for the optimised structure with  $f_1=0.528\text{Hz}$  (see the leftmost data points on the performance curves) to meet [ISO6879](#) comfort criterion. As established in section 7.4.3, this reduction can be conveniently achieved by incorporating an optimal TID with  $\beta=18.5\%$  (or  $b=87.27\text{tonnes}$ ) without altering in any other way the MRF lateral load-bearing system. As a remark, the inertia values examined in Fig. 7.7 are realistic and practically meaningful even for  $f_1=1.100\text{Hz}$  and  $\beta=100\%$ , in which case the floor acceleration is reduced by 21.9% compared to the uncontrolled case. Indeed, this inertia ratio corresponds to an inertia constant  $b=953.9\text{tonnes}$ , which is much smaller than the inertia achieved by the hydraulic inerter device discussed in [Nakaminami et al. \(2017\)](#) reaching  $>10000$  metric tons of inertia. Recalling that meeting [ISO6879](#) criteria through structural modification (member resizing) alone would require 315tonnes of additional steel to

stiffen the initial MRF as discussed in section 7.4.1, one concludes that optimal ground-floor TID is quite efficient in meeting occupant comfort criteria in wind-excited buildings leading to lightweight design and material savings.

### **7.5.3 Structural weight reduction potential of optimally tuned TIDs for building structures deficient to occupants' comfort**

Numerical results furnished in Fig. 7.7 suggest that the code-compliant performance in terms of RMS floor acceleration can be achieved using different sets of structural self-weight/fundamental frequency and inertance constant. This is an important consideration from a practical viewpoint as it enables self-weight reduction of the primary structural system via increasing inertance within a performance-oriented design context (i.e., aiming to achieve a pre-set performance level). By repetitive application of the proposed design framework for different inertance values, it is possible to reach a Pareto optimal set of structural-plus-DVA designs from which designers can decide.

To illustrate this point and quantify potential gains in terms of steel usage reduction, Fig. 7.8(a) plots the performance surface of the optimised TID-equipped case-study structure on the self-weight and inertance design plane. Notably, each data point on the surface is associated with a unique optimal design of the integrated structural system, obtained employing the first two steps in the design framework detailed in section 7.2. Further, the [ISO 6897](#) demand surface is superposed in the design space by extruding the demand curve (black dashed line in Fig. 7.7(a)) along the inertance axis. This is facilitated by the fact that comfort threshold value is only affected by the fundamental frequency of host structure but not inertance of the TID. It is seen in Fig. 7.8(a) that the two surfaces intersect at the red dashed curve, which defines the Pareto front separating feasible designs from infeasible ones. Evidently, the portion of the performance surface that locates above the demand surface corresponds to infeasible designs violating the codified threshold, while the portion below corresponds to feasible, though non-optimal, designs. This intersected curve is then projected onto the self-weight and inertance plane, as shown in Fig. 7.8(b). Importantly, it is seen in Fig. 7.8(b) that the Pareto front (depicted as the blue dashed line) has a negative slope, indicating the optimised TID-equipped multi-storey buildings with reduced self-weight can still meet the comfort requirement through increasing the inertance of ground-floor TID. Apparently, any point along the Pareto front corresponds to a unique optimal design for which no further self-weight reduction can be achieved without increasing the inertance and vice versa. This fact establishes a direct material reduction effect for the primary structural system endowed by optimal ground-floor TIDs leading to overall more lightweight inertial dampers that do not commandeer high-premium space at upper floors of the buildings as opposed to TMD(I): a practically important advantage in designing new slender minimal-weight tall buildings.

Quantitatively, for every tonne the inertance constant increases, the required steel tonnage

for the MRF lateral load-bearing system of the case-study building is reduced by about 3.8 tonnes. From a financial perspective, the optimal TID with an 87.27-tonne inerter has reduced the upfront (structural) cost of the lateral load resisting system by \$723625 or 33.2% compared to the uncontrolled structure redesigned optimally to satisfy the occupant comfort requirement. The above cost reduction is estimated by relating linearly the upfront costs of TID and steelwork (for 10-15 storey frame buildings with easy access and repetitive grids) to inertance value and steel tonnage through proportionality constants of \$2500/tonne based on Tse et al. (2012) and \$2770/tonne according to SteelConstruction.Info, respectively. Note that the herein adopted cost value for TIDs is based on the attached mass of conventional TMDs. This is justified by the fact that a ground-floor TID behaves equivalently to a classical TMD installed at the first-floor slab. Therefore, the two passive vibration absorbers should have comparable costs as a large proportion of the upfront cost comes from the mechanical devices, e.g., stiffeners and dampers, and tuning of the device.

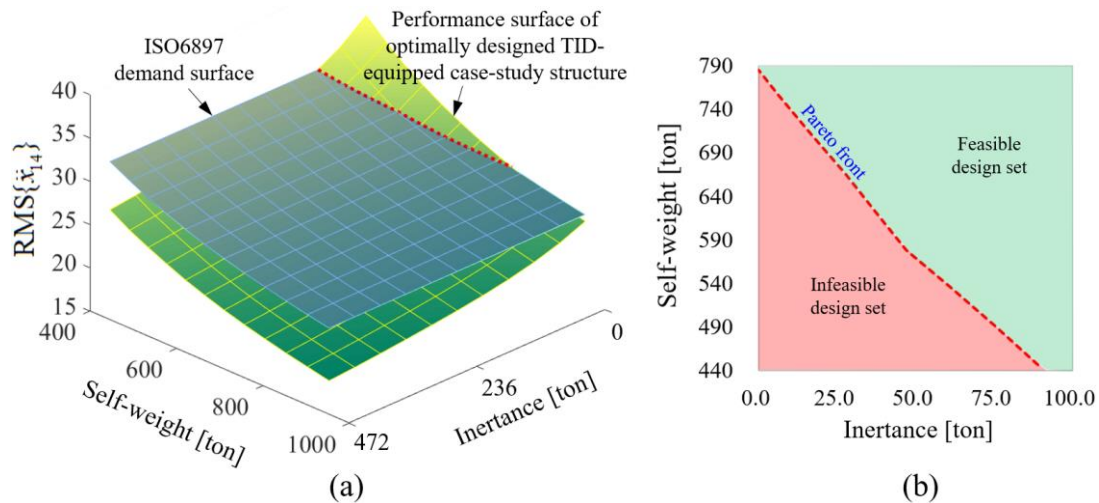


**Fig. 7.8.** (a) performance surface of optimally designed TID-equipped case-study structure versus ISO6897 occupant comfort demand surface; and (b) quantification of structural self-weight-and-inertance trade-off and pareto front in self-weight and inertance design plane.

### 7.6 Closure

In this chapter, a novel framework for the optimal design of wind-excited DVA-equipped tall buildings subject to serviceability comfort criteria has been proposed, enabling (structural) material use reduction for comfort-governed building structures by exploiting the motion control capability of inerter-based DVAs. The framework relies on the optimal sizing algorithm in Chapter 6 for the minimum-weight design of skeletal structures under a frequency constraint (restated in terms of modal strain energy) in conjunction with the optimal TMDI tuning method in Chapter 3 for occupant comfort under cross-wind excitation. For exemplification, a routine regular mid-rise MRF building, deficient in meeting the ISO 6897 comfort requirement under moderate wind action, has been chosen as the paradigm to showcase the applicability and usefulness of the proposed framework as well as of inerter-based DVAs in simultaneous self-

weight reduction and optimal vibration control. This consideration supports the potential impact of inerter-based DVAs used collaboratively with the herein proposed design framework. Notably, although the case-study building for demonstration purpose is a mid-rise MRF structure, the framework and idea behind are believed to work equally well for any skeletal structural system of tall buildings (including ultra-tall landmark structures in Chapter 3) and any inerter-based DVA encompassing, but not limited to, TMD, TID, and TMDI.

For the adopted case-study building, major conclusions in view of the herein furnished numerical results are: (1) Optimally tuned ground-floor TID for floor acceleration minimisation is a potent retrofitting measure to meet occupant comfort criteria without structural modifications leading to a considerable increase in steel tonnage (up to 67% increase for the considered structure) and upfront structural cost (up to 33.2%); and (2) Increasing inertance within an optimal TID design setting is beneficial for suppressing accelerations at all upper floors without noticeably affecting the fundamental frequency of host structure. The latter is another important advantage of employing vibration control devices (instead of stiffening the primary structure directly) when addressing the discomfort issue as the codified requirement/threshold also tightens with the fundamental frequency increasing. Overall, it is concluded that ground-floor TID is a promising DVA configuration to achieve occupant comfort in mid-rise buildings.

---

## Chapter 8

---

### Concluding Remarks

In this final Chapter, the main conclusions drawn and novel contributions pursued in each Chapter of this thesis are summarised and pertinent remarks on theoretical formulations and numerical results are furnished in Section 8.1. The objectives progressively contribute new knowledge through the development of novel computational and optimisation tools, models, and data sets capitalising on and significantly extending prior research work on the TMDI for wind-excited tall buildings (Giaralis and Petrini 2017), on optimal design of linear passive energy dissipation devices (Marian and Giaralis 2014, Giaralis and Taflanidis 2018), and on structural (sizing) optimisation of elastic structures with fixed layout subjected to generalised stiffness (e.g., frequency) constraints (Chan and Chui 2006). Further, the main limitations and potential directions for future research are outlined in section 8.2.

#### 8.1 Summary of achievements and contributions

In chapter 1, an introduction to the structural needs/requirements of tall buildings related to the impacts of static and dynamic wind loads together with current mitigation measures is provided. In addition, a conspectus of the objectives of the research effort is provided with the thesis organisation outlined.

In chapter 2, the development and technological aspects of the inerter device, including different inerter-based configurations implemented for motion control of tall buildings subject to seismic and wind excitation, are briefly reviewed. The research gaps and needs are next identified.

In chapter 3, a novel optimal TMDI tuning problem, aiming to minimise acceleration response at a selected location under given wind action for occupant comfort, is formulated and numerically solved using a custom-made pattern search algorithm with an adaptive design variable search range for computational efficiency, thereby, achieving the objective (I). The search range is continuously updated/narrowed within the feasible solution set based on the optimal solution found in the previous iterative step, with a logarithmic increase of precision/resolution by which optimal parameters are determined. Notably, the proposed numerical solution approach entailing the "zoom-in" strategy can be easily extended to include more primary design variables (e.g., the installation location), in addition to stiffness and damping properties, of the inerter-based dynamic vibration absorbers into the optimisation formulation for any desired combination of secondary design parameters. In order to reduce the computation time for optimal tuning process, the density of the orthogonal mesh grid can be leveraged, e.g., by having a coarser discretisation of the search domain, to reduce the total

number of performance assessments/dynamic analyses required to determine the optimal solution provided that the objective function is well-behaved (i.e., does not have any local extremum other than the global within the initial search range). Novel numerical results regarding the optimal design of a top-floor TMDI with given inertial properties (i.e., secondary mass/weight and inertance) and judicious connectivity (defined by the number of floors spanned by the inerter device to connect the secondary mass to the building structure) in a 74-storey benchmark structure are presented to showcase the effectiveness and convergence behaviour of the proposed method.

Further, in Chapter 3, the TMDI efficacy has been established numerically to achieve the occupant comfort performance in wind-excited tall buildings susceptible to vortex shedding effects. This was achieved through application of the TMDI tuning algorithm and efficient frequency-domain analysis utilising a surrogate low-order planar model of the benchmark building. The latter captured faithfully structural dynamic behaviour along the critical direction. Attention has been focused on exploring the influence and benefits of TMDIs in wind-induced motion control of real slender buildings within an optimal TMDI design setting. To this aim, optimally designed TMDIs, minimising the peak top-floor acceleration for a wide range of inertial properties and three different topologies, have been obtained through the numerical solution of the underlying optimisation problem formulated in section 3.2 for a 305.9m tall benchmark building with a rectangular floorplan and a height-to-width ratio more than six subjected to experimentally calibrated spatially-correlated crosswind force field accounting for vortex shedding effects. Strict convexity of the objective function in solving the optimisation problem for all cases considered has been noted *near the optimum* as well as improved robustness of optimal TMDIs (over a same-mass TMD as long as the inertance value is over a critical value) to their optimal design parameters, changes of the building's structural properties, and varying reference wind velocity. Additionally, it was demonstrated that TMDIs with fixed secondary mass/weight reduce peak top-floor acceleration frequency response function coordinates for all higher vibration modes (i.e., wide-band dampening effect) as opposed to the TMD solely mitigating one particular mode. More importantly, it was confirmed that more lightweight TMDIs for fixed performance could be achieved by letting the inerter span more floors or increasing the inertance coefficient. To this end, the TMDI applicability to control vortex shedding-prone slender tall buildings and to retrofit existing TMD-equipped buildings has been established. The latter case involves adding inerters connecting the TMD attached mass to an appropriate lower floor with no changes to the secondary mass and necessary retuning to address tightened requirements for occupant comfort.

In Chapter 4, a simplified 2-DOF model, representing the TMDI-equipped flexural cantilever with continuously distributed mass and flexibility, is proposed to pursue/facilitate the systematic quantification of the influence of the uncontrolled fundamental mode shape on TMDI vibration suppression efficacy, thereby meeting the objective **(II)**. This is achieved through an innovative and thorough parametric investigation considering a wide range of



primary structures modelled/simplified as continuous tapered (cantilever) beams with various (geometric) shapes and, thus, different mass and stiffness distribution. The simplified model entails approximating the host structure as a generalised SDOF oscillator through its uncontrolled fundamental mode shape. Non-dimensional analytical FRFs of practical interest are derived using the 2-DOF model in terms of five TMDI parameters (i.e., frequency, damping, attached mass, and inertance ratios, as well as connectivity ratios) and the uncontrolled modal coordinate of the host structure to expedite the dynamic analyses in the frequency domain. Optimal TMDI design problem, aiming to minimise the free-end steady-state displacement of the host structure accounting for resonant harmonic and white noise excitations, is formulated and solved numerically utilising the closed-form FRFs and the same "zoom-in" strategy from chapter 3 for efficiency. The main findings of the chapter are two-fold. Firstly, from the control device standpoint, the TMDI performance improves (compared to a same-weight TMD) for all considered cantilever shapes by adopting smaller attached mass, larger inertance, or higher CR values (i.e., allowing the inerter span a longer distance). Secondly, from the host structure standpoint, the TMDI becomes even more effective than the TMD for cantilevered structures whose upper part is more (laterally) flexible from the lower. However, for each TMDI-equipped cantilever beam and given inertial properties, there seems to exist a minimum connectivity-ratio threshold value only beyond which the TMDI starts to outperform the TMD, indicating for relatively small connectivity ratios, the inerter inclusion may be detrimental (i.e., worsening the TMD performance). From a practical viewpoint, it is concluded that, with judiciously upwards (stiffness) tapering, the TMDI can achieve better suppression effect than the TMD with a smaller attached mass, hence enabling more lightweight construction in the design of flexible cantilever structures such as tall buildings, wind turbine/solar towers, and industrial chimneys. Finally, the dependence of TMDI control potential on the host structure properties motivates local modification/manipulation of the lateral stiffness to purposely create a larger modal-coordinate difference between the two terminals of the TMDI for enhanced vibration suppression.

Upon meeting objective (II), in Chapter 5, the effectiveness and advantages of using an optimal top-floor TMDI in conjunction with a local structural modification, namely, top-storey softening, have been numerically explored as an effective alternative to the inerter spanning more than one floor for mitigating crosswind floor accelerations of slender high-rise buildings governed by serviceability comfort criteria. This is accomplished by furnishing pertinent numerical data for a low-order dynamical system capturing faithfully in-plane modal properties (mode shapes and natural frequencies) of a 34-storey square-plan core-frame benchmark building with softened top-floor by discontinuing the central r/c core and increasing the top-storey height. The optimal TMDI tuning problem in chapter 3 has been extended to include the top-floor height as a secondary design parameter (in addition to TMDI inertial properties) and numerically solved to minimise the peak floor acceleration under crosswind excitation modelled as a stationary spatially-correlated random field accounting for VS effects. Notably,

the proposed structural modification for improving the TMDI control potential extends the applicability of TMDI to more routine structures in which spanning the inerter over a longer distance is prohibitive, thereby directly addressing objective **(III)**.

Numerical results for different TMDI inertial properties and top-storey heights show that improved structural performance in terms of peak floor acceleration and attached mass stroke are achieved by increasing inertance and/or by reducing top-storey stiffness for fixed TMDI attached mass. In contrast, no improved performance is achieved by TMDs through top-storey softening. In this regard, it was demonstrated that the required TMDI mass/weight can be reduced by either increasing inertance, as seen in previous chapters, or softening the top-storey for a preset performance level. The latter strategy is rather advantageous in the design of VS-sensitive buildings because (1) it does not occupy premium space on the upper floors as the TMDI is fully contained within a single (last) storey, and (2) top-storey softening can be readily implemented by simple local modifications such as discontinuation of the r/c core at the last floor and increasing the top-storey height as seen in this chapter, or by other means such as reduction of member sizes. More interestingly, it was shown that a decrease of the top-storey stiffness leads to decreased sensitivity of structural performance to the optimal TMDI properties and the assumed inherent structural damping, and hence yielding more robust TMDI designs to detuning effects and inaccurate knowledge of structural properties. Lastly, it is seen that the performance of optimal TMDI-controlled case-study building improves as the flexural contribution coming from the r/c core increases in the coupled core-frame (lateral load resisting) system, suggesting that the optimal top-floor TMDIs work the best for flexure-typed (compared to shear-typed) building structures. This observation is readily attributed to the fact that the flexure-typed cantilever structures with no abrupt change in lateral stiffness allow a larger modal-coordinate difference to be developed around their free-ends. Looking further into the case of existing tall/slender buildings, the herein reported numerical data suggests that the addition of a relatively soft top-storey housing a properly tuned *lightweight* TMDI is an effective retrofitting measure to enhance serviceability performance. In this manner, more stringent serviceability design requirements than those considered in the initial design due to site-specific climate change effects or changes to the surrounding built environment (i.e., increased wind exposure) can be achieved.

In Chapter 6, a rigorous sizing optimisation algorithm, centred on a novel strain energy-based optimality criteria formulation, is developed for the minimum-weight design of *uncontrolled* elastic skeletal structures with fixed layout while satisfying a target frequency of the chosen vibration mode. The latter quantity is used in the optimality criteria formulation as a quantitative measure of the overall lateral stiffness of the optimised structure, which is inversely related to the floor accelerations under given wind excitation. The resizing method, entailing sensitivity analyses of a nonlinear behavioural constraint function concerning the total modal strain energy of the structure, relies on parallel computing to expedite the optimising process. The algorithm is exemplified using a trivial planar MRF with two active design

variables subjected to a frequency constraint on its fundamental mode. It is shown that the resizing routine can accurately and efficiently solve the frequency-constrained weight-minimisation problem of skeletal structures with less iterative effort compared to the intuitive uniform-strain-energy-density optimality criteria method, provided that a stationary point indeed exists in the feasible solution set. Notably, the herein proposed algorithm can be readily generalised to cover stability- and displacement-constrained optimisation problems of skeletal structures by restating the performance constraints (e.g., upper limits on displacement and lower limit on critical buckling load factor) in terms of induced strain energy. The algorithm is used in the proceeding chapter collaboratively with the generic TMDI tuning algorithm (see chapter 3) for the *optimal integrated* design of TMDI-equipped tall buildings to achieve simultaneous material use minimisation of the primary structure and optimal suppression effect of the dynamic vibration absorber.

For the adopted case-study building, major conclusions in view of the herein furnished numerical results are: (1) Optimally tuned ground-floor TID for floor acceleration minimisation is a potent retrofitting measure to meet occupant comfort criteria without structural modifications leading to a considerable increase in steel tonnage (up to 67% increase for the considered structure) and upfront structural cost (up to 33.2%); and (2) Increasing inertance within an optimal TID design setting is beneficial for suppressing accelerations at all upper floors without noticeably affecting the fundamental frequency of host structure. The latter is another important advantage of employing vibration control devices (instead of stiffening the primary structure directly) when addressing the discomfort issue as the codified requirement/threshold also tightens with the fundamental frequency increasing. Overall, it is concluded that ground-floor TID is a promising dynamic vibration absorber configuration for achieving occupant comfort in mid-rise buildings. Still, further numerical and experimental work is warranted to examine ground-floor TID efficiency for different wind excitation intensity in a performance based design context and compare it to widely used alternative solutions such as top-floor TMD and distributive VD.

In Chapter 7, a novel structure-plus-TMDI optimal design framework has been developed for (structural) material use reduction of the primary structural system of vortex shedding-prone tall buildings while meeting code-prescribed occupant comfort criteria by leveraging/exploiting the motion control potential of optimally tuned inerter-based dynamic vibration absorbers, thereby addressing the objective **(IV)**. The integrated design approach relies on the resizing algorithm in Chapter 6 for the minimum-weight design of the host structure under a frequency constraint in conjunction with the generic tuning method in Chapter 3 for optimal TMDI design under given wind excitation. For the sizing optimisation process, the target frequency for the fundamental vibration mode of the host structure is chosen such that a lower target value would cause the optimally designed integrated system (i.e., the host structure plus the control device) to no longer satisfy the codified threshold without changing/increasing the secondary design parameters of the control device (e.g., inertance, connectivity). The proposed framework is

believed to be applicable to any skeletal structural system of tall buildings and any inerter-based dynamic vibration absorber such as TMD, TID, and TMDI. A regular 15-storey moment resisting frame building, initially deficient in meeting the ISO 6897 comfort requirement under moderate wind action, has been considered as the paradigm to showcase the applicability and usefulness of the proposed framework as well as of inerter-based dynamic vibration absorbers in concurrent material use reduction and optimal vibration control. Numerical results pertinent to the case-study building evidenced that an optimal TID, placed on the ground floor of vortex shedding-prone mid-rise buildings, can effectively contain/influence the crosswind accelerations on all higher floors. Major conclusions in view of the herein furnished numerical results include: (i) Optimal ground-floor TIDs for floor acceleration minimisation is a potent retrofitting measure to meet the comfort criteria without stiffening the primary structure leading to a considerable increase of steel usage (up to 67% increase for the considered structure); (ii) For a preset performance level, there is a trade-off between the self-weight of the host structure and inertance value of the ground-floor TID from which the designers or owners can decide; and (iii) The herein proposed design approach can sufficiently address the optimal design problem of TMDI-equipped tall buildings, supporting material-efficient design and lightweight construction.

As a closing remark, the results exhibited in this thesis suggest the potential use of TMDI in an appropriate configuration (e.g., top-floor TMDI, ground-floor TID), as a lightweight alternative solution with improved effectiveness and robustness to conventional TMDs, for vibration control of wind-excited vortex shedding-prone tall buildings ranging from mid-rises to ultra-tall landmark structures. It has been shown that the TID configuration and inerter device(s) can be incorporated in existing uncontrolled and TMD-equipped tall buildings, separately, as a retrofitting measure to either enhance comfort-related serviceability performance or maintain the current performance level under increased wind exposure due to site-specific climate change effects or changes to the surrounding built environment. More importantly, the herein developed/proposed integrated design framework has provided a clear direction and paved the way towards the sustainable and innovative tall building design through the use of inerter-based dynamic vibration absorbers within a multi-objective context, leading to reductions not only in the upfront cost but also in embodied energy consumption. Through successfully addressing the four objectives set out in the introduction, this thesis progressively contributes new knowledge through the development of novel computational and optimising tools, models, and data sets capitalising on and extending prior research works on the use of TMDI for motion control of wind-excited tall buildings ([Giaralis and Petrini 2017](#)), on the optimal tuning of linear passive inerter-based dynamic vibration absorbers ([Marian and Giaralis 2014](#), [Giaralis and Taflanidis 2018](#)), and on the sizing optimisation of elastic skeletal structures with fixed layout under generalised stiffness (e.g., frequency) constraints ([Chan and Chui 2006](#)).

## 8.2 Main limitations and future directions

The main limitations of this PhD research are identified as follows. Firstly, the work is based on two-dimensional/planar analysis such that coupling between flexural and torsional modes is ignored. This simplification is deemed appropriate and accurate for symmetric tall buildings whose first several translational and torsional modes are well-separated, such as in the case-study building studied in Chapter 3. For asymmetric tall buildings, however, a more realistic low-order model, with two orthogonal translational DOFs in the principal directions of the building plus a torsional DOF around the vertical axis (i.e., three DOFs per floor), is required for investigating vibration control effectiveness of inerter-based DVAs under different wind directions/incidence angles in a computationally tractable manner. Moreover, the work is centred on the common assumption of stochastic input/output processes that are steady/stationary and ergodic, and therefore overlooked fast and transient responses as well as potential benefits of TMDI incorporation under stormy winds and tornadoes. Finally, design considerations, which are essential for implementing inerter-based DVAs in real tall buildings, are not considered in the research, including local connections of TMDI to the primary structure and physical embodiments of various TMDI configurations studied.

As far as extensions are concerned, future research can arise in the following four areas. Firstly, the conclusions regarding the motion control potential of inerter-based dynamic vibration absorbers are valid for ideal linear inerter and for ignoring nonlinear behaviour of the TMD. Whilst inerter device prototypes do deviate from the ideal inerter element behaviour depending on the employed technology and the application-dependent frequency range of operation (e.g. [Papageorgiou and Smith 2005](#), [Swift et al. 2013](#)), recent studies demonstrate that such deviations do not significantly influence the benefits of the inertance in dynamic vibration absorbers (e.g., [Gonzalez-Buelga et al. 2016](#), [Brzeski and Perlikowski 2017](#), [Pietrosanti et al. 2020b](#)). Therefore, it is anticipated that the herein reported trends and conclusions are valid even for non-ideal inerter devices, although it is recognised that quantification of benefits and performance accounting for non-ideal inerter behaviour warrants further research work.

Secondly, further numerical work is required to examine the ground-floor TID efficiency for different wind excitation intensities in a performance based design context and to compare it to alternative widely used solutions such as top-floor TMD(I)s and distributive viscous dampers. Special attention is to be placed on quantifying its limitations in suppressing wind-induced accelerations at upper floors of slender tall buildings as the building height increases.

Thirdly, the sizing optimisation formulation (section 6.2) and associated algorithm (section 6.3.1) need to be extended beyond skeletal structures by including two-dimensional shell elements such that the resizing routine becomes applicable to building structures that comprise reinforced concrete shear walls and/or cores in the lateral load-resisting system. The method is readily applicable for accommodating buckling and (multiple) displacement constraints. Therefore, it can readily serve for minimal weight design in buckling-sensitive structures as

well as in displacement-based design of tall buildings (e.g., in the serviceability design for inter-storey drifts). Moreover, the sizing formulation and algorithm presented in this thesis are both continuous in nature - that is, the cross-section area of structural members can take on any real value provided that the value is within the side constraint. In practice, however, the final optimal design would only make sense if the design variables take on discrete values. To this end, an additional algorithm needs to be developed for automated mapping from the continuous optimal solution to the closest discrete solution at the end of the sizing design, so that the true gains in weight reduction and financial savings can be examined.

Fourthly, upon addressing the last limitation, a more detailed life-cycle cost analysis, composed of the TMDI and primary structural upfront costs as well as potential losses over the lifetime of structures due to either downtime or non-structural repairs, needs to be conducted by adopting realistic tall buildings to accurately quantify the overall financial gain achieved by the use inerter-based vibration absorbers.

## Appendix A - Frequency domain random vibration analysis for structural response estimation to crosswind excitation forces

Optimal TMDI design/tuning requires computationally efficient determination of peak or RMS response of TMDI/TID/TMD-equipped building models to cross-wind forces. Throughout this thesis linear models defined in terms of mass,  $\mathbf{M}$ , damping,  $\mathbf{C}$ , and stiffness,  $\mathbf{K}$ , matrices are considered. Further, cross wind floor forces are modelled through spatially correlated stationary processes expressed in frequency domain in terms of a  $n$ -by- $n$  power spectral density (PSD) matrix  $\mathbf{S}_{FF}^n$ , where  $n$  is the number of building floors. In this setting, computationally efficient structural response determination is facilitated through standard frequency domain random vibrations analysis. Specifically, the response displacement, velocity, and acceleration PSD matrices of TMDI-equipped building models are obtained by (Roberts and Spanos 2003)

$$\mathbf{S}_{xx}(\omega) = \mathbf{B}(\omega)^* \mathbf{S}_{FF}(\omega) \mathbf{B}(\omega), \quad \mathbf{S}_{\dot{x}\dot{x}}(\omega) = \omega^2 \mathbf{S}_{xx}(\omega), \quad \text{and} \quad \mathbf{S}_{\ddot{x}\ddot{x}}(\omega) = \omega^4 \mathbf{S}_{xx}(\omega), \quad (\text{A.1})$$

respectively. In Eq. (A.1),  $\mathbf{S}_{FF}$  is the PSD wind force matrix  $\mathbf{S}_{FF}^n$ , expanded by adding a zero row and a zero column corresponding to the DOF of the TMDI/TID/TMD which is not subjected to any wind load (internally housed). Further, the “\*” superscript denotes complex matrix conjugation, and the transfer matrix  $\mathbf{B}$  is given as

$$\mathbf{B}(\omega) = (\mathbf{K} - \omega^2 \mathbf{M} + i\omega \mathbf{C})^{-1}, \quad (\text{A.2})$$

where  $i = \sqrt{-1}$ .

Moreover, the response displacement, velocity and acceleration variances of the  $k$ -th floor are determined by

$$\sigma_{x_k}^2 = \int_0^{\omega_{\max}} S_{x_k x_k}(\omega) d\omega, \quad \sigma_{\dot{x}_k}^2 = \int_0^{\omega_{\max}} S_{\dot{x}_k \dot{x}_k}(\omega) d\omega, \quad \text{and} \quad \sigma_{\ddot{x}_k}^2 = \int_0^{\omega_{\max}} S_{\ddot{x}_k \ddot{x}_k}(\omega) d\omega, \quad (\text{A.3})$$

respectively. That is, by integrating the response auto-spectra populating the main diagonal elements of the response PSDs in Eq. (A.1),  $S_{x_k x_k}(\omega) = \mathbf{S}_{xx}[k, k]$ ,  $S_{\dot{x}_k \dot{x}_k}(\omega) = \mathbf{S}_{\dot{x}\dot{x}}[k, k]$ , and  $S_{\ddot{x}_k \ddot{x}_k}(\omega) = \mathbf{S}_{\ddot{x}\ddot{x}}[k, k]$ , up to a maximum (cut-off) frequency,  $\omega_{\max}$ , above which the energy of the underlying stochastic processes is negligible. Furthermore, the variance of the relative response displacement, velocity, and acceleration between two different floors, or more generally between two different DOFs,  $k$  and  $l$  is obtained by



$$\begin{aligned}\sigma_{x_{kl}}^2 &= \sigma_{x_k}^2 + \sigma_{x_l}^2 - 2 \int_0^{\omega_{\max}} S_{x_k x_l}(\omega) d\omega, \\ \sigma_{\dot{x}_{kl}}^2 &= \sigma_{\dot{x}_k}^2 + \sigma_{\dot{x}_l}^2 - 2 \int_0^{\omega_{\max}} S_{\dot{x}_k \dot{x}_l}(\omega) d\omega, \text{ and} \\ \sigma_{\ddot{x}_{kl}}^2 &= \sigma_{\ddot{x}_k}^2 + \sigma_{\ddot{x}_l}^2 - 2 \int_0^{\omega_{\max}} S_{\ddot{x}_k \ddot{x}_l}(\omega) d\omega,\end{aligned}\tag{A.4}$$

where  $S_{x_k x_l}(\omega) = \mathbf{S}_{xx}[k, l]$ ,  $S_{\dot{x}_k \dot{x}_l}(\omega) = \mathbf{S}_{\dot{x}\dot{x}}[k, l]$  and  $S_{\ddot{x}_k \ddot{x}_l}(\omega) = \mathbf{S}_{\ddot{x}\ddot{x}}[k, l]$  are the response displacement, velocity, and acceleration cross-spectra corresponding to the  $k$  and  $l$  DOFs. Ultimately, the peak displacement, velocity and acceleration of the  $k$ -th DOF are estimated by the expressions

$$\text{peak}\{x_k\} = g\sqrt{\sigma_{x_k}^2}, \text{ peak}\{\dot{x}_k\} = g\sqrt{\sigma_{\dot{x}_k}^2}, \text{ and } \text{peak}\{\ddot{x}_k\} = g\sqrt{\sigma_{\ddot{x}_k}^2},\tag{A.5}$$

respectively, and the peak relative displacement, velocity, and acceleration between  $k$  and  $l$  DOFs, are estimated by the expressions

$$\text{peak}\{x_{kl}\} = g\sqrt{\sigma_{x_{kl}}^2}, \text{ peak}\{\dot{x}_{kl}\} = g\sqrt{\sigma_{\dot{x}_{kl}}^2}, \text{ and } \text{peak}\{\ddot{x}_{kl}\} = g\sqrt{\sigma_{\ddot{x}_{kl}}^2},\tag{A.6}$$

respectively. In the Eqs. (A.5) and (A.6),  $g$  is the peak factor estimated by the widely used semiempirical formula due to [Davenport \(1964\)](#)

$$g = \sqrt{2\ln(\eta T_{\text{wind}})} + \frac{0.577}{\sqrt{2\ln(\eta T_{\text{wind}})}},\tag{A.7}$$

where  $\eta=2\pi/\omega$  is the effective structural response frequency in Hz (e.g., can be taken equal to the fundamental natural frequency of the uncontrolled primary structure model), and  $T_{\text{wind}}$  is an assumed time duration of exposure to the wind action during which the peak response quantities in Eqs. (A.5) and (A.6) are evaluated under the common assumption of stochastic input/output processes being stationary/ergodic time-limited processes. As a remark, the quantity  $\eta$  in Eq. (A.7) should be interpreted physically as the frequency at which most of the energy in the spectrum is concentrated ([Davenport 1961<sup>b</sup>](#)). For lightly damped systems, this will generally be close to the natural frequency of the structure ([Davenport 1964](#)).

## Appendix B - Modelling of wind loads to building structures and verification against wind tunnel force data

### B.1 Overview of wind loading to structures

PBD of structures to dynamic loads relies on accurate external force modelling across different intensity levels. For wind-excited buildings, uncertainties rise from aerodynamic wind loading characteristics as well as from system properties, i.e., mass, stiffness and inherent damping properties. Wind loading is dependent on statistical properties of wind field velocity, which could be quantified based on statistical wind speed data analysis (Huang 2017). In 1960s, Davenport used random vibrations theory to study the effects of wind loading to structures and outlined a modelling approach, illustrated in Fig. B.1, to determine the wind-induced response of structures to turbulent, gusty wind fields by representing wind velocity field as a stationary Gaussian random process (Davenport, 1961, 1963, 1964). This process is expressed as

$$U(t) = \bar{U} + u(t), \tag{B.1}$$

where  $\bar{U}$  is a mean time-invariant component;  $u(t)$  is a time-varying fluctuating component with zero mean. By introducing some necessary modifications to account for the speed gradient in the atmospheric boundary layer and for the mode shape of the structure, the above wind field modelling approach is adequate for the estimation of along-wind response of buildings, slender towers, and certain types of bridge structures (Tamura et al. 2013).

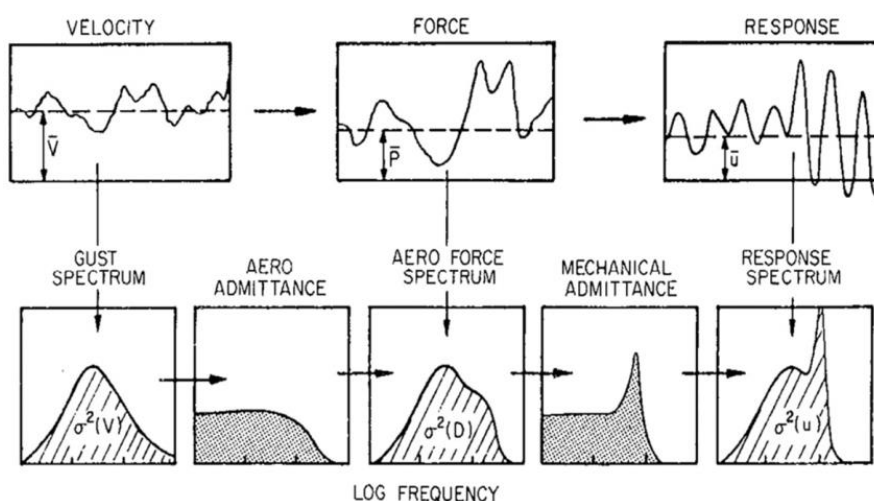


**Fig. B.1** Davenport's approach for determining the wind-induced resonant response of buildings and structures (Isyumov 2012).

In this context, the wind loading to building structures consists of a mean (static) component and a zero-mean fluctuating (dynamic) component. For sufficiently rigid structures

(e.g. tall buildings), the design wind loading is mainly associated with the pressure on the surface of the structure being, as a first rough approximation, proportional to the square of the wind speed (Huang 2017). The thus-developed total response process of structures comprises three components: a static component due to the mean wind loading part, and a background dynamic component and a resonant dynamic component due to the fluctuating part of wind loading. While the static response can be obtained via static analysis, predicting the dynamic response of buildings to wind excitation requires dynamic analysis either in time domain through response history analysis or in frequency domain through spectral representation of wind load fluctuation and random vibration theory. Depending on their relative direction to the mean wind component, wind-induced force and structural response are resolved into two orthogonal directions: the along-wind (drag) and the crosswind (lift) direction. While many tall buildings are dominated by drag, there are buildings in which crosswind direction effects or even torsion become critical (Isyumov 2012). In the along-wind direction, turbulence buffeting is the dominant excitation mechanism, whereas the excitation mechanisms in the crosswind direction and response processes of buildings are more complex (Tamura et al. 2013). According to Solari (1985), the crosswind dynamic load of tall buildings is induced by three mechanisms: along-wind turbulence, crosswind turbulence and wake excitation, with the latter being the main contributor of the three. In wake excitation, vortices are created at the back of the body and detach periodically from either side of the body when a fluid such as air or water flows past a bluff body. For tall buildings with aspect ratio (height to width) over 3 (such as those considered in this thesis), crosswind response usually exceed along-wind response and may actually be several times larger (Liang et al. 2002).

For illustration, Fig. B.2(a) plots the first-order probability density function (PDF) of the turbulent along-wind force (i.e. after deducting the mean component) at the 73<sup>rd</sup> floor of the benchmark building from Ciampoli and Petrini (2012) and Spence and Gioffrè (2012), while Fig. B.2(b) plots the second-order or joint PDF of two random variables, i.e., the turbulent along-wind forces at 37<sup>th</sup> floor and 73<sup>rd</sup> floor. Details of the benchmark building can be found in section 3.3.1. The time history data of along-wind force, for generating these two plots, were obtained from a wind tunnel test conducted at the boundary layer wind tunnel of CRIACIV (Inter-University Research Centre on Buildings Aerodynamics and Wind Engineering) in Prato Italy and made available to the author. In both plots, the “bell-shaped” probability distribution with zero mean, i.e. Gaussian distribution for many naturally occurring random processes, can be seen.

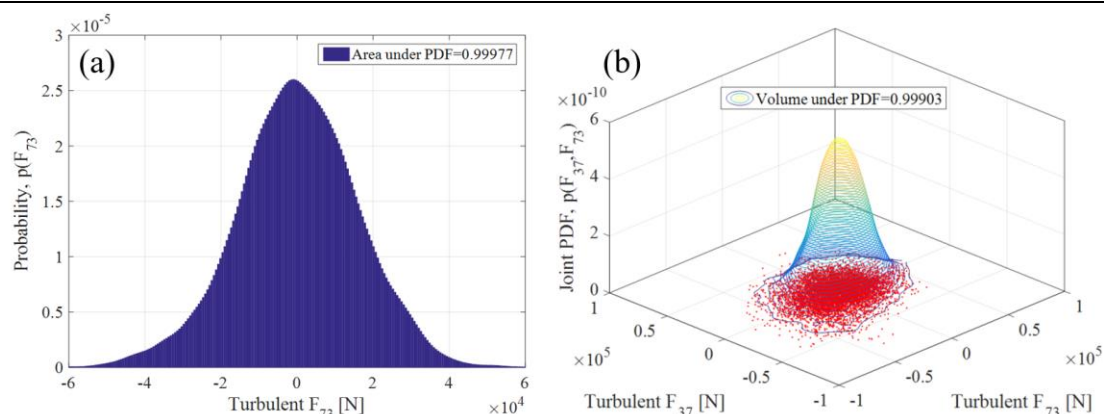


**Fig. B.2.** (a) First-order probability density function (PDF) of the turbulent along-wind force at 73<sup>rd</sup> floor, and (b) second-order or joint PDF of turbulent along-wind forces at 37<sup>th</sup> and 73<sup>rd</sup> floors.

## B.2 Modelling of wind loads to structures in the along-wind direction

There are many mathematical models developed over the past few decades for wind spectra in meteorology and wind engineering. The most commonly considered one for the longitudinal turbulence is the von Karman/Harris spectrum developed for laboratory turbulence by [von Karman \(1948\)](#) and adapted for wind engineering by [Harris \(1968\)](#). Based on the results of a study of about 70 spectra of the horizontal components of gustiness in storing wind, [Davenport \(1961<sup>a</sup>\)](#) proposed an expression for the spectrum of horizontal gustiness. Height-dependent wind spectra were later proposed by [Kaimal et al. \(1972\)](#) and by [Solari \(1993\)](#). The mathematical expressions for these four gust spectra are summarised in Table B.1 in non-dimensional form. Most building codes adopt the Karman-type spectrum to represent wind-induced pressures in the along-wind direction ([Tamura et al. 2013](#)).

**Table B.1.** Mathematical expressions of gust spectra of the along-wind turbulence.

	Gust spectrum of the along-wind turbulence
von Karman (1948) / Harris (1968)	$\frac{f \cdot S_u(f)}{u_*^2} = \frac{24 \left( \frac{fL_u}{\bar{U}(10)} \right)}{\left( 1 + 70.8 \left( \frac{fL_u}{\bar{U}(10)} \right)^2 \right)^{5/6}} \quad (\text{B.2})$
Davenport (1961 <sup>a</sup> )	$\frac{f \cdot S_u(f)}{u_*^2} = \frac{4 \left( \frac{fL_u}{\bar{U}(10)} \right)^2}{\left( 1 + \left( \frac{fL_u}{\bar{U}(10)} \right)^2 \right)^{4/3}} \quad (\text{B.3})$
Kaimal (1972)	$\frac{f \cdot S_u(z, f)}{u_*^2} = \frac{200 \left( \frac{fz}{\bar{U}(z)} \right)}{\left( 1 + 50 \frac{fz}{\bar{U}(z)} \right)^{5/3}} \quad (\text{B.4})$

Solari (1993)	$\frac{f \cdot S_u(z, f)}{\sigma_u(z)^2} = \frac{6.868 \left( \frac{f L_u}{z} \right)}{\left( 1 + 10.302 \frac{f L_u}{z} \right)^{5/3}} \quad (\text{B.5})$
---------------	---

In the expressions of Table B.1,  $S_u$  is the gust spectrum of the along-wind turbulence,  $f$  is the frequency,  $z$  is the height,  $u_*$  is the friction velocity,  $L_u$  is a turbulence length scale (the average size of the turbulent eddies of the air flow),  $\bar{U}(z)$  is the mean speed at height  $z$ , and  $\sigma_u(z)$  is the standard deviation of along-wind turbulence at height  $z$ . For illustration, Fig. B.3 plots the first three spectral shapes for  $L_u = 1200\text{m}$ ,  $z = 10\text{m}$ ,  $\bar{U}(10) = 22\text{m/s}$ , and  $u_* = 2.12\text{m/s}$ . In the low frequency range (e.g.,  $f < 0.01\text{Hz}$ ), the Davenport spectrum attains the lowest values, while in the higher frequency range (e.g.,  $f > 0.1\text{Hz}$ ), it traces closely the Kaimal spectrum of turbulence. Since the spectral distribution in the lower frequency range has little influence on tall building responses, the Davenport spectrum is still widely used in wind engineering and design wind codes.

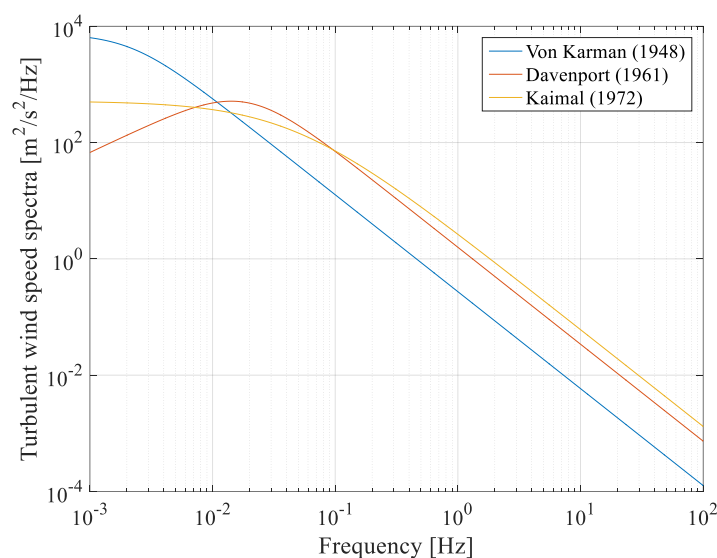


**Fig. B.3.** Spectrum of horizontal gustiness.

Once the spectrum of longitudinal turbulence is evaluated, the spectrum of fluctuating drag force,  $S_F$ , can be evaluated in the frequency domain by multiplying the spectrum of turbulence,  $S_u$ , with the aerodynamic admittance function, i.e.,  $x(f)^2 [C_D A(z) \rho \bar{U}(z)]^2$ , for the first three types of spectrum in Table B.2. The empirical factor,  $x(f) = 1/[1 + (2f\sqrt{A}/\bar{U}(z))^{4/3}]$ , is used to reflect the dependence of force (acting on structures) on the size of disturbance or gust in relation to the size of structure. Further to these three spectrum, [Solari \(1993\)](#) proposed a different approach which allows practitioners to evaluate the generalised force spectrum associated with any resonant mode of the building and with any given mode shape (Eq. (B.5)). With this approach, it is possible to model the building as a SDOF system and consider any

particular mode of vibration individually.

**Table B.2.** Mathematical expressions of force spectra of the along-wind turbulence.

	Force spectrum of the along-wind turbulence
von Karman (1948)/ Harris (1968)	$S_F(f) = x(f)^2 [C_D A(z) \rho \bar{U}(z)]^2 S_u(f)$ (B.6)
Davenport (1961 <sup>a</sup> )	
Kaimal (1972)	$S_F(z, f) = x(f)^2 [C_D A(z) \rho \bar{U}(z)]^2 S_u(z, f)$ (B.7)
	$S_F(f) = [\rho B Z C_D \bar{U}(z) \sigma_u(z) K_b]^2 S_{ueq}(f)$ (B.8)
Solari (1993)	$S_{ueq}(f) = \frac{S_u(z, f)}{\sigma_u(z)^2} L \left[ 0.4 \frac{f C_x B}{\bar{U}(z)} \right] \frac{1}{C_D^2} \left[ C_w^2 + 2 C_w C_L \frac{f C_y D}{\bar{U}(z)} + C_L^2 \right] L \left[ 0.4 \frac{f C_z Z}{\bar{U}(z)} \right]$ (B.9)
	$L(\eta) = \frac{1}{\eta} - \frac{1}{2\eta^2} (1 - e^{-2\eta})$ (B.10)
	$K_b = \frac{1}{Z \bar{U}(z) \sigma_u(z)} \int_0^z \bar{U}(z) \sigma_u(z) \Psi_1(z) dz$ (B.11)

In the expressions of Table B.2,  $S_F$  is the along-wind force spectrum,  $\rho$  is air density,  $B$  and  $D$  are frontal width and depth of the building,  $Z$  is the height of building,  $C_x$  and  $C_z$  are lateral and vertical exponential decay coefficients respectively,  $C_y$  is the cross-correlation coefficient of pressure acting on the windward and leeward face,  $C_D$  is drag coefficient,  $C_w$  and  $C_L$  are absolute values of pressure coefficients on windward and leeward faces, and  $\Psi_1(z)$  is the first mode shape of the building at height  $z$ .

### B.3 Modelling of wind loads to structures in the crosswind direction

In the crosswind direction, the dynamic wind loading on tall buildings is mainly induced by the wake excitation (Solari 1985). The vortex shedding mechanism is known to strongly correlate with side ratio, aspect ratio of the building, and turbulence intensity of incident flow (Liang et al. 2002). Since the 1970s, much research has been conducted to investigate the crosswind dynamic loads on rectangular tall buildings via wind tunnel testing (see e.g. Saunders and Melbourne 1975, Kareem 1982, Cheng et al. 1992, Choi and Kanda 1993). Nonetheless, these tests only involved a limited number of side ratios, and the proposed mathematical spectral models do not fit well with the experimental data, especially in the high frequency range. To this end, Liang et al. (2002) proposed empirical formulae of crosswind force spectra based on wind tunnel tests, conducted on rectangular prismatic models with a wide range of side ratios and two different model heights. The proposed mathematical model is in good

agreement with the experimental results in low and high frequency ranges.

In this model, tall buildings are further categorized into two groups, i.e., the ones whose side ratio is between 1/4 and 3, and the others with side ratio between 3 and 4. In the former case, the power spectra of crosswind force have a single peak at the vortex shedding frequency as shown in Fig. B.4 (a), whereas in the latter case, the spectra have two peaks, which are due to the primary and sub-vortex shedding, respectively, as shown in Fig. B.4 (b).

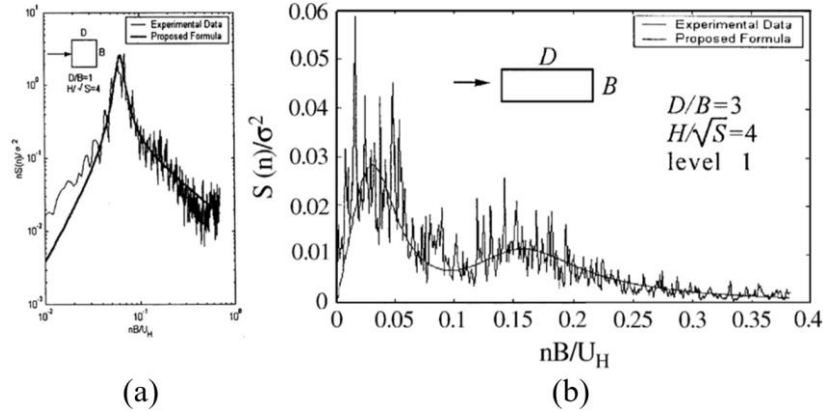


**Fig. B.4.** Power spectra of crosswind for side ratio (a)  $1/4 \leq D/B < 3$ , and (b)  $3 \leq D/B \leq 4$  (Liang et al. 2002).

Normalized formulae for crosswind spectra for the two categories of tall buildings are summarised in Table B.3. In these expressions,  $S_F(f)$  is the spectrum of the crosswind force,  $f$  is the frequency,  $\sigma(z) = 1/2 \rho \bar{U}(z)^2 \bar{C}_L B$  is the RMS crosswind force at height  $z$ ,  $\bar{C}_L$  is empirical lift coefficient,  $\bar{f} = f / f_s$  (where  $f_s = S_t \bar{U}(z) / B$ ) is the frequency of vortex shedding,  $S_t$  is the empirical Strouhal number,  $\bar{U}(z)$  is the mean speed at height  $z$ ,  $S$  is the area of floor plan,  $B$ ,  $D$  and  $H$  is the building's breadth, depth, and height, respectively,  $I_u^b = \sigma_u(z) / \bar{U}(z)$  is the turbulence intensity,  $\sigma_u(z)$  is the RMS (or standard deviation) of the turbulent velocity fluctuations at height  $z$ . As a remark, the dimension of  $\sigma(z)$  is in [F]/[L], i.e., force per length. To compute the RMS crosswind force at height  $z$  in [F], one needs to multiply  $\sigma(z)$  with the tributary height of buildings such that  $f \times S(f) / \sigma^2$  is in non-dimensional form.

**Table B.3.** Mathematical expressions of force spectra of the crosswind turbulence.

Side ratio	Normalized formula for crosswind spectrum
$1/4 \leq D/B < 3$	$\frac{f S_F(f)}{\sigma^2} = A \frac{H(C_1) \bar{f}^2}{(1 - \bar{f}^2)^2 + C_1 \bar{f}^2} + (1-A) \frac{C_2^{0.50} \bar{f}^3}{1.56 [(1 - \bar{f}^2)^2 + C_2 \bar{f}^2]}, \quad (\text{B.12})$
	$H(C_1) = 0.179 C_1 + 0.65 \sqrt{C_1}, \quad (\text{B.13})$
	$C_1 = [0.47(D/B)^{2.8} - 0.52(D/B)^{1.4} + 0.24] / (H / \sqrt{S}), \quad (\text{B.14})$



	$C_2 = 2, \quad (B.15)$
	$A = (H / \sqrt{S}) [-0.6(D / B)^2 + 0.29(D / B) - 0.06]$ $+ [9.84(D / B)^2 - 5.86(D / B) + 1.25], \frac{1}{4} \leq D / B < \frac{1}{2},$ $A = (H / \sqrt{S}) [-0.118(D / B)^2 + 0.358(D / B) - 0.214]$ $+ [0.066(D / B)^2 - 0.26(D / B) + 0.894], \frac{1}{2} \leq D / B < \frac{1}{3}$
	$\frac{fS_f(f)}{\sigma^2} = A \frac{1.275\bar{f}^2}{(1-\bar{f}^2)^2 + C_1\bar{f}^2} + (1-A) \frac{C_2^{0.50}(\bar{f}/k)^3}{1.56[(1-(\bar{f}/k)^2)^2 + C_2(\bar{f}/k)^2]}, \quad (B.17)$
	$k = -0.175(H / \sqrt{S}) + 4.7, 4 \leq H / \sqrt{S} \leq 8, \quad (B.18)$
	$C_1 = 2, \quad (B.19)$
$3 \leq D/B \leq 4$	$C_2 = 2/k, \quad (B.20)$
	$A = aI_u^b, \quad (B.21)$
	$a = 0.17(H / \sqrt{S}) + 3.32, \quad (B.22)$
	$b = 0.18(D / B) + 0.26, \quad (B.23)$

#### B.4 Modelling of the spatial correlation of wind forces

The cross-spectrum of two continuous records is a measure of their degree of correlation. The cross-spectrum amplitude of along-wind and crosswind forces at different heights decay as the height difference increases indicating smaller correlation.

For longitudinal dynamic wind loads (in the along-wind direction), the cross-spectrum can be estimated by

$$S_{F_j F_k}(f) = \exp(-\hat{f}_{jk}) \sqrt{S_{F_j}(f) S_{F_k}(f)}, \quad (B.24)$$

where  $S_{F_j}(f)$  and  $S_{F_k}(f)$  are the along-wind force auto-spectra at locations  $j$  and  $k$ , respectively (see Table B.2), and  $\hat{f}_{jk}$  is a frequency dependent coherence function for longitudinal velocity fluctuations proposed by [Davenport \(1968\)](#) and given by

$$\hat{f}_{jk} = \frac{fC_z |z_j - z_k|}{\frac{1}{2} [\bar{U}(z_j) + \bar{U}(z_k)]}, \quad (B.25)$$

in which  $C_z$  is a non-dimensional, vertical decay coefficient and usually taken equal to 10,  $f$  is frequency in Hz,  $z_j$  and  $z_k$  are height at locations  $j$  and  $k$  respectively,  $\bar{U}(z_j)$  and  $\bar{U}(z_k)$  are mean velocity at locations  $j$  and  $k$ .

For transverse velocity fluctuations in the crosswind direction, [Vickery and Clark \(1972\)](#) proposed the following empirical expression

$$r_{ij} = \cos(\alpha_1 \Delta) \exp \left\{ - \left[ \frac{\Delta}{\alpha_2} \right]^2 \right\}, \quad \Delta = \frac{|z_i - z_j|}{B}, \quad (\text{B.26})$$

which is widely used in the literature as a coherence function. Further to the above, [Liang et al. \(2002\)](#) proposed a similar expression of coherence function.

$$r_{ij} = \exp \left\{ - \left[ \frac{\Delta}{\alpha} \right]^2 \right\}; \quad \Delta = \frac{|z_i - z_j|}{B} \quad (\text{B.27})$$

In Eqs. (B.26) and (B.27),  $\Delta$  is the vertical distance between two levels,  $z_i$  and  $z_j$ ,  $B$  is the building breadth,  $\alpha$ ,  $\alpha_1$ , and  $\alpha_2$  are three empirical coefficients. With the auto-spectra and coherence functions in place, the cross spectra of dynamic wind loads in the crosswind direction can be evaluated by

$$S_{F_j F_k}(f) = r_{jk} \sqrt{S_{F_j}(f) S_{F_k}(f)}, \quad (\text{B.28})$$

in which the two terms under the square root denote the auto-spectra of dynamic wind loading at  $z_i$  and  $z_j$  respectively.

Finally, the PSD wind force matrix (in both along-wind and crosswind directions),  $\mathbf{S}_{FF}^n(\omega)$ , for a  $n$ -storey building structure represented by a  $n$ -DOF surrogate model defined through mass, stiffness, and damping matrices can be evaluated as follows

$$\mathbf{S}_{FF}^n(\omega) = \frac{1}{2\pi} \begin{bmatrix} S_{F_1 F_1}(f), & S_{F_1 F_2}(f), & \cdots & S_{F_1 F_n}(f) \\ S_{F_2 F_1}(f), & S_{F_2 F_2}(f), & \cdots & S_{F_2 F_n}(f) \\ \vdots & \vdots & \ddots & \vdots \\ S_{F_n F_1}(f), & S_{F_n F_2}(f), & \cdots & S_{F_n F_n}(f) \end{bmatrix}, \quad (\text{B.29})$$

where  $\omega$  is the circular frequency in rad/s, and the element  $S_{F_j F_k}(f)$  can be determined using either Eq. (B.24) or Eq. (B.28).

### **B.5 Case-study structural response verification of wind models vis-à-vis experimental wind tunnel force data**

To verify the spectral/mathematical models of fluctuating wind loads peak responses of uncontrolled primary structure, e.g., peak floor displacement, inter-storey drift, and floor acceleration, of the 74-storey benchmark building (see section 3.3.1) are first obtained in frequency domain by assuming the Kaimal spectrum in the along-wind direction and the Liang spectrum in the crosswind direction. The thus-evaluated responses are then compared against the corresponding peak responses obtained in time domain, by a step-by-step time integration method (e.g. Newmark-beta method), using experimental wind tunnel test data. The frequency domain and time domain structural analysis algorithms have been both custom-coded in MATLAB®.

The wind tunnel test was carried out on a 1:500, 0.61m-tall, rigid building model with a 0.1m-by-0.1m square footprint and an aspect ratio of 6.1 at the boundary layer wind tunnel of CRIACIV (Inter-University Research Centre on Buildings Aerodynamics and Wind Engineering) in Prato Italy, as shown in Fig. B.5. Experimental measures, i.e., the drag, lift and torque at each floor, were taken at the mean wind velocity  $V_m$  of 19.6 m/s at the top of the building model, which is equivalent to 35 m/s in full-scale with a return period of 1 year. The sampling interval is approximately 1/250 s, and the duration of time history is 30 s. These time-history data were made available to the author.

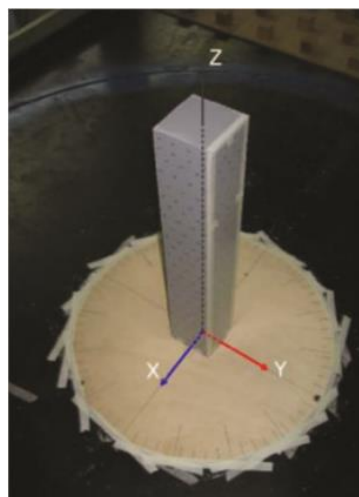


**Fig. B.5.** Experimental model in the wind tunnel test (Petrini and Ciampoli 2012).

The frequency-domain and time-domain responses in the along-wind and crosswind directions are plotted in Fig. B.6 and Fig. B.7, respectively, for comparison. It is seen that, by assuming the same micrometeorological conditions, the peak responses, estimated in the frequency domain by making use of the Kaimal and Liang spectrum, are found in good agreement with the corresponding peak values evaluated in the time domain using the wind tunnel data. Notably, the peak displacements and inter-storey drift ratios in Figs. B.6 are induced by the fluctuating component of wind loading in the along-wind direction, and should not be

confused with the static displacement response (which is much larger in amplitude) due to the mean component.

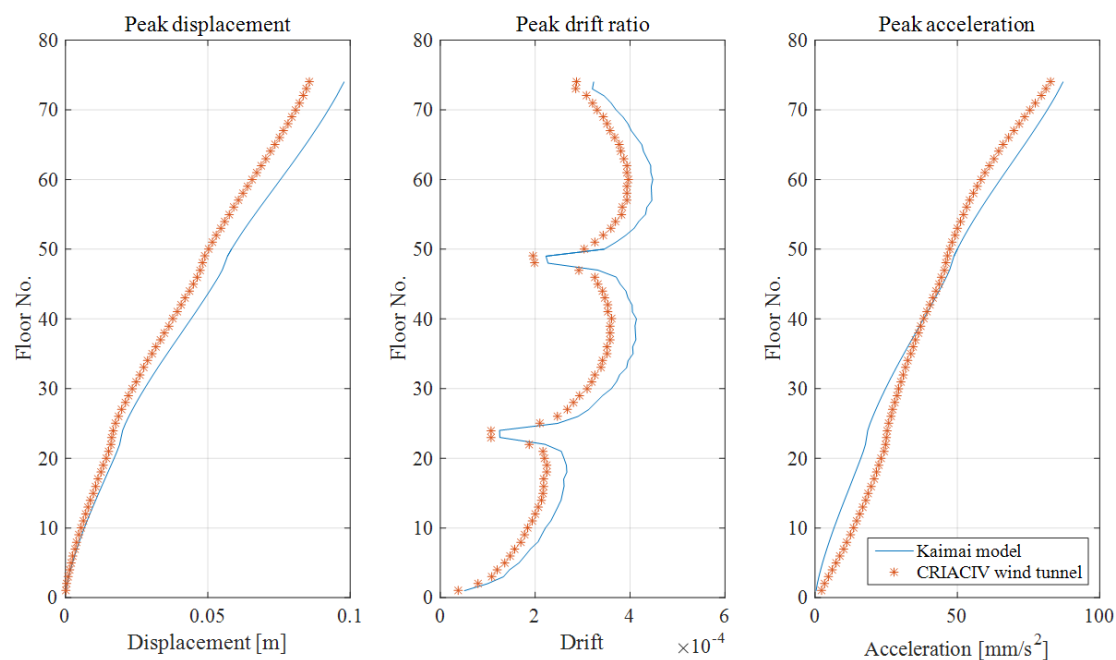


**Fig. B.6.** Verification of frequency domain analysis vis-à-vis time-domain analysis using experimental wind tunnel test data in the along-wind direction of the benchmark 74-storey structure in Fig.3.3 (Ciampoli and Petriani 2012).

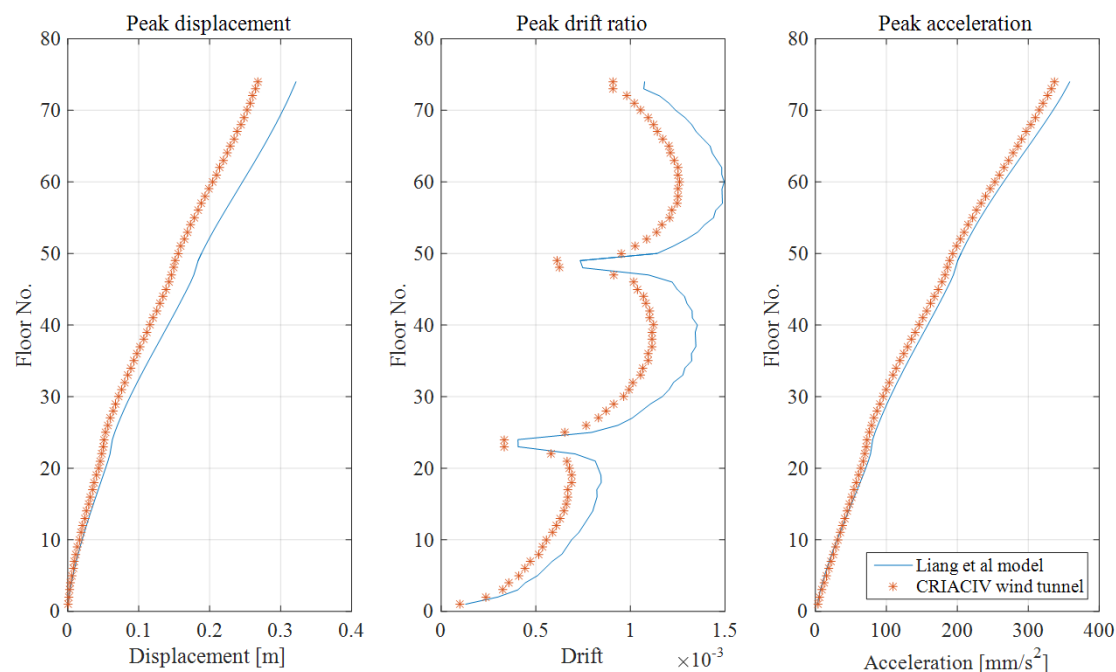


**Fig. B.7.** Verification of frequency domain analysis vis-à-vis time-domain analysis using experimental wind tunnel test data in the crosswind direction of the benchmark 74-storey structure in Fig.3.3 (Ciampoli and Petriani 2012).

## References

- Allwood, J., Ashby, M., Gotwski, T., and Worrel, E. (2011). "Material efficiency: a white paper." *Resour. Conserv. Recycl.*, 55 (2011): 362–381.
- Amano, T. (1995). "The effect of corner-cutting of three dimensional square cylinders on vortex-induced oscillation and galloping in uniform flow." *J. Struct. Constr. Eng.*, AIJ 60 (478), 63–69.
- American Society of Civil Engineer. (1995). *Standard on Minimum Loads for the Design of Buildings and Other Structures*. (ASCE 7-95). New York, U.S.
- Amin, J.A., and Ahuja, A.K. (2010). "Aerodynamic modifications to the shape of the buildings: a review of the state-of-the-art." *Asian Journal of Civil Engineering (Building and House)*, 11(4): 433-450.
- Arakaki, T., Kuroda, H., Arima, F., Inoue, Y., and Baba, K. (1999). "Development of seismic devices applied to ball screw: part 1 basic performance test of RD-series." *AIJ Journal of Technology and Design*, 8: 239–244.
- Asami, T., Nishihara, O., and Baz, A.M. (2002). "Analytical solutions to  $H_{\infty}$  and  $H_2$  optimisation of dynamic vibration absorber attached to damped linear systems." *J. Vib. Acoust.*, 124(2): 284- 295.
- Bakre, S.V., and Jangid, R.S. (2007). "Optimum parameters of tuned mass damper for damped main system." *Struct. Control Health Monit.*, 14(3): 448–470.
- Berke, L. (1970). "An efficient approach to the minimum weight design of deflection limited structures." *AF Flight Dynamics Laboratory Technical Memorandum*, TM-70-4-FDTR.
- Berke, L., and Khot N.S. (1987). "Structural Optimisation Using Optimality Criteria." In: Mota Soares, C.A. (eds), *Computer Aided Optimal Design: Structural and Mechanical Systems*, NATO ASI Series (Series F: Computer and Systems Sciences), vol 27. Springer, Berlin, Heidelberg.
- Bernardini, E., Spence, S.M.J., Kwon, D.K., and Kareem, A. (2015). "Performance-Based Design of High-Rise Buildings for Occupant Comfort." *J. Struct. Eng.*, 141(10), DOI:10.1061/(ASCE)ST.1943-541X.0001223.
- Boggs, D. (1997). "Acceleration indexes for human comfort in tall buildings - Peak or RMS?" *CTBUH Monograph*, Chapter 13: Motion Perception Tolerance and Mitigation.
- Bortoluzzi, D., Casciati, S., Elia, L., and Faravelli, L. (2015). "Design of a TMD solution to mitigate wind induced local vibrations in an existing timber footbridge." *Smart Struct. Syst.*, 16(3): 459-478.
- Brincker, R., and Ventura, C.E. (2015). *Introduction to Operational Modal Analysis*, John Wiley & Sons, Ltd., U.K.
- Brock, J.E. (1946). "A note on the damped vibration absorber." *J. Appl. Mech.*, 13, A284.
- Brownjohn, J.M.W., Carden, E.P., Goddard, C.R., and Oudin, G. (2009). "Real-time performance monitoring of tuned mass damper system for a 183 m reinforced concrete

- chimney.” *J. Wind Eng. & Ind. Aerodyn.*, 98: 169-179.
- Brzeski, P., Lazarek, M., and Perlikowski, P. (2017). “Experimental study of the novel tuned mass damper with inerter which enables changes of inertance.” *J. Sound Vib.*, 404: 47-57.
- BS EN 15978, (2011). *Sustainability of Construction Works. Assessment of Environmental Performance of Buildings. Calculation Method*. BSI.
- Burton, M.D., Denoon, R.O., Roberts, R.D., Kwok, K.C.S., and Hitchcock, P.A. (2003). “A motion simulator to investigate wind-induced building motion.” In: *Proc. of 11th International Conference of Wind Engineering*, 1341–1348, Texas, USA.
- Burton, M.D., Kwok, K.C.S., Hitchcock, P.A., and Denoon, R.O. (2006). “Frequency dependence of human response to wind-induced building motion.” *J. Struct. Eng.*, 132(2): 296-303.
- Cabeza, L., Barreneche, C., Miro, L., Morera, J., Bartoli, E., and Fernandez, A. (2013). “Low carbon and low embodied energy materials in buildings: a review.” *Renew. Sust. Energ. Rev.*, 23, 536–542.
- Cacciola, P., Tombari, A., and Giaralis, A. (2020). “An inerter-equipped vibrating barrier for non-invasive motion control of seismically excited structures.” *Struct. Control Health Monit.*, 27(3): e2474.
- Canfield, R.A., Venkayya, V.B., and Grandhi, R.V. (1989). “Structural optimization with stiffness and frequency constraints.” *Mechanics of Structures and Machines*, 17(5): 95-110. DOI: 10.1080/089054508915631.
- Cangelli, E., and Fais, L. (2012). “Energy and environmental performance of tall buildings: state of the art.” *Advances in Building Energy Research*, 6(1): 36-60, DOI: 10.1080/17512549.2012.671497.
- Caracoglia, L. (2018). “Unified stochastic dynamic and damage cost model for the structural analysis of tall buildings in thunderstorm-like winds.” *J. Risk Uncertain. Eng. Syst. Part B*, 4(4): 04018043.
- Carrato, P.J., and Santamont, K. (2012). “Tuned mass damper control of cross-wind excitation of a solar tower.” In: *Proc. of Structures Congress 2012*, March 29-31, 2012, Chicago, Illinois, U.S.
- CEN (European Committee for Standardization). (2005). *Eurocode 1: Actions on structures, Part 4: Wind actions*. (EN 1991-1-4). Brussels, Belgium.
- Chan, C.M. (1992). “An optimality criteria algorithm for tall buildings design using commercial standard sections.” *Structural Optimisation*, 5: 26–9.
- Chan, C.M. and Chui, J.K.L. (2006). “Wind-induced response and serviceability design optimisation of tall steel buildings.” *Eng. Struct.*, 28: 503-513.
- Charles, A., and Dennis, Jr., J.E. (2003) “Analysis of Generalized Pattern Searches.” *SIAM Journal on Optimisation*, 13(3): 889–903.
- Chen, M., Papageorgiou, C., Scheibe, F., Wang, F.C., and Smith, M. (2009). “The missing mechanical circuit element.” *IEEE Circuits Syst. Mag.*, 9: 10–26.

- Cheng, C.M., Lu, P.C., and Chen, R.H. (1992). “Wind loads on square cylinder in homogeneous turbulent flows.” *J. Wind Eng. Ind. Aerodyn.*, 41(1-3): 739–749.
- Choi, H., and Kanda, J. (1993). “Proposed formulae for the power spectral densities of fluctuating lift and torque on rectangular 3-D cylinders.” *J. Wind Eng. Ind. Aerodyn.*, 46–47: 507–516.
- Chopra, A.K. (2000). *Dynamics of Structures: Theory and Applications to Earthquake Engineering*, 2<sup>nd</sup> ed., Prentice-Hall, U.S.
- Christensen, P., and Klarbring, A. (2009). *An introduction to structural optimisation*, Springer Science + Business Media B.V.
- Christenson, R.E. (2001). “Semiactive control of civil structures for natural hazard mitigation: analytical and experimental studies.” (Ph.D. Thesis, Department of Civil Engineering and Geological Sciences, University of Notre Dame, US).
- Christopoulos, C., and Filiatrault, A. (2006). *Principles of Passive Supplemental Damping and Seismic Isolation*, 1<sup>st</sup> ed., IUSS Press, Pavia, Italy.
- Chu, S.Y., Soong, T.T., and Reinhorn, A.M. (2005). *Active, hybrid and semi-active structural control – a design and implementation handbook*, John Wiley & Sons, Ltd., England.
- Chuan, L., Liang, M., Wang, Y.X., and Dong, Y.T. (2012). “Vibration suppression using two terminal flywheel Part I: Modeling and characterization.” *J. Vib. Control*, 18(8): 1096-1105.
- Chung, L.L., Wu, L.Y., Yang, C.S., Lien, K.H., Lin, M.C., and Huang, H.H. (2013). “Optimal design formulas for viscous tuned mass dampers in wind-excited structures.” *Struct. Control Health Monit.*, 20: 320–336.
- Ciampoli, M. and Petrini, F. (2012). “Performance-Based Aeolian Risk assessment and reduction for tall buildings.” *Prob. Eng. Mech.*, 28: 75–84.
- Clough, R.W. and Penzien, J. (1995). *Dynamics of Structures*, 3<sup>rd</sup> ed., Computers & Structures, Inc., U.S.
- Cluni, F., Gioffrè, M., and Gusella, V. (2013). “Dynamic response of tall buildings to wind loads by reduced order equivalent shear-beam models.” *J. Wind Eng. Ind. Aerodyn.*, 123: 339-348.
- CNR - National Research Council of Italy. (2010). *Guide for the assessment of wind actions and effects on structures*. (CNR-DT 207/2008). Roma, Italy.
- Cooper, K.R., Nakayama, M., Sasaki, Y., Fediw, A.A., Resende-Ide, S., and Zan, S.J. (1997). “Unsteady aerodynamic force measurements on a super-tall building with a tapered cross section.” *J. Wind Eng. Ind. Aerodyn.*, (72): 199-212.
- Council on Tall Buildings and Urban Habitat. (2020). *CTBUH Height Criteria for Measuring & Defining Tall Buildings*. Retrieved from [https://cloud.ctbuh.org/CTBUH\\_HeightCriteria.pdf](https://cloud.ctbuh.org/CTBUH_HeightCriteria.pdf).
- Cui, W. and Caracoglia, L. (2020). “Performance-Based Wind Engineering of Tall Buildings Examining Life-Cycle Downtime and Multisource Wind Damage.” *J. Struct. Eng.*, 146(1): 04019179.



- Dai, J., Xu, Z.D., and Gai, P.P. (2019). “Tuned mass-damper-inerter control of wind-induced vibration of flexible structures based on inerter location.” *Eng. Struct.*, 199(15): 109585.
- Davenport, A.G. (1961<sup>a</sup>). “A statistical approach to the treatment of wind loading on tall masts and suspension bridges.” (Ph.D. Thesis, Department of Civil Engineering, University of Bristol, UK).
- Davenport, A.G. (1961<sup>b</sup>). “The application of statistical concepts to the wind loading of structures.” In: *Proc. of the Institution of Civil Engineers*, 19(4): 449-412.
- Davenport, A.G. (1963). “The buffeting of structures by gusts.” In: *Proc. of International Conference on Wind Effects on Buildings and Structures*, 358–391, June 26-28, 1963, Teddington, England.
- Davenport, A.G. (1964). “Note on the distribution of the largest values of a random function with application to gust loading.” In: *Proc. of the Institution of Civil Engineers*, 28, 187-196.
- Davenport, A.G. (1968). “The dependence of wind load upon meteorological parameters.” In: *Proc. of the International Research Seminar on Wind Effects on Buildings and Structures*, 19-82, University of Toronto Press, Toronto.
- De Angelis, M., Perno, S., and Reggio, A. (2012). “Dynamic response and optimal design of structures with large mass ratio TMD.” *Earthq. Eng. Struct. Dyn.*, 41(1): 41-60.
- De Angelis, M., Giaralis, A., Petrini, F., and Pietrosanti, D. (2019). “Optimal tuning and assessment of inertial dampers with grounded inerter for vibration control of seismically excited base-isolated systems.” *Eng. Struct.*, 196: 109250.
- De Domenico, D. and Ricciardi, G. (2018). “An enhanced base isolation system equipped with optimal tuned mass damper inerter (TMDI).” *Earthq. Eng. Struct. Dyn.*, 47(4): 1169-1192.
- De Domenico, D., Qiao, H.S., Wang, Q.H., Zhu, Z.W., and Marano, G. (2020). “Optimal design and seismic performance of Multi-Tuned Mass Damper Inerter (MTMDI) applied to adjacent high-rise buildings.” *Struct. Des. Tall Spec. Build.*, 29: e1781.
- Den Hartog, J.P. (1956). *Mechanical Vibrations*, 4<sup>th</sup> ed., McGraw-Hill, New York.
- Deng, T., Yu, X., and Xie, Z. (2015). “Aerodynamic measurements of crosswind loads and responses of tapered super high-rise buildings.” *Wind Struct.*, 21(3): 331-352.
- Deng, T., Fu, J., Zheng, Q., Wu, J., and Pi, Y. (2019). “Performance-based wind-resistant optimisation design for tall building structures.” *J. Struct. Eng.*, 145: 04019103.
- Denoon, R.O., Letchford, C.W., Kwok, K.C.S., and Morrison, D.L. (1999). “Field measurements of human reaction to wind-induced building motion.” In: *Proc. of 10th International Conference on Wind Engineering*, 647-644, Copenhagen, Denmark.
- Denoon, R.O. (2000). “Designing for wind-induced serviceability accelerations in buildings.” (Ph.D. thesis, Univ. of Queensland, Brisbane, Australia).
- Dunant, C., Drewniok, M., Eleftheriadis, S., Cullen, J., and Allwood, J. (2018). “Regularity and optimisation practice in steel structural frames in real design cases.” *Resour. Conserv. Recycl.*, 134, 294–302.

## References

---

- Dutton, R., and Isyumov, N. (1990). "Reduction of tall building motion by aerodynamic treatments." *J. Wind Eng. Ind. Aerodyn.*, 36(2): 739-747.
- Dym, C.L., and Williams, H.E. (2007). "Estimating fundamental frequencies of tall buildings." *J. Struct. Eng.*, 10(1479): 1479-1483.
- Elias, S., and Matsagar, V. (2017). "Research developments in vibration control of structures using passive tuned mass dampers." *Annual Reviews in Control*, 44: 129-156.
- Elias, S., and Matsagar, V. (2018). "Wind response control of tall buildings with a tuned mass damper." *J. Build. Eng.*, 15: 51-60.
- European Commission. (2010). *Directive 2010/31/EU of the European Parliament and of the Council of 19 May 2010 on the Energy Performance of Buildings*. European Parliament, Brussels.
- Fang, J.Q., Jeary, A.P., Li, Q.S., and Wong, C.K. (1997). "Random damping in buildings and its AR model." *J. Wind Eng. Ind. Aerodyn.*, 79: 159—167.
- Ford, L.R. (2005). *Cities and Buildings: Skyscrapers, Skid Rows and Suburbs*, The Johns Hopkins University Press, Baltimore, U.S.
- Frahm, H. (1911), "Device for Damping Vibrations of Bodies", U.S. Patent 989958, USPTO.
- Fujino, Y., and Abe, M. (1992). "Dynamic characterization of multiple tuned mass dampers." In: *Proc. of 1st International Conference on Motion and Vibration Control*, 176-181, Sep 7-11, 1992.
- Gaur, S., Elias, S., Hobbel, T., Matsagar, V.A., and Thiele, K. (2020). "Tuned mass dampers in wind response control of wind turbine with soil-structure interaction." *Soil Dyn. Earthq. Eng.*, 132: 106071.
- Gellatly, R.A. and Berke, L. (1972). "Optimality criteria based algorithm." *Optimal Structural Design*, eds.: Gallagher, R.H. and Zienkiewicz, O.C. John Wiley, 33-49.
- Ghosh, A., and Basu, B. (2007). "A closed-form optimal tuning criterion for TMD in damped structures." *Struct. Control Health Monit.*, 14(4): 681-692.
- Giaralis, A., and Marian, L. (2016). "Use of inerter devices for weight reduction of tuned mass-dampers for seismic protection of multi-story building: the Tuned Mass-Damper-Inerter (TMDI)." In: *Proc. of the SPIE 9799, Active and Passive Smart Structures and Integrated Systems 2016*, March 20-24, 2016, Las Vegas, Nevada, doi: 10.1117/1112.2219324.
- Giaralis, A., and Petrini, F. (2017). "Wind-induced vibration mitigation in tall buildings using the tuned massdamper-inerter (TMDI)." *J. Struct. Eng.*, 143(9), DOI:n10.1061/(ASCE)ST.1943-541X.0001863.
- Giaralis, A., and Taflanidis, A.A. (2015). "Reliability-based design of tuned-mass-damper-inerter (TMDI) equipped stochastically support excited structures." In: *Proc. of the 12th International Conference on Applications of Statistics and Probability in Civil Engineering (ICASP12)*, July 12 - 15, 2015, Vancouver, Canada.
- Giaralis, A., and Taflanidis, A.A. (2018). "Optimal tuned mass-damper-inerter (TMDI) design for seismically excited MDOF structures with model uncertainties based on reliability criteria." *Struct. Control Health Monit.*, DOI: 10.1002/stc.2082.

## References

---

- Gonzalez-Buelga, A., Lazar, I., Jiang, J.Z., Neild, S.A., and Inman, D.J. (2016). "Assessing the effect of nonlinearities on the performance of a Tuned Inerter Damper." *Struct. Control Health Monit.*, DOI: 10.1002/stc.1879.
- Griffis, L.G. (1993). "Serviceability limit states under wind load." *Engineering Journal*, AISC, 30: 1-16.
- Guo, Y.L., Kareem, A., Ni, Y.Q., and Liao, W.Y. (2012). "Performance evaluation of Canton Tower under winds based on full-scale data." *J. Wind Eng. Ind. Aerodyn.*, 104-106: 116-128.
- Hansen, R.J., Reed, J.W., and Vanmarcke, E.H. (1973). "Human Response to Wind-Induced Motion of Buildings," *J. Struct. Eng.*, 99(ST7).
- Harris, R.I. (1968). "On the spectrum and auto-correlation function of gustiness in high winds." *Electrical Research Association*, Technical Report, No: 5273.
- Hayashida, H., and Iwasa, Y. (1990). "Aerodynamic shape effects of tall building for vortex induced vibration." *J. Wind Eng. Ind. Aerodyn.*, 33(1-2): 237-242.
- Hixson, E.L., (1976). "Mechanical impedance." In: *Shock and Vibration Handbook*, 2<sup>nd</sup> ed., chapter 10, McGraw-Hill Education.
- Huang, M.F. (2017). *High-Rise Buildings Under Multi-Hazard Environment: Assessment and Design for Optimal Performance*, Science Press and Springer Science + Business Media, Singapore.
- Hwang, J.S., Kim, J., Kim, and Kim, Y.M. (2007). "Rotational inertia dampers with toggle bracing for vibration control of a building structure." *Eng. Struct.*, 29: 1201–1208.
- Ierimonti, L., Caracoglia, L., Venanzi, I., and Materazzi, A.L. (2017). "Investigation on life-cycle damage cost of wind-excited tall buildings considering directionality effects." *J. Wind Eng. Ind. Aerodyn.*, 171: 207–218.
- Ierimonti, L., Venanzi, I., and Caracoglia, L. (2018). "Life-cycle damage-based cost analysis of tall buildings equipped with tuned mass dampers." *J. Wind Eng. Ind. Aerodyn.*, 176: 54-64.
- Ikago, K., Saito, K., and Inoue, N. (2012). "Seismic control of single-degree-of-freedom structure using tuned viscous mass damper." *Earthq. Eng. Struct. Dyn.*, 41(3): 453–474.
- International Organization of Standardization. (1984). *Guidelines for the evaluation of the response of occupants of fixed structures to low frequency horizontal motion (0.063 to 1 Hz)*. ISO Standard 6897.
- International Energy Agency. (2017a). *Global Status Report 2017 - Towards a Zero Emission, Efficient, and Resilient Buildings and Construction Sector*. Global Alliance for Building and Construction.
- International Energy Agency. (2017b). *World Energy Balances*.
- Islam, M.S., Ellingwood, B., and Corotis, R.B. (1990). "Dynamic response of tall buildings to stochastic wind load." *J. Struct. Eng.*, 116(11): 2982–3002.
- Isyumov, N. and Poole, M. (1983). "Wind Induced Torque on Square and Rectangular Building Shapes." *J. Wind Eng. Ind. Aerodyn.*, 13.

- Isyumov, N. (1993). "Criteria for acceptable wind-induced motions of tall buildings." In: *Proc. of International Conference on Tall Buildings*, 411–423, May 17-19, 1993, Rio de Janeiro, Brazil.
- Isyumov, N. and Kilpatrick, J. (1996). "Full-scale experience with wind-induced motions of tall buildings." In: *Proc. of 67th Regional Conference Council on Tall Buildings and Urban Habitat*, 401-411, Chicago, US, 15–18 April.
- Isyumov, N. (2012). "Alan G. Davenport's mark on wind engineering." *J. Wind Eng. Ind. Aerodyn.*, 104-106: 12-24.
- Jeary, A.P. (1986). "Damping in buildings—a mechanism and a predictor." *Earthq. Eng. Struct. Dyn.* 14: 733–750.
- Jokic, M., Stegic, M., and Butkovic, M. (2011). "Reduced-order multiple tuned mass damper optimisation: A bounded real lemma for descriptor systems approach." *J. Sound Vib.*, 330: 5259-5268.
- Kaimal, J.C., Wyngaard, J.C., Izumi, Y., and Coté, O.R. (1972). "Spectral characteristics of surface-layer turbulence." *Journal of the Royal Meteorological Society*, 98: 563–589.
- Kareem, A. (1982). "Acrosswind response of buildings." *J. Struct. Div.*, ASCE 108(4): 869–887.
- Kareem, A. (1983). "Mitigation of wind induced motion of tall buildings." *J. Wind Eng. Ind. Aerodyn.*, 11(1–3): 273–284.
- Kareem, A. (1992). "Serviceability issues and motion control of tall buildings." In: *Proc. of Structures Congress*, Reston, VA.
- Kareem, A., Kijewski, T., and Tamura, Y. (1999). "Mitigation of motions of tall buildings with specific examples of recent applications." *Wind and Structures*, 2(3): 201-251.
- Kareem, A., and Kline, S. (1995). "Performance of Multiple Mass Dampers under Random Loading." *J. Struct. Eng.*, 121(2): 348-361.
- Karim, A. (1983). "Mitigation of wind-induced motion of tall buildings." *J. Wind Eng. Ind. Aerodyn.*, 11: 273-284.
- Kaveh, A., Farzam, M.F., and Jalali, H.H. (2020). "Statistical seismic performance assessment of tuned mass damper inerter." *Struct. Control Health Monit.*, 27: e2602.
- Kawamata, S., Yoneda, M., and Hangai, Y. (1973). "Development of a vibration control system for structures by means of mass pump." Retrieved from: <http://www.ers.iis.u-tokyo.ac.jp/PDF/ERSNo.07/1973-12-No.07-03.pdf>.
- Khodaie, N. (2020). "Vibration control of super-tall buildings using combination of tapering method and TMD system." *J. Wind Eng. Ind. Aerodyn.*, 196(2020): 104031.
- Khot, N.S. (1983). "Nonlinear analysis of optimized structure with constraints on system stability." *AIAA Journal*, 21(8): 1181-1186.
- Kijewski-Correa, T., et al. (2007). "Full-scale performance evaluation of tall buildings under winds." In: *Proc. of 12th Int. Conf. on Wind Engineering*, July 1-6, 2007, Cairns, Australia.

- Kijewski-Correa, T., and Pirnia, D. (2009). “‘Pseudo-full-scale’ evaluation of occupant comfort in tall buildings.” In: *Proc. of 11th Americas Conf. on Wind Engineering*, June 22-26, 2009, San Juan, Puerto Rico.
- Kim, Y.M., and You, K.P. (2002). “Dynamic response of a tapered tall building to wind loads.” *J. Wind Eng. Ind. Aerodyn.*, 90 (12–15): 1771–1782.
- Kim, Y.C., Kanda, J., and Tamura, Y. (2011). “Wind-induced coupled motion of tall buildings with varying square plan with height.” *J. Wind Eng. Ind. Aerodyn.*, 99(5): 638-650.
- Kim, Y.C., and Kanda, J. (2013). “Wind pressures on tapered and set-back tall buildings.” *J. Fluid Struct.*, 39(2013): 306-321.
- Kirsch, U. (1993). *Structural Optimization Fundamentals and Applications*. Springer-Verlag Berlin Heidelberg.
- Kiusalaas, J. (1973). “Optimal design of structures with buckling constraints.” *Int. J. Solids Struct.*, 9: 863-878.
- Krenk, S. (2005). “Frequency analysis of the tuned mass damper.” *J. Appl. Mech.*, 72: 936–942.
- Kwok, K.C.S., and Bailey, P.A. (1987). “Aerodynamic devices for tall buildings and structures.” *J. Eng. Mech.*, 113: 349–65.
- Kwok, K.C.S. (1988). “Effect of building shape on wind-induced response of tall buildings.” *J. Wind Eng. Ind. Aerodyn.*, 28: 381–90.
- Kwok, K.C.S., Hitchcock, P.A., and Burton, M.D. (2009). “Perception of vibration and occupant comfort in wind-excited tall buildings.” *J. Wind Eng. Ind. Aerodyn.*, 97(7-8): 368–380.
- Lagaros, N., Plevris, V., and Mitropoulou, C.C. (2012). *Design Optimisation of Active and Passive Structural Control Systems*, IGI Global.
- Lagomarsino, S. (1993). “Forecast models for damping and vibration periods of buildings.” *J. Wind Eng. Ind. Aerodyn.*, 48(2-3): 221-239.
- Lamb, S., Kwok, K. C. S., and Walton, D. (2013). “Occupant comfort in wind-excited tall buildings: Motion sickness, compensatory behaviours and complaint.” *J. Wind Eng. Ind. Aerodyn.*, 119, 1–12.
- Lazar, I.F., Neild, S.A., and Wagg, D.J. (2014). “Using an inerter-based device for structural vibration suppression.” *Earthq. Eng. Struct. Dyn.*, 43(8): 1129-1147.
- Leung, A.Y.T., and Zhang, H. (2009). “Particle swarm optimisation of tuned mass dampers.” *Eng. Struct.*, 31(3): 715-728.
- Levy, R. (1994). “Optimal design of trusses for overall stability.” *Comput. Struct.*, 53(5): 1133-1138.
- Liang, S.G., Liu, S.C., Li, Q.S., Zhang, L.L., and Gu, M. (2002). “Mathematical model of acrosswind dynamic loads on rectangular tall buildings.” *J. Wind Eng. Ind. Aerodyn.*, 90: 1757–1770.
- Li, Q.S., Cao, H., Li, G., Li, S., and Liu, D. (1999). “Optimal design of wind induced vibration

- control of tall buildings and high-rise structures.” *Wind Struct.*, 2(1), 69–83.
- Li, Q.S., Yang, K., Wong, C.K., and Jeary, A.P. (2003). “The effect of amplitude-dependent damping on wind-induced vibrations of a super tall building.” *J. Wind Eng. Ind. Aerodyn.*, 91(9): 1175–1198.
- Li, Q.S., Xiao, Y.Q., Wong, C.K., and Jeary, A.P. (2004). “Field measurements of typhoon effects on a super tall building.” *Eng. Struct.*, 26(2): 233–244.
- Li, Q.S., Xiao, Y.Q., Wu, J.R., Fu, J.Y., and Li, Z.N. (2008). “Typhoon effects on super-tall buildings.” *J. Sound Vib.*, 313(3–5): 581–602.
- Li, Q.S., Zhi, L.H., Tuan, A.Y., Kao, C.S., Su, S.C., and Wu, C.F. (2011). “Dynamic behavior of Taipei 101 tower: Field measurement and numerical analysis.” *J. Struct. Eng.*, 137(1): 143–155.
- Li, Y.Y., Zhang, S.Y., Jiang, J.Z., and Neild, S. (2019). “Identification of beneficial mass-included inerter-based vibration suppression configurations.” *J. Franklin Inst.*, 356(14): 7836-7854.
- Lógó, J. (2005). “New Type of Optimal Topologies by Iterative Method.” *Mechanics Based Design of Structures and Machines*, 33(2): 149-171.
- Longarini, N., Cabras, L., Zucca, M., Chapain, S., and Aly, A.M. (2017). “Structural Improvements for Tall Buildings under Wind Loads: Comparative Study.” *Shock and Vibration*, <https://doi.org/10.1155/2017/2031248>.
- Lu, X.L., Zhang, Q., Weng, D., et al. (2017). “Improving performance of a super tall building using a new eddy current tuned mass damper.” *Struct. Control Health Monit.*, 24: e1882.
- Luenberger, D.G. (1969). *Optimisation by Vector Space Methods*, John Wiley & Sons, Ltd., New York.
- Makris, P.A. and Provatidis, G.C. (2002). “Weight minimization of displacement-constrained truss structures using a strain energy criterion.” *Comput. Methods Appl. Mech. Eng.*, 191: 2159-2177.
- Makris, P.A., Provatidis, C.G., and Rellakis, D.A. (2006). “Discrete variable optimization of frames using a strain energy criterion.” *Struct. Multidiscip. Optim.*, 31(5): 410-417. DOI: 10.1007/s00158-005-0588-z.
- Marian, L., and Giaralis, A. (2013). “Optimal design of inerter devices combined with TMDs for vibration control of buildings exposed to stochastic seismic excitations.” In: *Proc. of 11<sup>th</sup> ICOSSAR Int. Conf. on Structural Safety and Reliability*, 1025-1032, June 16-20, 2013, New York.
- Marian, L., and Giaralis, A. (2014). “Optimal design of a novel tuned mass-damper–inerter (TMDI) passive vibration control configuration for stochastically support-excited structural systems.” *Prob. Eng. Mech.*, 38: 156–164.
- Marian, L. and Giaralis, A. (2017). “The tuned mass-damper-inerter for harmonic vibrations suppression, attached mass reduction, and energy harvesting.” *Smart Structures and Systems*, 19(6): 665-678.
- McNamara, R., Kareem, A., and Kijewski, T. (2002). “Ask the experts... Perception of motion



## References

---

- criteria for tall buildings subjected to wind: A panel discussion.” In: *Proc. of Structures Congress*, ASCE, Reston, VA.
- Moynihn, M., and Allwood, J. (2014). “Utilization of structural steel in buildings.” In: *Proc. of The Royal Society A*, 470(2168), <https://doi.org/10.1098/rspa.2014.0170>.
- Nakaminami, S., Kida, H., Ikago, K., and Inoue, N. (2017). “Dynamic testing of a full-scale hydraulic inerter-damper for the seismic protection of civil structures.” In: *Proc. of the 7th International conference on advances in experimental structural engineering*, Sep 6 – 8, 2017, Pavia, Italy.
- Nakamura, Y., Fukukita, A., Tamura, K., Yamazaki, I., Matsuoka, T., Hiramoto, K., et al. (2014). “Seismic response control using electromagnetic inertial mass dampers.” *Earthq. Eng. Struct. Dyn.*, 43: 507–527.
- Noguchi, K., Hiwatashi, A., Kobayashi, A., Tsujita, O., and Goto, T. (1993). “Human response to horizontal motion of tall buildings.” In: *Proc. of International Colloquium on Structural Serviceability of Buildings*, IABSE Reports, 69: 53-58, Goteborg, Sweden.
- Ormondroyd, J., and Den Hartog, J.P. (1928). “The theory of dynamic vibration absorber.” *Trans.*, ASME, APM-50-7, 9-22.
- Orr, J., Drewniok, M.P., Walker, I., Ibell, T., Copping, A., and Emmitt, S. (2019). “Minimising energy in construction: Practitioners’ views on material efficiency.” *Resour. Conserv. Recycl.*, 140: 125-136.
- Pacheco-Torgal, F., Faria, J., and Jalali, S. (2013). “Embodied energy versus operational energy. Showing the shortcomings of the energy performance building directive (EPBD).” *Mater. Sci. Forum*, 730: 587–591.
- Papageorgiou, C., and Smith, M.C. (2005). “Laboratory experimental testing of inerters.” In: *Proc. of 44th IEEE Conf. Decision Control*, 3351-3356.
- Park, H.S. and Park, C.L. (1998). “Drift control of high-rise buildings with unit load method.” *Struct. Des. Tall Spec. Build.*, 6(1): 23-35.
- Patnaik, S.N., Guptill, J.D., and Berke, L. (1995). “Merits and limitations of optimality criteria method for structural optimisation.” *Int. J. Numer. Meth. Eng.*, (38)18: 3087-3120.
- Petrini, F., and Ciampoli, M. (2012). “Performance-based wind design of tall buildings.” *Struct. Infrastruct. Eng.*, 8(10), 954–966.
- Petrini, F., Giaralis, A., and Wang, Z. (2020). “Optimal tuned mass-damper-inerter (TMDI) design in wind-excited tall buildings for occupants’ comfort serviceability performance and energy harvesting.” *Eng. Struct.*, 204: 109904.
- Pietrosanti, D., De Angelis, M., and Basili, M. (2017). “Optimal design and performance evaluation of systems with Tuned Mass Damper Inerter (TMDI).” *Earthq. Eng. Struct. Dyn.*, 46: 1367–1388.
- Pietrosanti, D., De Angelis, M., and Basili, M. (2020a). “A generalized 2-DOF model for optimal design of MDOF structures controlled by Tuned Mass Damper Inerter (TMDI).” *Int. J. Mech. Sci.*, 185: 105849.
- Pietrosanti, D., De Angelis, M., and Giaralis, A. (2020b). “Experimental shaking table study of



## References

---

- nonlinear SDOF system equipped with tuned mass damper inerter (TMDI) under harmonic excitation.” *Int. J. Mech. Sci.*, 184: 105762.
- Prager, W., and Shield, R.T. (1968). “Optimal design of multi-purpose structures.” *Int. J. Solids Struct.*, 4: 469-475.
- Prager, W., and Taylor, J. L. (1968). “Problems of Optimal Structural Designs.” *J. Appl. Mech.*, (90)1: 102-106.
- Radu, A., Lazar, I.F., and Neild, S.A. (2019). “Performance-based seismic design of tuned inerter dampers.” *Struct. Control Health Monit.*, 26, DOI: 10.1002/stc.2346.
- Rana, R., and Soong, T.T. (1998). “Parametric study and simplified design of tuned mass dampers.” *Eng. Struct.*, 20(3): 193–204.
- Randall, S.E., Halsted, D.M., and Taylor, D.L. (1981). “Optimum vibration absorbers for linear damped systems.” *J. Mech. Des.*, 103: 908–913.
- Reinhold, T.A. et al. (1979). “Mean and fluctuating wind forces and torques on a tall building model of square cross-section as a single model, in the wake of a similar model, and in the wake of a rectangular model.” Report VP1-E-79-11, Department of Engineering Science and Mechanics, Virginia Polytechnic Institute, Blacksburg, VA.
- Ricciardelli, F., Pizzimenti, A.D., and Mattei, M. (2003). “Passive and active mass damper control of the response of tall buildings to wind gustiness.” *Eng. Struct.*, 25: 1199–1209.
- Roberts, J.B., and Spanos, P.D. (2003). *Random Vibration and Statistical Linearization*, Dover Publications Inc.
- Ruiz, R., Taflanidis, A.A., Lopez-Garcia, D., and Vetter, C. (2015). “Life-cycle based design of mass dampers for the Chilean region and its application for the evaluation of the effectiveness of tuned liquid dampers with floating roof.” *Bulletin of Earthquake Engineering*, 14: 943–970.
- Ruiz, R., Taflanidis, A.A., Giaralis, A., and Lopez-Garcia, D. (2018). “Risk-informed optimisation of the tuned mass-damper-inerter (TMDI) for the seismic protection of multi-storey building structures.” *Eng. Struct.*, 177: 836-850.
- Saaed, T.E., Nikolakopoulos, G., Jonasson, J.E., and Hedlund, H. (2013). “A state-of-the-art review of structural control systems.” *J. Vib. Control*, 21(5): 919-937.
- Salvi, J., and Rizzi, E. (2016). “Closed-form optimum tuning formulas for passive tuned mass dampers under benchmark excitations.” *Smart Struct. Syst.*, 17(2): 231-256.
- Sarkar, R. and Fitzgerald, B. (2019). “Vibration control of spar-type floating offshore wind turbine towers using a tuned mass-damper-inerter.” *Struct. Control Health Monit.*, 27: e2471.
- Satake, N., Suda, K., Arakawa, T., Sasaki, A., and Tamura, Y. (2003). “Damping evaluation using full-scale data of buildings in Japan.” *J. Struct. Eng.*, 129(4): 470-477.
- Saunders, J.W., and Melbourne, W.H. (1975). “Tall rectangular building response to cross-wind excitation.” In: *Proc. of the Fourth International Conference on Wind Effects on Buildings and Structures*, 369–379, London.

- Shimada, K., and Hibi, K. (1995). "Estimation of wind loads for a super-tall building (SSH)." *Struct. Des. Tall Build.*, 4 (1): 47–60.
- Shioya, K. and Kanda, J. (1993). "Human perception thresholds of horizontal motion." In: *Proc. of International Colloquium on Structural Serviceability of Buildings*, IABSE Reports, 69: 45-52, Goteborg, Sweden.
- Simiu, E., and Scanlan, R.H. (1996). *Wind effects on structures: fundamentals and applications to design*, John Wiley & Sons Ltd., New York.
- Smith, B.S., and Coull, A. (1991). *Tall Building Structures: Analysis and Design*, John Wiley & Son, Inc., USA.
- Smith, M.C. (2002). "Synthesis of mechanical networks: The Inerter." *IEEE Trans. Autom. Control*, 47: 1648-1662.
- Smith, M.C. (2020). "The inerter: a retrospective." *Annual Review of Control, Robotics, Autonomous Systems*, 3: 361-391.
- Solari, G. (1985). "Mathematical model to predict 3-D loading on buildings." *J. Eng. Mech.*, 111(2): 254– 275.
- Solari, G. (1993). "Gust buffeting. I: peak wind velocity and equivalent pressure." *J. Struct. Eng.*, 199(2): 383-398.
- Solari, G. (1993). "Gust buffeting. II: dynamic alongwind analysis." *Journal of Structural Engineering*, 199(2), 365-382.
- Soong, T.T., and Dargush, G.F. (1997). *Passive energy dissipation system in structural engineering*, John Wiley & Sons Ltd., Chichester, England.
- Soto, M.G., and Adeli, H. (2013). "Tuned mass dampers." *Arch. Comput. Methods Eng.*, 20(4): 419-431.
- Spence, S.M.J. (2018). "Optimisation of uncertain and dynamic high-rise structures for occupant comfort: An adaptive kriging approach." *Structural Safety*, 75(2018): 57-66.
- Spence, S.M.J., and Giofrè, M. (2012). "Large scale reliability-based design optimisation of wind excited tall buildings." *Prob. Eng. Mech.*, 28: 206-215.
- Spence, S.M.J., and Kareem, A. (2014). "Tall buildings and damping: A concept-based data-driven model." *J. Struct. Eng.*, DOI: 10.1061/(ASCE)ST.1943-541X.0000890.
- SteelConstruction.Info. (n.d.). Cost of structural steelwork. Retrieved Oct 28, 2020, from <https://www.steelconstruction.info/Cost of structural steelwork>.
- Steenbergen, R.D.J.M, Koster, T., and Geurts, C.P.W. (2012). "The effect of climate change and natural variability on wind loading values for buildings." *Building and Environment*, 55: 178- 186.
- Sugimura, Y., Goto, W., Tanizawa, H., Saito, K., and Ninomiya, T. (2012). "Response control effect of steel building structure using tuned viscous mass damper." In: *Proc. of 15th World Conference on Earthquake Engineering 2012 (15WCEE)*, Sep 24-28, 2012, Lisbon, Portugal.

- Svanberg, K. (1984). "On local and global minima in structural optimisation." In: *New Directions in Optimum Structural Design*, 327–341. Wiley, New York.
- Swift, S.J., Smith, M.C., Glover, A.R., Papageorgiou, C., Gartner, B., and Houghton, N.E. (2013). "Design and modelling of a fluid inerter." *Intern. J. Control*, 86(11): 2035–2051.
- Taflanidis, A.A., Giaralis, A., and Patsialis, D. (2019). "Multi-objective optimal design of inerter-based vibration absorbers for earthquake protection of multi-storey building structures." *J. Franklin Inst.*, 356(14): 7754–7784.
- Tallin, A. and Ellingwood, B. (1983). "Serviceability limit states: Wind induced vibrations." *J. Struct. Eng. ASCE*, 110(10): 2424–2437.
- Tamura, Y., Kawai, H., Uematsu, Y., Okada, H., and Ohkuma, T. (2004). "Documents for wind resistant design of buildings in Japan." available at: <http://wind.arch.t-kougei.ac.jp/APECWW/Report/2004/JAPANA.pdf>.
- Tamura, Y., Kawana, S., Nakamura, O., Kanda, J., and Nakata, S. (2006). "Evaluation perception of wind-induced vibration in buildings." In: *Proc. of ICE – Structures and Buildings*, 159(5): 283–293.
- Tanaka, H., Tamura, Y., Ohtake, K., Nakai, M., and Kim, Y.C. (2012). "Experimental investigation of aerodynamic forces and wind pressures acting on tall buildings with various unconventional configurations." *J. Wind Eng. Ind. Aerodyn.*, 107–108: 179–191.
- Takewaki, I., Murakami, S., Yoshitomi, S., and Tsuji, M. (2012). "Fundamental mechanism of earthquake response reduction in building structures with inertial dampers." *Struct. Control Health Monitor.*, 19(6): 590–608.
- Tamura, Y., et al. (2013). *Advanced Structural Wind Engineering*, Springer, Japan.
- Tanaka, H., Tamura, Y., Ohtake, K., Nakai, M., and Kim, Y.C. (2012). "Experimental investigation of aerodynamic forces and wind pressures acting on tall buildings with various unconventional configurations." *J. Wind Eng. Ind. Aerodyn.*, 107–108: 179–91.
- Taranath, S.B. (2016). *Tall building design, steel, concrete, and composite systems*, CRC Press, Boca Raton, Florida.
- Thompson, A.G. (1981). "Optimum tuning and damping of a dynamic vibration absorber applied to a force excited and damped primary system." *J. Sound Vib.*, 77: 403–415.
- Tributsch, A., and Adam, C. (2012). "Evaluation and analytical approximation of Tuned Mass Dampers performance in an earthquake environment." *Smart Struct. Syst.*, 10(2): 155–179.
- Tsai, H.C., and Lin, G.C. (1994). "Explicit formulae for optimum absorber parameters for force-excited and viscously damped system." *J. Sound Vib.*, 176: 585–596.
- Tse, K.T., Kwok, K.C.S., and Tamura, Y. (2012). "Performance and cost evaluation of a smart tuned mass damper for suppressing wind-induced lateral torsional motion of tall buildings." *J. Struct. Eng.*, 138(4): 514–525.
- Venkayya, V.B., Khot, N.S., and Reddy, V.S. (1968). "Optimisation of structures based on the study of strain energy distribution." In: *Proc. of the 2nd Conference on Matrix Methods in Structural Mechanics, WPAFB, AFFDL-TR-68-150*, 111–153.

- Venkayya, V.B. (1971). "Design of optimum structures." *Comput. Struct.*, (1): 265 – 309.
- Venkayya, V.B., Khot, N.S., and Berke, L. (1973). "Application of optimality criteria approaches to automated design of large practical structures." *Second Symposium on Structural Optimization*, AGARD-CP-123.
- Vickery, B.J., and Clark, A.W. (1972). "Lift or crosswind response of tapered stacks." *J. Struct. Div.*, ASCE 98 (ST1), 1–20.
- Von Karman, T. (1948). "Progress in the statistical theory of turbulence." In: *Proc. of the National Academy of Sciences*, 530–539.
- Wang, F.C., Hong, M.F., and Lin, T.C. (2011). "Designing and testing a hydraulic inerter." In: *Proc. Inst. Mech. Eng., Part C: J. Mech. Eng. Sci.*, 1(265): 66–72.
- Wang, Q.H., Qiao, H.S., De Domenico, D., Zhu, Z.W., and Xie, Z.N. (2019). "Wind-induced response control of high-rise buildings using inerter-based vibration absorbers." *Appl. Sci.*, 9: 5045; doi:10.3390/app9235045.
- Wang, Z. and Giaralis, A. (2020). "Top-storey softening in optimal tuned mass damper inerter (TMDI)-equipped wind-excited tall buildings for enhanced serviceability performance under vortex shedding effects." *J. Struct. Eng.*, DOI: 10.1061/(ASCE)ST.1943-541X.0002838.
- Warburton, G.B., and Ayorinde, E.O. (1980). "Optimum absorber parameters for simple systems." *Earthq. Eng. Struct. Dyn.*, 8: 197–217.
- Warburton, G.B. (1982). "Optimum absorber parameters for various combinations of response and excitation parameters." *Earthq. Eng. Struct. Dyn.*, 10: 381–401.
- Watanabe, Y., Ikago, K., Inoue, N., Kida, H., Nakaminami, S., Tanaka, H. et al. (2012). "Full-scale dynamic tests and analytical verification of a force-restricted tuned viscous mass damper." In: *Proc. of 15th World Conference on Earthquake Engineering*, Sep 24-28, 2012, Lisbon, Portugal.
- Wen, Y.K., and Shinozuka, M. (1998). "Cost-effectiveness in active structural control." *Eng. Struct.*, 20(3): 216-221.
- Xu, K., and Igusa, T. (1992). "Dynamic characteristics of multiple substructures with closely spaced frequencies." *Earthq. Eng. Struct. Dyn.*, 21: 1059–1070.
- Yamaguchi, H., and Harnpornchai, N. (1993). "Fundamental characteristics of multiple tuned mass dampers for suppressing harmonically forced oscillations." *Earthq. Eng. Struct. Dyn.*, 22(1), 51-62.
- Yao, J.T.P. (1972). "Concepts of structural control." *J. Struct. Eng.*, 98: 1567-1574.
- Yin, L.Z. and Yang, W. (2001). "Optimality criteria method for topology optimisation under multiple constraints." *Comput. Struct.*, 79: 1839-1850.
- You, K.P., Kim, Y.M., and Ko, N.H. (2008). "The evaluation of wind-induced vibration responses to a tapered tall building." *Struct. Des. Tall Special Build.*, 17: 655–667.
- Zhang, S.Y., Jiang, J.Z., and Neild, S. (2017). "Optimal configurations for a linear vibration suppression device in a multi-storey building." *Struct. Control Health Monit.*, 24(3): 1545-

2255.

Zhang, R.F., Zhao, Z.P., Pan, C., Ikago, K., and Xue, S.T. (2018). "Damping enhancement principle of inerter system." *Struct. Control Health Monit.*, DOI: 10.1002/stc.2523.

Zhao, B., Gao, H., Wang, Z., and Lu, Z. (2018). "Shaking table test on vibration control effects of a monopile offshore wind turbine with a tuned mass damper." *Wind Energy*, 21: 1309-1328.